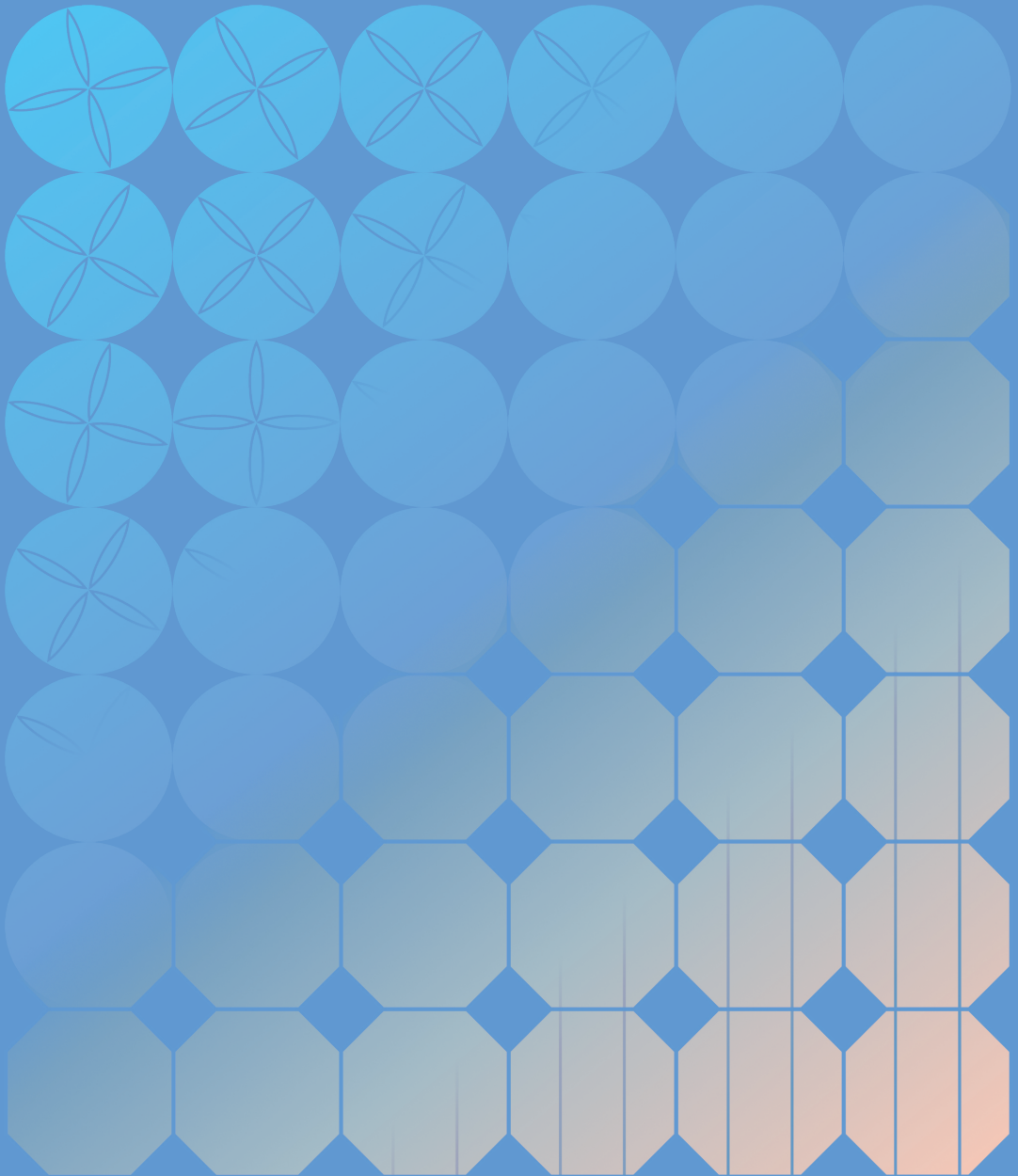


CO₂ Capture and H₂ Production



Assessment of Two Key Components for Synthetic Renewable Fuels

Alexa Grimm

CO₂ Capture and H₂ Production: Assessment of two Key Components for Synthetic Renewable Fuels

Alexa Grimm

ISBN: 978-90-393-7519-8
Cover design: Arno Schlipf, <https://arno-schlipf.info>
Print: Ridderprint | www.ridderprint.nl

Copyright © 2022 by Alexa Grimm

All rights reserved. No part of this publication may be reproduced, stored in a retrieval system, or transmitted in any form or by any means, electronic, mechanical, by photocopying, recording, or otherwise, without the prior written permission of the author.

CO₂ Capture and H₂ Production: Assessment of two Key Components for Synthetic Renewable Fuels

**CO₂-afvang en H₂-productie: Beoordeling van twee centrale
componenten voor synthetische hernieuwbare brandstoffen**

(met een samenvatting in het Nederlands)

Proefschrift

ter verkrijging van de graad van doctor aan de
Universiteit Utrecht
op gezag van de
rector magnificus, prof.dr. H.R.B.M. Kummeling,
ingevolge het besluit van het college voor promoties
in het openbaar te verdedigen op
maandag 19 december 2022 des middags te 4.15 uur

door

Alexa Grimm

geboren op 11 oktober 1988
te Malsch, Duitsland

Promotor:

Prof. dr. G.J. Kramer

Co-Promotor:

Dr. M. Gazzani

Beoordelingscommissie:

Prof. dr. M. van Sint Annaland

Prof. dr. C.A. Ramirez Ramirez

Prof. dr. C. Petit

Prof. dr. A. Rajendran

Dr. A. van der Made

To Adrian and Simon

SUMMARY

Our current energy system and infrastructure depend mainly on fossil fuels. Since these resources were created millions of years ago, on the human timescale, they are considered non-renewable. Burning fossil fuels has contributed significantly to the increase of atmospheric CO₂ from around 277 ppm to 419 ppm in the last 250 years [1], causing considerable environmental damage. Therefore, reducing the dependence on fossil fuels and limiting greenhouse gas emissions from all human activities has become one of the critical challenges of our generation. From the latest IPCC report it is clear that it is not enough to reduce carbon dioxide emissions, but to also directly remove CO₂ from the atmosphere [2]. There are a few viable negative emission technologies, with direct air capture (DAC) being one of the most promising when coupled with CO₂ storage. In addition, its captured CO₂ can be used as a source to make carbon-neutral synthetic fuels. Here, besides capturing CO₂, the other two main steps for producing a synthetic fuel are hydrogen production followed by fuel synthesis. The interest in DAC has significantly grown over the last years, within both academia and industrial environments. However, if these fuels are to play a substantial role in mitigating climate change, their costs need to decrease significantly. For the captured CO₂ using DAC, on the one hand, further optimization is needed within the process design and material development. On the other hand, the choice of the process is a major criterion for hydrogen production, including the use of more advanced electrolyzers or novel routes like photoelectrochemical cells. The aim of this thesis is to contribute to the research of carbon-neutral synthetic fuels by quantifying possible pathways for CO₂ capture from the air and H₂ production from water and identifying the most promising routes, both in terms of process performance and economics.

Beginning with a brief introduction in Chapter 1, the core of this thesis starts in Chapter 2 with a comparative technical assessment of the two main routes for capturing CO₂ from the air: aqueous scrubbing and solid-based processes. Using process simulations and mathematical optimization, energy consumption and productivity are computed consistently. The results show that all technologies can provide high purity CO₂ and that the solid-based process has the potential to offer the best performance. By translating productivity and energy performance into the cost of CO₂ capture, it is shown that capital expenditure is the main cost driver. While all technologies have the potential to operate below 200 \$ ton⁻¹_{CO₂}, the solid-sorbent process achieves this under broader conditions and becomes less dependent on the installation cost if a high mass transfer is possible. Therefore, the solid-based process

is explored in more detail. In the second part of chapter 2, the modeling and optimization are extended by including the effect of time-dependent ambient conditions, i.e., varying temperature and humidity. Based on an exemplary vacuum-temperature swing (VTSA) cycle, a stand-alone DAC system's optimal design and operation are investigated by calculating the energy consumption and the minimum system costs for multiple temperature-humidity combinations. The results show that capturing costs are significantly smaller in cold and humid conditions. Surprisingly, both capturing costs and energy requirements depend more on the ambient temperature than the humidity; this holds for sorbents where CO₂ adsorption is enhanced by water and those negatively affected by water.

The adsorbent selection plays a critical role when designing a DAC plant. The ample design space of sorbent structure and the associated capability of tailoring properties to match process requirements make adsorption-based technologies suitable candidates for CO₂ capture processes. So far, several hundreds of thousands of adsorbent materials exist in the literature, real and hypothetical, with only a few tested for DAC application. In Chapter 3, a vast database is screened to identify promising sorbents for dilute and ultra-diluted processes. For this purpose, an equilibrium-based model for rapid simulation of VTSA cycles is developed. The accuracy and prediction capabilities of the equilibrium model are improved by incorporating feed-forward neural networks, allowing to include the process productivity as a key performance indicator. The screening reveals 12 promising materials for DAC application with reasonable energy consumption and productivity performance. It is found that capturing CO₂ from dilute feed streams places different requirements on the sorbents compared to the capture from conventional large point sources. This naturally leads to the question of what an optimal sorbent for DAC should look like. Because of the diversity of phenomena concurring in adsorption processes, simple metrics like working capacity or selectivity do not necessarily translate into promising performance and costs. Moreover, capacity, regenerability, and costs are often contrasting objects that are difficult to consider in synthesizing new sorbents. Therefore, in Chapter 4, the effect of different sorbent properties on the performance of a VTSA cycle is examined, which is done by applying a *process inversion* approach, where the process performance is optimized by both including adsorbent properties and process performance parameters as decision variables. By optimizing the parameters of different CO₂ isotherm models, the design space for DAC is identified. The technical assessment is complemented by a detailed bottom-up economic analysis of the hypothetical materials. The resulting costs are in the range of 360 to over 1000 \$/tCO₂ and are strongly dependent on the assumptions for the sorbent, i.e. the purchase price and lifetime, as well as on the kinetics.

Having assessed the capture processes for CO₂, the second part of the thesis focuses on the production of H₂. To begin with, in Chapter 5, an overview of

different water splitting devices to produce H₂ using solar energy is given. To better understand photoelectrochemical water splitting in general, a modeling framework based on equivalent circuits is introduced, which allows for a computationally efficient yet precise prediction of the system performance. The results show that under real operating conditions, the solar-to-hydrogen efficiency is significantly lower than under ideal conditions. The presented model is a powerful tool for untangling the performance of photoelectrochemical water splitting devices and comparing different concepts. Following this analysis, a techno-economic analysis of two solar-assisted hydrogen production technologies is presented in Chapter 6: a photoelectrochemical (PEC) system and its main competitor, a photovoltaic system connected to a conventional water electrolyzer (PV-E). In addition, since PEC systems are not yet commercialized, the estimated costs in the economic analysis are subject to various assumptions and high uncertainty which necessitate sensitivity analyses. The results show that the levelized costs of hydrogen for the already commercialized PV-E system are considerably lower compared with the PEC system. Even under generous assumptions, PEC devices are costlier and less flexible in their application, which makes it unlikely for the PEC system to achieve lower hydrogen production costs compared to photovoltaic-electrolysis systems. Still, research into photoelectrochemical cells remains of interest.

Finally, in Chapter 7 the main findings of this thesis are summarized.

SAMENVATTING

Ons huidige energiesysteem en onze infrastructuur zijn voornamelijk afhankelijk van fossiele brandstoffen. Aangezien deze grondstoffen miljoenen jaren geleden zijn ontstaan, op de menselijke tijdschaal, worden ze op de menselijke tijdschaal als niet- hernieuwbaar beschouwd. Het verbranden van fossiele brandstoffen heeft aanzienlijk bijgedragen aan de stijging van atmosferische CO₂ van ongeveer 277 ppm tot 419 ppm in de laatste 250 jaar [1], wat ernstige milieuschade heeft veroorzaakt. Daarom is het verminderen van de afhankelijkheid van fossiele brandstoffen en het beperken van de uitstoot van broeikasgassen door menselijke activiteiten een van de belangrijkste uitdagingen van onze generatie. Uit het laatste IPCC-rapport blijkt duidelijk dat het niet volstaat de uitstoot van kooldioxide te verminderen, maar dat CO₂ rechtstreeks uit de atmosfeer moet worden verwijderd [2]. Er zijn enkele bruikbare negatieve emissietechnologieën, waarbij 'Direct Air Capture' (DAC) in combinatie met CO₂-opslag een van de meest veelbelovende is. Bovendien kan het afgevangen CO₂ worden gebruikt als bron voor het maken van koolstofneutrale synthetische brandstoffen. Naast het afvangen van CO₂ zijn de twee belangrijkste stappen bij de productie van een synthetische brandstof de waterstofproductie en de daaropvolgende brandstofsynthese. De belangstelling voor DAC is de laatste jaren sterk toegenomen, zowel in de academische wereld als in het bedrijfsleven. Indien deze brandstoffen echter een belangrijke rol zullen spelen bij het matigen van de klimaatverandering, zouden de kosten aanzienlijk moeten dalen. Enerzijds vereist CO₂-afvang met behulp van DAC een verdere optimalisering van het procesontwerp en de materiaalontwikkeling. Anderzijds is de keuze van het proces een belangrijk criterium voor de waterstofproductie, met inbegrip van het gebruik van geavanceerde elektrolytische cellen of nieuwe processen zoals foto-elektrochemische cellen. Het doel van deze proefschrift is bij te dragen tot de exploratie van koolstofneutrale synthetische brandstoffen door de mogelijke routes voor CO₂-afvang uit lucht en H₂-productie uit water te kwantificeren en de meest veelbelovende routes te identificeren in termen van zowel procesprestaties als economische aspecten.

Na een korte inleiding in hoofdstuk 1 begint het belangrijkste deel van deze proefschrift in hoofdstuk 2 met een vergelijkende technische evaluatie van de twee belangrijkste processen voor het afvangen van CO₂ uit de lucht: waterige gaswassing en processen op basis van vaste stoffen. Processimulaties en wiskundige optimalisatie werden gebruikt om het energieverbruik en de productiviteit te berekenen. Uit de resultaten blijkt dat alle technologieën CO₂ met een hoge zuiverheidsgraad kunnen produceren en dat het op vaste stof gebaseerde proces de beste prestaties levert.

Door de productiviteit en het energieverbruik te vertalen naar de kosten van CO₂-afvang wordt aangetoond dat de investeringskosten de belangrijkste kostenfactor zijn. Hoewel alle technologieën potentieel hebben om onder 200 \$ ton⁻¹_{CO₂} te werken, bereikt het op vaste stof gebaseerde proces dit onder meer diverse omstandigheden en wordt het minder afhankelijk van de installatiekosten wanneer een hoge massa-overdracht mogelijk is. Daarom wordt het proces op basis van vaste stoffen meer in detail onderzocht. In het tweede deel van hoofdstuk 2 wordt de modellering en optimalisering verder uitgebreid naar tijdsafhankelijke omgevingscondities, d.w.z. variërende temperatuur en vochtigheid. Aan de hand van een voorbeeld van een vacuümtemperatuur- wisselcyclus (VTSA) wordt het optimale ontwerp en de optimale werking van een autonoom DAC-systeem onderzocht door het energieverbruik en de minimale systeemkosten te berekenen voor verschillende temperatuur- vochtigheidscombinaties. Uit de resultaten blijkt dat de kosten voor CO₂ opvang aanzienlijk lager zijn in koude en vochtige omstandigheden. Verrassend is dat zowel de sensorkosten als de energievraag sterker afhankelijk is van de omgevingstemperatuur dan van de vochtigheid; dit geldt voor sorptiemiddelen waarbij de CO₂-adsorptie door water wordt versterkt en voor sorptiemiddelen die negatief door water worden beïnvloed.

De keuze van het adsorbens speelt een kritieke rol bij het ontwerp van een DAC-installatie. De grote ontwerpruimte van sorptiemiddelstructuur en de daarmee samenhangende mogelijkheid om eigenschappen aan te passen aan de procesvereisten maken adsorptiegebaseerde technologieën geschikte kandidaten voor CO₂-afvangprocessen. Tot op heden zijn er in de literatuur enkele honderdduizenden adsorbentia beschreven, zowel echte als hypothetische, waarvan er slechts enkele voor DAC-toepassingen zijn getest. In hoofdstuk 3 wordt een grote databank doorzocht om veelbelovende adsorbentia voor verdunde en ultraverdunde processen te identificeren. Daartoe wordt een op evenwicht gebaseerd model ontwikkeld voor de snelle simulatie van VTSA-cycli. De nauwkeurigheid en het voorspellend vermogen van het evenwichtsmodel worden verbeterd door de integratie van neurale netwerken, waarmee het mogelijk is de productiviteit van het proces als een belangrijke prestatie-indicator te berekenen. Uit de screening komen 12 veelbelovende materialen voor DAC-toepassingen met een redelijk energieverbruik en een redelijke productiviteit naar voren. Het is aangetoond dat het afvangen van CO₂ uit verdunde stromen andere eisen stelt aan de sorbentia dan het afvangen uit conventionele grote puntbronnen. Dit leidt tot de vraag hoe een optimaal sorptiemiddel voor DAC eruit moet zien. Door de diversiteit aan verschijnselen die zich bij adsorptieprocessen voordoen, vertalen zich eenvoudige maatstaven als werkcapaciteit of selectiviteit niet noodzakelijkerwijs in prestaties en kosten. Bovendien zijn capaciteit, regenereerbaarheid en kosten vaak tegenstrijdige doelstellingen die moeilijk in aanmerking kunnen worden genomen bij de synthese van nieuwe sorbentia. Daarom wordt in hoofd-

stuk 4 het effect van verschillende sorbent eigenschappen op de prestaties van een VTSA-cyclus onderzocht. Dit wordt gedaan door een procesinversie benadering toe te passen, waarbij de procesprestatie wordt geoptimaliseerd door zowel de adsorbent parameters als de procesparameters te integreren als beslissingsvariabelen. Door het optimaliseren van de parameters voor verschillende CO₂-isothermmodellen, wordt de ontwerpruimte voor DAC geïdentificeerd. De technische evaluatie wordt aangevuld met een gedetailleerde economische bottom-up analyse voor hypothetische materialen. De daaruit voortvloeiende kosten bedragen tussen 360 en meer dan 1000 \$/t_{CO₂} en zijn sterk afhankelijk van de veronderstelde sorptiemiddelen, d.w.z. de aankoop prijs, de levensduur, en de kinetica.

Na de evaluatie van de processen voor het afvangen van CO₂, richt het tweede deel van het proefschrift zich op de productie van H₂. Om te beginnen wordt in hoofdstuk 5 een overzicht gegeven van verschillende watersplittingsinstallaties voor de productie van H₂ met behulp van zonne-energie. Om de foto-elektrochemische watersplitsing beter te begrijpen wordt een modelleerkader op basis van equivalente schakelschema's geïntroduceerd, die een rekenkundig efficiënte en toch nauwkeurige voor-spelling mogelijk maakt van de systeemprestatie. Uit de resultaten blijkt dat onder reële bedrijfsomstandigheden het rendement van waterstof op zonne-energie aanzienlijk lager is dan onder ideale omstandigheden. Het gepresenteerde model is een krachtig instrument om de prestaties van foto-elektrochemische watersplittingsystemen te ontcijferen en om verschillende concepten met elkaar te vergelijken. Na deze analyse volgt in hoofdstuk 6 een technisch-economische analyse van twee technologieën voor waterstofproductie met behulp van zonne-energie: een foto-elektrochemisch (PEC) systeem en zijn voornaamste concurrent, een fotonvoltaïsch systeem gekoppeld aan een conventionele waterelektrolyse-installatie (PV-E). Aangezien de PEC-systemen nog niet op de markt zijn, zijn de geraamde kosten van de economische analyse gebaseerd op verschillende aannames en grote onzekerheden die gevoeligheidsanalyses noodzakelijk maken. Uit de resultaten blijkt dat de 'levelized costs' van waterstof voor het reeds gecommercialiseerde PV-E systeem aanzienlijk lager zijn in vergelijking met het PEC-systeem. Zelfs bij genereuze veronderstellingen zijn PEC-apparaten duurder en minder flexibel in hun toepassing, waardoor het onwaarschijnlijk is dat met het PEC-systeem lagere kosten voor waterstofproductie kunnen worden bereikt dan met fotonvoltaïsche elektrolysesystemen. Desalniettemin blijft het onderzoek naar foto-elektrochemische cellen van belang.

Tot slot worden in hoofdstuk 7 de belangrijkste resultaten van dit proefschrift samengevat.

CONTENTS

1	INTRODUCTION	1
1.1	Capture of carbon dioxide	3
1.2	Solar hydrogen production	5
1.3	Research objectives and thesis structure	5
2	A COMPARATIVE ENERGY AND COSTS ASSESSMENT AND OPTIMIZATION FOR DIRECT AIR CAPTURE TECHNOLOGIES	9
2.1	Introduction	10
2.2	Process schemes and methodology	13
2.3	Multi-objective optimization	24
2.4	Economic evaluation	27
2.5	Results and discussion	27
2.6	Processes comparison and economic evaluation	37
2.7	Conclusions	43
2.8	Direct Air Capture Processes at Varying Ambient Conditions	44
3	A MACHINE LEARNING-AIDED EQUILIBRIUM MODEL OF VTSA PROCESSES FOR SORBENTS SCREENING APPLIED TO CO ₂ CAPTURE FROM DILUTED SOURCES	57
3.1	Introduction	58
3.2	Equilibrium model for VTSA	60
3.3	Model Validation	71
3.4	Sorbents Screening	80
3.5	Discussion	86
3.6	Conclusions	87
4	HOW DOES AN IDEAL SORBENT IMPROVE THE TECHNICAL AND ECONOMIC PERFORMANCE OF DAC?	89
4.1	Introduction	89
4.2	Methodology	92
4.3	Results optimizing isotherm parameters	100
4.4	Cost Assessment	107
4.5	Discussion	112
4.6	Conclusions	112
5	MODELING PHOTOVOLTAIC-ELECTROCHEMICAL WATER SPLITTING DEVICES FOR THE PRODUCTION OF HYDROGEN UNDER REAL WORKING CONDITIONS	115
5.1	Introduction	116
5.2	Modeling PV-EC systems with equivalent electric circuit	119

5.3	Comparison of PV-EC cells under varying working conditions	131
5.4	Conclusion	136
6	RENEWABLE HYDROGEN PRODUCTION: A TECHNO-ECONOMIC COMPARISON OF PHOTOELECTROCHEMICAL CELLS AND PHOTOVOLTAIC-ELECTROLYSIS	137
6.1	Introduction	138
6.2	Methodology	138
6.3	Component-level technical analysis and cost assessment	141
6.4	Results and discussion	148
6.5	Conclusion	155
7	SUMMARY AND CONCLUSION	157
7.1	Recommendations	160
7.2	Outlook	161
A	APPENDIX FOR CHAPTER 2	165
B	APPENDIX FOR CHAPTER 3	211
C	APPENDIX FOR CHAPTER 4	239
D	APPENDIX FOR CHAPTER 5	267
	BIBLIOGRAPHY	277

PUBLICATIONS

This dissertation is based on the following articles.

1. Grimm, A., de Jong, W. A. & Kramer, G. J. Renewable hydrogen production: A techno-economic comparison of photoelectrochemical cells and photovoltaic-electrolysis. *International Journal of Hydrogen Energy* **45**, 22545 (2020).
2. Sabatino, F., Grimm, A., Gallucci, F., van Sint Annaland, M., Kramer, G. J. & Gazzani, M. A comparative energy and costs assessment and optimization for direct air capture technologies. *Joule* **5**, 2047 (2021).
3. Grimm, A., Sainte-Marie, A., Kramer, G. J. & Gazzani, M. Modeling photovoltaic-electrochemical water splitting devices for the production of hydrogen under real working conditions. *International Journal of Hydrogen Energy* **47**, 11764 (2022).
4. Grimm, A. & Gazzani, M. A machine learning-aided equilibrium model of VTSA processes for sorbents screening applied to CO₂ capture from diluted sources. *Industrial & Engineering Chemistry Research* **61**, 14004 (2022).
5. Wiegner, J., Grimm, A., Weimann, L. & Gazzani, M. On the optimal design and operation of solid sorbent direct air capture processes at varying ambient conditions. *Industrial & Engineering Chemistry Research* **61**, 12649 (2022).
6. Grimm, A., Kramer, G. J. & Gazzani, M. How does an ideal sorbent improve the technical and economic performance of DAC? *in preparation* (2022).

Author's contribution

Alexa Grimm is the principal author and investigator of publications 1, 3, 4 and 6. The authorship for publication 2 is shared with Francesco Sabatino. Both authors contributed equally and thus share the first authorship. While they have both worked on all DAC technologies presented in the paper, A. Grimm led the work on adsorption-based technologies, while F. Sabatino led the work on absorption-based technologies.

The principal author of publication 5 is Jan Wiegner, who was responsible for the framework and the planning of the work. Alexa Grimm provided all the simulated data for the direct air capture processes and was involved in planning the different humidity and temperature cases. The development of the Mixed Integer Linear Program was developed by Jan Wiegner. In addition, this publication includes a section about integrating direct air capture units in a multi-energy system, for which Jan Wiegner takes the primary responsibility with help from Lukas Weimann. Since

Alexa Grimm was not part of this section, it is not printed in the present thesis but can be found in the original publication.

Other publications:

1. Sabatino, F., Mehta, M., Grimm, A., Gazzani, M., Gallucci, F., Kramer, G. J. & Van Sint Annaland, M. Evaluation of a Direct Air Capture Process Combining Wet Scrubbing and Bipolar Membrane Electrodialysis. *Industrial and Engineering Chemistry Research* (2020).
2. Wenderich, K., Kwak, W., Grimm, A., Kramer, G. J., Mul, G. & Mei, B. Industrial feasibility of anodic hydrogen peroxide production through photoelectrochemical water splitting: a techno-economic analysis. *Sustainable Energy & Fuels* (2020).
3. Weimann, L., Grimm, A., Nienhuis, J., Gabrielli, P., Kramer, G. J. & Gazzania, M. Energy System Design for the Production of Synthetic Carbon-neutral Fuels from Air-captured CO₂ (2020).

INTRODUCTION

This chapter introduces synthetic fuels and the process route from the two components, CO_2 and H_2O , to carbon-neutral synthetic fuels. The reader is introduced to the basic concepts of capturing CO_2 from the air as well as solar hydrogen production from water, which will be the two main topics of this thesis. Finally, the scope and the outline of the thesis are presented.

Historical records show a substantial increase of the CO₂ concentration in the atmosphere from pre-industrial values of around 277 ppm to 419 ppm by June 2022, an increase of nearly 51% [1, 3]. The increase of CO₂ emissions originates mainly from the use of fossil fuels and amounts to around 33 GtCO₂/year [4]. Today, it is widely accepted that an increase in CO₂ concentrations in the atmosphere contributes to global warming, yet a decrease in fuel use is not expected; on the contrary, the world energy use is predicted to increase in the coming years [4]. The Paris Agreement was designed to keep the global temperature increase below 2 °C, and possibly below 1.5 °C [5]. To avoid an overshoot, many scientists and governments agree that net zero needs to be achieved by 2050, i.e. a balance between the anthropogenic net greenhouse gas (GHG) emissions and the absorbed greenhouse gas emissions by sinks [6]. Besides reducing the use of fossil fuels and increasing energy efficiency, the removal of CO₂ from large point sources and the atmosphere, i.e. Carbon Capture and Storage (CCS), is an essential approach to mitigate climate change [3]. Another pathway is carbon capture and utilization (CCU), which includes the recycling of CO₂ to fuels and other materials, also called power-to-X [7, 8]. These synthetic fuels can be used for decarbonizing e.g. the transport sector, especially in areas where only a few low-carbon alternatives exist, such as heavy-duty vehicles, aviation, and maritime shipping [9].

Inspired by nature, taking the three feedstocks, i.e. CO₂, H₂O and solar energy, an integrated device can be used, where solar energy conversion and the synthesis of the fuel are combined in one step. These devices, which mimic the function of natural photosynthesis, are called artificial photosynthesis or artificial leaf. In recent years, the interest in realizing this technology has grown [10, 11]; however, the reaction chemistry is complex, and the technical implementation is still in its infancy. Another route for the production of synthetic fuels is the reduction of CO₂ and H₂O to CO and H₂, respectively, followed by catalytic conversion to the desired fuel.

In general, three main steps are required to produce a sustainable hydrocarbon solar fuel: solar water splitting for the production of H₂, carbon capture, and fuel synthesis [12]. For the latter proven industrial technologies can be employed, and depending on the process, different fuels can be synthesized, e.g. methane (via methanation), methanol (via methanol synthesis), or petrol/diesel/jet fuel (via Fischer-Tropsch or Methanol-to-Gasoline synthesis) [13, 14]. The other two main steps, i.e. water splitting for H₂ production and capturing of CO₂, are the most energy- and cost-intensive steps of the chain and are introduced in the following sections.

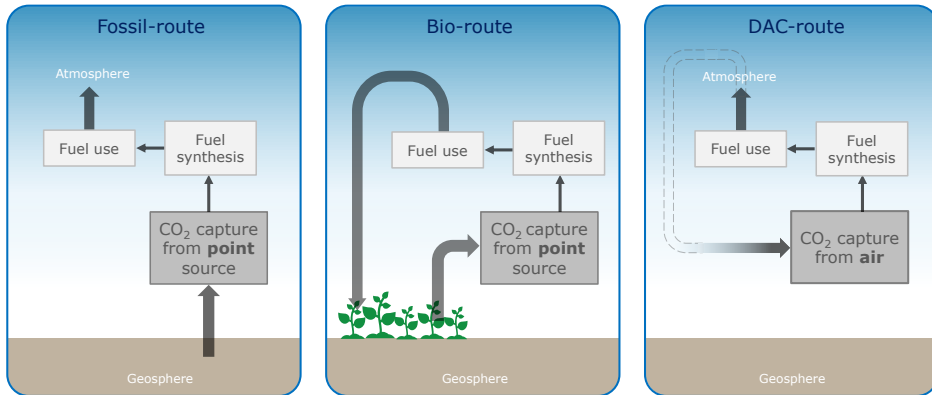


FIGURE 1.1: Three different routes for capturing CO_2 with a) fossil fuels, b) biomass, and c) the ambient air as resources.

1.1 CAPTURE OF CARBON DIOXIDE

Figure 1.1 gives a schematic overview of three different routes for capturing CO_2 from different sources. The fossil route includes capturing the CO_2 from a point source powered by fossil fuels, e.g. a coal power plant but also cement and aluminum factories. Although capturing CO_2 from point sources is an important capture process for mitigating climate change when CO_2 is permanently stored, either underground or as a mineral, this route cannot be seen as a sustainable route for the production of synthetic fuels since it includes the combustion of fossil resources. Within the second route, biomass is burned in a power plant, and the emitted CO_2 is captured from the flue gas. Although the resulting biogenic CO_2 is consistent with net-zero systems, drawbacks are the slow-growing of suitable plants and burning biomass is competing with other utilization possibilities of biomass. The third route represents capturing CO_2 directly from the ambient air, which, when powered by renewable energies, can be considered a sustainable route.

Compared to the emitted CO_2 from point sources, the CO_2 in the air is a location-independent source. While flue gases typically have a CO_2 concentration of 5-15% for power plants and between 15-30% for the cement and steel industry [15], the concentration of CO_2 in the ambient air is significantly lower with around 0.04 vol%. Still, although the concentration is more than 100 times smaller, the energy consumption is not multiplied by this factor, as shown in Figure 1.2. Here, the exergy consumption for different capture processes from point sources is compared with a

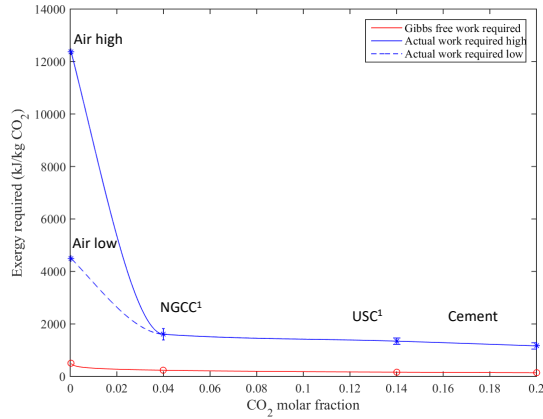


FIGURE 1.2: Energy requirement DAC. Energy for post-combustion from [16].

typical range for the DAC case. From a theoretical perspective, the minimal energy required to separate one mole of CO_2 from the air at ambient conditions (expressed by the Gibbs free energy) is 497 kJ/kg CO_2 , while capturing from point-sources requires 30-50% less energy (150-250 kJ/kg CO_2). In practice, real processes require larger amounts of energy. For capture plants from point sources, the exergy demand is in the area of 1.6-1.9 MJ/kg CO_2 [16] while the estimated exergy demand for DAC range from about 4-12 MJ/kg CO_2 . This comparison shows no thermodynamic limit for capturing CO_2 from the air. Besides the energy consumption, another major challenge for DAC is the processing of large volumes of air, which depends on the reactor's design and the process engineering.

There exist two main technological pathways to implement DAC: one makes use of established liquid solvents, e.g. potassium-based alkaline solutions, where CO_2 is removed in a classical liquid scrubbing process. The research group of Keith, among the others, at Harvard University is working on such a process, while the company Carbon Engineering is developing an alkaline hydroxide process commercially. The second major pathway is using a solid sorbent to separate the CO_2 from the air. Several research groups are working on this capture technology, e.g. the group of Jones at Georgia Tech or the group of Lackner at Arizona State University. The company Climeworks has realized this technology within two pilot plants in Switzerland and Iceland.

1.2 SOLAR HYDROGEN PRODUCTION

The global demand for hydrogen is expected to grow within various sectors such as power, heating, industry, and transportation [17]. Still, at present, over 95% of the global hydrogen production is made from fossil fuel feedstock [17, 18]. It is possible to combine hydrogen production from natural gas with CO₂ capture, transport and storage (CCS), resulting in low-carbon hydrogen [19]. The current alternative is to produce hydrogen from water via electrolysis. Using carbon-free electricity such as wind, solar, or hydropower as input results in renewable hydrogen. Here, we will focus on the use of solar-powered technologies; the produced hydrogen is then called solar hydrogen. The main water electrolysis technologies are alkaline electrolysis (AEL), proton exchange membrane electrolysis (PEMEL), and solid oxide electrolyzer cell (SOEC). While these devices are mature and benefit from modularity, i.e. they consist of at least two components, one for collecting the light and one for splitting the water, they therefore require at least two housing and support structures. An alternative is to use integrated devices that combine light absorption and water splitting in a single component, which can simplify the architecture. These so-called photoelectrochemical devices (PEC) are less mature and not yet commercially available but are potentially a sustainable and affordable solution to produce solar hydrogen.

1.3 RESEARCH OBJECTIVES AND THESIS STRUCTURE

The availability of cheap and abundant CO₂ and H₂ as reactants is indeed the main hurdle for the production of synthetic solar fuels which leads to the overarching question of this thesis: *What are the technical limits of CO₂ capture from air and H₂ generation from H₂O?*

There exist several technological pathways to supply the two initial components for hydrocarbon synthetic fuels, i.e. capturing CO₂ from fossil power plants or the ambient air, and water splitting to produce H₂, but the uncertainties are high in terms of technical performance and economic feasibility. Therefore, the research reported in this thesis addresses these two key components for the production of solar fuels: i) carbon dioxide obtained from the air and ii) hydrogen produced from water using solar energy. The aim is to assess different routes for the supply of CO₂ and H₂ in terms of technological and economic performance, and to identify the key challenges for bringing down the costs. To achieve the research objective, the following research questions, summarized in Table 1.1, are formulated:

1. Which are the main technological pathways to capture CO₂ from the air and how do they compare in terms of performance and economics?

There exist three main technologies for capturing CO₂ from the air, i.e. two aqueous scrubbing processes based on potassium hydroxide or alkanolamines, and one solid-sorbent process. In **Chapter 2** these technologies are studied in detail using process simulations and mathematical optimization. The comparison is based on the energy consumption and productivity, which are computed consistently, followed by an evaluation of the costs. In addition, a comparison between absorption, i.e. the use of a liquid solvent, and adsorption, i.e. the use of a solid sorbent, for DAC application is reported. While this extensive study revealed no clear winner, the solid sorbent process showed the most promising potential in terms of process performance and economics. Therefore, this process route is investigated in more detail. First, the performance of a DAC process under real weather conditions is investigated in the second part of **Chapter 2**. Here, the effect of varying ambient conditions, i.e. temperature and humidity, on the performance of a vacuum temperature swing adsorption (VTSA) process at different locations is studied.

While there exist huge databases with several hundreds of thousands of adsorbent materials, there is only a small number studied for the application in DAC processes. Therefore, the next question which arises is:

2. Are there already existing adsorbents in databases that show promising performance for DAC applications, and how can we find them across several thousands of possible structures?

This question is addressed in **Chapter 3**. An equilibrium model for VTSA cycles is developed, which is suitable for large throughput sorbents screening. The accuracy and prediction capabilities of the equilibrium model are improved by incorporating feed-forward neural networks. The model is then applied to screen and identify promising sorbents for capturing CO₂ from dilute streams. Analysing existing materials naturally leads to the next question:

3. *What are the performance and cost limits for DAC using an ideal adsorbent with VTSA?*

Following the results of the screening, in **Chapter 4** a theoretical experiment is carried out to identify the limits of VTSA when capturing CO₂ from dilute streams. Process conditions together with isotherm parameters are used as decision variables for the optimization. The effect of adsorption kinetics and physical properties of the sorbent is investigated. In addition, the cost performance of the hypothetical adsorbents is compared with existing materials and it is investigated what it would take to bring the DAC costs below 100 \$/t_{CO₂}.

Having analyzed the supply of CO₂ by sequestration from the air, the following research questions concern the production of H₂ from water using solar energy. To begin with, the following question is formulated:

4. *What technologies are available for electrochemical production of hydrogen from solar energy and water, and how do they operate under real working conditions?*

This question is addressed in **Chapter 5**. First, an overview over possible technologies is given and the most promising one, a photoelectrochemical (PEC) device, is selected for further assessment. An equivalent circuit model is developed to compute the steady-state performance of several different PEC devices. Given the infancy stage of the PEC technology, most experiments are carried out under ideal laboratory conditions. Therefore, in a second step, the model is adapted to handle real light operating conditions. Besides innovative solutions like integrated PEC devices, it is also possible to produce H₂ from water using stand-alone electrolyzers and PV panels (PV-E), a more mature technology. With this in mind, the following question is formulated:

5. *What is the techno-economic performance of PEC and PV-E systems, and how do they compare?*

In **Chapter 6** a techno-economic analysis of the two solar-assisted hydrogen production technologies is carried out: a photoelectrochemical (PEC) system and a more mature photovoltaic system connected to a conventional water electrolyzer (PV-E). A comparison based on the levelized cost of hydrogen is performed to identify the more promising technology.

Finally, the research questions are answered in **Chapter 7** and a brief summary of this work is given .

TABLE 1.1: Overview of the chapters and their corresponding research questions and publications (P).

Chapter	Topic	Research questions and relevant publications				
		Q1	Q2	Q3	Q4	Q5
2	Comparative energy and costs assessment of DAC technologies	x P2, P5				
3	Equilibrium model for VTSA processes		x P4			
4	Ideal sorbent analysis			x P6		
5	Techno-economic comparison of PEC devices				x P1	
6	Modeling PV-EC devices under real working conditions					x P3

2

A COMPARATIVE ENERGY AND COSTS ASSESSMENT AND OPTIMIZATION FOR DIRECT AIR CAPTURE TECHNOLOGIES

This chapter provides a comparative technical assessment of three technologies for CO₂ removal from air: two aqueous scrubbing processes based on potassium hydroxide or alkanolamines, and one solid-sorbent process. Using process simulations and mathematical optimization we consistently compute exergy and energy consumption, and productivity. Moreover, we evaluate the cost range and discuss the challenges that need attention for large-scale implementation. We show that all technologies can provide high purity CO₂, and that the solid-based process has the potential to offer the best performance, having a specific exergy demand of Translating productivity and energy performance into cost of CO₂ capture via a simple model, we show that the capital cost is the main cost driver. All technologies have the potential to operate below 200 \$ ton_{CO₂}⁻¹ under favorable, yet realistic, energy and reactor costs. The solid-sorbent process achieves this under broader conditions, and becomes less dependent on the installation cost if high mass transfer is possible.

The results presented in the main part of this chapter are reported in: Sabatino, F., Grimm, A., Gallucci, F., van Sint Annaland, M., Kramer, G. J., Gazzani, M. A comparative energy and costs assessment and optimization for direct air capture technologies. *Joule* 5, 2047 (2021). The results of section 2.8 are part of: Wiegner, J., Grimm, A., Weimann, L., Gazzani, M. On the optimal design and operation of solid sorbent direct air capture processes at varying ambient conditions. *Industrial & Engineering Chemistry Research* (2022).

2.1 INTRODUCTION

Currently, there exist a few processes that can be used for capturing CO_2 from the air. Frank Zeman and Klaus Lackner were the first to describe a process in which CO_2 is extracted from air through wet scrubbing with an aqueous alkali hydroxide [20]. This DAC system consists of two cycles. In the first one, sodium or potassium hydroxide reacts with carbon dioxide to produce carbonates, which are soluble in water. In the second cycle, the carbonates are causticized with lime (i.e. $\text{Ca}(\text{OH})_2$) resulting in the precipitation of CaCO_3 , which is finally heated above 900°C to release CO_2 . This concept was further developed by Baciocchi et al. [21], who provided the first conceptual design based on mass and energy balances. Several issues were pointed out, the most important being the high and essentially unavoidable energy demand of the solvent regeneration. Later, in a report by the American Physical Society (APS) alkali scrubbing was selected as the benchmark process for DAC; they estimated a cost of about \$600 per ton of CO_2 captured [22]. Later estimates based on a different absorption unit design are, however, lower. Due to the concentration of CO_2 in the atmosphere, large volumes of air have to be processed to capture a relevant amount of carbon dioxide. Hence, efficient air contact with the solvent is extremely important. This is where the DAC company Carbon Engineering has focused the early development efforts. By using a different design of the absorption unit, tailor-made for air capture applications, Holmes and coworkers estimated that the total costs of the air contactor alone (that is, neglecting the costs for the regeneration of the solvent) could be drastically reduced from the 240 $\$/\text{ton}_{\text{CO}_2}$ assessed by the APS [22] to 60 $\$/\text{ton}_{\text{CO}_2}$ [23]. The air contactor [24] and some of the units involved in the solvent regeneration [25] have also been tested at pilot scale with promising results, prompting Carbon Engineering to plan the construction of a 1 $\text{Mton}_{\text{CO}_2}/\text{year}$ DAC plant. However, the major drawbacks related to the caustic recovery of the alkali hydroxide have not been overcome and alternative regeneration techniques show limited potential [26].

An alternative absorption-based DAC process has been described by Custelcean et al. [27]. In this process CO_2 is extracted from air by an aqueous solution of amino acids, such as glycine or sarcosine, yielding the corresponding bicarbonate salts. The amino acid is subsequently recovered by crystallization of the carbonate anions with a bis-iminoguanidine solid. Finally, the carbonate crystals are decomposed at temperatures between 60 and 120°C , thus releasing high purity CO_2 . While the temperature required for the regeneration of the solvent is lower compared to the alkali scrubbing process, the energy demand of the process proposed by Custelcean et al. is higher [28]. Indeed, amino acid solvents provide fast absorption kinetics, but low cyclic capacity.

Surprisingly, liquid scrubbing via alkanolamines (e.g. monoethanolamine - MEA) have been hardly considered for applications in DAC. In fact, amine scrubbing is the benchmark technology for post combustion CO₂ capture, and has been applied in hundreds of gas separation processes [29]. In its basic form, the process consists of the extraction of CO₂ from (flue) gases near ambient temperature with an aqueous solution of amines, followed by regeneration of the solvent through stripping at about 120°C. Alkanolamines have a high affinity for CO₂, which is enough for CO₂ capture from air [30]. Despite this, liquid scrubbing with MEA has only very recently been assessed as an option for DAC. Barzagli et al. have conducted an experimental screening of amine-based solutions as solvents for DAC [31]. Aqueous primary amines appeared to be the best candidates, with MEA capturing 87.3% of CO₂ from air in a 24 hours period. Kiani et al. have carried out a simulation study and economic evaluation in Aspen Plus, adapting the conventional MEA-based absorption process for the capture of CO₂ from air [32]. The total estimated cost for this process was, in the base case, 1690 \$/ton_{CO₂}. The high cost is substantially due to the high capital expenditure required for the absorption column, but Kiani et al. have adopted a conventional packed column as absorber, which is not an optimal design for DAC. In fact, they report that using a cooling tower inspired system, as the one designed by Carbon Engineering, could reduce the cost of the absorber by 83%. It however remains that amine scrubbing requires great amounts of low-grade heat for regeneration, and that amines are generally corrosive and toxic and degrade over time due to oxidation [33].

These disadvantages can partly be overcome through immobilization of amines on solid supports. By exchanging H₂O with a solid support with lower heat capacity, the amount of energy required to regenerate the amines can be reduced significantly [34]. Moreover, degradation and corrosion in supported amine are less of a problem [35]. In fact, amine-functionalized sorbents are currently receiving significant attention in the DAC scientific community [36, 37], and early DAC companies adopted them for their commercial processes. Among them, Climeworks proposed porous granulates modified with amines applied in vacuum-pressure temperature swing adsorption (VTSA) cycles [38]. In this process, unloaded sorbent material is contacted with air to capture carbon dioxide at ambient condition; subsequently, the unit is evacuated to a pressure in the range of 20–400 mbar and heated to a temperature of 80–130°C to desorb CO₂ [39]. The combination of vacuum and temperature allows for a higher cyclic capacity, therefore limiting the amount of sorbent needed. Finally, the unit is repressurized and cooled down to ambient conditions. Climeworks and Global Thermostat are two established startups developing and commercializing such DAC processes, with multiple pilot plants already running or being built [40]. In addition to the specific sorbents, which differ in composition and structure, the two companies have opted for different contactors: while Climeworks employs air-filter

like structures [41], Global Thermostat uses honeycomb monoliths [42]. In both cases, a VTSA cycle is used as process.

Another class of solid materials that has shown promising performances both as sorbents [43, 44] and supports [45, 46] are metal-organic frameworks (MOFs). MOFs are hybrid structures with metal nodes linked by organic bridges in bi- or three-dimensional crystalline structures. Their large design space and versatility have made MOFs good candidates for various gas-separation applications: surface area and pore characteristics can be tailor-tuned and open metal sites allow for additional functional groups. On the other side, production and commercialization of MOFs at large scale is still an unsolved challenge [47].

An important point that need attention when considering solid sorbents is the behavior with respect to water adsorption. Depending on the ambient conditions and the solid characteristics, H_2O can affect the adsorption of CO_2 and therefore the process productivity and energy requirements. More specifically, it is important to obtain high quality experimental data and implement a suitable model for water competitive or cooperative adsorption [35, 48]. So far, this point has largely been overlooked in open scientific literature.

We can conclude that two DAC technologies stand out in light of the scale at which they have been deployed and the technological readiness they have achieved: wet scrubbing with aqueous alkali hydroxide solutions [25] and VTSA on supported sorbents [49]. Moreover, we argue that MEA scrubbing should also be regarded as an equally ready DAC technology. These processes have different advantages and disadvantages. Liquid scrubbing is a continuous process that can take advantage of mature and inexpensive components. The regeneration is, however, costly and complex, especially for alkali solvents. The VTSA process is in principle simpler, since the CO_2 capture and the sorbent regeneration are carried out in the same unit. Moreover, the regeneration of the sorbent takes place at low temperature. On the other hand, the process is not as mature as liquid scrubbing, the sorbent stability is still an issue and achieving high CO_2 purity requires customized and more energy-demanding cycles.

Choosing between these two approaches and prioritizing their research and development is therefore not trivial; the projected cost of both technologies once deployed at large scale has been estimated to be around \$100 per ton of CO_2 captured [40]; while this value might be too optimistic, \$200 per ton of CO_2 is a likely target that DAC companies are pursuing. However, it remains unclear what specific actions need to be taken to get there and where improvements are most needed.

With this chapter we provide a thorough process analysis for aqueous- and solid-based DAC technologies. We do this by coupling advanced rate-based process modelling with mathematical multi-objective process optimization. For the thermo-

dynamic modelling, we use Aspen Plus for liquid solvents, and a state-of-the-art in house code for fixed bed cycles with solid sorbents [50]. For the process optimization, we directly connect the first-principles rate-based models to Matlab, where we use suitable mathematical algorithms to identify the optimal design. As a result, we are able to compute the specific energy consumption [$\text{MJ kg}_{\text{CO}_2}^{-1}$] and CO_2 productivity [$\text{kg}_{\text{CO}_2} \text{m}^{-3} \text{h}^{-1}$] starting from thermodynamic models of specific reactor designs, which are adopted from existing pilot plants. These two key performance indicators (KPI) provide the required input for a simplified cost model that, despite its simplicity, is able to clearly map the main contributions to the total specific cost [$\text{\$ kg}_{\text{CO}_2}^{-1}$] and the directions to follow for further improvements, e.g. benefits from reduction in fixed costs vs. reduction in operating costs. When comparing to existing literature, although a few techno-economic analyses of DAC have been published, they either rely on simple process models [51], or on energy assumptions from literature [40, 52], or analyze a single process [32, 53–55]. In addition, we here consider the presence of water and its co-adsorption. Accordingly, this chapter advances compared to existing literature as it (i) provides a detailed model-based comparison of the key DAC processes, (ii) assesses the potential of each DAC process via process models and optimization, (iii) identifies the main weak points of the selected technologies, thus providing input for future R&D, and (iv) quantifies how process/material improvements could enhance the performance.

This chapter is organized as follows. In Section 2.2 we describe the considered DAC processes and the modelling approach adopted for their analysis. This is complemented by an exhaustive supplemental information document. In Section 2.3 we describe the process optimization and in Section 2.4 the economic analysis methodology. In Section 2.5 we present the main results. Finally, in Section 2.6 and 2.7 we discuss the results and summarize the main conclusions, respectively.

2.2 PROCESS SCHEMES AND METHODOLOGY

Alkali Scrubbing

The alkali scrubbing process is shown in Figure 2.1. The process has been thoroughly discussed in past literature [20, 21, 25], however, it has never been systematically optimized. Here, we shortly discuss the process features, especially in light of modelling and optimization, while the reader can refer to literature or the SI for more details on the process units.

In the alkali scrubbing, carbon dioxide is captured in a dedicated air contactor unit, where it is absorbed in an aqueous solution of KOH in the form of K_2CO_3 . The K_2CO_3 solution is regenerated by forming calcium carbonate, which is then fed to a calciner and decomposed to CaO and CO_2 . In this work, the whole process is

modelled using Aspen Plus V11, which allows for precise computation of relevant thermodynamics via the electrolyte NRTL method while also providing a reliable rate-based model (available within *radfrac*).

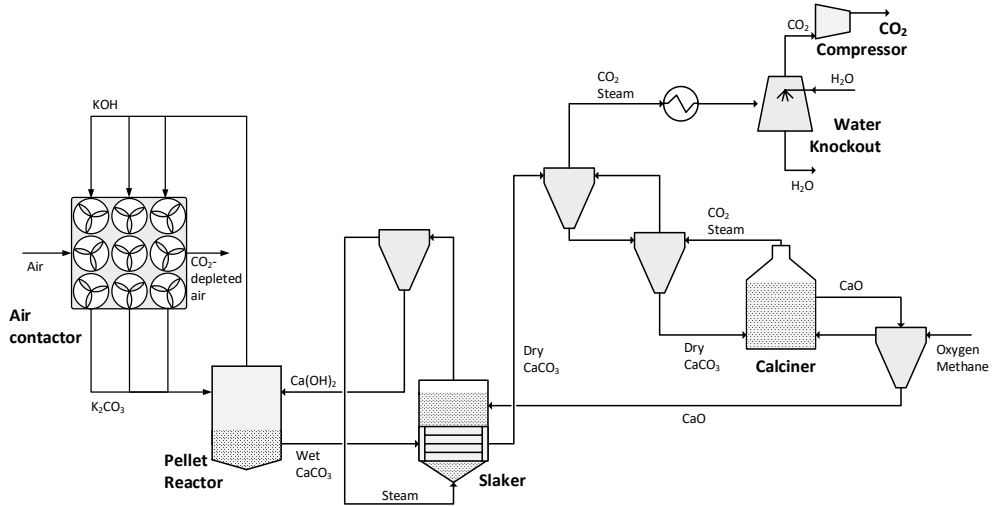
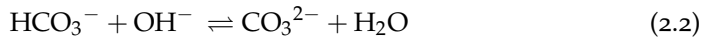


FIGURE 2.1: Schematic representation of the alkali scrubbing DAC process.

The absorption mechanism of carbon dioxide in alkaline solutions is well known and takes place through a two-step process [56]:



The rate-limiting step of the absorption mechanism is represented by Equation 2.1. This mechanism is common to all alkali hydroxide sorbents, but it is reported that KOH provides the fastest kinetics [24, 57]. In our simulations, we consider the air contactor design developed by Carbon Engineering [23], who adapted commercial cooling tower technologies to fit liquid scrubbing for DAC application (see SI for additional details). Notably, such original units are devised to efficiently bring very large quantities of ambient air into contact with water. The kinetics for the absorption reactions have been adapted from the work of Pinsent et al. [58], while pressure drops are estimated using the built-in correlations in Aspen Plus for the selected packing.

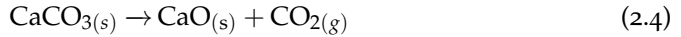
The regeneration of the solvent and collection of CO₂ are carried out through a calcium-based thermo-chemical cycle, a process that has been adapted from the Kraft pulping widely used in the paper industry [59]. The CO₂-rich solution coming

from the air contactor is fed to the pellet reactor, where K_2CO_3 is converted back to KOH through causticization with lime according to the following reaction:

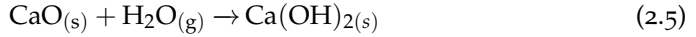


Calcium carbonate has an extremely low solubility in water and, therefore, precipitates and it is easily separated from the liquid phase, which is sent back to the air contactor. However, the rate of Reaction 2.3 is driven by the concentration of Ca^{2+} ions, which is low in highly alkaline solutions due to the low solubility of $Ca(OH)_2$ in these conditions [20]. This could be an issue, as the CO_2 -rich solution coming from the air contactor still contains a considerable amount of KOH, but it can be tackled by having calcium hydroxide as the limiting reactant and by long residence times in the pellet reactor [25, 60].

The wet $CaCO_3$ particles are collected from the bottom of the pellet reactor and are dried and pre-heated before being fed to the calciner, where CO_2 is released upon decomposition of calcium carbonate:



The final step of the regeneration cycle is carried out by the slaker, where the hydration of CaO to $Ca(OH)_2$ takes place according to:

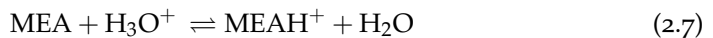


The design of the regeneration process and the performances of the unit operations comprising it have been based upon the data published by Keith et al. [25]. Key parameters used for modelling the alkali scrubbing process are reported in the Supplemental Information in Table A.1.

Amine Scrubbing

The amine scrubbing process differs from the alkali scrubbing in the regeneration section, where it is considerably simpler. The process layout is shown in Figure 2.2.

The air contactor designed by Carbon Engineering is adopted also in this case, as it provides a clear advantage over conventional absorption columns. The chemical absorption of CO_2 in the aqueous MEA solution takes place via reaction with the hydroxide ion (Equation 2.1 and 2.2) and according to the following reactions [61]:



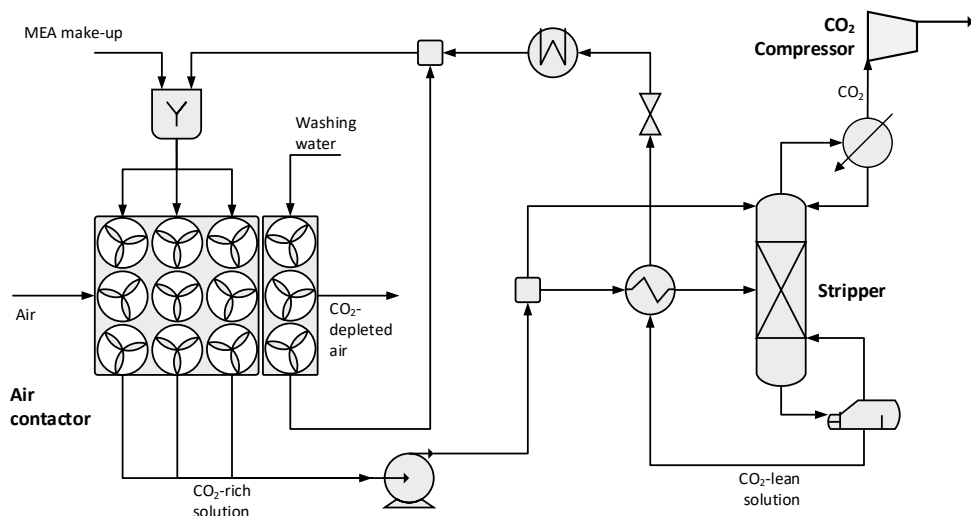


FIGURE 2.2: Schematic representation of the amine scrubbing process.

As opposed to K_2CO_3 , MEA has a relatively high vapor pressure, resulting in a considerable potential loss of solvent to the atmosphere. Additionally, MEA is a much more toxic substance and its impact on both humans and environment could be detrimental [62]. For this reason, a water-wash section has been employed to reduce the emissions of MEA. Additional details for this unit, which has been modelled following the same approach adopted for the air contactor, are reported in Table A.1.

The rich solvent stream is first pumped to the stripper pressure and then split in two flows: the largest is preheated in conventional fashion by the lean/rich heat exchanger, while the other is kept cold and fed at the top of the stripper. With this arrangement, the vapor released from the hot rich stream is exploited to heat up the cold stream flowing from the top - a conventional practice in CO_2 capture from flue gases [63]. The rich solvent stream is regenerated through stripping with steam.

The properties of the liquid phase are evaluated with the unsymmetrical electrolyte NRTL method, while for the gas phase SRK equation of state is employed, a proven approach for amine systems [64]. The absorption reactions are implemented in the air contactor blocks through kinetically controlled reactions. The kinetic constants are as in the work of Amirkhosrow et al. [65], who validated them under different operating conditions.

An equilibrium RadFrac block has been adopted to model the stripper, as the regeneration is usually carried out at conditions close to equilibrium. Details regarding the stripper are reported in Table A.1.

Solid sorbent process

The simplified flow scheme of the adsorption process is shown in Figure 2.3. The plant consists essentially of: the air contactor, controlling valves, a vacuum pump, and heat and cold supply. When looking at the details of the air contactor, the most mature version of the solid sorbent process is a cyclic process, where a single unit undergoes successively a loading (adsorption) and a regeneration (desorption) step at different pressures (PSA). Because DAC treats air at ambient conditions and in very large flow rates, air compression is not a viable option, which leaves temperature and vacuum as the only regeneration drivers. We therefore consider a vacuum-temperature swing adsorption (VTSA) cycle, as illustrated with exemplary column status in Figure 2.4a. This cycle was synthesized to allow the production of CO_2 at high purity (dry) and consists of four different steps, i.e. (i) adsorption, (ii) purge, (iii) regeneration and (iv) repressurization.

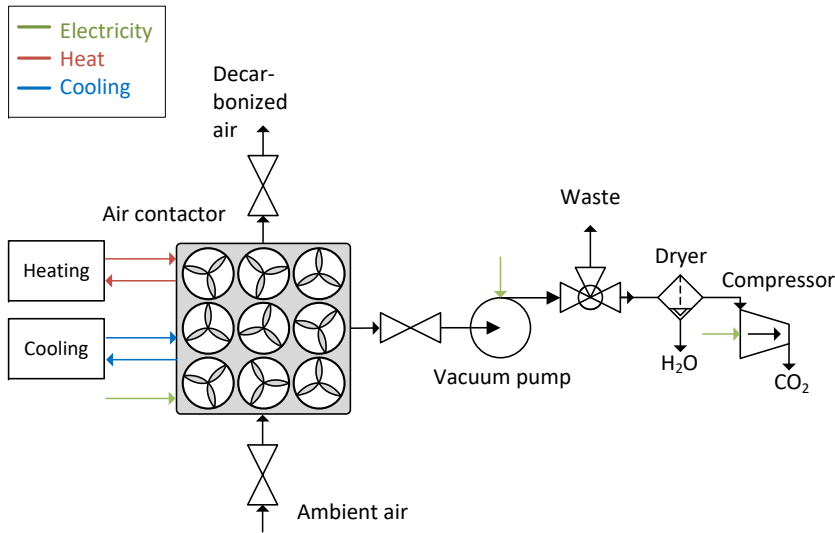


FIGURE 2.3: Simplified flowsheet of the capturing process using a solid sorbent.

During the adsorption step, the air mixture enters the adsorber unit at ambient conditions. CO_2 (and H_2O) is selectively removed by the sorbent, and CO_2 -lean

air leaves the system. When the CO_2 front reaches the end of the bed this step is terminated. In order to increase the purity of the CO_2 , a preliminary heating step is introduced, whereby the air, mainly N_2 , in the void space is removed. The sorbent is heated up to a temperature $T_1 < T_2$ by an external heating fluid, where 1 refers to the pre-heating and 2 refers to the heating step. At the same time, vacuum is generated using vacuum pumps. Small amounts of CO_2 and H_2O are already desorbed during this step. During the main desorption step the sorbent is heated to the highest working temperature T_2 while the vacuum condition is maintained or even tightened. High purity CO_2 in H_2O vapor is produced during this step and withdrawn from the column. Compared to the aqueous solution-based systems, lower temperatures at around 100°C are sufficient to regenerate the sorbent. Subsequently, the valve at the entrance is opened and ambient air streams in which cools down the sorbent material and repressurizes the system until the column is back to the starting conditions.

As for the air contactor geometry, we have adopted the design described in patents of Climeworks [41, 66, 67]. In such a configuration, the air contactor, which is shown in Figure 2.4b, resembles an air ventilation system rather than a conventional adsorber column. The physical dimensions of the module, e.g. the length of the sorbent layer, as well as the void space within the contactor are set choosing arbitrarily from the design range provided in [41, 66, 67]. Additional parameters used in the process model are listed in Table A.16. It is worth stressing that DAC companies may use different types of VTSA cycles and air contactor designs.

Extensive data is needed to model the adsorption process: from sorbent isotherms to transport parameters. We address them in the following section. Because adsorption-based DAC is not as established as liquid scrubbing, we provide more details than in section 2.2-2.2.

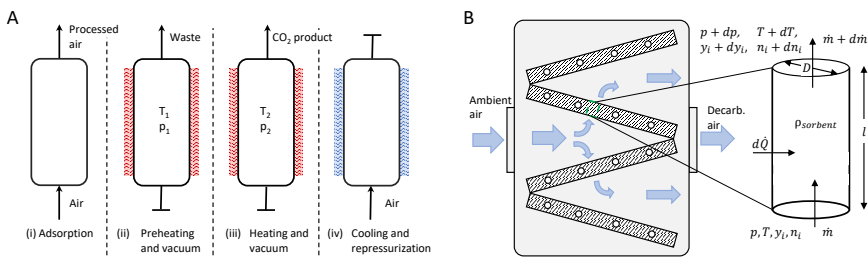


FIGURE 2.4: Representation of the adsorption process, showing in a) the schematic design of the VTSA process, divided into four cycles. Note that here we use a column-type cycle representation for the sake of clarity. More information about the structure are given in Figure 2.3 simplified flowsheet of the capturing process, and in b) a schematic design of the air contactor unit comprising a number of plates containing the solid sorbent, similar to a design published in [67].

Key for the process performance is indeed the sorbent. So far, several sorbents have been presented in literature but only few possess the minimum thermodynamic requirements for a successful DAC process. This can be clearly shown by plotting the CO_2 cyclic working capacity of the sorbent, i.e. the difference between the equilibrium CO_2 loading at adsorption and at desorption conditions, with respect to the desorption temperature (see Figure 2.5).

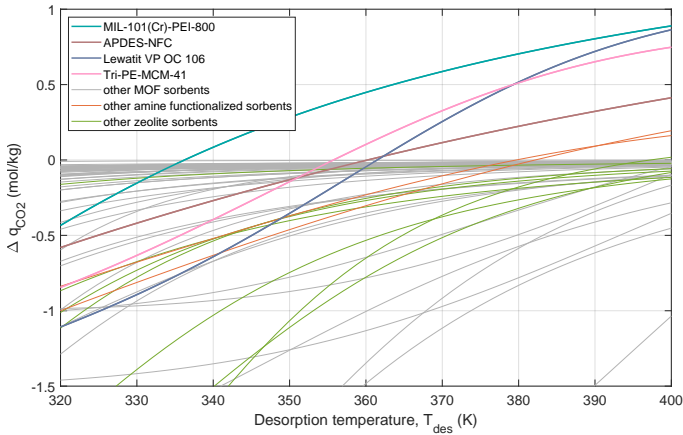


FIGURE 2.5: Working capacity for several solid sorbents including zeolites (green lines), MOFs (grey lines) and amines (orange lines). The capacity is calculated with ambient conditions for the adsorption step ($T=293$ K, $p=1$ bar, $p_{\text{CO}_2}=400$ ppm) and a desorption pressure of 100 mbar. The four sorbents selected for this study are shown by thick lines and named in the legend.

The sorbent selection in this work is therefore based on the following constraints: (i) cyclic capacity larger than zero when considering CO_2 partial pressure in the air for the adsorption, and $T_{\text{max}} = 120^\circ\text{C}$ and $p_{\text{min}} = 0.1$ bar for the regeneration, and (ii) data availability in open scientific literature for relevant isotherms and sorbent physical properties. As a result, we selected four promising sorbents, which are highlighted in Figure 2.5, namely APDES-NFC [41], Tri-PE-MCM-41 [68], MIL-101(Cr)-PEI-800 [45] and Lewatit VP OC 106 [48, 69, 70]. It is worth noting that, because DAC is a relative young application, experimental data are currently limited. On the one hand, data are missing about H_2O and N_2 adsorption under different conditions. On the other hand, multicomponent isotherms are not available to the best of our knowledge. More specifically: for the APDES-NFC and the Lewatit sorbent comprehensive experimental data for both water and CO_2 isotherms are available; MIL-101(Cr)-PEI-800 shows the highest CO_2 working capacity, but no

data were found for the H₂O isotherm in the pressure and temperature range of interest. In this work we cope with the limited availability of data for the considered DAC sorbent by combining the sorbent-specific CO₂ isotherm with different H₂O isotherms, which allows us to better evaluate the role of water in the process. To this end we consider the H₂O isotherms of APDES-NFC, Lewatit and MCF-APS-hi [71], which feature a high, medium and low water adsorption, respectively. Moreover, as the current sorbent landscape does not allow us to set a reference sorbent, e.g. among the four selected, we include in our analysis an exemplary sorbent for CO₂, obtained by combining the equilibrium data of the four materials highlighted in Figure 2.5. The resulting different cases are listed in Table 2.1. The matrix of cases obtained in such a fashion allows us to consider sorbents well characterized (APDES-NFC and Lewatit), as well as a promising sorbent missing experimental data (MIL-101(Cr)-PEI-800), and an exemplary sorbent representing the average behavior.

TABLE 2.1: Different combinations for CO₂ and H₂O isotherms.

CO ₂ isotherm	H ₂ O isotherm		
	APDES-NFC	MCF-APS-hi	Lewatit VP OC 106
APDES-NFC	case 1: A-A	-	-
Exemplary	case 2: E-A	case 3: E-M	case 4: E-L
MIL-101(Cr)-PEI-800	case 5: MP-A	case 6: MP-M	case 7: MP-L
Lewatit VP OC 106	-	-	case 8: L-L

For the four sorbents highlighted in Figure 2.5, we fitted experimental adsorption data by applying suitable isotherm models. For CO₂ adsorption, we identified two different models that returned the best fitting. For APDES-NFC we apply the temperature-dependent Toth model:

$$q_i(p, T) = \frac{n_s b p_i}{(1 + (b p_i)^t)^{1/t}}, \quad i = \text{CO}_2 \quad (2.8)$$

For the remaining sorbents we adopted a modified version of the classical Toth equation, where two terms are present, one for describing physisorption and one for describing chemisorption, as proposed by Elfving et al. [72]. This model showed the best fitting for three out of four sorbents, since it describes two independent adsorption mechanisms - chemisorption by the amine groups, and physisorption by the surface interaction [73].

$$q_i(p, T) = \left[\frac{n_s b p_i}{(1 + (b p_i)^t)^{1/t}} \right]_{chem} + \left[\frac{n_s b p_i}{(1 + (b p_i)^t)^{1/t}} \right]_{phys} \quad (2.9)$$

where in both Equations 2.8 and 2.9 p_i is the partial pressure of the component i , and n_s , b and t are temperature-dependent parameters of the Toth model. The temperature dependent coefficients, which have the same functional form for the chemical and the physical term, are defined as follows

$$n_s(T) = n_{so} \exp \left[\chi \left(1 - \frac{T_0}{T} \right) \right] \quad (2.10)$$

$$b(T) = b_0 \exp \left[\frac{\Delta H}{RT_0} \left(\frac{T_0}{T} - 1 \right) \right] \quad (2.11)$$

$$t(T) = t_0 + \alpha \left(1 - \frac{T_0}{T} \right) \quad (2.12)$$

where the terms are as defined in the variable list [74].

The fitting was carried out with the optimization routine *fmincon* in Matlab version R2018b by minimizing the error between the experimental and modeled data using the normalized standard deviation. Further details for the fitting of the different sorbents as well as the calculation of the isosteric heat can be found in the Supporting Information A. The resulting parameters for the different CO₂ isotherms are shown in the Supplementary Information in Table A.3. It can be noted that R-squared is rather high in all cases.

The adsorption isotherms of water were described in all cases by using the Guggenheim-Anderson-de Boer (GAB) model [41, 75]:

$$q_{\text{H}_2\text{O}}(T, p_{\text{H}_2\text{O}}) = C_m \frac{C_G K_{\text{ads}} \frac{p_{\text{H}_2\text{O}}}{p_0}}{\left(1 - K_{\text{ads}} \frac{p_{\text{H}_2\text{O}}}{p_0} \right) \left(1 + (C_G - 1) K_{\text{ads}} \frac{p_{\text{H}_2\text{O}}}{p_0} \right)} \quad (2.13)$$

with

$$C_G(T) = C_{G,o} \exp \left(\frac{\Delta H_C}{RT} \right) \quad (2.14)$$

$$K_{\text{ads}}(T) = K_0 \exp \left(\frac{\Delta H_K}{RT} \right) \quad (2.15)$$

$$C_m(T) = C_{m,o} \exp \left(\frac{\beta}{T} \right) \quad (2.16)$$

where the terms are as defined in the variable list. As mentioned before, the equilibrium data of water are from three different sorbents, namely APDES-NFC [41], MCF-APS-hi [71] and Lewatit VP OC 106 [76].

Most of the DAC processes modeled in literature are either based on dry conditions [73] or disregard the effect of water on the CO₂ isotherm. However, the presence of water in the feedstream enhances the CO₂ capacity of amine-based sorbents, depending on the temperature and partial pressure of H₂O in the stream [35, 48]. Despite the very limited set of data available, modeling the co-operative adsorption of water and CO₂ is key to compute a realistic process performance. Ideally, multicomponent competitive isotherms should be used but, as those are not yet available for the sorbents of interest, we use single component isotherms and describe empirically the interaction of CO₂ and H₂O. Wurzbacher et al. [75] added an enhancing factor dependent on the partial pressure of CO₂ and the humidity, to describe the humid adsorption of CO₂. However, this factor is applicable in a small pressure range and lead to wrong estimates in other conditions of interest. Using a physical approach, Stampi-Bombelli et al. [55] proposed a new isotherm model for the APDES-NFC sorbent, where the water uptake is embedded in the Toth isotherm for CO₂. This method is physically sound, but depends on having comprehensive experimental water isotherms, including competition and cooperative adsorption with CO₂. Here, we applied a robust, yet empirical approach by including an equivalent adsorption temperature T_{eq} , which is dependent on the humidity RH and the actual temperature T , in the form of

$$T_{eq}(T, RH) = T - a \left(\frac{278K}{T} \right)^b RH \quad (2.17)$$

with a and b being two fitting parameters. The expression allows to have $T_{eq}=T$ for $RH=0\%$ while also including a minimum T_{eq} for $RH=100\%$, i.e. the most favorable adsorption condition for CO₂ as function of humidity. The calculation of a and b was carried out by fitting data provided in Veneman et al. [48] and applied to all sorbents considered in this work. Details can be found in the Supporting Information A, including the comparison with data reported for APDES-NFC. For the Toth-cp model, the equivalent temperature is included only in the chemisorption, as the physisorption mechanism is not as strongly affected by humidity.

Finally, while we do consider the presence of N₂ in the feed gas and in the void part of the bed, which influences the CO₂ purity, we neglect the adsorption of N₂. It is worth noticing that, given the chemisorption role, the adsorption of N₂ will be very limited.

The adsorption column is simulated by using a deterministic in-house model, which was originally developed for cyclic adsorption processes in fixed beds in

the group of Mazzotti at ETH Zurich and that has been adapted here to describe the sorbents of interest. The operation of the process is modeled by solving mass, energy and momentum balances for a unique column which undergoes the cycle steps sequentially. It is completed when a cyclic steady state (CSS) is reached, or, in other words when the overall mass balance and the internal column parameters, like composition and temperature, are the same for the n and the $n - 1$ cycle. More details can be found in [77, 78]. The underlying modelling approach is well established and state-of-the-art in the field of CO₂ adsorption [79, 80]. The tool has been validated against experiments for PSA, TSA and VSA conditions conditions [50, 81–83] and has been used in several scientific publications for analysis of adsorption processes [83–85].

The additional process components, like the air blower and the vacuum pump, are modeled by using MATLAB, details can be found in the Supporting Information section A.

Along with the equilibrium data, transport parameters, namely the mass transfer and heat transfer coefficients, are needed. Unfortunately, the data availability for these is even more limited than isotherms. Here, we have tackled this by estimating data from existing experiments, and by adding extensive sensitivity analysis to provide a range of performance, rather than a single point value. In the adsorption model, the mass transfer resistance is described using the linear driving force (LDF) model

$$\frac{\partial q_i}{\partial t} = k_i (q_i^{\text{eq}} - q_i) \quad (2.18)$$

with the (lumped) mass transfer coefficient k_i of component i and the equilibrium adsorbed phase concentration q_i^{eq} . The reference CO₂ coefficient was assumed to be $k_{\text{CO}_2} = 0.1 \text{ s}^{-1}$, which is in the same range compared to other literature [86, 87], however other references provide smaller values, e.g. [55] who fitted the limited set of data from [41, 75, 88] resulting in a coefficient of $k_{\text{CO}_2} = 0.0002$. Since the kinetics have a large impact on the performance of the process and given the lack of kinetic data in literature, especially for the specific sorbents we have chosen, a sensitivity analysis is carried out by varying the mass transfer coefficient for CO₂ in the range of $k_{\text{CO}_2,1} = 0.0001 \text{ s}^{-1}$, $k_{\text{CO}_2,2} = 0.01 \text{ s}^{-1}$ and $k_{\text{CO}_2,3} = 0.1 \text{ s}^{-1}$, while keeping the kinetics for water constant. Since experimental data in [75, 89] showed faster kinetics for H₂O, we assumed $k_{\text{H}_2\text{O}} = 1 \text{ s}^{-1}$ for the mass transfer coefficient.

The heat transfer coefficient was calculated by fitting experimental data provided in [41]; details of the calculation can be found in the Supporting Information A. The resulting coefficient is $6.7 \text{ W}/(\text{m}^2\text{K})$, which is comparable with values used by other authors [77, 90]. Since this calculation is only based on one experimental set of data,

we included a sensitivity analysis for $h_1 = 4.0 \text{ W}/(\text{m}^2\text{K})$, $h_2 = 6.7 \text{ W}/(\text{m}^2\text{K})$ and $h_3 = 6.0 \text{ W}/(\text{m}^2\text{K})$.

Finally, the specific properties of the different sorbents can be found in the Supporting Information in Table A.14.

2.3 MULTI-OBJECTIVE OPTIMIZATION

In order to determine the optimal performance of the different capture systems and the associated operating and design variables, a multi-objective optimization was carried out [91]. It includes two competing objectives, namely productivity, which can be seen as an indicator for the resulting equipment costs, and the electrical and thermal energy consumption coupled in the mass-specific exergy e value, which reflects the operating costs. The problem is defined as:

$$\begin{aligned} & \underset{x}{\text{minimize}}(-Pr, e) \\ & \text{subject to } \Phi \geq \Phi_{\text{spec}} \end{aligned} \quad (2.19)$$

where x are decision variables, Φ the purity and Φ_{spec} the required minimum purity (here assumed 95%, as for CO_2 storage applications). Since these objectives are conflicting, the trade-off is identified by a Pareto line; e.g. for a given reactor size, an increase in productivity requires capturing more CO_2 , which can be achieved processing more air (i.e. larger energy consumption for the fan) or working with higher recovery (i.e. larger heat consumption for regeneration). The productivity is calculated as

$$Pr = \frac{\dot{m}_{\text{CO}_2}}{V_{\text{aircontactor}}} \quad (2.20)$$

where \dot{m}_{CO_2} is the mass rate of CO_2 captured from the air and $V_{\text{aircontactor}}$ the volume of the air contactor. The specific exergy requirement e is calculated differently for every process as described below.

Exergy consumption of the alkaline scrubbing process. The specific exergy demand using KOH as a solvent is expressed by

$$e = \frac{1}{\dot{m}_{\text{CO}_2}} [\dot{m}_{\text{CH}_4} LHV_{\text{CH}_4} + \dot{W}_{\text{ASU}} + \dot{W}_{\text{blower}} + \dot{W}_{\text{comp}}] \quad (2.21)$$

where the product $\dot{m}_{\text{CH}_4} LHV_{\text{CH}_4}$ is the exergy demand for the calcination, which is provided by an oxyfuel combustion of methane with oxygen from an ASU consuming \dot{W}_{ASU} . In addition, the energy requirement for the air blower \dot{W}_{blower} and the compression of the CO_2 \dot{W}_{comp} is included.

Exergy consumption of the MEA scrubbing process. In this case, the exergy demand is calculated as

$$e = \frac{1}{\dot{m}_{\text{CO}_2}} \left[\dot{Q}_{\text{reboiler}} \left(1 - \frac{T_0}{T_{\text{reb}}} \right) + \dot{W}_{\text{refr}} + \dot{W}_{\text{pump}} + \dot{W}_{\text{blower}} + \dot{W}_{\text{comp}} \right] \quad (2.22)$$

with $\dot{Q}_{\text{reboiler}}$ representing the heat required for the reboiler of the stripper, \dot{W}_{refr} the power used for cooling the lean stream and \dot{W}_{pump} the energy requirement of the pumps.

Exergy consumption of the VTSA process. For solid sorbent DAC the specific exergy requirement is calculated as:

$$e = \frac{1}{\dot{m}_{\text{CO}_2}} \left[\dot{Q}_{\text{purge}} \left(1 - \frac{T_0}{T_{\text{purge}}} \right) + \dot{Q}_{\text{reg}} \left(1 - \frac{T_0}{T_{\text{reg}}} \right) + \dot{W}_{\text{vac,purge}} + \dot{W}_{\text{vac,prod}} + \dot{W}_{\text{blower}} + \dot{W}_{\text{comp}} \right] \quad (2.23)$$

where \dot{Q}_{purge} and \dot{Q}_{reg} represent the heat required for the purge and regeneration step, $\dot{W}_{\text{vac,purge}}$ as well as $\dot{W}_{\text{vac,prod}}$ the required electrical energy of the vacuum pump, \dot{W}_{blower} the energy for the air blower and \dot{W}_{comp} the energy for CO_2 compression. All input variables are calculated in our optimization framework.

As for the exergy consumption, also the optimization variables are specific to process type.

Optimization variables of the alkali scrubbing process:

- Absorber loading (ξ), defined as the ratio between the moles of KOH in the lean stream and the moles of CO_2 in the air stream;
- Air velocity in the contactor unit (u_{air});
- Mass fraction of water in the K_2CO_3 slurry ($w_{\text{H}_2\text{O}}$).

Optimization variables of the MEA scrubbing process:

- Absorber loading (ξ), defined in this case as the ratio between the number of moles of MEA in the lean stream and the number of moles CO_2 in the air stream;
- Air velocity in the contactor unit (u_{air});
- Specific reboiler duty (d), defined as the ratio between the set duty of the reboiler and the mass flowrate of the lean stream;

- Split fraction (f_{Split}), the fraction of rich stream which is directly fed to the top stage of the stripper.

Optimization variables of the VTSA process:

- time of the adsorption phase t_{ads} , of the CO₂ production phase t_{prod} , and of the purge step t_{purge} ;
- vacuum pressure of the preheating and CO₂ production step p_{vac} ;
- temperature of the heating step T_{prod} ;
- temperature difference between the CO₂ production and the purge step ΔT_{purge} ;
- air velocity u_{air} at the feed (the upper boundary is dependent on the specific material properties and is calculated as the minimum fluidizing velocity).

All decision variables and their respective lower and upper boundaries in the optimization are reported in the Supplemental Information in Table A.7. The boundaries were chosen to be large enough to explore the optimum for all sorbents while being computationally feasible within some hours.

In all simulations, the optimization is carried out using state-of-the-art mathematical algorithms implemented or available in Matlab (R2018b). For the liquid scrubbing processes, Matlab was directly connected to Aspen Plus V11 using the ActiveX software framework, i.e. the data exchange is fully automated. For these cases, the non-dominated Sorting Genetic Algorithm version II (NSGA-II) as available in Matlab was employed. More details can be found in the Supplemental Information section A. For the solid sorbent process, the optimization was carried out using a new algorithm that (part of) the authors have specifically coded in Matlab for tackling adsorption processes. The algorithm is directly connected to the Fortran-based adsorption model: it receives results from it and provides new set of optimization variables. The algorithm is a modified version of the global optimization algorithm multi-level coordinate search (MCS) which is extended to deal with multiple objectives (MO-MCS). Details can be found in [91].

In addition to the objective functions and optimization variables, we report throughout this work also the capture rate. This indicator is defined as the ratio between the amount of CO₂ captured over the amount of CO₂ fed to the air contactor:

$$Cr = \frac{\dot{m}_{\text{CO}_2}}{w_{\text{CO}_2}^{\text{Air}} \dot{m}_{\text{Air}}} \quad (2.24)$$

For all processes, the simulations are carried out considering as ambient conditions $T = 293 \text{ K}$, $p = 1.001 \text{ bar}$, relative humidity of 43%, and CO₂ content: $4 \times 10^{-4} \text{ mol}_{\text{CO}_2}/\text{mol}$.

2.4 ECONOMIC EVALUATION

As complement to the detailed technical analysis, we carried out a simplified economical evaluation of the different processes. The goal is not to present a detailed economic analysis of the specific technologies, which would require to compute all components of the capital expenditures (CAPEX) and the operational expenditures (OPEX) - out of scope here, but to identify the main cost drivers of the processes and to compare their potential from an economic perspective. In gas separation, energy and air contactor volume are first proxies for operating and capital cost respectively. Using the consistent computation of energy performance and productivity we therefore map the CO₂ capture cost c_{CO_2} as function of (i) the air contactor cost per m³ γ , (ii) the electricity price c_{el} , and (iii) the heat price c_{th} . These can also be regarded as proxy for CAPEX (point (i)), and OPEX (point (ii) and (iii)). The resulting equation is:

$$c_{\text{CO}_2} = \frac{\gamma}{Pr \cdot a} + c_{\text{th}}e_{\text{th}} + c_{\text{el}}e_{\text{el}} \quad (2.25)$$

where Pr , e_{th} , and e_{el} are taken from the Pareto fronts computed with the optimization, and a is the lifetime of the plants, which was assumed to be 20 years (note that unit conversion factors have been omitted in the equation). For γ , a range of 2000 to 50000 \$/m³ was chosen. The order of magnitude of the two values has been chosen to cover a broad range of plant costs; from a rather simple and cheap traditional column (as reference a contactor cost of 2000 \$/m³ was back-calculated from [25]) to the higher cost of a full VTSA system (calculated considering a cost of 600 \$/ton_{CO₂} and the design and capacity of Hinwil Climeworks plant).

For c_{th} and c_{el} we chose a realistic range of 1 – 10 \$cents/kWh. It should be stressed that, while we show the full $c_{\text{th}}-c_{\text{el}}$ plane, cases where heat is more expensive than electricity should be disregarded.

2.5 RESULTS AND DISCUSSION

Alkali Scrubbing

The Pareto front obtained for the KOH process is reported in Figure 2.6a. The region below the curve is unfeasible while that above represents a sub-optimal operation.

It is worth noting that the exergy does not change much along the Pareto front, as opposed to the productivity. On the one hand, there is not much room for the reduction of the exergy demand of the KOH scrubbing process with the chosen decision variables and their respective boundaries. The demand is mainly determined by the oxy-combustion, which is around 5 MJ/kg_{CO₂}. A better understanding can

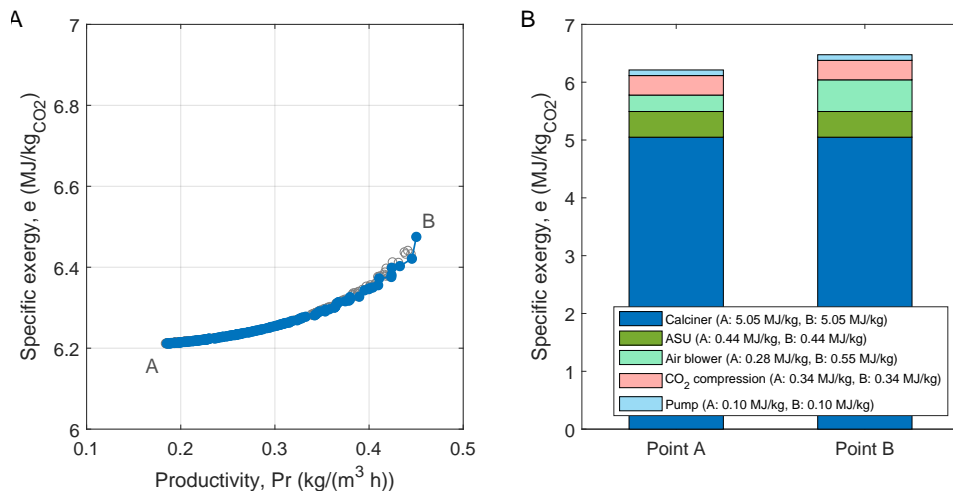


FIGURE 2.6: Resulting graphs for the KOH process. a) Specific exergy-productivity Pareto front for the KOH process; point A: minimum exergy consumption; point B: maximum productivity. Empty points represent sub-optimal conditions obtained during the optimization. b) Breakdown of the exergy demand of the alkali scrubbing process for the two extremes, i.e. point A and B, of the Pareto front. The energy demand is equal to the exergy demand. With the specific values for the calciner A/B: 5.05 MJ/kg, the air separation unit A/B: 0.44 MJ/kg, the air blower A: 0.28 MJ/kg and B: 0.55 MJ/kg, the CO₂ compression A/B: 0.34 MJ/kg and the pumps A/B: 0.10 MJ/kg.

be achieved by examining Figure 2.6b, which shows the breakdown of the exergy demand for the two extremes of the Pareto front. The energy demand is almost equal to the exergy demand, since the calcination is a high temperature process, where energy and exergy converge to the same value.

For both points, the largest share of the exergy demand is due to the calciner and the ASU. The methane and oxygen streams to achieve 98% conversion of CaCO₃ at a fixed temperature of 900°C are constant along the pareto as a result of the decoupling between the capture and the regeneration sections. As for the purity, the CO₂ concentration in the dried product stream does not differ much from the value of 94.7% and, consequently, the specific energy consumption of the compressors is constant throughout all the simulations.

The energy consumption of the air blowers, on the other hand, significantly changes along the Pareto. As a matter of fact, the pressure drop across the air

contactor units increases with increasing air velocity, the latter being one of the design variables chosen for this process.

These results are in line with those presented in literature. Keith et al. estimate a total exergy demand of 6.57 MJ/kg_{CO₂}, with the calcination representing the largest portion at 5.25 MJ/kg_{CO₂} [25]. The biggest discrepancy can be identified in the CO₂ compression work, as Keith et al. report 0.475 MJ/kg_{CO₂}, while, as it is shown in Figure 2.6b, we estimate 0.34 MJ/kg_{CO₂}. This is likely due to different compressor isentropic efficiencies.

As for the effects of the design variables on the process performance, which are shown in Figure A.2, we find that the air velocity has the prominent influence. With increasing air velocity, both the specific energy demand and the productivity increase, thus delineating the Pareto frontier. Because of the shorter residence time, higher air velocity leads to lower capture rate, which is compensated by the larger amount of CO₂ fed to the contactor. The absorber loading as well as the moisture content of the CaCO₃, on the other hand, do not effect the performance significantly. This is a peculiarity of the double ions exchange process, which, from an optimization perspective, allows to decouple the flow rates in the air contactor from the flow rates in the regeneration. Additional details can be found in the supplementary information in Section A.

The purity of the captured CO₂ is independent of the considered design variables, and was found to be 94.7% on a dry basis. The remaining impurities consist of N₂, Ar and O₂ and depend on the ASU and the oxy-combustor design. The CO₂ purity of the alkali scrubbing process could increase when adopting a gas cleaning process - as done in conventional CCS oxycombustion processes - or when using an ASU with a third column for Ar recovery. It is in fact worth noting that only negligible amounts of N₂ and Ar are transferred from the air in the air contactor to the regeneration section.

Amine Scrubbing

Amine scrubbing is a well-established and widely adopted CO₂ capture process. The DAC version described in this work is based on the unconventional air contactor units of its alkali counterpart, while the solvent regeneration is carried out through conventional steam stripping. The Pareto front for the amine scrubbing process is reported in Figure 2.7a.

It can be noted that both productivity and exergy demand change significantly along the Pareto, suggesting the importance of optimization for this process. As for the alkali scrubbing process, the solvent regeneration is the biggest contributor to the energy demand. Figure 2.7b shows that, for both extremes of the Pareto, the energy

demand consists almost entirely of the reboiler duty. Moreover, it can be noticed that the reboiler duty increases dramatically when moving towards higher productivity.

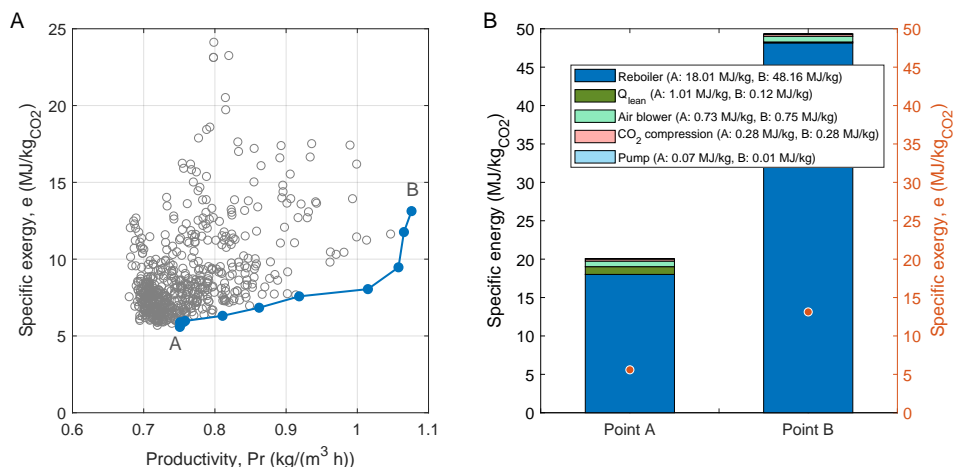


FIGURE 2.7: Resulting graphs for the MEA process. a) Specific exergy - productivity Pareto front for the amine scrubbing process; point A: minimum exergy consumption; point B: maximum productivity. Empty points represent sub-optimal conditions. b) The breakdown of the energy demand for the two extremes, i.e. point A and B, of the Pareto front. With the specific values for the Reboiler A: 18.01 MJ/kg and B: 48.16 MJ/kg, the lean stream A: 1.01 MJ/kg and B: 0.12 MJ/kg, the air blower A: 0.73 MJ/kg and B: 0.75 MJ/kg, the CO₂ compression A/B: 0.28 MJ/kg and the pumps A: 0.07 MJ/kg and B: 0.01 MJ/kg. The overall exergy demand for both points is shown by orange dots, using the right axis.

Although in terms of exergy demand the amine and alkali scrubbing processes are similar, amine scrubbing requires much more energy than its alkali counterpart. Figure 2.7b shows the energy demand for point A of the Pareto, that is the point for which the energy consumption is the lowest. Even in these conditions, the amine scrubbing process requires almost three times the energy consumed by the alkali process. However, only low-grade heat has to be provided to the reboiler, which explains the significant difference between energy and exergy demand. The results reported in this section are in line with those already published in the literature. However, for operating conditions similar to those adopted in this work, Kiani et al. [32] reported a reboiler duty of 21.9 MJ/kg_{CO2} and electrical energy requirement of 5.04 MJ/kg_{CO2}. The energy demand breakdown for point A and B of the Pareto is represented in Figure 2.7b. The much lower energy requirement of the air blowers

reported in this work can be explained by the lower pressure drops provided by the Carbon Engineering type of air contactor.

The influence of the design variables on the productivity and energy demand is shown in Figure A.3 in the Supplementary Information. The weight fraction of MEA in the lean stream is kept to the well-established optimal value of 30% throughout all the simulations. This means that an increase in the absorber loading (ζ) determines an increase in the lean flow rate. When moving towards high productivity, both ζ and the air velocity steadily increase. This implies that the lean flow rate is significantly higher, while the CO₂ recovered is about constant, thus explaining the rise in energy demand. Remarkably, the specific reboiler duty (d) does not steadily increase as the productivity rises, but it shows a maximum in the middle of the Pareto and then decreases for the points with the highest productivity. This can be explained by the influence of the absorber loading. This design variable increases when moving towards high productivity, meaning that more MEA than CO₂ is present in the system. Therefore, the rich stream becomes more diluted in carbon-carrying components, which affects the energy demand of the reboiler. Indeed, less energy is required to regenerate a more diluted stream, thus the reduction in specific reboiler duty in the high productivity region. Moreover, less CO₂ is released by regenerating a diluted rich stream, therefore, although d decreases, the specific energy demand still increases.

The split fraction does not show a clear trend with respect to the energy demand or the productivity. However, the Pareto points in the high productivity, high energy demand region are all characterized by a high split fraction, meaning that this design variable does have an effect on the performances of the process.

Interestingly, we show that the kinetic performance of MEA would allow for capturing CO₂ from air. As reported in Figure 2.8, the capture rate achieved at the Pareto is as high as 89%. The alkali scrubbing process can provide an even higher capture rate of 97%, although at the expense of productivity. This is due to the fact that higher productivity is achieved via higher air velocity and, therefore, lower air residence times. In this way more air is processed per time and volume of the reactor. For the highest productivity the capture rate of the alkali scrubbing process is 50%. For the amine scrubbing, on the other hand, the capture rate is almost independent of the productivity (i.e. air velocity). This is due to the fast kinetics of MEA, which determine extensive CO₂ removal in the optimal range of the air residence time. Similar performance has also been reported in recent literature: Barzagli et al. [31] achieved a capture rate of 87.3 % using an aqueous solution of MEA.

Extremely high CO₂ purities exceeding 97% are achieved. This is not surprising, since MEA is a remarkably selective solvent. The other main components contained in the CO₂ product stream are H₂O, N₂ and O₂. Thanks to the washing section, the MEA content in the CO₂-lean air stream is negligible. The purity is constant

throughout all the operating conditions, but tends to slightly decrease with increasing energy demand. An increase in energy demand is determined by a rise in the reboiler duty, meaning that more water is vaporized, partly ending up in the CO₂ stream. However, on a dry basis, the purity achieved with this process is constant.

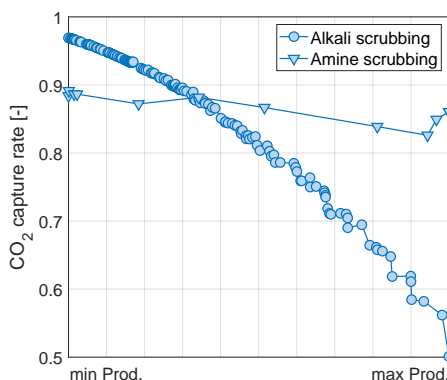


FIGURE 2.8: CO₂ capture rate for the resulting Pareto points for both liquid scrubbing processes over the normalized productivity.

Solid sorbent

The Pareto curves for the different solid sorbent materials are shown in Figure 2.9, while the breakdown of the specific exergy and energy consumption can be found in Figure 2.10. The values for the design variables for each Pareto curve are attached in the Supporting Information in Figures A.5- A.11. From Figure 2.9 it can be noted that the solid sorbent process covers a rather broad range both in terms of exergy (1.5-3.7 MJ/kgCO₂) and productivity (3.8-10.6 kg/m³/h). This is because of the different chemical-physical properties of the sorbents. The highest exergy consumption was achieved with the Lewatit sorbent. One reason is that the heat of adsorption for the chemisorption is 91.2 kJ/mol, which is higher than for the other sorbents and leads to a higher thermal energy demand. Furthermore, the working capacity of the water adsorption is high, which further increases the energy demand during the regeneration step. In addition, the lower particle density and particle diameter limits the maximum air velocity, resulting in a lower productivity. The MIL-101(Cr)-PEI-800 sorbent shows high working capacity and low energy consumption, which depends on the water isotherm. The MFC-APS-hi water isotherm shows the lowest H₂O working capacity and leads to a lower exergy consumption for the combinations

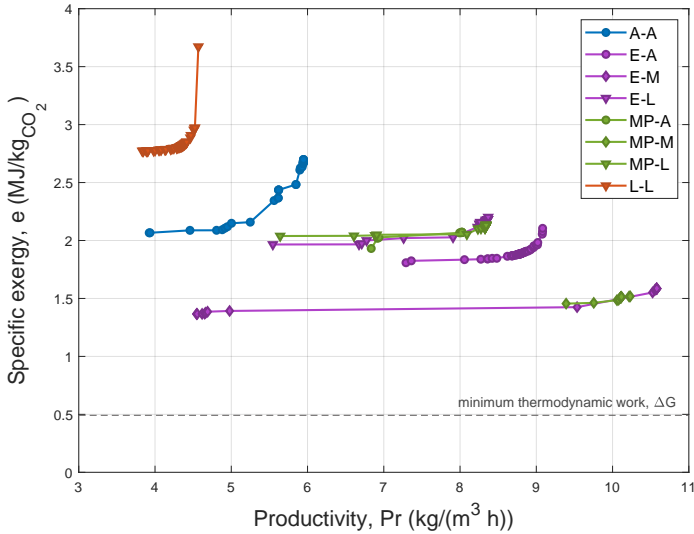


FIGURE 2.9: Productivity-exergy Pareto curves for the solid sorbent optimization using different combinations of isotherms for CO_2 and H_2O (the shortcuts of the cases are explained in Table 2.1). In all simulations the mass transfer coefficient for CO_2 is 0.1s^{-2} and the heat transfer coefficient $6.7\text{ W/m}^2/\text{K}$. The different colors represent different CO_2 isotherms, while the different symbols change with the different H_2O isotherms.

using this sorbent, i.a. MP-M and E-M. For the APDES-NFC sorbent (case A-A), the lower exergy point is comparable with the MIL-101(Cr)-PEI-800 sorbent but the high productivity is limited to about $6\text{ kg/m}^3/\text{h}$. This is due to the high porosity and low density of the sorbent and the lower working capacity of the CO_2 isotherm, which requires a higher regeneration temperature and a lower vacuum pressure during the production step. For all cases, the main exergy (energy) demand is required by the heat consumption during the regeneration. The energy consumption for the vacuum pump during the purge step is very low, since this step only ensures that all the N_2 in the void space is removed to achieve a high purity, which proceeds very quickly. The vacuum pump for the CO_2 production step has a higher share on the overall energy consumption and varies mainly with the different vacuum pressures needed for the regeneration. For the MP-A case, e.g., the vacuum pressure is comparably high, which results in a very low energy consumption for the pump. The energy consumption for the air blower as well as the CO_2 compression is similar for all cases. The former has a higher impact on the productivity. While keeping the

dimensions of the air contactor the same, a higher air velocity leads to an increase in the productivity for the considered range of values. Because of the low temperature of the regeneration, and similarly to MEA, there is a large difference between the energy and exergy demand for all solid sorbents (see Figure 2.10).

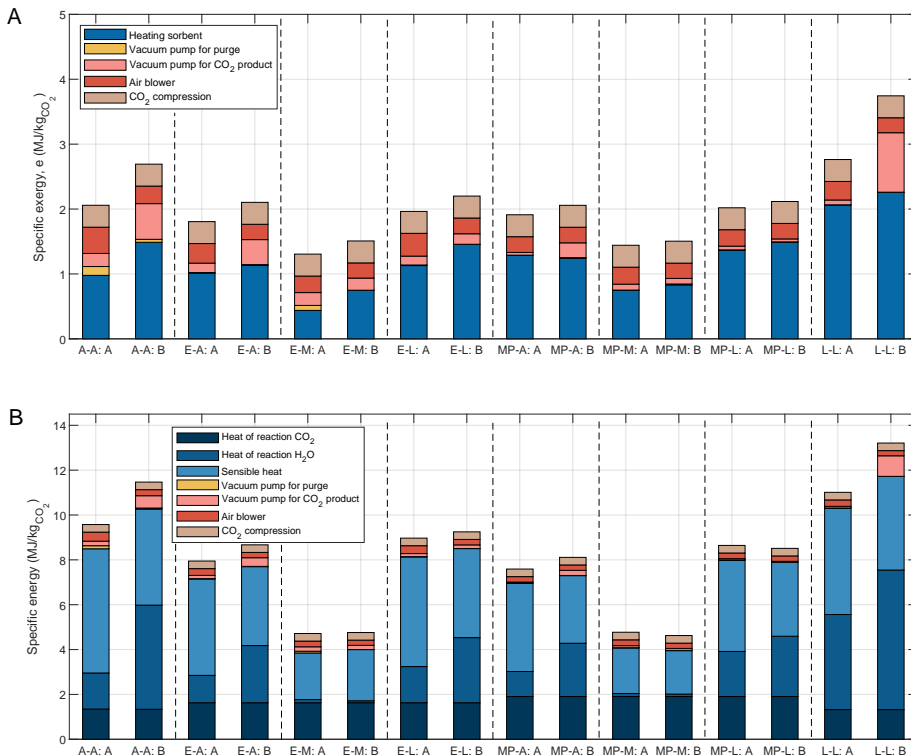


FIGURE 2.10: Detailed energy and exergy demand for the different cases of the solid sorbent process. a) Breakdown of the exergy demand. b) Breakdown of the energy demand. The thermal energy demand is shown in blue, with different shades referring to the reaction heat of CO₂ and H₂O, which were calculated at equilibrium ($T = 373\text{ K}$, $p = 0.1\text{ bar}$), and the sensible heat of the sorbent, CO₂ and H₂O. In both graphs X-X:A refers to the minimum exergy/energy on the Pareto, and X-X:B to the maximum productivity.

In all cases, the CO₂ purity is in the range of 94 to 99% with water being the main impurity. The only exception is APDES-NFC, where the purity was slightly lower, in the range of 0.89-0.94; this is due to the higher porosity of the sorbent and the

additional amount of nitrogen present in the pores. The recovery is similar for all simulations and varies between 60 and 99%, as shown in Figure A.4.

Sensitivity analyses were carried out for two highly uncertain parameters: the mass transfer and the heat transfer coefficients. The Pareto fronts for varying the kinetics are shown in Figure 2.11a. Three cases were analyzed here, depending on their resulting Pareto curves shown in Figure 2.9: the case with the lowest exergy consumption (E-M), the one with the highest exergy consumption (L-L) and one in between (E-A). It can be noted, that the mass transfer highly affects the shape of the Pareto front. While the minimum energy consumption is similar, the productivity varies significantly when reducing the mass transfer coefficient because of the higher cycle time required. For a specific mass transfer coefficient of $k = 0.1 - 0.01 \text{ s}^{-1}$ the Pareto is rather flat - the productivity can be increased with minor additional energy expenditure. However, the Pareto becomes very steep for $k = 0.0001 \text{ s}^{-1}$ - the productivity can be slightly increased at great energy costs. This effect is similar for all three materials tested. Varying the heat transfer coefficient mainly affects the productivity, i.e. lower productivity for smaller heat transfer coefficient, which is due to the longer heating time required as shown in Figure 2.11b. Differently from the mass transfer, heat transfer does not strongly affect the adsorption step.

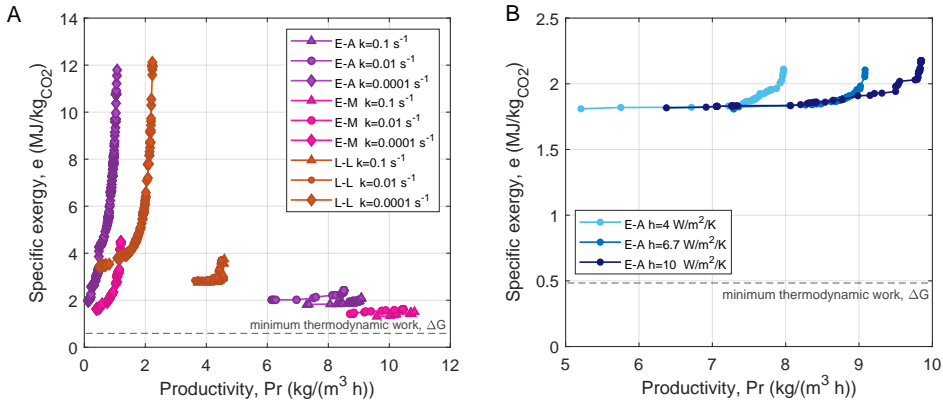


FIGURE 2.11: Pareto curves for the sensitivity analysis: (a) Changing the kinetics from $k = 0.1 \text{ s}^{-1}$ to $k = 0.0001 \text{ s}^{-1}$ (for material E-A, E-M and L-L) and (b) changing the heat transfer coefficient ($\text{W/m}^2\text{K}$) (for material E-A).

For the solid sorbent process, we find that the total energy demand varies in a range of 4.9-13.3 MJ/kg CO₂. The thermal energy is the largest contribution (4 – 11.8 MJ/kg) while the electrical energy accounts for 0.8-1.8 MJ/kg.

We can compare the results presented here with values reported in literature; this is possible for the energy consumption only, as – to the best of our knowledge – no other study reports the CO₂ productivity (or required volume). Moreover, it is worth stressing that different literature works rely often on different assumptions and different sorbents. Finally, the results we present are obtained with an extensive process optimization, while literature results are either single data point or outcome of sensitivity analysis.

The process developed by Climeworks requires 1.8-2.6 MJ_{el}/kg and 5.4-11.9 MJ_{th}/kg, where the minimum represents future target and the maximum the current consumption [92]; for our case A-A, which includes the APDES-NFC sorbent supposedly similar to Climeworks material, the energy demand is 1.1-1.3 MJ_{el}/kg and 8.6-10.1 MJ_{th}/kg, therefore in line with published data. As for the electricity consumption, likely sources of deviations include the vacuum pump and blower efficiency, and the pressure drops in the contactor (e.g. we do not account for concentrated pressure drops). As for the heat consumption, the main difference is found when comparing the future Climeworks target, which includes heat integration options between heating and cooling and that we do not include in our models.

Bajamundi et al report measured data of a modular DAC system using an amine-functionalized polystyrene sorbent, operating as a VTSA cycle. The resulting thermal energy demand is in the area of 27.4 MJ/kg and the mean electrical energy demand is 8.6 MJ/kg [93]. The test was carried out with varying atmospheric temperature and humidity, which is a possible source of higher energy consumption. However, the reported energy consumption is significantly higher than other experimental and numerical studies, which might be linked to the specifics of the experimental plant.

Kulkarni and Sholl report modelling results with an energy requirement of 0.79 MJ_{el}/kg and 6.0 MJ_{th}/kg when using an amino-modified silica adsorbent, TRI-PE-MCM-41 [73]. We cannot directly compare these with our results because we didn't run specific simulations for TRI-PE-MCM-41 – but rather consider it when deriving the exemplary sorbent. In fact, the performance is similar to the exemplary sorbent (namely E-A, E-M and E-L cases), for which we obtain 0.8-1.0 MJ_{el}/kg and 7.1-7.7 MJ_{th}. Despite a few differences between the system configuration affecting the heat consumption, e.g. they consider direct steam heating, energy results are similar.

Sinha et al [53] report modelling result for a VTSA system similar to the system of Kulkarni and Sholl, but using two amino-modified MOFs, MIL-101(Cr)-PEI-800 and mmen-Mg₂(dobpdc). The reported total energy demand is 5.11 MJ/kg for the former sorbent and 3.6 MJ/kg for the latter. In our simulations for MIL-101(Cr)-PEI-800, we obtain 4.7-8.9 MJ/kg, depending on the adsorption of water. The key difference here is due to the water adsorption, which is not included in the work of Sinha et al while it is here: when considering the low capacity water isotherm (i.e. case MP-M), we obtain a total energy demand of 4.7 MJ/kg, fully in line with Sinha et al.

Yu and Brilman measured experimentally an energy consumption of $6.5 \text{ MJ}_{\text{th}}/\text{kg}$ and $0.6 \text{ MJ}_{\text{el}}/\text{kg}$ using Lewatit in a fixed bed reactor [94]. Our corresponding case (L-L) shows values in the range of $10.1\text{-}11.8 \text{ MJ}_{\text{th}}/\text{kg}$ and $0.6\text{-}1.3 \text{ MJ}_{\text{el}}/\text{kg}$. The main difference can be found once again in the water, as the experiments were carried out using a dry feed. We estimate that removing water would decrease the energy consumption of about $3 \text{ MJ}_{\text{th}}/\text{kg}$ (see Figure A.1), thus in good agreement with the experimental value of Yu and Brilman.

Finally, we can do a back-of-an-envelope comparison of our productivity with a proximate value for Climeworks Hinwil plant. Considering that the demonstration plant is designed for $2460 \text{ kg}/\text{day}$ using 18 modules, whose unit size we estimate to be similar to a cube of 1.5 m side, and assuming $24 \text{ h}/\text{day}$ operation, we obtain about $1.7 \text{ kg}/\text{m}^3/\text{h}$, in line with our APDES-NFC case when using low linear driving force. Moreover, when comparing DAC to classical TSA applications for CCS, we see that the productivity decreases of approximately one order of magnitude: from $28\text{-}70 \text{ kg}/\text{m}^3/\text{h}$ to $0.5\text{-}10 \text{ kg}/\text{m}^3/\text{h}$.

Overall, the solid sorbent process model shows that the performance of different sorbents, here identified by different CO_2 isotherms and physical properties, are strongly affected by the H_2O isotherms and the heat and mass transfer. Within the limits of physics, it is convenient to design DAC sorbents that (i) limit the water adsorption capacity if the energy is to be minimized (ii) possess a positive $\text{CO}_2\text{-H}_2\text{O}$ cooperative adsorption if the productivity is to be maximized, and, in any case, (ii) show low mass transfer resistance.

2.6 PROCESSES COMPARISON AND ECONOMIC EVALUATION

The Pareto curves of all three processes are compared in Figure 2.12. When using KOH as a solvent the productivity is the lowest and considering the exergy-productivity range of all processes, the exergy does not change much with a change in productivity. The MEA process on the other hand is more sensitive for differences in productivity and the exergy consumption increases very steeply with increasing productivity. The optimization with the solid sorbent process results in the lowest exergy consumption with the highest productivity, however with the largest uncertainties. We have therefore highlighted the results with a blue area encompassing all computed exergy-productivity data. The area starts approximately nearby the KOH/MEA processes, but extends to much higher productivity/lower energy consumption ranges. Table 2.2 lists the share of the energy demand for the different processes; notably the lowest energy demand is obtained for the KOH process.

It is important to stress that the calculation of the productivity is here based on the largest contributor to the process footprint, i.e. the air contactor volume; the two liquid solvent processes do not include the size of additional components like

the calciner/reboiler or other equipment. Similarly, for the solid sorbent process, we did not consider the size of the piping and valves equipment. We note that by leaving these ancillary equipments out, the productivity calculations are slightly advantageous for the liquid solvent processes since the additional components take up more space compared to the solid sorbent process.

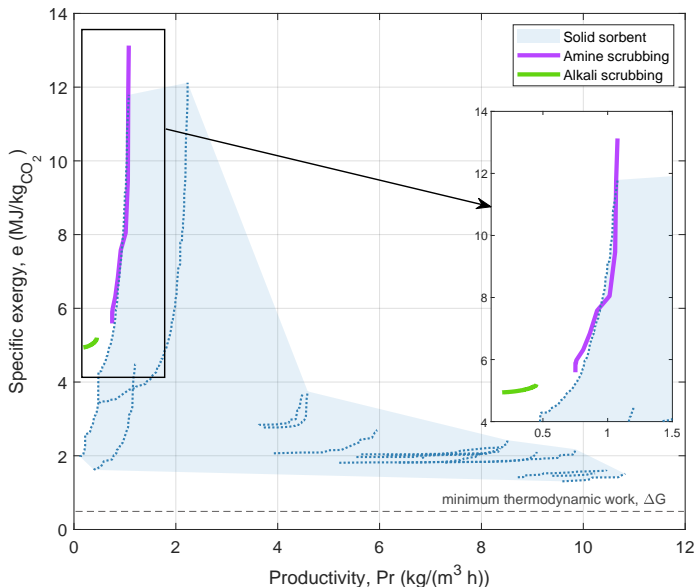


FIGURE 2.12: Resulting Pareto charts of all three processes. For the solid sorbent process an area is plotted, which comprises all Pareto plots, including the sensitivity analysis.

The results of the cost analysis is shown in Figure 2.13, which reports the maps of the total system costs as function of the heat price (c_{th}), the electricity price (c_{el}) as well as the air contactor cost (γ). We find that, for all processes but the solid sorbent with high mass transfer, the cost is strongly dependent on the module cost. Accordingly, low-cost area ($<200\$/\text{tonCO}_2$) is found for the low range of γ . The MEA economics (Figure 2.13b) strongly depends on the heat price, since the thermal energy demand is dominating. Accordingly, a low-cost area ($<200\$/\text{tonCO}_2$) can be found at low heat cost and low module cost. The total costs increases significantly for values of c_{th} above 5 \$cents/ kWh_{th} , irrespective of the module cost. Compared to the MEA process, the alkali scrubbing (Figure 2.13a) shows more favorable total costs, which do not depend strongly on the heat price thanks to the significantly

TABLE 2.2: Energy and exergy consumption of the three processes for the two extreme Pareto points A and B, referring to the Pareto charts shown in Figure 2.12. For the solid sorbent process the exemplary isotherm is considered (case E-A) and the range in brackets indicates the results of the sensitivity analysis.

	KOH		MEA		Solid sorbent	
	A	B	A	B	A	B
Energy (MJ/kgCO ₂)	6.21	6.48	20.04	49.32	7.96 (3.98-11.17)	8.68 (4.69-23.49)
Exergy (MJ/kgCO ₂)	6.21	6.48	5.59	13.13	1.81 (1.31-3.45)	2.1 (1.42-12.12)

smaller thermal energy demand. On the other hand, the low productivity makes the process more dependent on the module cost. The solid sorbent process is shown in Figure 2.13c and d, for low and high mass transfer rates, respectively. For materials allowing high mass transfer rates, the process shows on average the lowest costs thanks to the combination of low energy demand and high productivity compared to the two liquid solvent processes. In this case, the costs are mainly dependent on the heat price. However, this changes significantly in case of low mass transfer rates as the capture cost becomes strongly dependent on the module cost, with a resulting behavior similar to the MEA, though more favorable.

In this simplified economic calculation we did not differentiate between high and low temperature heat. However, we can reasonably assume that the requirement of low temperatures opens opportunities for recovering low-grade heat, typically wasted, especially if simple heat collection is possible. We can visualize this by using exergy rather than energy for computation of the heat costs; the results are shown in the Supporting Information in Figure A.13. Notably, for the KOH process results stay nearly the same, i.e. there are no opportunities to use waste heat in the calciner, whereas the MEA process becomes much cheaper compared to the previous results. The costs for the solid sorbent process decrease as well.

Overall, from the energy-productivity-costs analysis presented here we can reach the following recommendations:

- For the MEA process (and similar liquid scrubbing processes using amines as solvents), improvement efforts must be focused on lowering the thermal energy consumption, possibly via a combination of more favorable solvents and advanced process configurations, similarly to what has been done in standard CCS applications. Especially, new solvents need to nicely combine high CO₂ loading, fast reactions, limited toxicity, and simple manufacturing. More

advanced existing solvents (e.g. the proprietary solvent from MHI, Cansolv, AkerCCS), are worth testing in DAC applications.

- For the KOH process, it is key to keep the contactor cost low, which is likely possible thanks to the simple design and the use of established components (i.e. contactor packing). The low process productivity and resulting high dependency on contactor costs also call for a simpler regeneration process compared to the current configuration.
- For the solid sorbent process using existing sorbents, the cost optimal design requires to fully characterize the sorbent from a multi-component equilibrium and transport perspective. Once sorbent characteristics are known, the improvement priority can be either directed on decreasing the contactor costs, e.g. via additive manufacturing, or on designing a convenient energy system for heat provision, e.g. via integrating heat recovery options.
- The development of new solid sorbents, which can in principle exploit several thousands of possible new structures [95], should always prioritize high mass transfer, and should be connected to the environment and application where DAC is supposed to work. If the productivity is to be prioritized, new sorbents should exploit the cooperative adsorption of CO₂ and H₂O and be designed for operating in countries with moderate-to-high humidity. If the energy consumption is to be minimized, new sorbents should selectively adsorb CO₂ over H₂O and be designed for operating in arid countries with high renewable heat potential.

When comparing the different technologies, we can note that:

- Productivity: Both liquid solvent processes show a low productivity range, with [0.18–0.45 kgCO₂ m⁻³ h⁻¹] for the alkali scrubbing and [0.75–1.08 kgCO₂ m⁻³ h⁻¹] for the amine scrubbing. For the solid sorbent process this range is much broader with [3.8–10.6 kgCO₂ m⁻³ h⁻¹], but more data uncertainties are present.
- Energy consumption: The amine scrubbing process shows the highest energy demand, resulting in a 2nd law efficiency¹ of $\eta_{nd} = 3.8 - 8.8\%$. For the KOH process the energy demand is lower, but at high temperature, thus requiring hydrocarbon fuels, resulting in $\eta_{2nd} = 7.6 - 7.9\%$. For the solid sorbent process, the energy consumption is relatively low, and at low temperature, with potential for heat integration with other processes ($\eta_{2nd} = 13.1 - 37.7\%$).

¹ the 2nd law efficiency is calculated as the ratio between the exergy obtained here and the minimum thermodynamic work of separation $\eta_{2nd} = \frac{e}{\Delta g^{min}}$.

- Scalability: For the liquid solvent processes, the capture unit is modular and can be easily scaled up and down. Concerning the regeneration, a complex process is required for the alkali scrubbing, which fits better large scale plants. For the amine scrubbing, the regeneration process is moderately complex, requiring dedicated equipment (heat exchanger, stripper, etc.) and thus would not fit small scales. The solid sorbent process could be easily scaled up and down, but at large scale the piping and the number of valves would make the process design and control challenging. In addition, the process is discontinuous and therefore requires storage vessels (here not considered).
- Economic performance: All three processes have areas of cost lower than 200 \$/t_{CO₂}, but this is achieved for different boundary conditions. MEA benefits the most of low heat price while KOH of low contactor cost. Depending on the specific mass transfer coefficient, solid sorbent benefits of low heat price or low contactor cost. When looking at the contactor cost for the three different processes, it is worth noting that the volume-specific cost for liquid scrubbing is likely lower than for solid sorbents, as conventional packing and cheap solvents are used instead of expensive sorbents (i.e. in 2.13 the liquid scrubbing are more likely to work in the region of low contactor cost than solid sorbents).
- Fitness for 1.5°C scenario: The solvents for the liquid scrubbing processes are available at large scale, but the water consumption is high, which would be problematic in water-distressed areas. For the regeneration, the heat provision for the amine scrubbing, as well as the fuel for the alkali scrubbing process must be CO₂-neutral. For the solid sorbent process, a sorbent for DAC application is not yet available at the scale for capture of gton_{CO₂} per year, and the heat provision must be CO₂-neutral; on the other hand, there is the possibility to co-produce clean water. In all cases, the process must be designed with a system approach that includes the energy provision.
- Scientific challenges: The liquid solvent processes are already well understood. For the solid sorbent process, there is a lack of experimental data relevant for DAC applications and the underlying adsorption mechanisms are not yet fully understood.
- Technological challenges: A more efficient design of the different reactors of the regeneration section, as well as the electrification of the calciner can further improve the alkali scrubbing process. Concerning the amine scrubbing, research on the redesign of the absorber for handling more advanced amines (volatility, toxicity, etc.) is needed. Challenging fields for the solid sorbent process comprise the development of an efficient heat exchange within the contactor, heat integration (heating/cooling), an advanced design of the contactor as well as the identification of a leading sorbent.

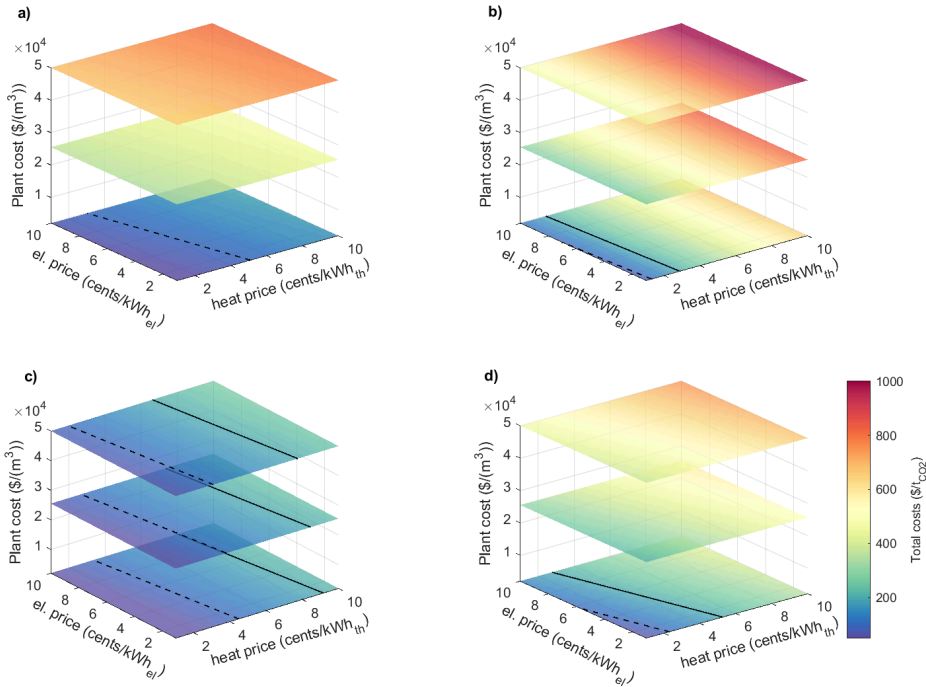


FIGURE 2.13: Maps of total system cost as a function of electricity price, heat price and plant cost, referring to the m^3 of air contactor for the three different processes: KOH using point B on the Pareto chart (highest productivity) (a), MEA using point A on Pareto chart (lowest exergy consumption) (b) and (c) + (d) solid sorbent case E-A (c: high kinetics $k = 0.1 \text{ s}^{-1}$ using point B on Pareto chart and d: low kinetics $k = 0.0001 \text{ s}^{-1}$ using a middle point on the Pareto chart with an exergy consumption similar to the KOH process). We have assumed full-load operation plant, a 20 year project life and an 10% discount rate. The dashed lines show total costs with a value of $100 \text{ \$/tCO}_2$ and the continuous lines a value of $200 \text{ \$/tCO}_2$. As an example: when assuming heat costs of $c_{th}=5 \text{ \$/kWh}_{th}$, electricity costs of $c_{el}=10 \text{ \$/kWh}_{el}$ and contactor costs of $\gamma=25000 \text{ \$/m}^3$, this would result in total costs of $419 \text{ \$/tCO}_2$, $537 \text{ \$/tCO}_2$, $149 \text{ \$/tCO}_2$ and $427 \text{ \$/tCO}_2$ for the KOH, MEA and the two solid sorbent processes, respectively.

2.7 CONCLUSIONS

In this chapter, three main DAC processes have been analyzed and their process line-ups optimized. They were subsequently compared on the basis of their exergy and energy demand as well as productivity. The alkali scrubbing and solid sorbent VTSA processes have been selected because of their comparative technical maturity amongst the novel DAC processes. For comparison, the conventional and technically mature amine scrubbing process has been added as a benchmark by extending its operating range from flue gas to air capture. These processes have been modelled with state-of-the-art tools and a rigorous multi-objective optimization has been carried out to identify the best design. The results have shown that the absorption-based processes perform generally worse than the solid sorbent process. The productivity for the alkali and amine scrubbing processes ranges between $0.18 - 0.45 \text{ kgCO}_2 \text{ m}^{-3} \text{ h}^{-1}$ and $0.75 - 1.07 \text{ kgCO}_2 \text{ m}^{-3} \text{ h}^{-1}$, respectively. For the solid sorbent process it can vary between $3.8 - 10.6 \text{ kgCO}_2 \text{ m}^{-3} \text{ h}^{-1}$, however, when accounting for the uncertainties surrounding the mass transfer in the adsorption process and including the lowest estimates presented in literature, the productivity range broadens to $0.13 - 10.6 \text{ kgCO}_2 \text{ m}^{-3} \text{ h}^{-1}$. The solid VTSA process also comes out on top when we consider exergy demand, which could be as low as $1.31 \text{ MJ kgCO}_2^{-1}$ in the best case and, moreover, of a lower temperature than the one required by the absorption processes. The three technologies have also been compared from an economic point of view. The aim, in this case, was not to provide an accurate cost evaluation, but to compare the economic potential of the processes on the basis of common assumptions. The total cost has been calculated using the productivity and energy demand computed with thermodynamic models, which makes the relative comparison strong, while providing a simple estimate of absolute values. To account for uncertainties and fluctuation in energy prices, the costs have been evaluated for a certain range of electricity, heat and contactor prices. From this analysis too the VTSA proves to be the most promising process. Its higher productivity makes its cost less dependent on the air contactor price, which is encouraging, as advanced design of the contactor and novel sorbents could be more expensive than what is currently expected. While the solid sorbent VTSA process comes forward from our analysis has the most attractive option, many questions are yet to be answered to be effectively deployed at large scale, with the most pressing involving the adsorbent itself. The adsorption/desorption kinetics and the affinity of the sorbent for H_2O have a tremendous influence on the performance of the VTSA process, but information on this is scarcely reported in the literature, even for the most prominent materials. Moreover, there are also technological issues to be solved. The sorbent regeneration requires considerable amounts of (low temperature) heat: an optimal air contactor design should allow efficient heat transfer and recovery. We believe that by addressing these challenges the

greatest benefits could be reaped. On the other hand, the alkali and amine scrubbing processes will likely be needed to meet the carbon removal targets consistent with 1.5 °C.

2.8 ON THE OPTIMAL DESIGN AND OPERATION OF SOLID SORBENT DIRECT AIR CAPTURE PROCESSES AT VARYING AMBIENT CONDITIONS

The growing academic body of literature on solid sorbent DAC has so far mainly focused on four main pillars: (1) the role of DAC technologies in the mitigation of climate change [96–101]; (2) the development of new materials capable of capturing CO₂ from air [72, 75, 102–110]; (3) the life-cycle assessment of DAC [111, 112]; and (4) the economics of DAC technologies [51, 98, 113–115]. Note that the reference list above is not meant to provide a comprehensive overview of the rapidly expanding works on DAC, but is rather exemplary. For that purpose, readers could refer to recent review papers. [107, 116, 117] However, so far little attention has been paid to investigate the DAC performance under varying ambient conditions (e.g. different geographic locations, varying seasons, daily fluctuations), despite these factors play a pivotal role for the performance of the technology [118]. Recently, Terlouw et al. (2021) has shown that the choice of installing location of a DAC system is a key factor for its global greenhouse gas removal potential, especially because of renewable heat and electricity availability. Moreover, there is an underlying thermodynamic behavior that controls the solid sorbent DAC performance at varying ambient conditions, notably temperature and humidity of the incoming air. First of all, the ambient temperature strongly affects the CO₂ adsorption on the material, which is an exothermic process. Higher air temperature leads to higher specific energy demand and lower productivity, especially at fixed regeneration temperatures; this is a direct consequence of the reduced cyclic capacity at higher air temperature. Second, the air humidity affects the performance of most solid sorbents currently considered for DAC (e.g. amine-functionalized sorbents, ion exchange resins), though in a more complex way: The coadsorption of water at high humidity levels leads to: (1) increased adsorption capacities and improved reaction kinetics, resulting in larger capturing capacities per cycle; and (2) higher energy requirements during the regeneration, since besides CO₂ also water must be desorbed.

Most academic work investigating the influence of temperature and humidity has been conducted in the realm of material science, including both theoretical and small-scale experimental analysis under lab-conditions. Table 2.3 provides an overview of studies that took into account the impact of humidity and/or temperature on the sorbent. It highlights the counteracting effect of increased humidity on the energy and adsorption capacity, and the straightforward effect of the temperature on the CO₂ adsorption capacities. The studies suggest, that materials used for solid sorbent

TABLE 2.3: Studies on the effect of temperature and humidity on the performance of sorbent materials.

Material	Humidity		Temperature		Source
	Capacity	Energy	Capacity	Energy	
Nanofibrillated cellulose framework coated with PEI	increase	na	na	na	Sehaqui et al. (2015) [108]
Fumed silica with PEI coating	ambiguous	na	na	na	Goeppert et al. (2011) [104]
Amine-functionalized cellulose	increase	increase	decrease	na	Gebald et al. (2014) [119]
Amine-functionalized cellulose	increase	increase	decrease	na	Wurzbacher et al. (2016) [75]
Amine-functionalized cellulose	increase	increase	decrease	none	Wurzbacher et al. (2012) [49]
Amine-functionalized proprietary resin	increase	na	decrease	na	Elfving et al. (2017a) [72]
Amine-functionalized proprietary resin	increase	na	decrease	na	Elfving et al. (2017b) [103]
Amine-functionalized CA silica fiber sorbents	increase	na	decrease	na	Sujan et al. (2019) [109]
Aminopolymer-impregnated hierarchical silica structures	increase	na	increase	na	Kwon et al. (2019) [106]
Amine-Impregnated MIL	increase	na	decrease	na	Rim et al. (2022) [110]

DAC typically perform best in humid and cold conditions. However, for a carbon neutral DAC process, renewable energy supply is needed. These renewable resources are typically located at warm and dry locations (especially cheap solar resources). It follows that the availability of renewable energy and the ambient air conditions lead to a trade-off between an optimal DAC performance and an economical energy supply.

With this work, we aim at better understanding the effect of climatic conditions (i.e. geographic locations) on the optimal operation and design of solid sorbent DAC processes as well as on the associated energy supply system. We therefore complement and extend the studies on sorbents behavior and characterization at different ambient conditions with a process and system level perspective so far

missing in the open scientific literature. We do this by bridging a robust, yet complex thermodynamic model of the process to a computationally efficient linear model, which can be used for hourly-resolved system design and operation.

Modelling framework for Solid Sorbent DAC processes at varying ambient conditions

Ambient conditions vary significantly following daily and seasonal cycles; understanding DAC behavior under such conditions therefore requires a yearly time horizon with an hourly resolution. Clearly, the classical thermodynamic approach of simulating adsorption cycles with energy, mass and momentum balances discretized in space and integrated in time is not viable in a similar framework: the computation of a full cycle and its CSS conditions requires significant computing time (typically in the order of minutes for CSS), which would make the analysis unfeasible when thousands (8760) of simulations must be performed. On the other hand, linear modelling, which is often used for complex time-discretized problems, has limited fidelity if not supported by thermodynamics; this can easily lead to wrong performance prediction. To tackle these shortcomings and properly evaluate the performance of a DAC process under varying ambient conditions, we developed a new modelling framework, which is shown in Figure 2.14. At the core of the method lies the interaction between a thermodynamic-based description of the process and its reformulation as a MILP. The thermodynamic framework (top box in figure 2.14) is used to evaluate and optimize the performance of the DAC VTSA cycle for an assigned set of temperature-humidity combinations. It is important to note, that the use of process optimization allows to identify the optimal working conditions - in terms of productivity and energy consumption - for any temperature-humidity combination. These results are then used to build model-based performance maps at different ambient conditions, which provide input to the hourly-discretized MILP optimization problem (bottom box in figure 2.14).

It is worth noting, that the thermodynamic modelling approach used here has been developed and applied to various processes in the past, e.g. to DAC in Sabatino et al. [120], to TSA in Joss et al. [84], and to DAC in Streb et al. [85]. On the other hand, the key modelling contributions of this work are (i) the development of the MILP-DAC model, and (ii) the development of the overarching modelling framework shown in Figure 2.14. Accordingly, the remaining of this section describes the MILP-DAC model and its embedding in the overall framework (i.e. with respect to the possible DAC operating modes). The performance maps are described at the end of this section, while all details on the thermodynamic framework can be found in the references mentioned above (for clarity, the main balance equations are also reported in the Supplementary Information).

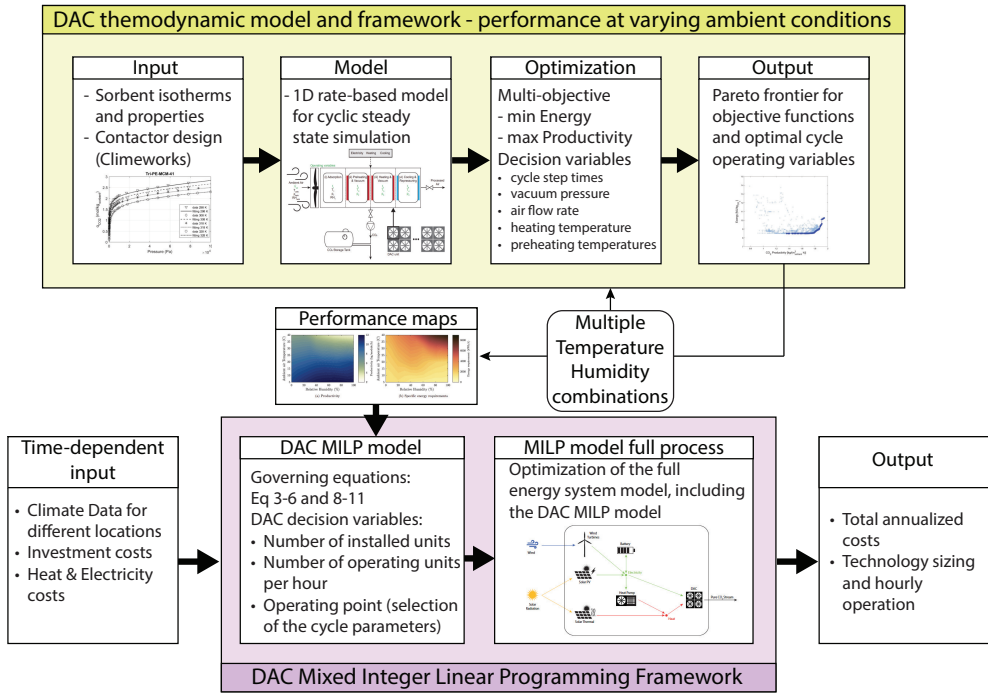


FIGURE 2.14: Modelling framework developed in this work to assess the performance of DAC at varying ambient conditions. The thermodynamic models adopted here and depicted in the top part of the figure were developed in the work of Sabatino et al. [120]. The MILP modelling framework includes the DAC model and the overall system model

Concerning the DAC cycle, we consider a VTSA process, which can be regarded as state-of-the-art for CO₂ capture from air with solid sorbents. This cycle consists of four different steps, i.e. (i) adsorption of the CO₂ from ambient air, (ii) preheating while pulling a vacuum to remove most of the nitrogen, (iii) heating at vacuum conditions to produce a highly concentrated stream of CO₂, and (iv) repressurization and cooling (see Figure 2.15). Such a VTSA process is affected by both exogenous and controllable variables. The ambient air conditions are exogenous and vary over time and space. The controllable variables include design and operation choices, such as the sorbent type, the contactor design, cycle times, pressure levels, and the regeneration temperature. Accordingly, a VTSA process will need to be equipped with a control strategy so as to guarantee high performance at varying exogenous variables by changing the operating parameters.

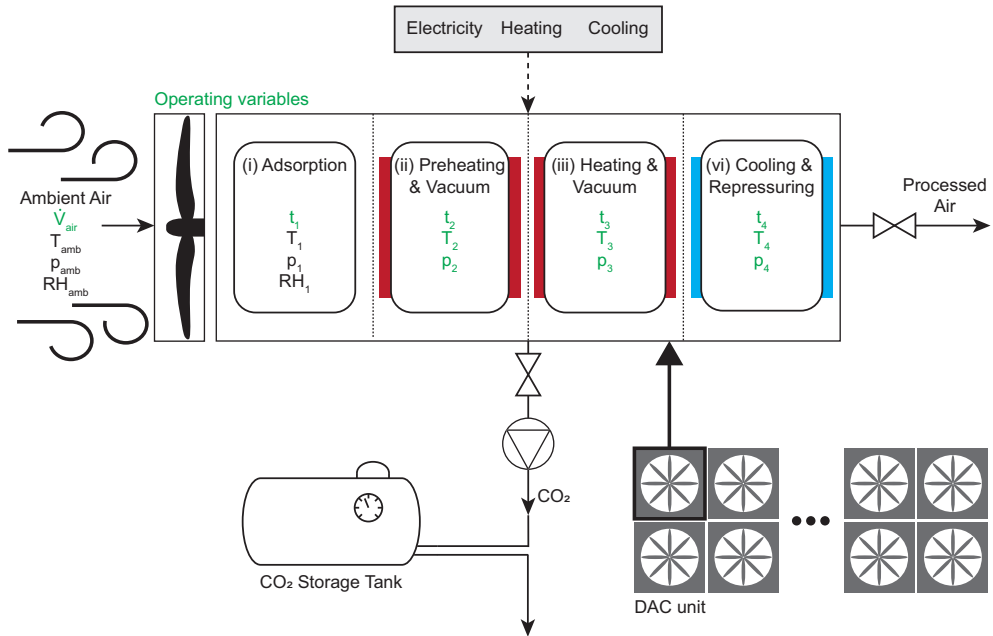


FIGURE 2.15: Scheme of a VTSA process for DAC including a representation of the four adsorption steps. Note that the process also produces water and other waste gases that were not illustrated for simplicity.

The mixed integer linear model presented requires data on the performance of a VTSA as a function of the exogenous variables and the respective control parameters. To this end, we simulated the process with a 1-D model, where the productivity and energy consumption are calculated starting from the cycle and sorbent characteristics. The 1-D model is rate-based and has been used and validated experimentally for multiple adsorption cycles. More details can be found in Sabatino et al. (2021), Cases et al. (2013), and Joss et al. (2015) [77, 82, 120, 121]. For the sorbent, we follow the approach presented in section 2.2, and consider an exemplary material, which was obtained by combining experimental data of four representative sorbents for Direct Air Capture. This allows us to study the average behavior of solid sorbents without focusing on a specific material². The isotherm parameters as well as the model parameters for the simulation are listed in Table A.19 and A.20 in the Supplementary Information. By including an equivalent temperature as explained in Section 2.2

² The details on the exemplary sorbent calculations can be found in section 2.2

the isotherm does not only change with temperature but also with humidity, which is shown in Figure 2.16. In order to obtain the data needed to fit $\alpha_i(\Theta_t)$, $\beta_i(\Theta_t)$,

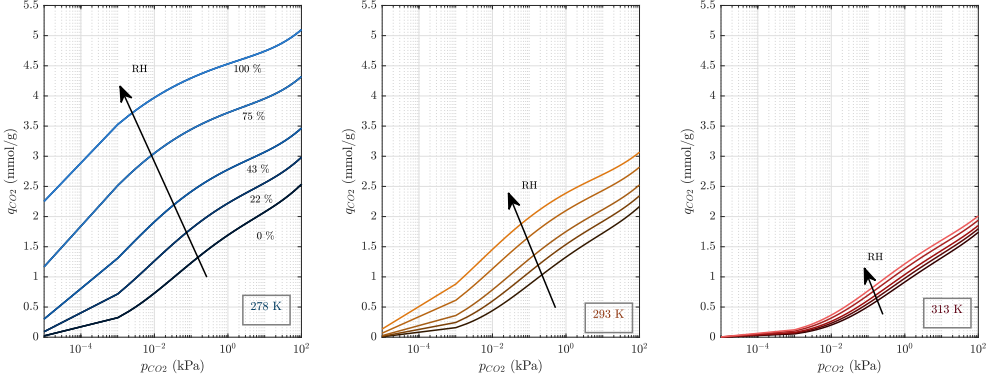


FIGURE 2.16: CO₂ isotherms for different temperatures and humidity levels of the exemplary sorbent material used in this work. a) 278 K, b) 293 K and c) 313 K.

$\gamma_k(\Theta_t)$ and $\delta_k(\Theta_t)$, we carried out several multi-objective simulations of the VTSA DAC process, whose two competing objectives are productivity Pr and energy consumption e [91]. The problem is therefore defined as:

$$\begin{aligned} & \min_x (-Pr, e) \\ & \text{subject to } \Phi \geq \Phi_{\text{spec}} \end{aligned} \quad (2.26)$$

where x are decision variables³, Φ the CO₂ (dry) purity and Φ_{spec} the required minimum purity (here 95%). Details of the calculation of the productivity and the energy consumption, as well as the range of the decision variables can be found in the Supplementary Information (Section A). To account for the influence of both temperature and humidity on the performance of the VTSA process, several cases were optimized by combining a range of ambient temperatures (5 °C, 20 °C, and 40 °C) with different humidity levels in the feed stream (0%, 22%, 43%, 75% and 100%).

It follows, that multiple Pareto fronts were obtained for several fixed ambient conditions. The results are shown in Figure 2.17.

Figure 2.18 shows the interpolation of the results in the investigated range of ambient conditions. As expected, the CO₂ capacity of the sorbent decreases with temperature and therefore the productivity is higher at low ambient temperature. In addition, the capacity increases with increasing humidity, especially for low

³ Decision variables are: adsorption, preheating and heating times, the vacuum pressure level, the air flow rate and the heating and preheating temperatures

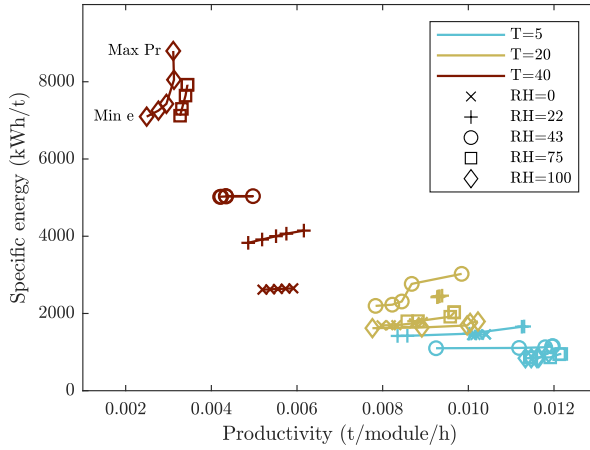


FIGURE 2.17: Sorbent Performance at different ambient air conditions

temperatures. However, for temperatures above 30°C, the productivity decreases with humidity. The reason is found in the trade-off between the two competing objectives of optimization. When having a higher humidity in the feed stream, more water has to be heated up during the regeneration; whilst for lower feed temperature this is compensated by the sorbent capacity, for higher feed temperature the capacity of the sorbent is low, and the heat required to heat up the water has a high effect on the overall energy consumption. Therefore, the process optimization keeps the energy requirement limited by allowing a loss in productivity.

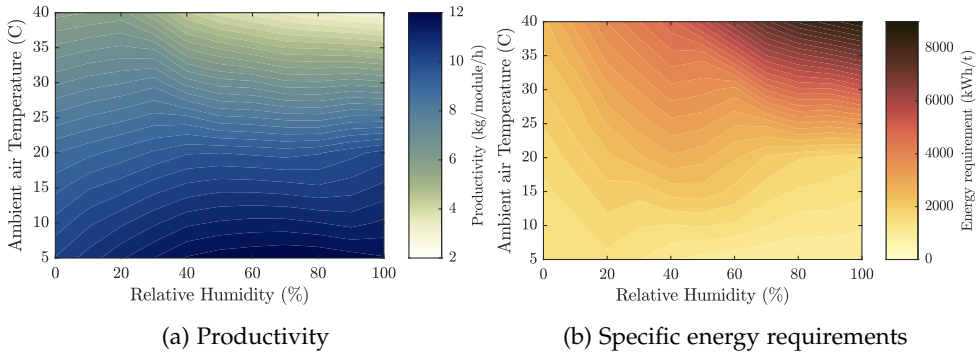


FIGURE 2.18: Productivity and specific energy requirements for maximal productivity optimization

Results

The cost minimization problem described is carried out for two overarching cases: First, we compute the performance of DAC for different fixed temperature-humidity combinations, i.e. their values do not vary in time and are constant for every hour of the year. This allows us to understand the performance of DAC for different ambient conditions but independent from their change in time and space and of the DAC operation strategy. Second, we compute the performance of DAC for varying temperature and humidity over the year according to real weather data. In order to investigate the system at (i) temperate-humid, (ii) hot-humid, and (iii) highly variable ambient conditions, we used the weather data of The Netherlands (Schiphol), Spain (Barcelona), and California, US (Lancaster), respectively.

Performance of DAC for different time-independent ambient conditions

Here, we solve the cost optimization of a DAC system for different, time-independent temperature-humidity combinations.

Figure 2.19 shows the normalized capturing costs and energy requirements for 66 cost optimizations with different temperature-humidity combinations. Each marker represents one optimization with the respective temperature and humidity level. The results are shown as contour lines for (a) specific normalized capturing costs and (b) specific total energy requirements.

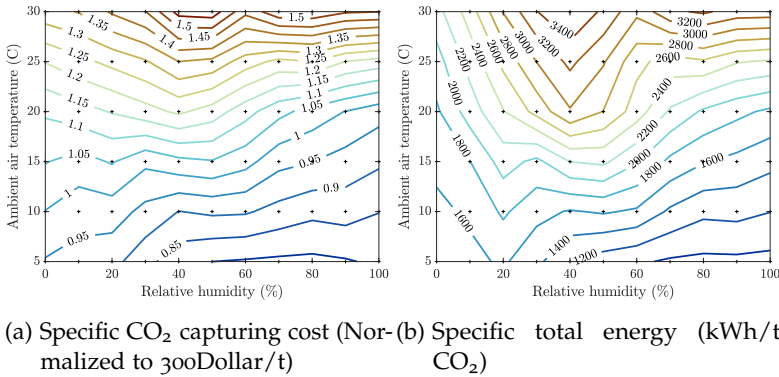


FIGURE 2.19: Normalized capturing costs and specific energy requirements at different ambient conditions.

The results suggest that the temperature is the major driver for both energy requirements and capturing costs. In fact, a 1 Kelvin increase in temperature leads

to a 3.4% increase in specific energy requirements and a 2.0% increase in costs on average. These relationships are though non-linear: The increase in specific energy requirement and cost is larger at higher temperature. The effect of higher temperatures on the capturing costs is caused by higher specific energy requirements and lower sorbent productivity. In contrast to temperature, humidity plays a subordinate role for the DAC performance. Both the specific total energy requirements and the capturing costs first increase with humidity, peaking between 40-60% and then decline again. The electric energy requirement follows the same shape but with steeper slopes while the thermal energy requirements increase in humidity only for dry conditions (below 30%) and reach a stable level for higher values (see Figure A.27 in the Supplementary Information). For the former, the reason lies in the higher CO₂ cyclic capacity with higher humidity: The presence of water reduces the partial pressure of CO₂ in the product thus requiring a lower vacuum level and therefore lower overall electricity consumption. However, there exists a trade-off between reducing the vacuum pressure to get a higher cyclic capacity and increasing the vacuum pressure to save energy. For moderate humidity (e.g. 40%), the electrical energy demand increases with higher temperature since the positive effects of the humidity during the adsorption and the higher CO₂ partial pressure during the desorption are limited. On the other hand, for lower temperatures, the vacuum pressure can be higher, since the cyclic capacity is already high. As for the effect of humidity, the productivity increases with humidity up to 30-40% and remains thereafter approximately constant (see A.28b in the Supplementary Information). The rising productivity and rising energy requirements with increasing humidity have two counteracting effects on the capturing costs: (i) Due to a higher productivity, less units are required for a fixed CO₂ capturing amount resulting in lower overall investment costs; (ii) rising energy requirements increase the operating costs of the unit. Consequently, the share of investment costs in the total capturing costs is lowest for humidity levels of around 40% (see also Figure A.28a in the Supplementary Information) and accounts for 76% of total cost. The lowest overall capturing costs are reached for cold and humid conditions, where the temperature has a leading role; these results confirm previous studies on sorbent performance [75, 103, 109].

Performance of DAC for time-varying ambient air conditions

To study the effect of different climatic conditions on the DAC process with plausible humidity and temperature profiles, we selected three representative locations: Schiphol (The Netherlands), Barcelona (Spain), and Lancaster (US). Schiphol is characterized by a humid and temperate climate throughout the year with limited variability. Barcelona exhibits a similarly small variability of humidity and temperature, however, the average temperature is about 6 °C higher while humidity 20

percentage points lower. Lancaster has a similar average temperature as Barcelona, but its climate is significantly drier; more importantly, humidity and temperature exhibit high fluctuations even within single days. The input data as well as temperature and humidity profiles of all three locations are reported in Table A.22 and Figures A.29-A.32 in the Supplementary Information. For simplicity, investment and maintenance costs are assumed to be equal at all locations. The findings are thus driven by different temperature and humidity profiles and the related differences in the process performance.

We minimize total annualized costs with an annual demand of 10,000 t of CO₂. All optimizations have the following configurations: (i) To reduce the run-time of the optimizations, full-year weather profiles are clustered into 100 typical days with a k-means algorithm. The days are clustered the same way for each model configuration of the same location. (ii) The minimum working temperature of the sorbent was assumed to be 5°C, i.e. the temperature has been fixed to 5°C also for colder days. This is a conservative approach, as colder temperatures are beneficial for the CO₂ cyclic capacity. We decided to implement this approach to prevent infeasible operation close to the water triple point, especially for the adsorption step. There exist multiple strategies to operate DAC at low temperature, but these need to be devised specifically for a given design (one simple possibility is to keep the sorbent above 0°C). (iii) The relationship between energy input and CO₂ capture is again modeled linearly with no breakpoints. For every location, we run the optimization for the three different operating configurations representing different control configurations and plant layouts. In this shortened version of the research work, the focus is set on the effect of the ambient conditions on DAC, therefore, the results of operating condition 1 (OC1) are explained below, while the additional cases and a sensitivity analysis can be found in the publication [122].

OC1: Flexible CO₂ production and tunable operating variables without water spraying. It can first be noted that Schiphol is the most suitable location for both the cost and energetic performance of the DAC: the capture costs at Schiphol are about 16% lower compared to Barcelona and Lancaster; likewise, the energy requirements are 33% lower. However, it can also be noted that the difference in costs among the various cases is limited and fully negligible between Lancaster and Barcelona. This is an inherent result of OC1, which allows for running the system at the operation points that are optimal for any temperature-humidity combination. In fact, at every location, the system works at full load over the whole modelled time-horizon, which is very much desirable for technologies with high investment cost share as for DAC. Hence, OC1 allows for exploiting the full potential of all installed units at all times, even though the ambient conditions at some time-steps result in unfavorable productivities and energy requirements. Figure A.35 in the appendix depicts the CO₂ output at all locations for different temperature and humidity levels and it

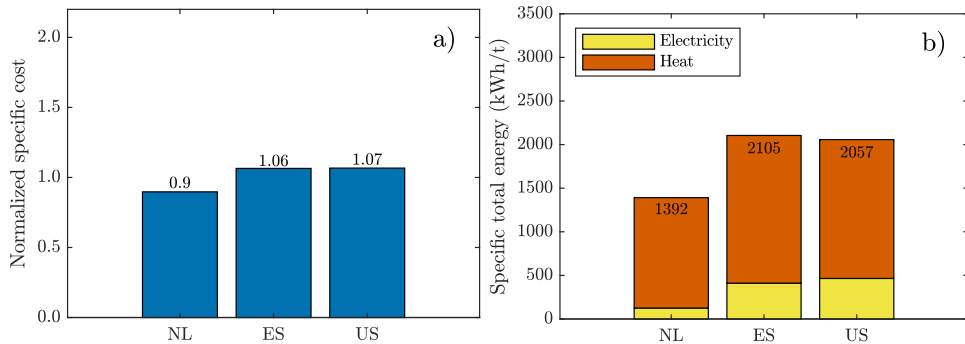


FIGURE 2.20: Cost and energy results for the stand-alone model for operational configuration OC₁.

confirms that the ambient temperature is the main cost and energy driver for the operation of DAC systems. In contrast, humidity plays a subordinate role.

Sensitivity analyses

One of the identified uncertainties that could affect the findings of the previous analysis is the performance of the solid sorbent at varying temperature and humidity. The productivity and energy requirements of the DAC process were obtained using the approach of Sabatino et al. (2021), where an exemplary sorbent was derived [120]. While the effect of temperature for different materials varies depending on the enthalpy of adsorption, the general trends hold for any adsorption material: capturing capacities decrease while energy requirements increase with increasing adsorption temperature (and fixed regeneration temperature). Thus, our results might change slightly with regards to the size of the effect, but not in their general trends. We tested two additional sorbent behaviors by (i) removing humidity dependencies from the data and (ii) by inverting the humidity effect on the performance. These two cases aim at mimicking a sorbent, where CO₂ adsorption is not affected by H₂O adsorption, and a sorbent where CO₂ adsorption decreases with H₂O respectively. In both cases, the results remained substantially similar, confirming the leading role of temperature. Further information and the respective optimization results can be found in the Supplementary Information (Figure A.38 and A.41).

Conclusion

In this section, we have investigated the performance of an exemplary VTSA DAC process under varying ambient conditions, i.e. temperature and humidity. More specifically, we have computed the energy consumption and the minimum system costs of the VTSA for multiple temperature-humidity combinations, and for three exemplary locations (The Netherlands, Spain, and California), where the ambient conditions are different both in terms of average values and daily/yearly profiles.

With this work, we show that when focusing on the stand-alone DAC process the annual average ambient temperature is the main climatic driver for both capturing costs and energy requirements. Surprisingly, humidity plays a subordinate role; this holds true for sorbents where CO₂ adsorption is enhanced by water, as well for those that are negatively affected by water. In cold and humid climates the capturing costs and energy requirements can be significantly lower than warmer locations: we found that the cost and the energy consumption of DAC deployed in The Netherlands are about 16% and 33% lower compared to Spain or California, respectively. This general trend remains true over a wide range of model setups and cost assumptions.

Accordingly, we can draw the following recommendations:

- DAC sorbents behavior at varying climatic conditions, especially at varying humidity, is still not fully understood and adequately investigated. However, the process performance is significantly affected by ambient conditions. Material scientists should consider this when synthesizing and characterizing sorbents.
- The optimal operation of VTSA DAC under time-varying ambient conditions requires adequate control algorithms and instruments. These have to be synthesized for specific process designs and associated dynamics. The vast research community of control systems should consider contributing to this research gap.
- The design of DAC technologies should take into account the fact that operation will inevitably take place under varying ambient conditions, varying electricity generation (i.e. electricity prices), and, likely, varying CO₂ demand.

A MACHINE LEARNING-AIDED EQUILIBRIUM MODEL OF VTSA PROCESSES FOR SORBENTS SCREENING APPLIED TO CO₂ CAPTURE FROM DILUTED SOURCES

The large design space of sorbents structure and the associated capability of tailoring properties to match process requirements make adsorption-based technologies suitable candidates for improved CO₂ capture processes. This is particularly of interest in novel, diluted and ultra-diluted separations, as direct CO₂ removal from the atmosphere. Here, we present an equilibrium model of vacuum temperature swing adsorption cycles that is suitable for large throughput sorbents screening, e.g. for direct air capture applications. The accuracy and prediction capabilities of the equilibrium model are improved by incorporating feed-forward neural networks, which are trained with data from rate-based models. This allows for example to include the process productivity, a key performance indicator typically obtained in rate-based models. We show that the equilibrium model reproduces well the results of a sophisticated rate-based model, both in terms of temperature and composition profiles for a fixed cycle, as well as in terms of process optimization and sorbents comparison. Moreover, we apply the proposed equilibrium model to screen and identify promising sorbents from the large NIST/ARPA-E database; we do this for three different (ultra)diluted separation processes: direct air capture, $y_{\text{CO}_2} = 0.1\%$, and $y_{\text{CO}_2} = 1.0\%$. In all cases, the tool allows for a quick identification of the most promising sorbents and the computation of the associated performance indicators. Also in this case, outcomes are very well in line with the 1D model results. The equilibrium model is available open access at the link provided in the SI.

The results presented in this chapter have been reported in: Grimm, A., Gazzani, M., A machine learning-aided equilibrium model of VTSA processes for sorbents screening applied to CO₂ capture from diluted sources, *Industrial & Engineering Chemistry Research* (2022).

3.1 INTRODUCTION

When looking at the DAC industrial and scientific landscape, separation based on solid sorbents has so far attracted most of the attention and has been successfully demonstrated at relevant scale [123, 124]. Moreover, significant scientific efforts are directed towards the development of new, better performing sorbents for DAC [37, 117, 125]. At the same time, adsorption-based technologies are being developed and researched for CO₂ capture from point sources, from flue gas to syngas to steel work gases [126, 127].

While several studies investigate from a process and material perspective the development of better performing sorbents for CO₂ capture from point sources, there are no works - to the best of our knowledge - that do so in the realm of diluted CO₂ sources, e.g. DAC.

The choice of the adsorbent is indeed a key factor for the optimal design of a capture process and several research groups have developed computational techniques to design new sorbents and to characterize their thermodynamic (and transport) properties [95, 128, 129]. Hundreds of thousands of theoretical sorbent materials have been simulated and could in principle be synthesized, provided the right experimental processes are available and the theoretical crystal is stable. On the other hand, the availability of all these theoretical materials requires a suitable screening procedure, which needs to be fast and accurate enough to provide a reliable ranking. To this end, different approaches exist. A first, simple approach is calculating characteristic parameters, like the working capacity or the heat of adsorption, based on the isotherm data of the materials [130–132]. While this analysis can be extremely fast, the results only provide a rough overview about the suitability of the materials. For a more reliable understanding, a process-based analysis is required [133–136]. Ideally, for every sorbent a detailed process simulation combined with process optimization is carried out; however, such a framework is computationally expensive and may take up to several days per sorbent [77, 137]. Two main alternatives exist to speed up the screening. On the one hand, rigorous process simulation can be coupled to machine learning techniques, for example in the convergence to cyclic steady state. Recently, Pai et al. [138] developed a generalized data-driven surrogate model which well reproduces a PSA/VSA process. The framework makes use of a dense feed forward neural network and can significantly reduce the simulation and optimization time while showing a high accuracy. The data-driven model is trained using the simulation results of different sorbents and operating conditions and can be used as a screening tool, as long as the CO₂ and N₂ adsorption isotherm of the material can be described by the implemented numerical adsorption model. This approach is showing great potential for bridging simulation, optimization and sorbents screening; however, it requires a large representable dataset for training

and testing the algorithms. The second, more traditional approach is to simplify rate-based process simulations by using equilibrium. In this case, simpler models are used to solve the material and energy balances. A few key works are available in literature that demonstrate the potential of equilibrium-based simulations. In their seminal work, Maring and Webley [139] developed a simplified pressure/vacuum swing adsorption (P/VSA) model for a binary mixture. They adopted a well-mixed bed approach for the cycle, consisting of three steps: blow-down, repressurization and adsorption. To further simplify the model, they assumed adiabatic operation and equilibrium between the adsorbed and gas phases. In addition, they proposed an approach to directly calculate the cyclic steady state (CSS). The model was validated for post-combustion CO₂ capture by VSA against rate-based numerical simulations; four different types of sorbents were tested. More recently, Balashankar et al. [140] expanded the approach of Maring and Webley by treating the process as isothermal, and by considering different VSA cycle configuration, which included blow-down, evacuation, pressurization and adsorption steps. Notably, the model was used to screen 197 adsorbents from the NIST/ARPA-E database for CO₂ capture application. When looking at the temperature swing adsorption (TSA) landscape, Joss et al. [78] developed a shortcut model for a four step TSA cycle and binary mixture. No spatial gradients were considered in the model and the partial differential equations were reduced to ordinary differential equations. In addition, the model directly calculates the CSS semi-analytically, which reduces the computational complexity. More recently, Ajenifuja et al. [141] further developed the work of Maring and Webley [139] and Joss et al. [78] and presented an equilibrium model to quickly scan adsorbents using a three-step TSA cycle. Instead of using partial differential equations, a set of nonlinear algebraic equations is used for mass and energy balances, which reduces the computational time. The methodology is applied to screen 75 adsorbents for capturing CO₂.

In this chapter, we further contribute to the topic of equilibrium-based modelling tools for computationally-efficient analysis of adsorption processes. The framework we present builds upon the excellent works discussed above, and further extend them by:

- Bridging the equilibrium-based approach to machine learning, i.e. we improve the accuracy and prediction capability of an equilibrium model using neural networks. This allows, for example, to include the productivity as key performance indicator, and to consider saturation levels in the bed during adsorption below 100%.
- Modelling a vacuum-temperature swing adsorption cycle, i.e. we add the vacuum step to the TSA cycle.

- Considering a ternary mixture as feed where CO_2 is not necessarily the most retained gas, i.e. we add H_2O adsorption, which is often the most adsorbed species in CO_2 capture with V/TSA.
- Including multiple CO_2 isotherm types in the model, i.e. Toth, extended Toth model (Toth-cp), Langmuir-Freundlich, Dual-Site-Langmuir (DSL) and s-shaped isotherm model.
- Applying the tool to dilute or ultradilute CO_2 concentrations, i.e. from CO_2 capture from air to fluegas with 1% CO_2 .

The model that we present here is benchmarked with a well-established detailed 1-D VTSA model. Furthermore, we apply the proposed method to efficiently scan the NIST/ARPA-E Database of Novel and Emerging Adsorbent Materials (NIST-ISODB) in search of promising sorbents to capture CO_2 . The NIST-ISODB database is the world's largest public collection of experimental gas adsorption isotherms [142]. It includes over 30000 isotherms for a wide range of adsorbent materials including MOFs, COFs, zeolites, activated carbons and amorphous porous polymers and serves as basis for several data-driven analyses [143, 144]. In addition, we complement the NIST database with adsorbents data from publications that have not been included yet [120, 133, 145].

This chapter is organized as follows: in Section 3.2 we describe the 4 step VTSA process and the mathematical modeling framework of the oD model. In addition, an overview over the key performance indicators is given. In Section 3.3, the oD model is validated against the rate-based model by comparing the performance for a specific simulation (e.g. in terms of time steps and temperatures) as well as optimization results. Finally, in Section 3.4, the model is applied for screening more than 2100 materials for CO_2 capture from diluted sources.

3.2 EQUILIBRIUM MODEL FOR VTSA

The VTSA cycle considered in this work is shown in Figure 3.1 and consists of four steps: adsorption, blow-down, heating, and cooling. This is a slightly simplified version (i.e. no preheating step) of the VTSA cycle adopted for CO_2 capture from air in Sabatino et al. [120]. Moreover, we consider a feed stream consisting of three components, i.e. CO_2 , H_2O and N_2 , where CO_2 and H_2O can adsorb, while N_2 is treated as an inert. It is worth noting that the model can be adapted to consider additional gas species. Differently from other simplified models [139–141], the targeted species is not necessarily the strongly adsorbed one but can also be the weakly adsorbed component, i.e. H_2O typically shows a higher adsorption capacity than CO_2 when using materials of interest for CO_2 capture from diluted streams.

The model builds upon the approach presented in previous works [139–141], where the key model assumptions are: (i) the bed is treated as a well-stirred reactor, (ii) the gas and the solid phases are in equilibrium during all steps of the cycle, (iii) the gas phase behaves like a perfect gas, (iv) the pressure drop in the bed as well as (v) heat transfer resistances are negligible. Accordingly, at any time instant, the total amount of moles of component i in the bed $N_{i,\text{total}}$ is calculated from the number of moles in the solid (s) and in the fluid (f) phase

$$N_{i,\text{total}}(t) = N_{i,s}(t) + N_{i,f}(t) \quad (3.1)$$

with

$$N_{i,s}(t) = m_s q_i^*(y_i, p, T) \quad (3.2)$$

$$N_{i,f}(t) = \frac{p y_i V_c \epsilon}{RT} \quad (3.3)$$

where p is the pressure in the column, y_i the mole fraction of species i , V_c the column volume, ϵ the void fraction, R the universal gas constant, T the temperature, m_s the mass of the adsorbent and $q_i^* = f(y_i, p, T)$ the equilibrium adsorbed amount. q_i^* can be calculated from any suitable isotherm; in this work we have implemented multiple isotherm equations so as to include in the screening as many materials from the NIST database as possible: Toth, extended Toth (Toth-cp), Langmuir-Freundlich, Dual-Site-Langmuir (DSL) and s-shaped isotherms. The detailed equations can be found in the SI in Table B.15. The overall material balance considering the column and the flows entering/leaving can be written as

$$\sum_i N_{i,\text{total}}(t_f) - \sum_i N_{i,\text{total}}(t_0) = \int_{t_0}^{t_f} \dot{N}_{\text{in}} dt - \int_{t_0}^{t_f} \dot{N}_{\text{out}} dt \quad (3.4)$$

The material balance is complemented by the energy balance, which can be written as

$$m_s c_{p,s} (T(t_f) - T(t_0)) = \int_{t_0}^{t_f} \dot{Q} dt + (N_{i,s}(t_f) - N_{i,s}(t_0)) \sum_i^n |\Delta H_{\text{ads},i}| \quad (3.5)$$

where \dot{Q} is considered positive when entering. The isosteric heat $\Delta H_{\text{ads},i}$ is calculated using the Clausius-Clapyron equation:

$$\left(\frac{\partial \ln p_i}{\partial T} \right) = \frac{-\Delta H_{\text{ads},i}}{RT^2} \quad (3.6)$$

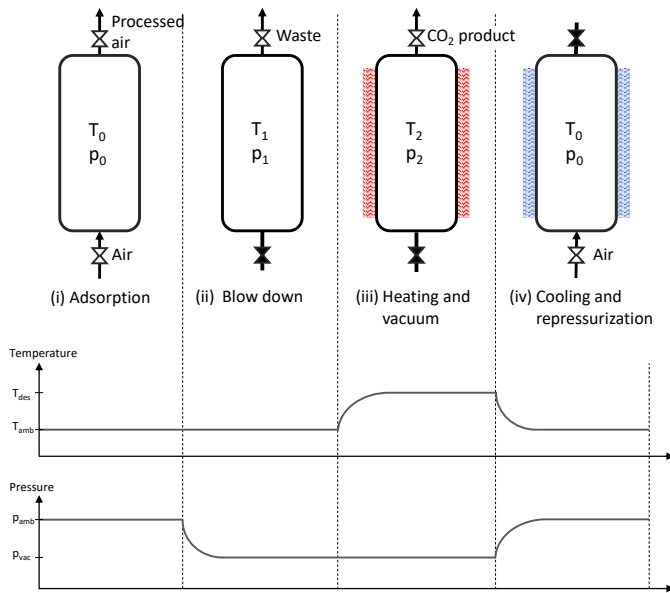


FIGURE 3.1: Simplified VTSA cycle. Indirect heating and cooling are performed with an open end or open entrance, respectively. The temperature and pressure profiles are indicative.

It is worth noting that the specific heat capacities of the gases are considered negligible with respect to the specific heat of the solid material, and therefore excluded from the energy balance.

In the following, we discuss how the material and energy balances are written and solved for each step in the cycle. The overall resolution strategy with known/unknown variables is also shown in Figure 3.2. A more detailed list of the equations used in each step (derived from the previous balances) are reported in Table B.6 in the SI. Similarly to previous works, the starting point of the oD simulation is the end of the adsorption, i.e. the blow-down step in our cycle. However, we propose a different approach for the resolution, which allows us to include the process productivity in the model despite using equilibrium, as well as to better represent real bed operation. This is enabled by targeted use of neural networks, as explained in the following.

Blow-down step

During the blow-down step, the total amount of gas leaving the column N_{out} , the gas composition y_i as well as the temperature T are calculated. The initial temperature and pressure are as during the adsorption, i.e. ambient conditions. When applying vacuum, a waste stream consisting mainly of the species present in the fluid phase is produced. Heating could also be applied to optimize the cycle, but given the difference in typical times of pressure and heat exchange, we neglect this and keep the model significantly simpler.

For the resolution of this step, the material and energy balances are solved for a discrete number of sub-steps, where the pressure is gradually decreased and gas is extracted from the bed until p_{vac} is reached. The pressure follows a time profile obtained from detailed 1D simulations and it is temperature- and material independent. Therefore, the material and energy balances for every step k of the blow-down are written as

$$N_{i,total}^{k-1} - y_i^k N_{out}^k = N_{i,total}^k \quad (3.7)$$

$$m_s c_{p,s} (T_{des}^k - T_{des}^{k-1}) = \sum_i^{CO_2, H_2O} (N_{i,s}^{k-1} - N_{i,s}^k) \left| \Delta H_{ads,i}^k \right| \quad (3.8)$$

where the superscript k refers to the current step of the blow-down, and $k-1$ to the preceding step. N_{out} is the total amount of gas which is removed from the column, and it is calculated for every step k . Since N_2 is treated as an inert, $N_{N_2,s} = 0$ and therefore only considered as present in the fluid phase. As for the energy balance, $c_{p,s}$ is the specific heat capacity of the sorbent, T_{des} the desorption temperature, $\Delta H_{ads,i}$ the isosteric heat of adsorption for every species i adsorbing (i.e. H_2O and CO_2). T_{des}^k

is calculated numerically from the energy balance for each sub-step k while $\Delta H_{\text{ads},i}$ is computed for each sub-step k using the Clausius Clapeyron expression, and - as suggested by Joss et al. [141] - is approximated by including the temperature, pressure and composition from the previous sub-step $k-1$, i.e. $\Delta H_{\text{ads},i}^k = f(y_i^{k-1}, p^{k-1}, T^{k-1})$. More details can be found in the SI in section B. The time length of the blow-down is directly retrieved from the vacuum pressure profile (see SI B).

In previous works [139–141], the initial conditions of the blow-down step were set assuming that full bed saturation was reached during the adsorption step. However, full saturation is hardly achieved in fixed bed separations, as the front of the targeted species propagating in the bed is not perfectly sharp. Therefore, depending on the process specifications and characteristics, a certain level of under-saturation is always present in the bed, which affects the amount of targeted species that can be recovered. Here, we propose to overcome this intrinsic limitation of equilibrium models by computing the saturation level α via a neural network trained with rate-based simulations:

$$\alpha = NN(\rho_p, T_{\text{des}}, p_{\text{vac}}, \dot{V}_{\text{feed}}) \quad (3.9)$$

In the following section 3.2 we provide more details about the neural networks. Accordingly, a level of saturation below 100% in the bed is assigned at the beginning of the blow-down depending on the particle density ρ_p , the desorption temperature T_{des} , the vacuum pressure p_{vac} , and the volume feed stream \dot{V}_{feed} .

Heating step

During the heating step, the total amount of gas leaving the column N_{out} , the gas composition y_i as well as the external heat provided Q_{heating} are calculated. The pressure is kept constant at p_{vac} during the whole step while the temperature is increased following a pre-assigned profile, which is calculated by fitting data from rate-based simulations. In contrast to the pressure profile, which is only dependent on the starting and end pressure, the temperature profile is dependent on the start and final temperature, the density and the heat capacity of the adsorbent material, and the bed pressure. Moreover, the length of the heating step is calculated via a dedicated neural network, whose training data are the same used for the saturation level. More details can be found in the SI in section B.

The material balance solved during heating is shown in Eq. 3.4, while the energy balance needs to be extended to include the external heating Q_{heating} :

$$Q_{\text{heating}}^k = \sum_i^{\text{CO}_2, \text{H}_2\text{O}} (N_{i,s}^k - N_{i,s}^{k-1}) \left| \Delta H_{\text{ads},i}^k \right| + m_s c_{p,s} (T_{\text{des}}^k - T_{\text{des}}^{k-1}) \quad (3.10)$$

As for the blow-down, the differential equations of the isosteric heat of adsorption are pre-solved at each sub-step, k , using the pressure, temperature and composition from the previous sub-step, $k-1$. The initial conditions of the heating are the final conditions of the blow-down, and the heating step is calculated till the final desired temperature is reached.

Cooling step

During the cooling step, the exit valve is closed and the system is repressurized with ambient air and cooled by an external cooling. The initial conditions of the cooling step are equal to the final state of the heating step. The composition of the three components, y_i , the air required for repressurization, N_{in} , and the amount of cooling, Q_{cool} , are calculated. Similar to the previous steps, the repressurization and cooling proceeds incrementally by adding a small amount of air during each sub-step. The length of the cooling and the temperature/pressure profile are fixed according to the 1-D model (more details can be found in the SIB). The cooling step is calculated till T_{des}^k reaches T_{amb} , and the following balance equations are used

$$\sum_{i=1}^n N_{i,total}^{k-1} + y_{i,feed} N_{in}^{Air,k} = \sum_{i=1}^n N_{i,total}^k \quad (3.11)$$

$$Q_{cooling}^k = \sum_i^{CO_2, H_2O} \left(N_{i,s}^{k-1} - N_{i,s}^k \right) \left| \Delta H_{ads,i}^k \right| + m_s c_{p,s} \left(T_{des}^k - T_{des}^{k-1} \right) \quad (3.12)$$

Besides using an external cooling it is also possible to implement an open cooling with ambient air. In this case, in Equation 3.12, the term $Q_{cooling}^k$ is substituted with $\left(m_{in}^{Air,k} c_p \Delta T \right)$. In addition, an outlet term needs to be added to the material balance in Equation 3.11. The closed cooling system is generally the most efficient one, while for DAC applications, for simplicity reasons, open cooling may be preferred which would lead to a lower recovery. For our further analysis we therefore choose the closed cooling system.

Adsorption step

During this step, the total amount of feed N_{feed} and waste N_{waste} are calculated. To keep the model simple and fast, the adsorption step is considered isothermal and isobaric at ambient temperature and pressure. The initial condition is set by the final condition of the cooling step and the bed is then fed with ambient air until the CO_2 saturation level set by the neural network is reached. Differently from the previous steps, the adsorption is not divided into multiple k steps but solved for the final conditions directly. Because of the presence of H_2O , CO_2 can be either the

weakly or the strongly-adsorbed species depending on the material. Especially for cases with very low CO_2 concentrations like in the ambient air, CO_2 is usually not the most strongly adsorbed species. Therefore, in order to avoid material balance errors, the adsorption step is divided into two sub-steps: the first sub-step is used to reach saturation of the strongly-adsorbed species, while the second sub-step is used to reach the desired level of saturation of the weakly-adsorbed species. Let's start with the case of CO_2 as weakly-adsorbed species. First, air is fed until the bed is saturated with H_2O ; here, both CO_2 and H_2O can adsorb. During the second sub-step, more air is fed until the bed reaches the CO_2 saturation level fixed by the neural network, while H_2O cannot adsorb anymore. On the other hand, if CO_2 is the strongly-adsorbed component, the adsorption step coincides with the first sub-step only, where the bed is fed until the CO_2 saturation level from the NN is reached. The material balances solved during the first sub-step of adsorption are:

$$N_{i,\text{total}}(t_f) - N_{i,\text{total}}(t_0) = y_i^{\text{feed}} \int_{t_0}^{t_f} \dot{N}_{\text{feed}} dt - y_i(t_0) \int_{t_0}^{t_f} \dot{N}_{\text{waste}} dt = N_i^{\text{in}} - N_i^{\text{out}} \quad (3.13)$$

where $N_{i,\text{total}}(t_0)$ and $N_{i,\text{total}}(t_f)$ are the total amount of component i in the column at the end of the cooling step and adsorption step, respectively; y_i^{feed} is the concentration of the component in the feed stream; $y_i(t_0)$ is the mole fraction of component i at the end of the cooling; N_i^{in} and N_i^{out} are the amount of species i fed and withdrawn from the column during the adsorption time, respectively. For the resolution of the material balances of the first sub-step of the adsorption and as far as H_2O is the strongly-adsorbed species, $N_{\text{H}_2\text{O},\text{total}}(t_f)$ corresponds to the conditions of full saturation in the column and Eq.3.13:

$$N_{\text{H}_2\text{O},\text{total}}(t_f) = m_s q_{\text{H}_2\text{O}}^* + y_{\text{H}_2\text{O}}^{\text{feed}} \frac{p_{\text{amb}} V_c \epsilon}{RT_{\text{amb}}} \quad (3.14)$$

If CO_2 is the strongly-adsorbed species, H_2O in Eq. 3.14 is substituted with CO_2 . The material balances of the second sub-step of the adsorption are written as for the first sub-step (Equation 3.13), but with the following differences:

- The initial conditions (t_0) correspond to the end of the first adsorption sub-step.
- $N_{\text{CO}_2,\text{total}}(t_f)$ corresponds to the saturation level assigned by the neural network.
- Water is treated as an inert, i.e. it flows through the column without adsorption.

The molar fraction of CO_2 at the end of the second sub-step, $y_{\text{CO}_2}(t_f)$, is equivalent to the initial composition of the blow-down step. Therefore, the total amount of

air and the waste stream leaving the column are: $N_{\text{ads}}^{\text{feed}} = N_i^{\text{in},1} + N_i^{\text{in},2}$, $N_{\text{ads}}^{\text{waste}} = N_i^{\text{out},1} + N_i^{\text{out},2}$. The total time of the adsorption step can be determined by including the air velocity u_{air} and the geometry of the considered sorbent (SI B). Figure 3.2 gives an overview of the whole cycle with the input and output parameters for each step, as well as the process performance parameters.

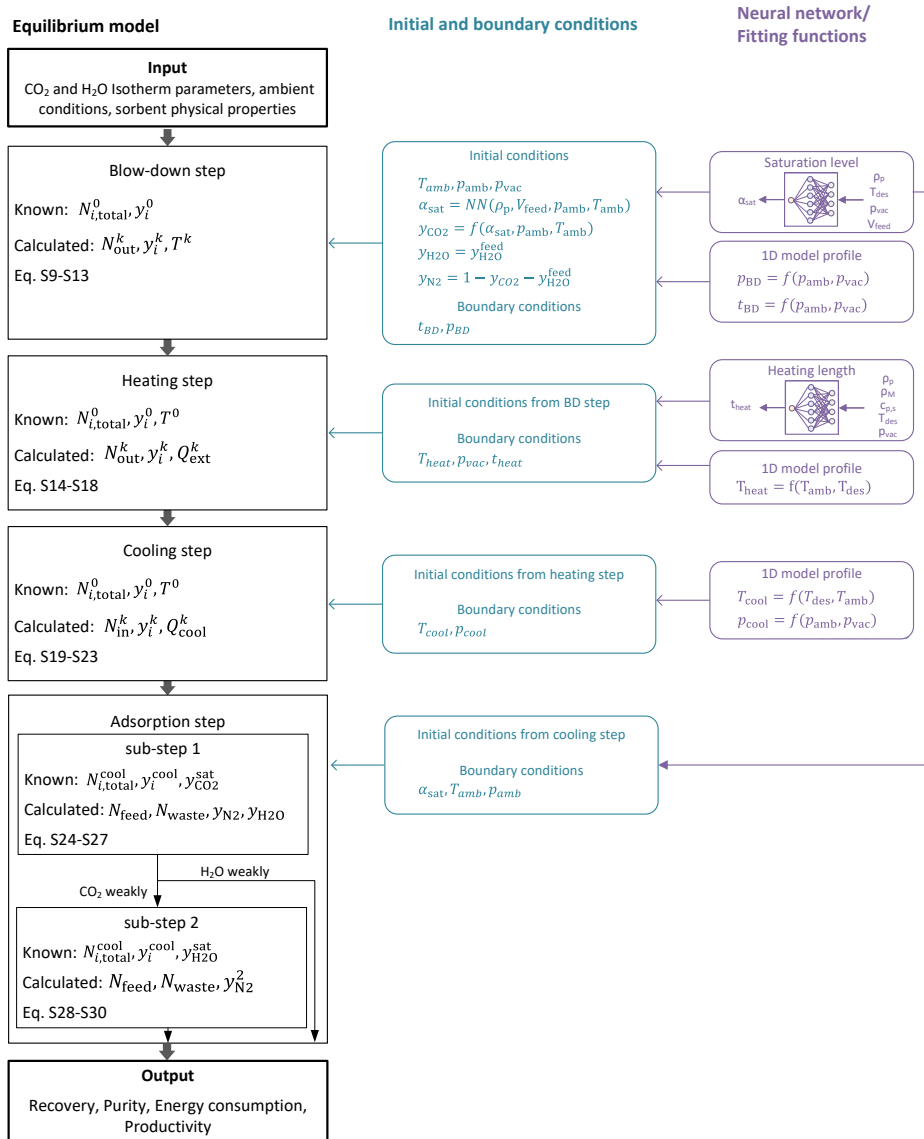


FIGURE 3.2: Architecture of the equilibrium model.

Neural Networks

Two independent neural networks are used in the framework we propose, and they allow for overcoming the inherent limitations of equilibrium models by providing: (i) the (under)saturation level of the bed α at the end of the adsorption step, and (ii) the time required for heating, which in turns allows for an estimate of the productivity, an indicator typically computed in rate-based models exclusively (see the next sub-section). This results in a more realistic and informative oD model. The first NN directly provides α for assigned particle density, desorption temperature, vacuum pressure, and volume of gas fed (varying these cycle operating parameters corresponds to exploring different purity-recovery combinations). The second NN provides the time required for heating the bed to the regeneration temperature t_{heat} , which is typically the longest step in the cycle, for assigned sorbent and particle density, sorbent specific heat, desorption temperature, and vacuum pressure. Indeed, the key for obtaining meaningful neural networks is in the dataset provided to the training step. Here, we used simulations carried out for eight different sorbents combinations obtained with the 1D rate-based model described in Sabatino et al. (the materials were taken from the same work). [120]. For the NN providing the heating time, a total of 4200 simulations were performed using the eight different material combinations and varying desorption temperature and vacuum pressure. For the NN providing the saturation level, we restricted the input dataset to the optimal pareto points of the eight sorbents described in Sabatino et al. [120], resulting in a total of 324 simulations. In Figure 3.3 we show the shape of the isotherms used for setting up the saturation neural network (red lines), those used for the database screening (gray), and those selected as optimum by the screening (light blue). We can note, that overall the isotherms shape is similar, but that those used for the neural network training span a smaller area in the isotherm plane. Including additional sorbents in the 1-D model data generation phase would likely strengthen the NN accuracy.

For both neural networks, the data-sets were divided into training, validation, and testing data with a ration of 60:20:20. The training was done using the Levenberg-Marquardt back-propagation method as implemented in the neural network toolbox provided in *MATLAB*. A summary of the input/output data for both neural networks is shown in Table 3.1.

Performance indicators

The adsorption cycle can be evaluated via four performance indicators, which are calculated at the end of the simulation, i.e. the productivity Pr_{CO_2} , the specific

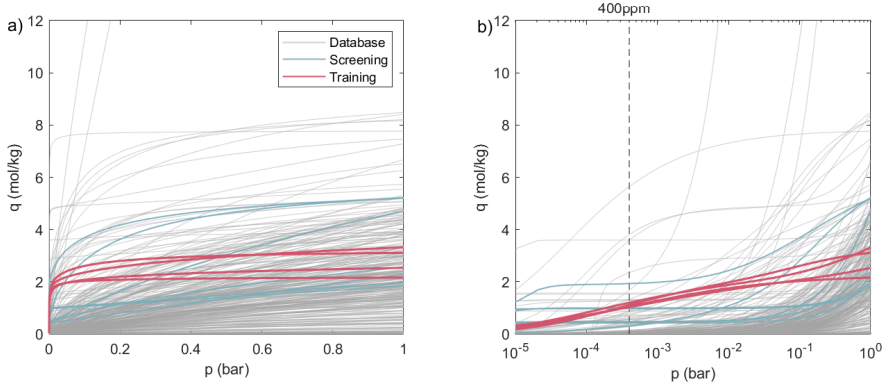


FIGURE 3.3: Overview over the isotherms included in the training data for the NN compared to the isotherms of the database. a) linear scale and b) logarithmic scale.

TABLE 3.1: Summary of the input, output, and boundary conditions of the neural networks.

input	output	# data-sets	T_{des} range (K)	p_{vac} range (bar)
$\rho_{\text{particle}}, \rho_{\text{Material}}, c_{p,s}, T_{\text{des}}, p_{\text{vac}}$	t_{heat}	4200	363-400	0.1-0.8
$\rho_{\text{particle}}, T_{\text{des}}, p_{\text{vac}}, \dot{V}_{\text{feed}}$	α	324	363-400	0.1-0.8

thermal energy consumption $e_{\text{CO}_2}^{\text{th}}$, the CO_2 recovery r , and the CO_2 (dry) purity $\Phi_{\text{CO}_2}^{\text{dry}}$.

$$Pr_{\text{CO}_2} = \frac{N_{\text{CO}_2} MM_{\text{CO}_2}}{t_{\text{cycle}} V_s} \quad (3.15)$$

$$e_{\text{CO}_2}^{\text{th}} = \frac{Q_{\text{th}}}{m_{\text{CO}_2}} \quad (3.16)$$

$$\Phi_{\text{CO}_2}^{\text{dry}} = \frac{N_{\text{CO}_2}}{N_{\text{total}} - N_{\text{H}_2\text{O}}} \quad (3.17)$$

$$r_{\text{CO}_2} = \frac{N_{\text{CO}_2}}{N_{\text{CO}_2}^{\text{in}}} \quad (3.18)$$

where N_{CO_2} is the amount of CO_2 produced during the heating step, t_{cycle} is the total duration of the cycle, and V_s is the volume of the adsorbent. The time of

the cycle required to compute the productivity is calculated by including all step times, i.e. $t_{\text{cycle}} = t_{\text{BD}} + t_{\text{heat}} + t_{\text{cool}} + t_{\text{ads}}$. As shown in Figure 3.2: the time for the blow-down is obtained with a fitting function; the heating time is retrieved using a neural network; the cooling time is set to 350s similar to our previous work [120]; the time of the adsorption step is determined by the air velocity and the geometry of the sorbent as explained in the previous section.

The oD model is implemented in MATLAB R2021 and the mass and energy balance equations are solved using the *lsqnonlin* solver and *trust-region-reflective* algorithm [146]. The model takes less than 10s to simulate one cycle, using a laptop machine with INTEL Core i7 2.50GHz processor and 8.00 GB of RAM.

3.3 MODEL VALIDATION

The equilibrium model validation is carried out by comparing the results with a rate-based adsorption model. In the 1D model, the material and energy balances of a fixed-bed are typically expressed in differential form and are numerically solved in space and time until a cyclic steady state is reached. Moreover, the mass transfer is approximated with the linear driving force approach. The 1D model adopted for the validation has been used in multiple previous publications, and it has shown to predict experimental results well [50, 81–83]. The detailed mathematical equations and the simulation parameters are reported in the SI B. Additional details can also be found in other previous publications [77, 78].

The validation of the oD model is structured in two different steps. We need in fact to recognize that not only does the oD model have to reproduce fairly well the performance of a specific cycle simulated with the 1D model, but it also has to correctly identify the potential of a given material when the process is optimized. If both conditions hold, then the oD model can be used for screening potential sorbents. Accordingly, first we compare the profiles and performance indicators of a single simulation by using the same input parameters (e.g. cycle times, inlet velocity, temperatures and pressure). Second, we compare the results when the process is optimized, i.e. the input parameters are varied. More specifically, the optimization of the four-step VTSA process is carried out by minimizing the energy consumption and maximizing the productivity [91]. The multi-objective optimization problem is formulated as follows:

$$\begin{aligned} & \underset{x}{\text{minimize}}(-Pr, e^{\text{th}}) \\ & \text{subject to } \Phi \geq \Phi_{\text{spec}} \end{aligned} \tag{3.19}$$

where x are decision variables, Φ the purity and Φ_{spec} the required minimum purity. This constraint is imposed as a penalty C on the resulting objective function in the form of

$$C = 10[\min(0, (\Phi - \Phi_{\text{spec}}))] \quad (3.20)$$

We would like to note that the minimum recovery Φ_{spec} value allowed in the optimization was set to 70%. This was required to include APDES-NFC - a DAC sorbent described in the early works of Climeworks' founders which we considered in previous work [120] and in the 1-D model simulations. This sorbent features a high porosity, and higher CO₂ purity can only be reached when a preheating-to-waste step is included with the blowdown. However, the constraint is never active in the screening and for the validation of other sorbents (see next section and Figures B.11, B.12, B.13). Therefore, the low-purity constraint does not affect the outcome of the fast screening.

The decision variables x for the oD model are: (i) the desorption temperature, (ii) the vacuum pressure, and (iii) the inlet feed velocity. The time of the different cycle steps depends on these parameters as well as on the material properties. The boundaries of the decision variables are given in Table B.11 in the SI. We repeat the same optimization for the 1D model using the same VTSA cycle and materials, but adding the step times as variables.

The optimization of the oD model is carried out using a particle swarm algorithm adapted for multi-objectives (MOPSO), as implemented in MATLAB [147]. The size of the particle and repository was set to 50 and the number of cycles to 35. These parameters are smaller than the ones recommended by Coello et al. [148], but they did show the same accuracy. For the 1D model optimization, we follow the same approach reported in Sabatino et al. [120]. The results of the optimizations with the oD and 1D models are compared in terms of energy and productivity range for the eight materials discussed by Sabatino et al. [120]. The nomenclature of the materials can be found in Table B.14 and includes four promising sorbents, namely APDES-NFC [41], Tri-PE-MCM-41 [68], MIL-101(Cr)-PEI-800 [45] and Lewatit VP OC 1065 [48, 69, 70] together with data for H₂O isotherms of three different materials, i.e. APDES-NFC, Lewatit and MCF-APS-hi [71]. More details on the choice of these materials can be found in Sabatino et al. [120].

Validation of a specific cycle simulation

Here, we compare the oD and 1D model for the same input parameters, i.e. same material, heating and cooling temperature, pressure, feed composition, feed velocity, and cycle times. The pure component isotherm equations as well as the parameters

for the different materials are reported in the SI B. We carry out this validation for two different materials: case s2/E-A and Cr-MIL(101). Case s2/E-A was among the materials used to build the data collection adopted to develop the profiles functions and the neural networks called in the oD model. On the other hand, Cr-MIL(101) was not used for this purpose; thus we use the Cr-MIL(101) validation to investigate the capability of the oD model to predict the performance of new materials. For all tested cases, we carry out the validation using air as feed, i.e. a direct air capture process.

The cycle times were defined by running the simulation with the 1D model and are long enough for the model to reach the vacuum pressure (t_{BD}), the desorption temperature ($t_{heating}$), and to ensure a high saturation in the bed (t_{ads}). The cooling time was set to $t_{cool} = 350s$ for all materials. This is done to ensure that the times, as well as the final temperature and pressure are the same for both models. For this case, the oD model structure was adapted to handle the times as additional input. Furthermore, the 1D model uses an equivalent temperature, to include the enhancing effect of water on the CO₂ adsorption; for consistency, this was also included in the oD model for the validation. More details on this approach can be found in Sabatino et al. [120]. The process conditions for this validation are reported in Table 3.3.

Figure 3.4 shows the temperature, pressure, and the molar fraction profiles of the three components for the oD and 1D models. Figure 3.4 a) and b) refer to material s2/E-A, while Figure 3.4 c) and d) refer to Cr-MIL(101). In addition, in the SI in Figure B.5 the profiles of the adsorbed amount of CO₂ and H₂O are added. Although the oD model is significantly simpler than the detailed 1D model, the profiles are in good agreement. Notably, also the concentration profiles show a good agreement between the models, which is hard to obtain for a well-stirred oD equilibrium model. When looking at the main differences between the oD and the 1D model, we notice the following. In the temperature profile (Fig. 3.4 a)) a deviation is present for the adsorption step: for the 1D model, the temperature increases at the beginning of this step, while the oD model shows a constant temperature. This is because we assume isothermal adsorption in the oD model.

When looking at Fig. 3.4 c) and d), i.e. the Cr-MIL(101) case, we can notice that the model predicts well the profiles also when a new material is considered. This is an important feature of the model, and it confirms that the oD model can effectively predict the performance of sorbents not used to build the NN functions, and can therefore be used as a screening tool.

Figure 3.5 shows the molar fractions of CO₂ and H₂O as a function of the temperature during the cycle, for both the oD model and the 1D model. Also here, Figure 3.5 a) and b) is for sorbent case s2/A-E, while Figure 3.5 c) and d) is for sorbent Cr-MIL(101) (the concentration-pressure profiles are reported in the SI). It can be

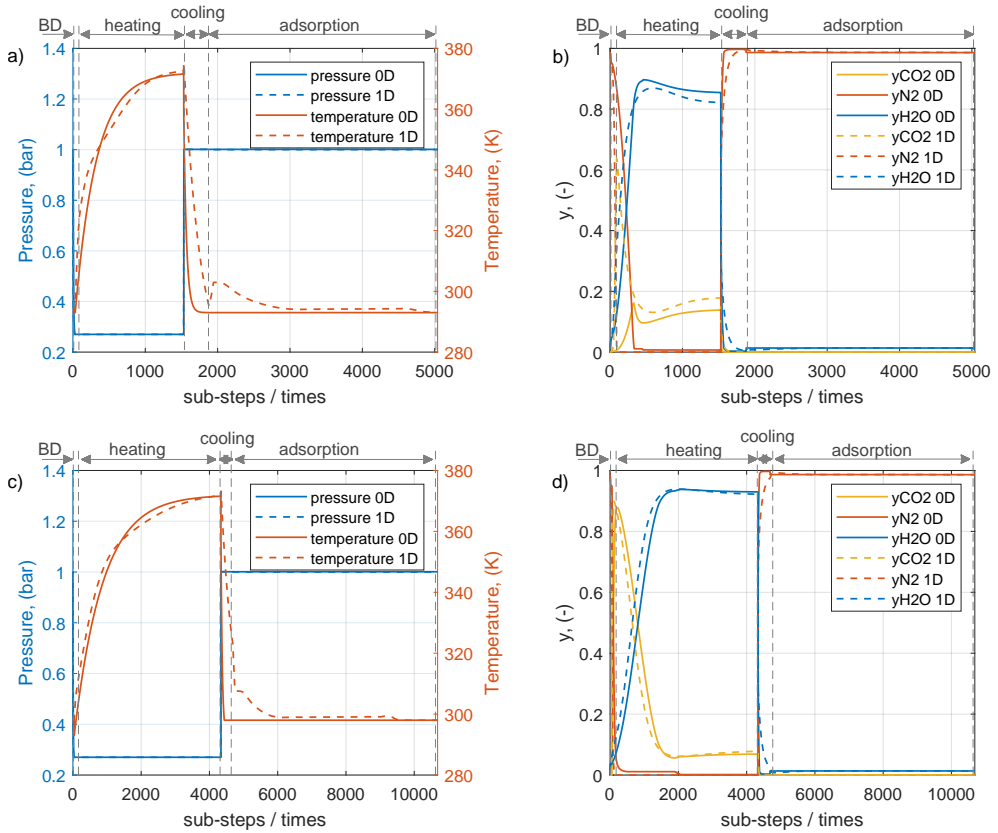


FIGURE 3.4: Temperature, pressure and concentration profiles for the 0D and 1D models. Figure a) and b) refer to $s_1/E-A$, while Figures c) and d) refer to Cr-MIL(101). For the 0D model profiles, the adsorption step is plotted over time.

TABLE 3.3: Process conditions for the validation of the oD model against the 1D model.

material	T_{des} (K)	p_{vac} (bar)	\dot{V}_{feed} (m ³ /s)	t_{ads} (s)	t_{prod} (s)	t_{cool} (s)	t_{purge} (s)	H ₂ O isotherm
s2/E-A	373	0.27	8.9×10^{-6}	3160	1500	350	30	APDES- NFC
Cr-MIL(101)	373	0.27	8.9×10^{-6}	5000	4300	350	300	APDES- NFC

noted that the compositions profiles follow a similar shape, both for sorbent s2/E-A and sorbent Cr-MIL(101).

The overall performance of the oD model with respect to the 1D model for all tested sorbents is shown in the parity plots in Figure 3.6, where the results are reported for the 9 different materials. Moreover, the parity plots for different CO₂ concentrations in the feed and same materials are reported in the SI B. The following can be concluded. (i) The purity predicted by the oD model underestimates the 1D model, which is a consequence of the well-stirred approach. The results are however within a 20% gap, with only material s1/A-A outside this gap. (ii) The capture rate is in good agreement and typically slightly overestimated by the oD model (20% gap still applies). (iii) The specific thermal energy demand is in good agreement with the 1D simulation. (iv) The productivity is in fair agreement with the 1D model; this is particularly surprising, given that the oD model is equilibrium based and the productivity is computed by means of a neural networks function. The higher productivity stems from the higher capture rate of the oD model. When considering the two additional cases for $y_{CO_2} = 0.1\%$ and $y_{CO_2} = 1\%$ vol., the parity plots show similar agreement for energy and productivity, and a better agreement for purity and capture rate (see SI B).

Although the error for the predicted performance parameters is in the range of $\pm 20\%$, it must be noted that the oD model does not aim at providing a very accurate prediction of the performance, but rather at consistently predicting the performance of multiple sorbents. Therefore, to examine better this feature, we need to compare the capability of the model when process optimization is used.

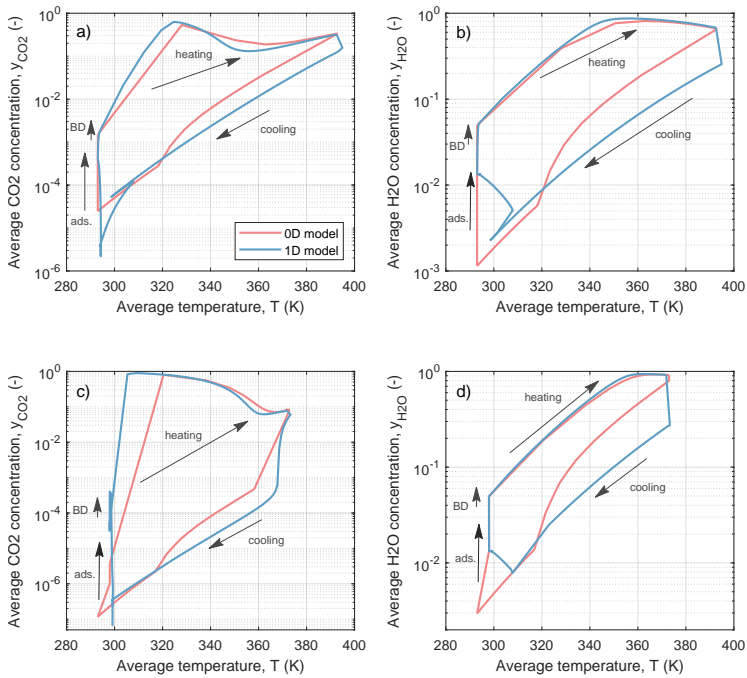


FIGURE 3.5: Composition profiles similar to Ajenifuja et al. [141] of CO₂ and H₂O over the temperature for case s2/E-A (a) and b)), and Cr-MIL(101) (c) and d)). For the 1D model, the temperature and composition plots refer to average values over the bed at cyclic steady state.

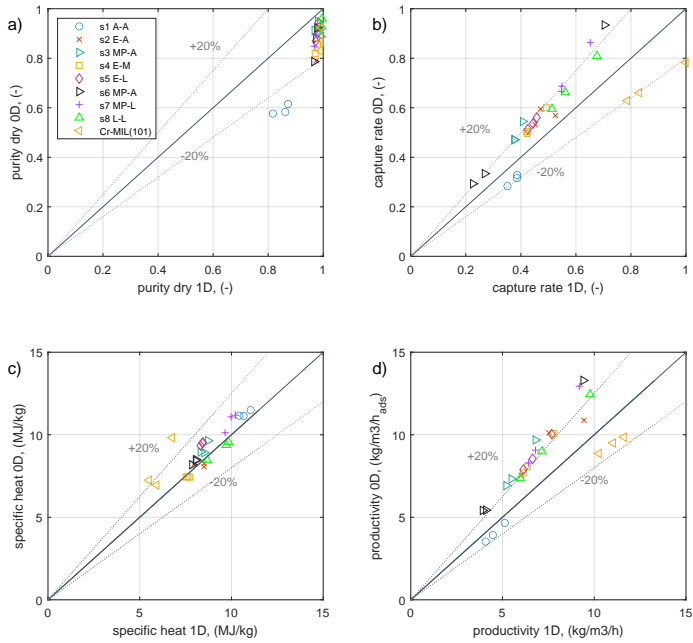


FIGURE 3.6: Parity plots of the performance parameters resulting from the oD model and the 1D model. Each material is shown by a specific symbol and color and each point features different input parameters for T_{des} and p_{vac} . The dashed lines show a margin of 20%.

Validation of sorbent comparison and optimization

As mentioned, the goal of the oD model is to identify the most promising adsorbents from large databases of possible sorbents, where the ranking is done using technical key performance indicators. Therefore, we here benchmark the oD model in terms of optimization of adsorbents. To this end, we consider again the 8 adsorbents used for the previous validation and compare the results of process optimization carried out using the oD and the 1D models. The design variables considered with the oD model are the desorption temperature T_{des} , the vacuum pressure p_{vac} , and the volume stream of the incoming air \dot{V}_{feed} . Same ranges across the different materials are considered for T_{des} and p_{vac} , while for \dot{V}_{feed} the range is material-specific (the maximum air velocity is set by the minimum fluidization velocity). In contrast to the oD model, the 1D model requires the cycle step times as input variables; in this case, the design variables and their upper and lower bounds are taken from Sabatino et al. [120] and are listed in the SI in Table B.11.

As optimization results, Pareto curves with the optimal productivity-energy points are obtained. The detailed optimization results including purity, recovery, and decision variables are found in the SI in section B. To improve the visualization of the comparison between the models, the optimal Pareto points are depicted in Figure 3.7 as interval bars for both productivity (left y axis) and specific energy consumption (right y axis). As comparison, the brighter bars show the corresponding results for the 1D model. When comparing the oD and 1D models, we now aim at obtaining similar sorbent ranking (i.e. the most performing sorbents are identified) and similar range for the performance indicators.

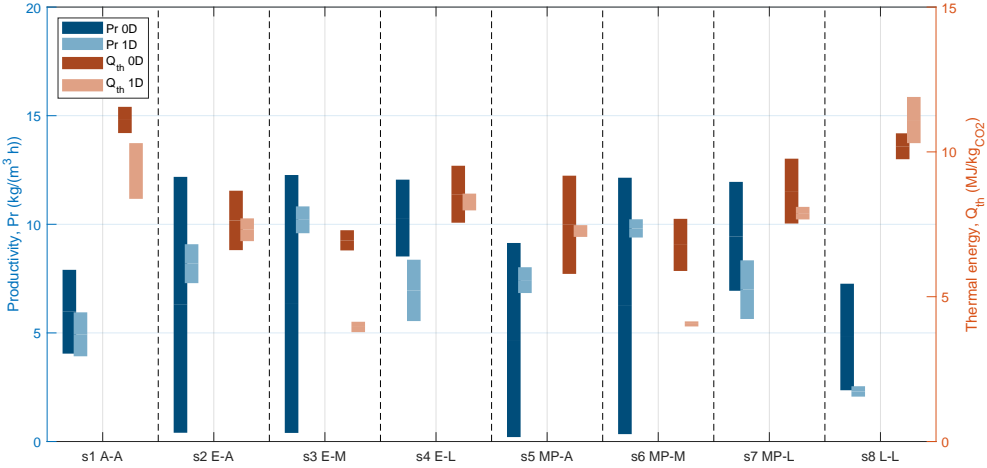


FIGURE 3.7: Resulting performance parameters (productivity in blue, thermal energy consumption in orange) from the oD and 1D optimization. The nomenclature for the different sorbent cases can be found in Table B.14

Looking at the comparison, we first notice that the optimization results of the oD model are in line with the 1D model, i.e. the simplified approach identifies similar values for energy consumption and productivity. Typically, the oD model identifies broader ranges compared to the 1D model, especially for the productivity. The latter is however the most difficult indicator to extract from an equilibrium model. Second, we notice that the oD model identifies the same well-performing and badly-performing sorbents of the 1D (see Table 3.5 for a summary of the ranking). For the oD model the two best performing materials are the s6/MP-A and s3/MP-A, while the two worst performing sorbents are s1/A-A and s8/L-L. The 1D model identifies the same worst sorbents and the same best sorbents (where the two best sorbents are swapped). These results let us conclude that the oD model reliably reproduces the screening performance by the 1D model, but in a fraction of the required time: around 2 hours are needed for an optimization with the oD model (per material) while from 8 hours to several days are needed for the 1D model (per material). It should be also stressed, that the oD model shall not fully substitute the 1D model, but complement it in the sorbent screening phase.

TABLE 3.5: Resulting ranking of the adsorbents for the validation of the oD model using the 1D model. The values of the maximum productivity and the corresponding thermal energy consumption are given for the best performing adsorbent. For the remaining materials, the deviation to the best performing one is given in a percentage.

	oD model		1D model		
	Pr (kg/m ³ /h)	Q _{th} (MJ/kg)	Pr (kg/m ³ /h)	Q _{th} (MJ/kg)	
s6 MP-M	12.1	7.7	s3 E-M	10.8	4.1
s3 E-M	+1%	-5%	s6 MP-M	-5%	0%
s2 E-A	0%	+13%	s2 E-A	-16%	+86%
s5 MP-A	-25%	+19%	s5 MP-A	+23%	+107%
s7 MP-L	-2%	+27%	s7 MP-L	-23%	+96%
s4 E-L	-1%	+24%	s4 E-L	-23%	+107%
s1 A-A	-35%	+50%	s1 A-A	-45%	+149%
s8 L-L	-40%	+38%	s8 L-L	-76%	+188%

3.4 SORBENTS SCREENING

We applied the model described above to screen and rank a large number of possible sorbents. The screening was carried out retrieving data from different sources, i.e. the NIST/ARPA-E database [142], adsorbents considered by Khurana and Farooq [133] and promising DAC sorbents from literature not included in the previous sources [145]. We do not limit the screening to specific classes of sorbents, but consider e.g. zeolites, activated carbon, and MOFs. Both real and hypothetical sorbents are included. The first objective is to demonstrate the potential of the oD model by screening all the data mentioned above and by ranking the most promising adsorbents. The second objective is to identify the most promising sorbents for CO₂ capture from diluted sources. To this end we apply the screening to CO₂ capture from air (400ppm) and from sources at 0.1% vol CO₂ and 1% vol CO₂. These latter may be representative compositions found in stables and in the aluminium industry, respectively. Therefore, for the last two cases an additional constraint is set, namely the capture rate needs to be higher than 90%. For the DAC case on the other hand, the capture rate is not restricted.

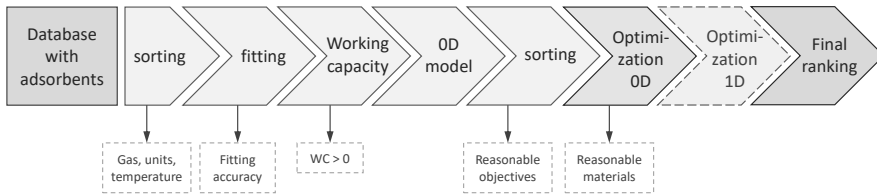


FIGURE 3.8: Overall screening approach.

Screening methodology

The screening process includes several steps, which are shown in Figure 3.8. All screening tools are made available as open source online - see SI. As a first step, the isotherm data of the NIST/ARPA-E needs to be retrieved from the online database and preliminary filtered to exclude adsorbents which cannot be further considered. This includes e.g. isotherms availability for the gas of interest, or converting the units of the data. More details are provided in Figure B.10 in the SI. In the next step, isotherm fitting is carried out for the remaining adsorbents. Since the isotherm of adsorbents can take various shapes, we allow for automatic selection among three common isotherm models during the fitting, i.e. the Langmuir-Freundlich, the Toth-cp and the S-Shaped methods (these three isotherm models can capture a wide range of experimental isotherm shapes). The fitting approach is further described in the SI B.

TABLE 3.6: Boundary conditions for the material screening.

	T_{des} (K)	T_{ads} (K)	P_{vac} (bar)	P_{ads} (bar)	$y_{\text{CO}_2}^{\text{feed}}$ (%)	$y_{\text{H}_2\text{O}}^{\text{feed}}$ (%)	$y_{\text{N}_2}^{\text{feed}}$ (%)
DAC (400ppm)	373	293	0.1	1.001	0.04	1.34	98.62
0.1%	373	293	0.1	1.001	0.1	1.34	98.56
1.0%	373	293	0.1	1.001	1.0	1.34	97.66

In the next step, the working capacity is calculated to identify those materials with positive capacity for the CO_2 adsorption of interest. A summary of these conditions is reported in Table 3.6. While these process conditions are here fixed, the screening could be carried out for varying inputs. Thereafter, the oD model is run for all materials with a positive working capacity. When no H_2O isotherm is provided in the database, we include the H_2O isotherm of APDES-NFC [41] and Lewatit [48] with a fitting provided by Sabatino et al. [120] (the H_2O uptake of the APDES-NFC isotherm lies somewhere in the middle, while Lewatit adsorbs higher amounts of H_2O). Moreover we consider the case of no water adsorption with a dry feed. For the screening process, no enhancing effect of water on the CO_2 adsorption was considered, as no specific and reliable information/data is generally available.

Another issue present for most of the materials, especially those from the NIST/ARPA-E database, concerns the availability of physical properties data (and associated units), like the material and particle density, heat capacity. For the cases where one or more properties are not available, the following generic assumptions are made: $\rho_{\text{material}} = 1130 \text{ kg/m}^3$, particle void fraction $\epsilon_{\text{particle}} = 0.35$ and $c_{p,s} = 1070 \text{ J/kg/K}$ [133, 141]. While this is certainly a simplification, any other assumptions would result in similar outcome.

In the next step, the results of the oD model are sorted: materials with specific energy consumption higher than $100 \text{ MJ/kg}_{\text{CO}_2}$ are excluded from further consideration. For the remaining adsorbents, an optimization is carried out using the oD model. The upper and lower bounds of the decision variables are the same as for the validation of the exemplary isotherm mentioned in the previous section (see Table B.11 in the SI). The optimization results allow for a final ranking of the sorbents. Possibly, the most promising sorbents are further evaluated by optimization with the 1D model.

Screening results

The screening considers initially around 2500 different materials, for which nearly 8000 isotherms are fitted and sorted. For the DAC case, only 12 materials show a positive working capacity and reasonable performance parameters. 13 and 30 materials were found for $y_{\text{CO}_2} = 0.1\%$ and $y_{\text{CO}_2} = 1.0\%$, respectively. Here we would like to remind the reader, that for the two latter cases the capture rate is constrained to be higher than 90% while it can vary freely for the DAC case. The screening results are shown in Figure 3.9, while Table 3.8 reports the ranking of the 10 best performing adsorbents for the three different cases. The ranking is based on the minimum specific energy consumption and the maximum productivity. Figure 3.9 shows that, as expected, the specific energy consumption is decreasing and the productivity is increasing for higher CO_2 concentrations in the feed. The model consistently predicts that for an increase in productivity, more thermal energy is needed. Notably, a few particularly sorbents can be identified for all applications.

For DAC, the MOFs Cr-MIL(101) and MIL-101 are the most performing both in terms of productivity, which can reach $20 \text{ kg}/(\text{m}^3\text{h})$, and energy; the latter can be potentially as low as $4.1 \text{ MJ}_{\text{th}}/\text{kg}_{\text{CO}_2}$. For 0.1%, PCN-11 is also an interesting sorbent in addition to the MOFs for DAC. The maximum productivity increases to above $40 \text{ kg}/(\text{m}^3\text{h})$. Finally, for the 1.0% case, the MOFs Mg-MOF-74, MIL-101(Cr)-250nm-PEI-399 and Ca-X are identified as most promising, with energy consumption as low as $4.3 \text{ MJ}_{\text{th}}/\text{kg}_{\text{CO}_2}$ and maximum productivity above $100 \text{ kg}/(\text{m}^3\text{h})$. Nicely, Zeolite 13-X is also identified as one of the most performing sorbents, in line with what has been reported for post-combustion CO_2 capture with VSA and TSA cycles.

All materials shortlisted from screening the 0.1% case are included in the results of the 1.0% case. The materials of the 0.04% case, on the other hand, are not all included in the higher CO_2 concentration cases, since for the DAC case we do not constraint the capture rate: the capture rate of the three excluded materials is lower than 90% (see SI Fig. B.11-B.12).

For the DAC case, an optimization with the 1D model is also carried out for the shortlisted sorbents, and the corresponding material ranking is reported in brackets in Table 3.8. The rankings for the two models is again very similar and the two best adsorbents are consistently identified. The three cases using a different water isotherm, i.e. from the Lewatit sorbent, are very similar to the screening with the APDES-NFC isotherm and the resulting ranking is the same (see SI). When looking at the screening cases using a dry feed stream, the results, on the contrary, are very much different. This was expected, since the concentration profiles are very different.

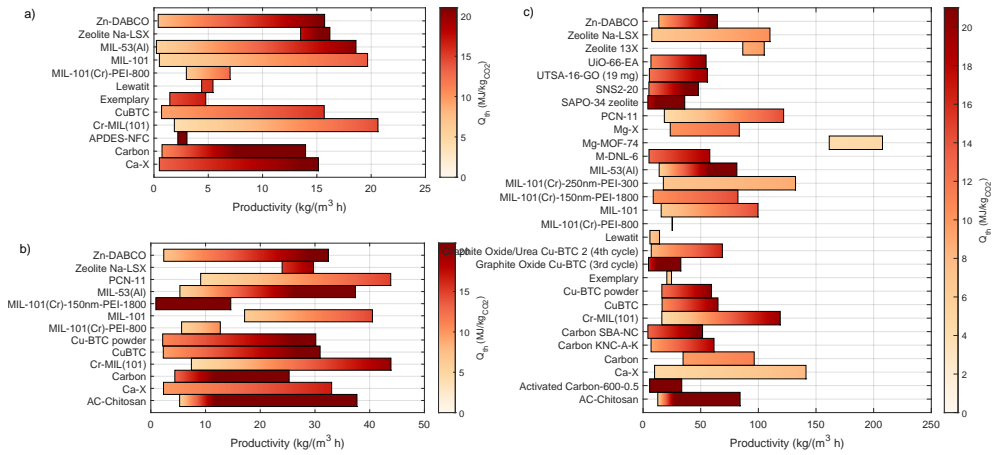


FIGURE 3.9: Resulting objectives for three case studies: a) humid air feed stream with $y_{CO_2} = 0.04\%$, b) $y_{CO_2} = 0.1\%$ and c) $y_{CO_2} = 1.0\%$. The best performing adsorbents show a high productivity P_r , given on the x-axis, and a low specific thermal energy demand Q_{th} represented by the colorbar. The upper limit of the color bar is set to a specific value to make the differences and best performing materials visual. The actual energy consumption can therefore be higher than the limit shown by the bar.

TABLE 3.8: Resulting rankings showing the 10 best performing materials for three different cases with varying CO₂ concentrations in the feed and including water. The results for case 1 using the 1D model are added next to the materials in brackets. The deviation of the productivity and thermal energy consumption between the best performing material and the rest is given in in Tables B.16-B.20 in the SI.^a

	400ppm	0.1%	1.0%
1	Cr-MIL(101) (2)	PCN-11	Mg-MOF-74
2	MIL-101 (1)	MIL-101	Ca-X
3	CuBTC (3)	Cr-MIL(101)	MIL-101(Cr)-250nm-PEI-300
4	MIL-53(Al) (4)	Ca-X	Zeolite Na-LSX
5	Zn-DABCO (5)	Zeolite Na-LSX	Zeolite 13X
6	MIL-101(Cr)-PEI-800 (6)	Cu-BTC powder	PCN-11
7	Lewatit (8)	CuBTC	MIL-101
8	Exemplary (7)	MIL-53(Al)	Carbon ^b
9	Zeolite Na-LSX (10)	Zn-DABCO	Cr-MIL(101)
10	Ca-X (9)	MIL-101(Cr)-PEI-800	Mg-X

^aThe names of the sorbents correspond to the naming in the NIST database.

^bActivated Carbon.

3.5 DISCUSSION

In this work, we showed that equilibrium models can effectively contribute to the overall design of adsorption processes for CO₂ capture from diluted sources and from air. Especially, they are useful tools to map the preliminary performance regions and to identify promising sorbents from large databases. Coupling equilibrium models with machine learning further enhances the outcome, e.g. by providing good estimates of the process productivity. However, as for all models, there are a few limits that are worth stressing (which are particularly relevant for scientists interested in re-using our MATLAB package provided on GITHUB).

First, it should be kept in mind that the purpose of the oD model is not to provide accurate predictions - for that, rate-based models shall be used - but to enable (i) otherwise non-viable simulations, e.g. high-throughput materials screening, (ii) and a better understanding of the process performance in an early stage of development. The oD model should be consistent with rate-based models' predictions but should not aim at substituting them.

Second, it is important to include in the oD model the adsorption of all relevant species, and adopt suitable adsorption models. For example, in this work we have considered N₂ as an inert, which is acceptable as far as N₂ adsorption is negligible (e.g. in amine-functionalized sorbents), but which should be included when dealing with more traditional sorbents (e.g. Zeolite 13X). N₂ must also be included when extending this model framework to non-diluted CO₂ capture applications, e.g. NGCC, coal, and industrial sources. Along a similar line, in this work we have neglected H₂O competition and enhancement effects: this should be corrected as soon as more experimental data become available.

The last limitation we would like to discuss here concerns the neural network modules. As all data-driven models, the quality of the NNs depends on the quality of the data input. In the development of the NN used in our model, we considered limited number of materials (see Fig. 3.3) and kinetic data, and we used such NN for extrapolation to different isotherms. While this led to outcomes in line with the rate-based model, the performance of the NN could be improved by adding training data from additional materials (e.g. considering the finding of this work as shown in Fig.3.9). When more experimental data become available, most of all about kinetics, the model should be updated accordingly: first, by retraining the NNs, second by rethinking the overall model structure. One possibility along the latter line might include the use of AI as surrogate model for equilibrium, and using the kinetics indicators to drive the sorbent selection.¹

¹ We would like to acknowledge that the idea of swapping the use of AI from surrogate for kinetics to surrogate for equilibrium was suggested by one of the reviewers of this work.

3.6 CONCLUSIONS

In this chapter, we presented a new equilibrium-based oD model for rapid simulation of vacuum temperature swing adsorption cycles. The model, which builds upon the key assumption of well-mixed conditions in the bed, was developed to enable fast, yet reliable screening of sorbents for CO₂ removal from diluted sources, e.g. direct air capture applications. Nonetheless the formulation is generic and portable to other separations of interest as far as the model is adapted to grasp the key separation characteristics. To this end, we extended the approaches presented in literature for equilibrium-based adsorption models by embedding neural networks sub-models trained from rate-based simulations, by including H₂O in the feed - i.e. CO₂ is not necessarily the strongly-adsorbed species, and by considering vacuum temperature adsorption cycle. The resulting model can predict the separation performance (capture rate and purity), the specific energy consumption, and the productivity. The latter is enabled thanks to the embedding of machine learning, as equilibrium models do not provide rate-connected performance. The resulting oD model can simulate a VTSA cycle in less than 10s, and a full cycle optimization in less than 2hr, therefore lowering significantly the computing time, especially on standard desktops, and thus enabling large screening of new materials.

We have shown that the resulting oD model can predict fairly well the different performance indicators of VTSA cycles. To this end, we compared the model with the results of a more sophisticated 1D rate-based model. The validation included the comparison of specific fixed cycles for several materials in terms of performance indicators and temperature/composition profiles, and also the comparison of the outcome of cycle optimizations for different sorbents. The findings confirm that (i) the oD model reproduces well specific cycles, and (ii) returns similar metrics when optimizing cycles, i.e. it is capable of substituting more sophisticated models in large screening of materials.

Finally, we applied the oD model to the screening of several thousands of sorbents, which were obtained from the NIST/ARPA-E database and additional literature [120, 133, 142, 145]. We carried out the screening to assess CO₂ capture from air and from other diluted sources ($y_{\text{CO}_2} = 0.1\%$ and $y_{\text{CO}_2} = 1.0\%$). The sorbent screening included also additional steps that are required to retrieve and polish the source data. We identified 12, 13, and 28 promising materials for the DAC, the $y_{\text{CO}_2} = 0.1\%$, and the $y_{\text{CO}_2} = 1.0\%$ case, respectively. In all cases, a couple of sorbents stood out as particularly promising both in terms of energy consumption and productivity. As final comparison, we run the optimization of the DAC promising sorbents with the 1D model; the outcome results were fully consistent with the oD model.

Overall, we can conclude that equilibrium models, and particularly the one we propose here, are a powerful tool for sorbents screening that could reliably substitute

more sophisticated models. We showed that this holds true also when using more complicated cycles, i.e. VTSA, and when considering more challenging separations, i.e. from (ultra)diluted sources.

HOW DOES AN IDEAL SORBENT IMPROVE THE TECHNICAL AND ECONOMIC PERFORMANCE OF DAC?

4.1 INTRODUCTION

Recent developments in material science have led to the ability of discovering new materials very quickly; the number of theoretical adsorbents is indeed increasing significantly. Today, hundreds of thousands of adsorbent materials, both real and hypothetical, are available in literature. Still, very few of the studied materials show promising CO₂ adsorption performance [149]. In the previous chapter we showed that only 12 suitable sorbents out of 2500 were identified for CO₂ capture from the air using a vacuum temperature swing adsorption (VTSA) cycle. Most of the discarded materials either showed a negative working capacity for the considered feed and desorption conditions, i.e. $y_{\text{CO}_2}^{\text{feed}} = 0.04\%$, $T_{\text{des}}^{\text{max}} = 373\text{K}$ and $p_{\text{vac}}^{\text{min}} = 0.1\text{bar}$, or showed poor performance leading to unfavourable capture costs. The development of DAC is just at the initial phase, and, therefore, there is large room for improving the performance and decrease the levelized costs of CO₂.

Several new classes of porous adsorbents have been discovered during the last years including metal-organic frameworks (MOFs), which open up for thousands theoretical materials [134]. With the emergence of computational molecular dynamics, the possibility of replacing experiments by molecular simulations came forth, which allowed for large screening studies, e.g. by Snurr et al. [150–152] and Smit et al. [131, 153]. These studies have in common, that the materials were compared using metrics like the Henry's constants or the isosteric heats of adsorption. Although these properties are important for designing materials at molecular level, they are not sufficient to predict the performance in a real process [133, 154]. Rather, the behaviour in the process itself has to be investigated as well. Therefore, a few studies focus on *multiscale screening*, where molecular and process modeling are combined [134, 155–157].

In the process modeling studies reviewed above, equilibrium adsorption data was obtained from molecular simulations (like Grand Canonical Monte Carlo (GCMC) simulations) and from experiments. These were then used in process modelling and techno-economic assessments. An alternative approach is called *process inversion*, where the aim is to find an "optimal" sorbent from a process perspective by optimizing both adsorbent properties and process performance parameters. This approach

This chapter builds upon a scientific manuscript under preparation.

helps in identifying the limits of a specific adsorption process and provides guidelines for the material discovery and synthesis [137]. A few studies have followed this approach to identify promising properties for post-combustion CO₂ capture, with the goal of decreasing the energy consumption and/or capture costs [90, 137–139, 158–160]. For example Danaci et al. [159] optimized three isotherm parameters of a single-site Langmuir isotherm for CO₂ and N₂ to maximize the capture costs. No trend between the CO₂ isotherms was found which could result in a high process performance. By applying a techno-economic optimization, Subraveti et al. [160] tried to identify an ideal adsorbent to find the limits of a pressure-vacuum swing adsorption (PVSA) process for post-combustion CO₂ capture. They optimized adsorbent properties, including isotherm parameters and the density and void fraction, together with the process design variables. The CO₂ and N₂ adsorption isotherms were modelled using the competitive dual-site Langmuir (DSL) equation. In the present work, we follow the same approach of *process inversion*, and extend it to also assess the separation of CO₂ from dilute feed stream like DAC.

So far, research has mainly been focusing on novel materials for capturing CO₂ from anthropogenic point sources. When developing these new materials, there is not one best sorbent, but a best match between a sorbent and a process. In this context, pressure swing adsorption (PSA) and temperature swing adsorption (TSA) have been studied extensively. The separation of CO₂ from dilute streams requires a different process, where the vacuum temperature swing adsorption (VTSA) cycle is mainly investigated. Therefore, while the overall approach of finding suitable sorbents for dilute feed streams can be similar to that of other separation processes, the resulting metrics with which the materials are evaluated, can be different. For example when capturing CO₂ from the air, the CO₂ recovery plays a minor role, while the co-adsorption of water has to be considered for most of the materials as well.

Let us start this analysis for DAC applications by looking at the properties of isotherms. The adsorption equilibrium information of the considered material is indeed one of the most important inputs. There exist different empirical and mechanistic isotherm models which can be categorized by the amount of parameters involved [161, 162] or by the shape [163–165]. In Fig. 4.1 three exemplary shapes of CO₂ isotherms relevant for DAC application are shown. The first two shapes (a) and (b) are type I isotherms [165], which are characterized by a horizontal plateau for high partial pressure. This shape can be fitted using e.g. a Langmuir-Freundlich, a Toth, a Toth-cp or a Dual-site-Langmuir (DSL) isotherm model. While shape (a) shows a steep slope at the begin, for isotherm (b) the increase is flatter. The third shape (c) shows an S-shaped isotherm, which belongs to a type V isotherm, and shows one inflection point. The adsorbed amount can reach a plateau or continue increasing for higher pressure. For the capture of CO₂ from dilute streams, the

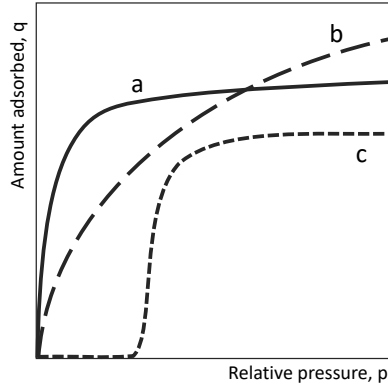


FIGURE 4.1: Schematic overview of different isotherm shapes.

isotherm shapes (a) and (c) are good candidates. Thanks to the steep slope at low partial pressure the material (a) can adsorb already at very low concentrations. If the step of the S-shaped isotherm occurs before the partial pressure of the CO_2 at feed concentration, the capture rate can be high as well. In addition to the capacity at ambient temperatures, the isotherm shape at desorption temperatures plays a crucial role as well. Figure 4.2 shows an exemplary isotherm for shape (a) and (c) at adsorption and desorption temperature. Both figures show isotherms which have a high CO_2 working capacity Δq using a dilute feed stream. Therefore, for DAC it is important to i) have an isotherm with a steep increase at low partial pressure and ii) a low loading at higher temperature, which narrows the choice of suitable isotherm models.

In this work, we consider a four-step vacuum temperature swing adsorption (VTSA) cycle and include several isotherm models in our analysis, i.e. Langmuir-Freundlich, Toth, Toth-cp, S-shaped, and DSL. Both adsorbent properties and process conditions are optimized to predict the performance limits, i.e. high productivity and low energy consumption using a simplified oD model. In addition, we analyze the effect of the kinetics and material properties by using a rate-based 1D model. In a last step, we carry out an economic analysis for the "optimal" materials. Although this is a theoretical experiment, the study can help in evaluating possible prospects of dilute CO_2 capture and can provide a framework for the potential in developing new materials.

The chapter is structured as follows: in section 4.2, the considered process as well as the considered isotherm models are discussed. In addition, existing databases are analyzed by screening and assessing the resulting materials based on their isotherms. In section 4.3 several theoretical experiments are carried out by optimizing isotherm

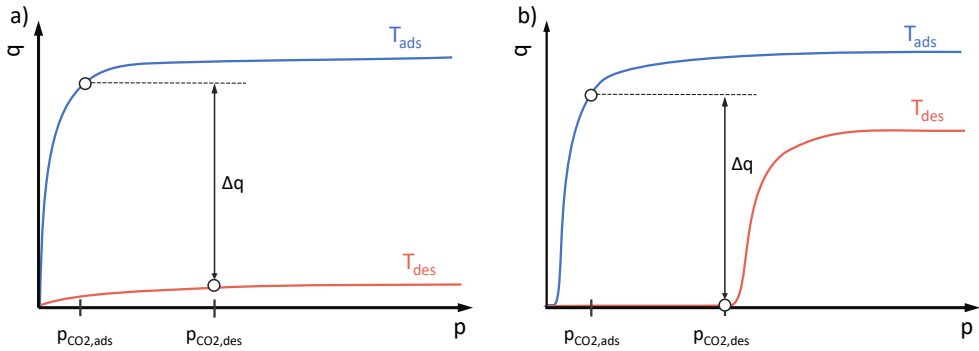


FIGURE 4.2: Illustrative isotherm at adsorption and desorption temperature. a) for a type I isotherm and b) for a type V isotherm shape.

parameters of the five isotherm models. In a second step, we use these results in a rate-based 1D model to also analyse the effect of the mass transfer coefficient. Finally, a cost analysis of the resulting hypothetical materials is carried out and the results are compared with existing materials.

4.2 METHODOLOGY

The analysis of the ideal sorbent consists of the following steps:

- Optimization of process performance parameters (T_{des} , p_{vac} , V_{feed}) and equilibrium isotherm parameters with the oD model. Including five different isotherm models and varying feed concentration ($y_{CO_2} = 0.04\%$, 0.1% , 1.0%).
- Optimization of the cycle times with the 1D model using the optimized isotherms as input.
- Techno-economic analysis of the performance of the hypothetical isotherms.

In the following we provide more details on the process simulation tools and on the optimization methods. The economic analysis is instead described in Section 4.4.

Process layout

We consider a simple four-step VTSA cycle, which is suitable to capture CO_2 from dilute feed streams like air. The process schematic is shown in Figure 4.3 and consists of four consecutive steps:

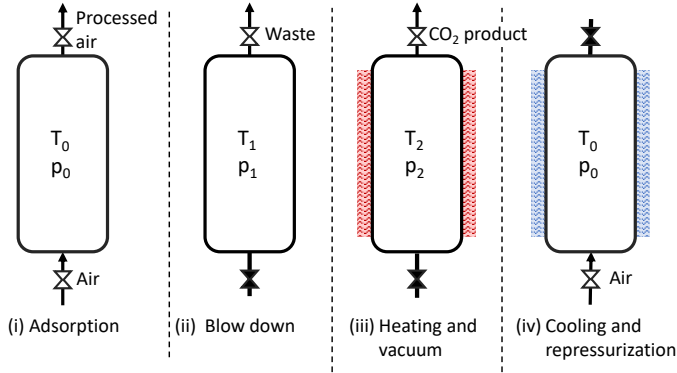


FIGURE 4.3: Process scheme of the four-step VTSA cycle.

- Adsorption at ambient pressure and temperature, where the feed stream enters the air contactor and CO_2 as well as H_2O are adsorbed, while N_2 is treated as an inert.
- Blow-down, where vacuum is pulled with the purpose of extracting N_2 in the void space. Some CO_2 and H_2O get desorbed, preheat of the system is possible.
- Heating at vacuum pressure and desorption temperature where the CO_2 and H_2O are desorbed and evacuated.
- Cooling and repressurization.

Given the effect of water on the adsorption process, especially for typical materials for DAC application like amine functionalized adsorbents, we consider a feed stream consisting of three components, i.e. CO_2 , H_2O and N_2 , where CO_2 and H_2O can be adsorbed by the sorbent, while N_2 is treated as an inert.

VTSA Simulation Models

The present work includes two parts: i) optimization of isotherm parameters together with process performance parameters using a simplified **oD model**, and ii) assessing the effect of mass transfer on the resulting optimal isotherms using a **1D model**.

oD model

First, the equilibrium model presented in the previous Chapter 3 is used to optimize the sorbent. Since it is designed to screen large databases, it is much faster than a **1D**

model, allowing us to include numerous decision variables during the optimization. The 0D model is based on the following key assumptions: (i) the bed is treated as a well-mixed reactor, (ii) the gas and the solid phases are in equilibrium during all steps of the cycle, (iii) the gas phase behaves ideally, and (iv) the pressure drop in the bed as well as (v) heat transfer resistances are not considered [149]. The equations can be found in the SI B.

1D model

Second, we consider the effect of mass transfer on the different isotherm models using a 1D rate based model, keeping the feed stream concentration at $y_{\text{CO}_2} = 0.04\%$. The 1D model has been used in multiple previous publications, and it has shown to predict experimental results well [50, 81–83]. The features of the mathematical model as well as the complete set of the equations and its validation are provided elsewhere [50, 81–83]. The physical dimensions of the module (the size of the air contactor or the length of the sorbent layer) are taken for the analysis carried out in Chapter 2 and are summarized in the Table C.3 in the SI. Mass transfer is included with the linear driving force (LDF) approximation, where the resistances are lumped into a single effective parameter. Besides the mass transfer, we also use the 1D model to investigate the influence of the material density of the adsorbent and the void fraction.

Equilibrium Isotherm Models

For our analysis we consider five different isotherm models: i) Dual-site-Langmuir (DSL), ii) Toth, iii) extended Toth with chemi- and physisorption (Toth-cp), iv) Langmuir-Freundlich (Sips), and v) S-shaped. The selection of this group is based on several criteria. First of all, we want to be able to screen the full q - p_i plane, and this is best done by considering multiple isotherm models. Second, we aim at representing the typical isotherm models reported in the databases (e.g. DSL isotherm model) but also the typical isotherm models for DAC (Toth and Toth-cp). The equations of the five equilibrium isotherm models are shown in Table 4.1. The number of isotherm parameters varies from 6 to 13 variables; their naming and units are listed in the Nomenclature. The water adsorption isotherm is kept the same for all simulations and is modeled using the GAB isotherm model, similar to previous studies [26, 41, 55]. While it would be also possible to include the parameters of the water isotherm in the optimization, the uncertainty for the choice of the boundaries would be high due to lack of experimental data. With more available experimental data, also with respect to the enhancing effect of water on the CO_2 adsorption, this would make an interesting future project.

TABLE 4.1: Equations for the five different isotherm models.

Model	Equation
Toth-cp	$q_{CO2} = n_{s,c} \frac{b_c p y_{CO2}}{(1 + (b_c p y_{CO2})^{t_c})^{1/t_c}} + n_{s,p} \frac{b_p p y_{CO2}}{(1 + (b_p p y_{CO2})^{t_p})^{1/t_p}}$ $n_{s,c/p} = n_{s0,c/p} \exp \left(X_{i,c/p} \left(1 - \frac{T}{T_0} \right) \right)$ $b_{c/p} = b_{0,c/p} \exp \left(\frac{\Delta H_{c/p}}{RT_0} \right) \left(\frac{T_0}{T} - 1 \right), t_{c/p} = t_{0,c/p} + \alpha_{c/p} \left(1 - \frac{T_0}{T} \right)$
DSL	$q_{CO2} = n_1 \frac{b(y_{CO2}^p)}{1 + b(y_{CO2}^p)} + n_2 \frac{d(y_{CO2}^p)}{(1 + d(y_{CO2}^p))}$ $b = b_0 \exp \left(\frac{H_b}{RT} \right), d = d_0 \exp \left(\frac{H_d}{RT} \right)$
Toth	$q_{CO2} = n_s \frac{b p y_{CO2}}{(1 + (b p y_{CO2})^t)^{1/t}}$ $n_s = n_{s0} \exp \left(X_i \left(1 - \frac{T}{T_0} \right) \right)$ $b = b_0 \exp \left(\frac{\Delta H}{RT_0} \left(\frac{T_0}{T} - 1 \right) \right), t = t_0 + \alpha \left(1 - \frac{T_0}{T} \right)$
Langmuir-Freundlich	$q_{CO2} = n_s \frac{(b p y_{CO2})^{1/t}}{(1 + (b p y_{CO2})^{1/t})}$ $n_s = n_{s0} \exp \left(X_i \left(1 - \frac{T}{T_0} \right) \right)$ $b = b_0 * \exp \left(\frac{\Delta H}{RT_0} \left(\frac{T_0}{T} - 1 \right) \right)$ $t = t_0 + \alpha \left(1 - \frac{T_0}{T} \right)$
S-shaped [166]	$q_{CO2} = q_L (1 - w) + q_U w$ $q_L = \frac{q_{L0} b_L (y_{CO2}^p)}{(1 + b_L (y_{CO2}^p))}$ $b_{L/U/H} = b_{L/U/H,0} \exp \left(\frac{\Delta U_{L/U/H}}{RT} \right)$ $w = \left(\exp \left(\frac{(\log(y_{CO2}^p) - \log(p_{step}))}{\sigma} \right) \right) / \left(1 + \exp \left(\frac{(\log(y_{CO2}^p) - \log(p_{step}))}{\sigma} \right) \right) \right)^\gamma$ $p_{step} = p_{step,0} \exp \left(\frac{-\Delta H_{step}}{R} \left(\frac{1}{T_0} - \frac{1}{T} \right) \right)$ $\sigma = x_{i1} * \exp \left(x_{i2} \left(\frac{1}{T_0} - \frac{1}{T} \right) \right), q_U = \frac{q_{U,0} * b_U (y_{CO2}^p)}{1 + b_U (y_{CO2}^p)} + b_H (y_{CO2}^p)$

Process optimization

The optimization problem was formulated to minimize the thermal energy consumption and maximize the productivity for different CO₂ feed concentrations, similar to the cases in Chapter 3. The multi-objective optimization problem is formulated as follows:

$$\begin{aligned} & \underset{x}{\text{minimize}}(-Pr, e) \\ & \text{subject to } \Phi \geq \Phi_{\text{spec}}, r \geq r_{\text{spec}} \end{aligned} \quad (4.1)$$

with

$$Pr = \frac{\dot{m}_{\text{CO}_2}}{V_s} \quad (4.2)$$

$$e = \frac{\dot{Q}_{\text{reg}}}{\dot{m}_{\text{CO}_2}} \quad (4.3)$$

where x are decision variables, Φ the purity, Φ_{spec} the required minimum purity, r the recovery, r_{spec} the required minimum recovery (for $y_{\text{CO}_2} > 0.04\%$), \dot{m}_{CO_2} is the mass rate of CO₂ captured from the air, V_s the volume of the sorbent, and \dot{Q}_{reg} represent the heat required during the regeneration step. The constraint of the purity and recovery is imposed as a penalty C on the resulting objective function in the form of

$$\begin{aligned} C &= 10[\min(0, (\Phi - \Phi_{\text{spec}}))] \\ C &= 10[\min(0, (r - r_{\text{spec}}))] \end{aligned}$$

For Φ_{spec} we are here assuming a value of 95%, which is a typical value for CO₂ storage applications. The constraint on the recovery is set to $r_{\text{spec}} > 90\%$ for CO₂ concentrations higher than 400ppm.

As mentioned, two types of multi-objective optimizations were performed. For the first case we carry out an optimization using the oD model and optimize both process and adsorbent parameters. For the second case, we use the 1D model to understand the effect of mass transfer by varying the linear driving force coefficient. Both approaches are presented below.

oD model. The design variables include both process and adsorbent decision variables:

- Operating process parameters are: desorption temperature T_{des} , vacuum pressure p_{vac} , and volume feed stream V_{feed} .

- isotherm decision variables, depending on the isotherm model. For the Toth-cp method, e.g., 12 variables are optimized: $n_{s0,c/p}$, $Xi_{c/p}$, $b_{0,c/p}$, $\Delta H_{c/p}$, $t_{0,c/p}$, and $\alpha_{c/p}$.

The range for the process parameters is given in Table C.6 and is in line with previous optimization runs for VTSA processes using dilute CO₂ feed streams [120, 149]. The maximum desorption temperature is limited to 373K, to allow for the use of low temperature heat during the regeneration. The boundaries for the material properties are chosen by scanning adsorbent properties published in literature [137, 166] and analysing isotherms from our previous screening [149]. The density and void fraction of the hypothetical materials are kept constant during the optimization. The constant adsorbent and process properties are listed in the SI in Table C.5 and C.3, respectively. When looking at the isotherm parameters for the different isotherm models, we can use similar boundaries for the enthalpy of adsorption and the saturation capacity of the physisorption $n_{s,0}$. Since the saturation loading can have a significant influence, we are carrying out a sensitivity analysis for the upper bound of this parameter. For the remaining isotherm parameters we need to have wider ranges, which are defined by carrying out a screening of several databases. The boundaries for the decision variables for the different isotherm models are listed in the SI in Table C.7. More details on the screening are provided in the following section 4.2.

It is important to note that for the range of the isotherm decision variables it can happen that the resulting isotherms are not physically meaningful; for example, a decreasing CO₂ loading with increasing partial pressure or with decreasing temperature. This effect was mainly seen for the s-shaped isotherm model. Therefore, special care needs to be taken during the optimization, for example by including a penalty function. More details can be found in the SI C.

The optimization of the oD model is carried out using a particle swarm algorithm adapted for multi-objectives (MOPSO), as implemented in Matlab R2021 [147]. The settings for the algorithm are reported in the SI C.

1D model. Taking the resulting isotherm and process parameters from the optimization with the oD model, an optimization with the rate-based model is carried out to also include the effect of the kinetics. In addition to the process decision variables for the oD model, the times of the different steps are included as well. For the optimization we follow the same approach reported in chapter 2. A list of all variables together with their upper and lower bounds can be found in C.6.

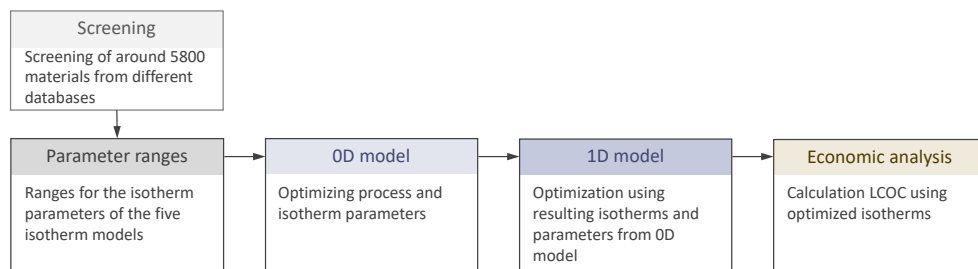


FIGURE 4.4: Outline of the overall approach.

Adsorbent evaluation and screening

Before designing new isotherms, already existing materials from databases are analyzed. This is done to identify the ranges of the isotherm parameters of the different isotherm models but also to be able to compare the optimized isotherm shape with existing adsorbents. A summary of all the steps involved in finding the ideal sorbent is shown in Figure 4.4.

The screening is carried out similar to the work in Chapter 3, but we include additional databases, obtaining around 5800 materials. More details concerning the databases can be found in the SI C.

Depending on the CO_2 concentration in the feed stream, different materials are left when screening the databases. The equilibrium isotherms for the resulting materials are plotted in Figure 4.5 on the left for the three different cases. The corresponding Pareto charts from optimizing a VTSA cycle using these materials are given by the right figures. For the most diluted case, only 12 materials showed a positive working capacity. For $y_{\text{CO}_2} = 0.1\%$ and $y_{\text{CO}_2} = 1.0\%$ the screening revealed more materials, namely 13 and 30 adsorbents, respectively.

For defining the ranges of the isotherm parameters, all fitted isotherms from the databases are considered. Most of the isotherms were fitted using the DSL, Toth-cp, and Langmuir-Freundlich isotherm models, and only a few were fitted using the Toth and s-shaped models. These fitting data were used to determine the parameter ranges for the different models, which are listed in Table C.7 in the SI.

In contrast, the isotherms resulting from screening, i.e., the isotherms showing a positive working capacity at $y_{\text{CO}_2} = 0.04\%$, only include materials fitted with the Toth-cp and the Langmuir-Freundlich methods. It can be seen that these remaining isotherms from the screening show a higher slope at low pressure. This trend can also be seen by a quantitative analysis using isotherm metrics. Further details on this study can be found in the SI C.

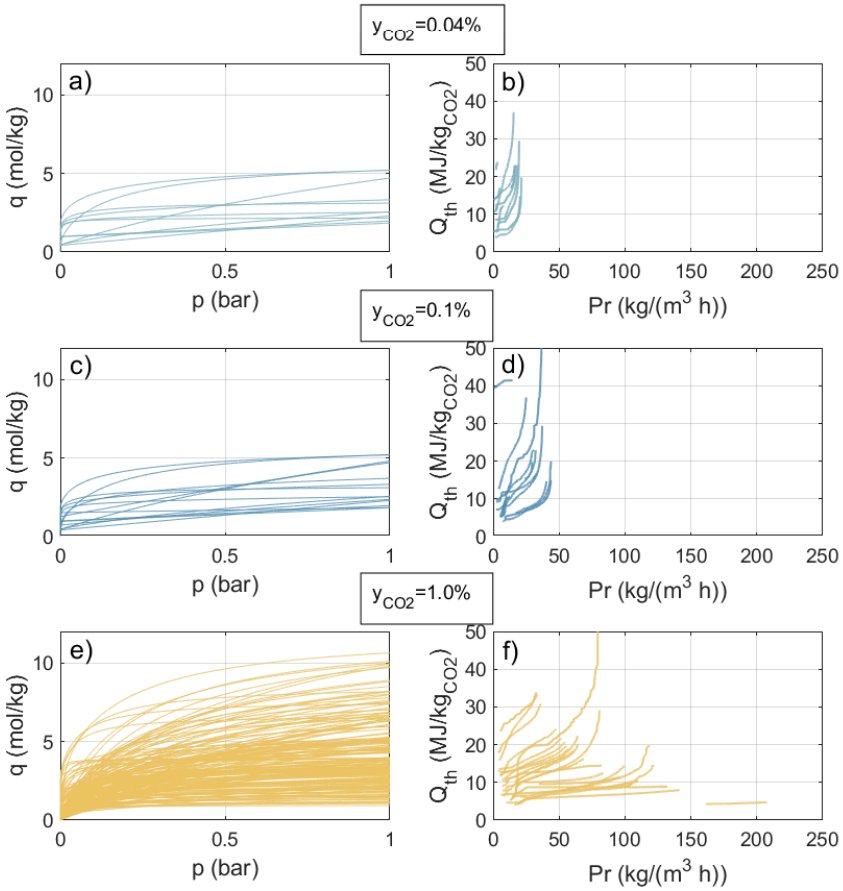


FIGURE 4.5: Screening results including several databases. The left column shows the resulting Pareto chart, while in the right column the isotherms are plotted for different CO₂ feed stream concentrations: a)+b) $y_{\text{CO}_2} = 0.04\%$, c)+d) $y_{\text{CO}_2} = 0.1\%$, and e)+f) $y_{\text{CO}_2} = 1.0\%$.

In contrast, the isotherms resulting from the screening, i.e., the isotherms showing a positive working capacity at 40, include only materials equipped with the Toth-cp and Langmuir-Friendly methods. It can be seen that these remaining isotherms from screening show a higher slope at low pressure. This trend can also be seen in a quantitative analysis using isothermal metrics.

4.3 RESULTS OPTIMIZING ISOTHERM PARAMETERS

Effect of isotherm parameters and feed concentration

For each isotherm model, a productivity - thermal energy optimization was carried out including process and isotherm parameters as decision variables. The resulting Pareto charts are plotted in Figure 4.6. Each Pareto point of the optimized isotherm models represents one hypothetical isotherm. The three graphs show the results using three different CO₂ feed stream concentrations, i.e. $y_{\text{CO}_2} = 0.04\%$, $y_{\text{CO}_2} = 0.1\%$, and $y_{\text{CO}_2} = 1.0\%$. For comparison, the grey lines show the resulting Pareto charts from the database screening for varying CO₂ concentrations, as explained in the previous section 4.2.

When looking at the DAC case (Figure 4.6 a)) and comparing the Pareto charts of the hypothetical isotherms with the materials from the databases, the thermal energy consumption is lower for all cases, which is mainly due to the lower desorption temperature of the hypothetical materials. The figure also shows, that the productivity of the optimized isotherms is in a similar range to several of the existing sorbents. While one might have expected the optimized isotherm models to outperform the database materials more significantly, there are several explanations for this behaviour. With the oD model optimization an increase in productivity is mainly achieved through higher adsorption capacity. This means that a very steep isotherm at low pressure for this ultra-dilute case is needed. However, depending on the boundary conditions for the isotherm parameters, this may not have room for further improvement: the boundaries were chosen by taking into account fitting values from existing materials. Another reason could be that the density considered for the ideal sorbent is lower than that of materials in the database (the density is kept constant for all hypothetical materials). In addition, the productivity is an outcome of the neural network trained without the performance of the improved sorbents.

In Figure 4.7 the optimal isotherms of all isotherm models for the DAC case are plotted, together with the isotherms from the databases. One can see that the capacity within the low and high pressure region at ambient conditions is higher for most of the hypothetical isotherms.

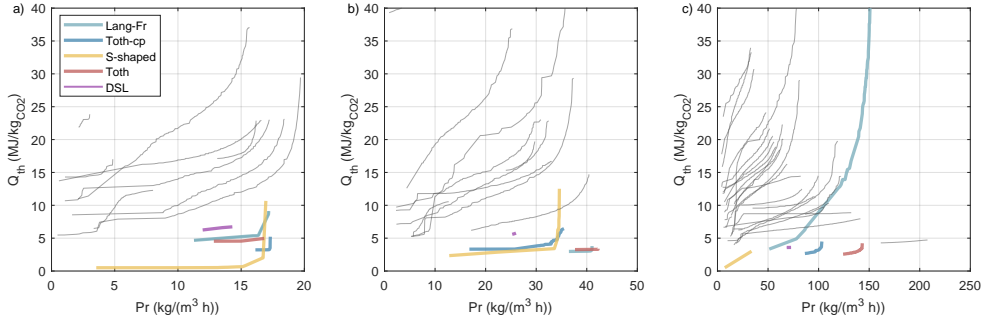


FIGURE 4.6: Resulting Pareto charts for the optimized isotherm models using a CO_2 feed concentration of a) $y_{\text{CO}_2} = 0.04\%$, b) $y_{\text{CO}_2} = 0.1\%$, and c) $y_{\text{CO}_2} = 1.0\%$. In addition, for case a) the Pareto plots of three real materials are plotted in black. Using oD model.

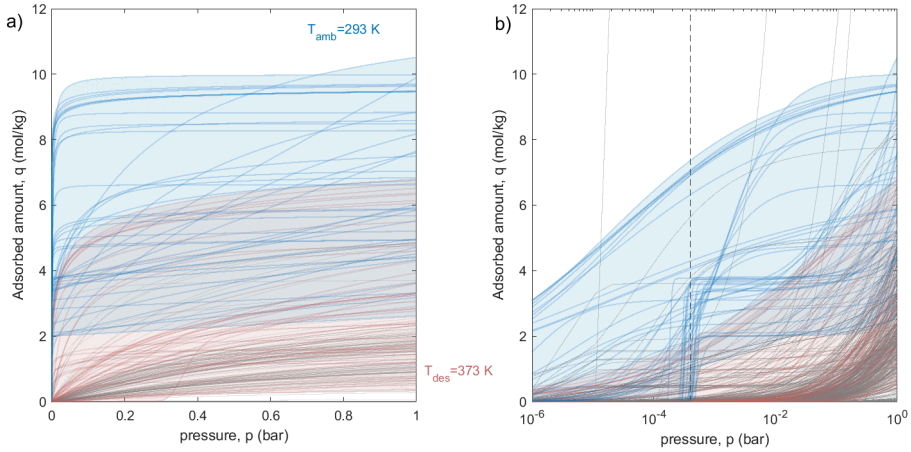


FIGURE 4.7: Optimized isotherms including all models (blue for adsorption temperature $T_{\text{amb}}=293\text{K}$ and red for desorption temperature $T_{\text{des}}=373\text{K}$) compared with real isotherms (grey) for $y_{\text{CO}_2} = 0.04\%$. Plotting a) linear scale and b) logarithmic scale.

When comparing the different isotherm models with each other, the S-shaped isotherm shows the best performance for the ultra-dilute case, with a very low minimum energy consumption of 0.55 MJ/kgCO₂. This is due to the isotherm step which requires limited heating. In the SI in Figures C.5 and C.6, all simulated isotherms are plotted both in linear and logarithmic-scale for a feed stream concentration of $y_{\text{CO}_2} = 0.04\%$. Here, the step of the S-shaped isotherm can be seen, which can lead to a higher working capacity and a lower desorption temperature during the regeneration. The resulting Pareto curves for the Toth-cp, the Toth and the Langmuir-Freundlich isotherm are in a similar range, while the DSL shows the worst performance for the ultra-dilute feed concentration. This, again, can be explained by the shape of the isotherms when looking at Figure C.6. Although the DSL isotherms can have a steep slope at low pressure region, this also leads to a steeper isotherm at higher temperature. Therefore, the low capacity must be compensated by a higher desorption temperature.

For higher CO₂ concentrations, the results are comparable with the DAC case, i.e. with respect to the productivity, the optimized isotherm models are in a similar range compared to the materials from the database while the thermal energy consumption is lower. The performance of the S-shaped isotherm model gets worse for higher concentrations, which may be due to the boundary range of the isotherm parameters and the constraint on the CO₂ recovery. The Toth model shows the best performance for higher concentrations. For the $y_{\text{CO}_2} = 1.0\%$ case, one adsorbent from the screening outperforms all optimized isotherm models, showing the highest productivity while also showing a low energy consumption (Mg-MOF-74). Overall, the results show that, depending on the CO₂ concentration in the feed, some isotherm models perform better than the others. This confirms the need to choose or design a sorbent specifically for a particular purpose and process.

1D optimization: Effect of kinetics and material properties

Using the optimal isotherms obtained with the oD model, we investigate the influence of the mass transfer coefficient, density and void fraction. This analysis is carried out for the ultra-dilute case, i.e. DAC application. Figure 4.8 shows two groups of Pareto charts: i) the results when optimizing the isotherm and process parameters using the oD model as presented in the previous section, ii) and the Pareto curves using the 1D model. For the latter, the Pareto front of each isotherm model is calculated using one optimal isotherm as input, which was received from the oD model optimization. As marked in Figure 4.8, we considered the optimal isotherm and process parameters at point A. The input parameters for the 1D optimizations as well as the process conditions and boundaries are listed in the SI in Tables C.3 -

C.11. For these optimization runs the linear driving force coefficient for CO_2 was set to $k_{LDF} = 0.1\text{s}^{-1}$.

While the energy consumption for the Toth-cp, Toth and Langmuir-Freundlich model are in a similar range for both models, the productivity is lower for all cases when using the 1D model. This difference between the two models was already identified in Chapter 3, where the validation between both models showed a consistent variance. On the other hand, for the S-shaped isotherm model the energy consumption obtained in the 1D model is significantly different from the results of the oD model. In addition, it was not possible to run the rate-based model with any of the optimized isotherms using the DSL method. A reason for this to happen is the assumption of isothermal adsorption in the oD model. Both isotherm models are very sensitive to a temperature change. Therefore, a set of isotherm parameters that lead to a positive working capacity using an isothermal desorption step in the oD model, can result in a negative uptake using a non-isothermal adsorption model. A temperature wave will propagate through the bed leading to a different local temperature and eventually to a different adsorbed amount compared to the oD model. A similar behaviour for a stepped isotherm model was also found in other literature [167, 168].

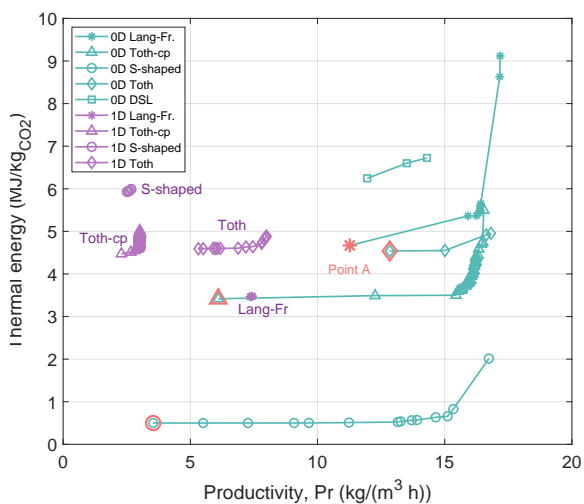


FIGURE 4.8: Comparison optimization results using the 0D and the 1D models for different isotherm models. The Pareto curve obtained with the 0D model shows the optimization of the respective isotherm model, while the corresponding Pareto chart using the 1D model shows the optimization using the optimal isotherm of point A obtained with the 0D model.

Since the optimization of the Toth-cp model showed the best performance while having results consistent with the 1D model, this equation is used for further investigations. First, we run an optimization for two other points along the oD Pareto using the rate-based model. Results are shown in Figure 4.9 a). The isotherm parameters for all three points are listed in Table C.13. The productivity calculated by the 1D model is lower but in the same range of the oD model. The energy consumption increases for point A and B while decreases for point C. The shape of these three optimal isotherms is shown in Figure 4.9 b) together with the other optimal isotherms from the Pareto front obtained with the oD model. While the isotherms show a similar uptake during the adsorption, i.e. at 293K and $y_{\text{CO}_2} = 0.04\%$, their shape is slightly different at desorption temperature. For point A the capacity is the lowest and for point C the highest, which is also represented by the Pareto points in the oD Pareto front and by the individual Pareto fronts using the 1D model: optimization with point A results in a lower productivity compared to point C.

In Figure 4.10 a) the influence of the linear driving force coefficient is shown for the three optimal isotherms. As expected, the performance worsens for lower values of k_{LDF} , both in terms of productivity and energy consumption. The influence of the kinetics is larger when starting at high productivity, i.e. the productivity of point C decreases by 78% compared to around 40% for point A, when looking at the two extreme LDF coefficients. This clearly shows, that optimal isotherms can increase the process performance but CO_2 removal from air is largely controlled by kinetics. Therefore, sorbent development should target both kinetics and equilibrium.

On the other hand, the density and void fraction only show a small effect on the performance. The Pareto fronts shown in Figure 4.10 b) are all similar in forms of minimum energy and maximum productivity. When looking at the purity and recovery of the different optimization runs in the SI in Figure C.8, and considering the other parameters fixed, a high void space and a low density show a lower purity. In addition, the adsorption and production time are higher for the higher density and small void volume sorbents.

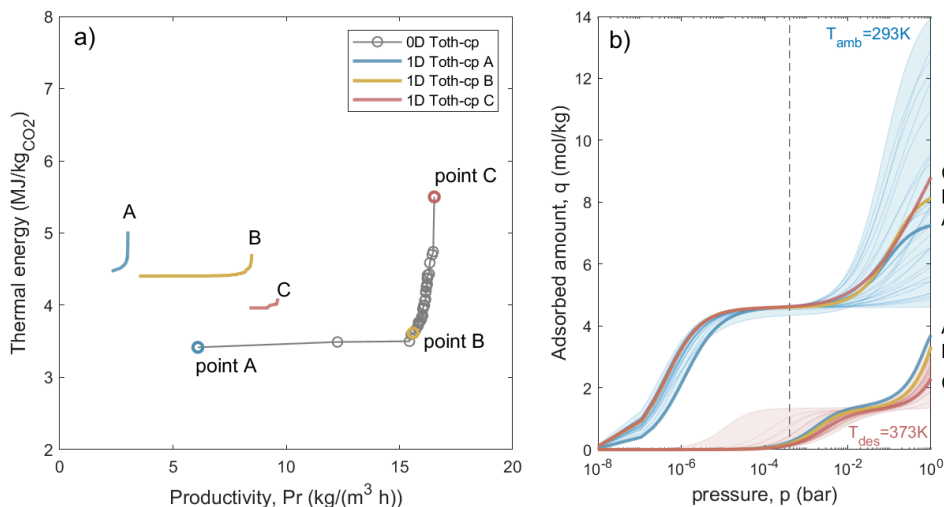


FIGURE 4.9: Details on the optimized Toth-cp isotherm model: a) Pareto fronts of the optimized isotherm obtained with the oD model (grey line) and the 1D model for three optimized isotherms (A, B, and C). b) The shape of the optimal isotherms obtained with the oD model, highlighting the three chosen isotherms correlating to point A, B, and C in the Pareto chart of a).

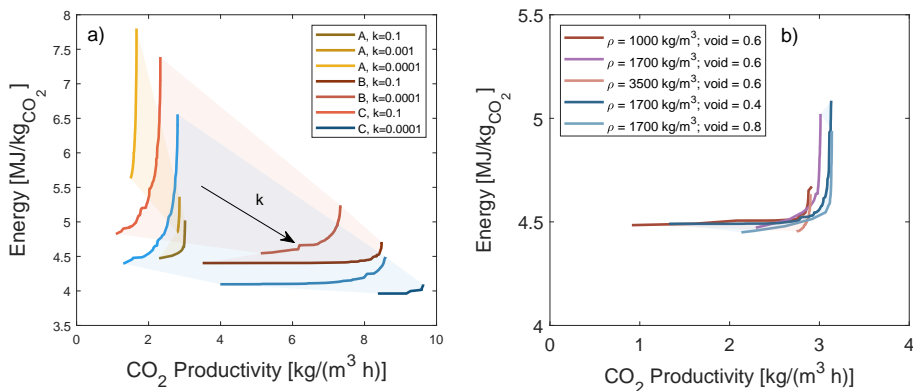


FIGURE 4.10: Optimization results using the 1D model: a) Pareto charts for Toth-cp model including three different optimal isotherms obtained with the oD model and varying LDF coefficients ($k_{LDF}^1 = 0.0001s^{-1}$, $k_{LDF}^2 = 0.001s^{-1}$, and $k_{LDF}^3 = 0.1s^{-1}$). b) varying rho and void ($\rho_1 = 1000kg/m^3$, $\rho_2 = 1700/m^3$, $\rho_3 = 3500/m^3$ and $void_1 = 0.4$, $void_2 = 0.6$, $void_3 = 0.8$).

4.4 COST ASSESSMENT

Methodology

Eventually, the choice of the optimal sorbent is driven by its economic performance. Therefore, starting with the results of the rate-based model, an economic analysis is carried out. The calculation of the levelized cost of CO₂ (LCOC) is kept simple but accurate enough, to compare different hypothetical materials with each other but also with existing ones. Therefore, the analysis is carried out applying a bottom-up methodology which requires sizing and costing of all components.

To determine the LCOC, we use the total annualized cost (TAC), which includes three cost blocks: sorbent cost, CAPEX, and OPEX, as well as the capital recovery factor (CRF) [169]. The recovery factor is calculated using the weighted average cost of capital (WACC) and the technical lifetime of the plant l

$$LCOC = \frac{CRF \cdot C_{CAPEX} + C_{OPEX} + C_{Sorbent}}{m_{CO_2}} = \frac{TAC}{m_{CO_2}} \quad (4.4)$$

$$CRF = \frac{WACC(1 + WACC)^l}{(1 + WACC)^l - 1} \quad (4.5)$$

Details concerning the calculation of the equipment purchase costs is given in the SI in Section C. All costs are provided in \$₂₀₂₀ and adjusted using the Chemical Engineering Plant Cost Index (CEPCI). The installed costs were determined by applying the Lang Factor method, where the purchase cost of the equipment is summed up and then multiplied by a Lang Factor f_L [170, 171]. In addition, the delivery costs of the equipment are considered by including a factor of $f_d = 1.05$ [172] resulting in

$$C_{CAPEX}^{unit} = \sum_{i=1}^n C_{p,i} f_L f_d \quad (4.6)$$

with $C_{p,i}$ being the purchase costs of equipment i .

The primary equipment components included in the capital cost calculations are the air contactor, the air blower, the vacuum pump, a condenser, adsorbent vessels, adsorbent material, and a storage tank for the temporary storage of the captured CO₂.

Currently, DAC is in an early stage of development, but with gaining more experience around the technology, cost reduction can occur. In addition, scaling up the process can lead to a reduction of the component costs due to mass production. Therefore, to calculate the total costs, two approaches are applied: i) economies of scale for the components which are already well-established [171, 172], and ii) the

concept of learning-by-doing for innovative technologies [173]. The former is used to scale up the storage tank and the condenser, while the latter is used to calculate the costs of one air contactor module. Such a module includes an air blower, the housing of the air contactor and a vacuum pump. The target cumulative capacity of the plant is set to 1 Mton_{CO₂} per year. More details on the economic calculation can be found in the SI C. The sorbent is considered to be not affected by a scaling up factor.

As for the OPEX, a fixed part and a variable part are considered. The fixed part refers to the annual maintenance cost and the labour cost. The former is calculated as 4% of the total plant cost, and the labor cost is 30% of the maintenance cost. The variable costs comprise the thermal energy and electricity price and are included with 0.026\$/kWh and 0.108\$/kWh, respectively. The operating costs include the electrical requirements for the rotating machinery, the heat requirement for the regeneration, as well as the adsorbent replacement costs.

For the theoretical case, the adsorbent cost was set to $c_s = 30 \text{ \$/kg}_{\text{CO}_2}$ and a lifetime of $l_s = 2$ years was assigned. These two parameters can vary depending on the specific materials, e.g. MOFs can have stability issues and their production can be costly. Compared to Zeolite 13X, which has costs of around 2\$/kg_{CO₂} and a lifetime between 7-10 years [171], our assumption is quite conservative but justified with the uncertainty DAC processes bring at the current status.

Cost limits of a VTSA cycle

First, we have computed the LCOC for all Pareto points. Results are shown in Figure 4.11 for the best performing material, i.e. case C from Figure 4.9; results for case A and B can be found in the SI in Figures C.11 and C.12, respectively. The three plots in Figure 4.11 show the three cases for varying the linear driving force coefficient. It can be clearly seen that, independent of the kinetics, the sorbent costs make up the most significant proportion of the total costs. The OPEX, in particular, only contribute to a small extent. In addition, the results show a clear trend between productivity and costs, i.e. a higher productivity leads to smaller total costs. Therefore, the costs increase with decreasing kinetics.

The cost range we obtain, 450 \$/t_{CO₂} to 2500 \$/t_{CO₂}, is in line with other cost estimations in open literature: depending on the assumptions and process design, costs from below 100 to over 1000 \$/t_{CO₂} can be found [22, 54, 174–176]. In 2018, Climeworks claimed the cost of their first commercial plant to be in the range of 600 \$/t_{CO₂} and estimates that it will fall below 100 \$/t_{CO₂} within the next 5-10 years [177].

As shown in Figure 4.11, the sorbent cost introduces a significant uncertainty. Therefore, we carried out a sensitivity analysis on the sorbent price and on the sorbent lifetime. The bar charts in Figure 4.12 show how the total costs depend

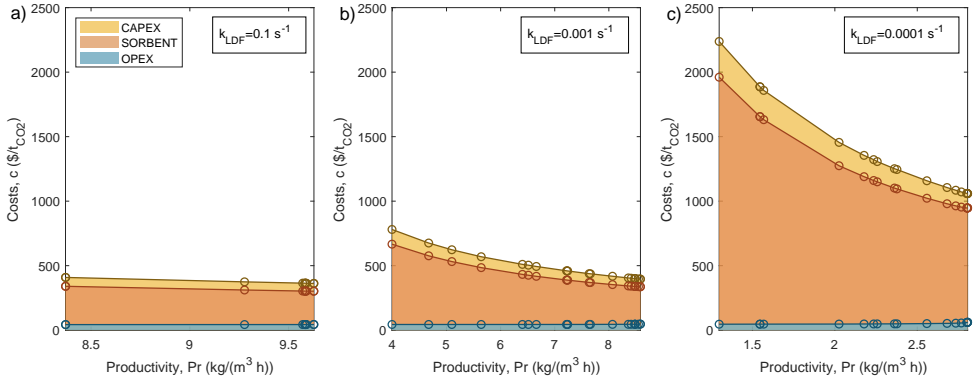


FIGURE 4.11: Cost calculation using the resulting Pareto charts obtained with the 1D model from Figure 4.10 case C for different kinetic coefficients: a) $k_{LDF} = 0.1\text{ s}^{-1}$, b) $k_{LDF} = 0.001\text{ s}^{-1}$, and c) $k_{LDF} = 0.0001\text{ s}^{-1}$.

on both parameters: for the sake of clarity, the costs are calculated for one Pareto point, and, since the productivity has the largest effect on the costs, the highest productivity point was chosen. In addition, we compute the costs for a simulation obtained with data from existing sorbents, i.e. Lewatit (as already reported in [26]) and a promising MOF, MIL-101. When looking at the ideal sorbent, the first three bar charts include different sorbent costs, i.e. i) $2\text{ \$/kg}_{\text{CO}_2}$ similar to the commercially available costs of Zeolite 13X, ii) $30\text{ \$/kg}_{\text{CO}_2}$ comparable with Lewatit VP OC 1065, and iii) $90\text{ \$/kg}_{\text{CO}_2}$ which is chosen to represent a more innovative material like e.g. a MOF. A detailed breakdown of the costs can be found in the SI in Figures C.16-C.18. With the following three bar charts the effect of the sorbent lifetime is investigated. We consider a range of 0.5 years to 5 years, with the upper bound being similar to Zeolite and the lower bound for MOFs. While the hypothetical sorbent outperforms Lewatit for both analyses, it can be seen that the costs of the sorbent need to be in the range of the ones of Zeolite for DAC to become attractive, i.e. to get close to the $100\text{ \$/t}_{\text{CO}_2}$. Even when combining both, i.e. long lifetime and low sorbent price, the resulting costs are slightly above the $100\text{ \$/t}_{\text{CO}_2}$ target, as shown in the SI in Figure C.14 a). When looking at the results using the MOF MIL-101 in Figure 4.12, this material is able to outperform Lewatit, but only when assuming the same sorbent costs, which is rather unrealistic. Keeping the sorbent costs and lifetime the same, the ideal sorbent shows the lowest costs.

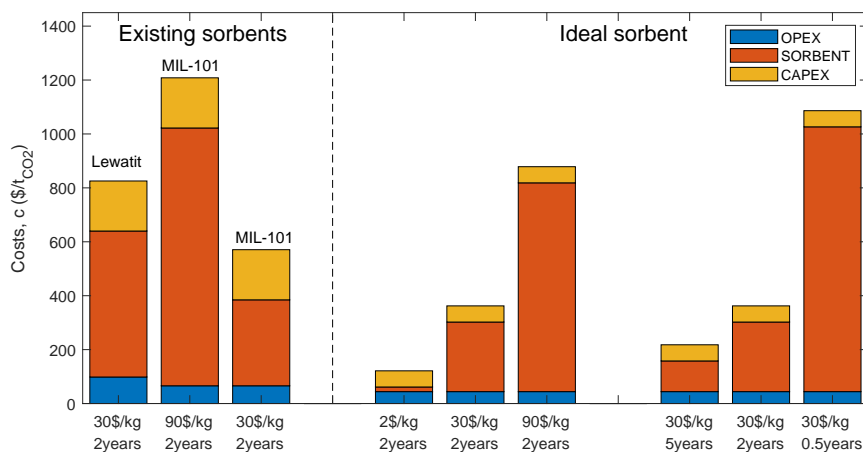


FIGURE 4.12: Cost breakdown showing existing sorbents and the optimized Toth-cp isotherm (case C) using the 1D model. From the Pareto chart in Figure 4.10 the point with the highest productivity was chosen ($k_{LDF} = 0.1 \text{ s}^{-1}$). The bars show resulting costs dependent on the sorbent costs and lifetime.

The graphs in Figure 4.11 show a clear correlation between the productivity and the total costs. Yet, we can't guarantee that an optimization based on costs minimization would lead to similar cost performance of an energy-productivity optimization. Therefore, we combined the cost calculation with the oD model and ran the isotherm optimization to minimize the total costs. The decision variables and boundaries were kept the same as in the previous section 4.3, including the isotherm and process parameters. The analysis was run using the Toth-cp isotherm model. The results are shown in Figure 4.13 a). The colored points show all the simulation data and the red circle represents the optimal point, i.e. the lowest costs. For comparison, the Pareto front obtained from the previous optimization is shown, using the productivity and thermal energy demand as objectives within the oD model. The results clearly show that the optimal costs are on the Pareto front. When zooming in, one can see that the cost-optimization shows a slightly better performance compared to the multi-objective optimization, which is due to the simpler approach, i.e. only one objective, and therefore faster execution. Since the costs are strongly dependent on the productivity, they are similar as well (238.3\$/t_{CO2} for optimizing the costs and a range of 241.5\$/t_{CO2}-516.9\$/t_{CO2} for the Pareto chart).

On the right in Figure 4.13, the shape of the isotherms are compared with each other, showing both a linear and logarithmic scale. The shaded area represents the optimal isotherms from the multi-objective optimization, while the thick, dashed

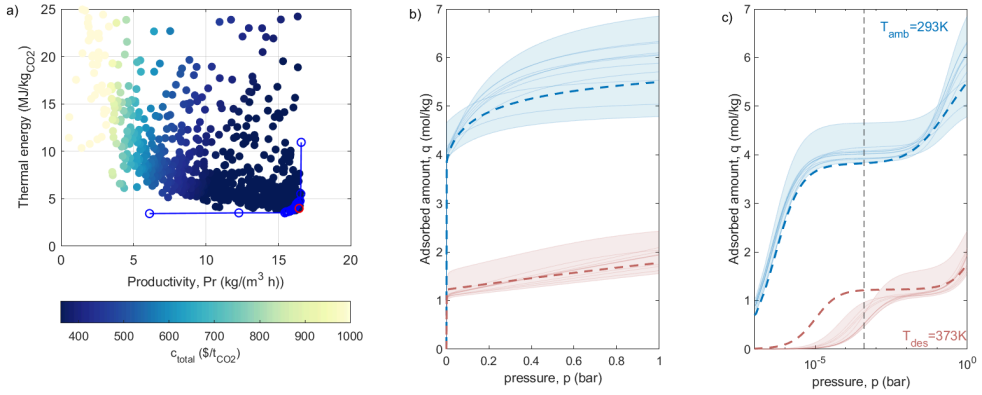


FIGURE 4.13: Results for optimizing for the total costs. a) Comparison of optimization results with the optimization for productivity and energy consumption. The latter is shown by the bright blue Pareto chart, while the optimal point for optimizing the costs is marked by a red circle. b)+c) comparison of the optimal isotherm shapes for both optimization approaches. The optimal isotherm for the lowest costs is shown by the thick dashed line.

lines represent the resulting isotherm when optimizing the costs. They show a similar shape, with the optimal isotherm for costs revealing a smaller capacity during adsorption and low loading during desorption, eventually leading to a higher working capacity.

The results clearly show that both, optimizing for the process performance parameters or the total costs of the plant, lead to similar results. When comparing these findings with CO₂ post-combustion capture, where the CO₂ concentration in the feed stream is higher and sorbent materials are already commercially available, the objectives show a different correlation [160, 178]. In this case, the points revealing the lowest investment costs lie in the sub-optimal region of the Pareto plot and not on the Pareto front, which is due to the complex scale-up of vacuum swing adsorption processes from single-column simulations. On the other hand, DAC is mainly affected by the productivity (between 5 and 15 kg/m³/h, vs. over 500 kg/m³/h for post-combustion capture). This effect was also seen in our analysis for a CO₂ feed concentration of $y_{\text{CO}_2} = 1.0\%$ (see Figure C.15 in the SI).

4.5 DISCUSSION

Before concluding, we would like to put the main findings into perspective and discuss some limitations and possible future research subjects. In this work, we explored the limits of CO₂ adsorption from the ambient air in terms of process performance and economics. To do so, we not only focus on one isotherm model, but included five models to represent a broader sorbent spectrum. While we were able to find several hypothetical isotherms which could outperform existing materials, our approach had some limitations.

First, we optimized the isotherm parameters using a simple equilibrium model. While this allowed us to include also complex isotherm models like the S-shaped model with 13 parameters, and carry out the optimization in a reasonable time of maximum 2 days, the optimized isotherms do behave differently when run with a rate-based model. One reason is the assumption of isothermal adsorption for the 0D model. For several optimized isotherms with temperature sensible isotherms in our pressure region like the DSL and the S-shaped isotherm, the results were completely different when running them with the 1D model. Therefore, for these isotherm models the presented approach is not applicable. When including these isotherm models, the equilibrium model needs to be updated to make the adsorption step non-isothermal.

In addition, the resulting performance of the isotherm models is limited by the boundary conditions of the isotherm parameters. While we chose parameters in the area of already existing materials, this might not necessarily be the case for new sorbents. When doing so, one has to carefully check the resulting isotherm shape and evaluate the feasibility.

Another important point is the modeling of the water adsorption. Since experimental data for co-adsorption of water is rare, we kept the isotherm model and also the isotherm parameters constant throughout the analysis. With more experimental data available, the adsorption of water can be adapted as well, e.g. by including competitive CO₂ and H₂O isotherms.

Still, with our approach we were able to identify material properties sets that improve the performance of DAC, both when using an equilibrium- and a rate-based model. With our approach, we provide a broad guideline on the limits of sorbents for dilute feed streams.

4.6 CONCLUSIONS

In this study, we have investigated the performance and cost limits of a four step VTSA cycle for capturing CO₂ from the air. In our work we follow the approach of *process inversion*, where both the adsorbent properties and process design variables

are optimized. In the first part of the analysis, we optimize five different CO₂ equilibrium isotherm models to represent different isotherm shapes. The optimization is carried out using a oD model with the aim of maximizing the productivity and minimizing the thermal energy demand. In addition, we have considered different CO₂ capture scenarios by considering three feed stream concentrations, i.e. $y_{\text{CO}_2} = 0.04\%$ (DAC case), $y_{\text{CO}_2} = 0.1\%$, and $y_{\text{CO}_2} = 1.0\%$. When comparing with existing materials from several databases, the results show that the optimized isotherms outperform all of them. The best performing isotherm models for the ultra-dilute feed concentration were the extended Toth equation showing the highest productivity up to $17 \text{ kg/m}^3/\text{h}$ and the S-shaped model showing the lowest thermal energy consumption of $0.55 \text{ MJ/kg}_{\text{CO}_2}$. For higher concentrations the order changed with the S-shaped model getting worse while for the Toth and Langmuir-Freundlich models the performance improved.

Focusing on the DAC case, sensitivity analyses on the mass transfer coefficient, the density, and void fraction were carried out to understand the impacts of uncertainty. For this purpose, the optimized isotherm and process parameters were used as an input for a rate-based model. The results show a strong dependence on the kinetics, while the density and void fraction have only a small influence on the performance. However, the magnitude can vary depending on the situation.

Finally, these results served as a starting point for an economic analysis of DAC. Depending on the kinetic factor, the levelized cost of CO₂ for a plant producing 1Mt CO₂ per year varies between 450 to 2500 \$/t_{CO₂}. This leads to the question: what does it take to bring the cost down, preferably below 100 \$/t_{CO₂}, to be competitive with other negative emissions technologies such as afforestation or BECCS [176]? The technical and economic performance of a DAC process is strongly affected by the adsorbent material. While the productivity, and therefore the mass transfer play a very important role, the results also show a strong dependency on the sorbent costs, including the sorbent purchase cost as well as its lifetime, which account for a share of nearly 70% when considering 30 \$/kg_{sorb} and 2 years life. Bringing down the overall costs would require either a sorbent with a particularly high performance at the same costs resulting in a productivity of around $60 \text{ kg/m}^3/\text{h}$, or sorbent costs similar to the commercially available Zeolite 13X (2 \$/kg) and/or a longer lifetime.

Although this research is based on hypothetical sorbents obtained by theoretical experiments, this framework can serve as a basis for the evaluation of future VTSA plants and provides guidelines on the practical limitations of adsorbents for capturing CO₂ from dilute feed streams. In addition, the framework could be used as a guide for choosing key criteria in adsorbent development.

MODELING PHOTOVOLTAIC-ELECTROCHEMICAL WATER SPLITTING DEVICES FOR THE PRODUCTION OF HYDROGEN UNDER REAL WORKING CONDITIONS

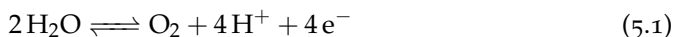
Photoelectrochemical splitting of water is potentially a sustainable and affordable solution to produce hydrogen from sun light. Given the infancy stage of technology development, it is important to compare the different experimental concepts and identify the most promising routes. The performance of photoelectrochemical devices is typically measured and reported under ideal irradiation conditions, i.e. 1 sun. However, real-life operating conditions are very different, and are varying in time according to daily and seasonal cycles.

In this chapter, an equivalent circuit model for computing the steady state performance of photoelectrochemical cells is presented. The model allows for a computationally efficient, yet precise prediction of the system performance and a comparison of different devices working in real operating conditions. To this end, five different photoelectrochemical devices are modeled using experimental results from literature. The calculated performance shows good agreement with experimental data of the different devices. Furthermore, the model is extended to include the effect of illumination and tilt angle on the hydrogen production efficiency. The resulting model is used to compare the devices for different locations with high and low average illumination and different tilt angles. The results show that including real illumination data has a considerable impact on the efficiency of the PV-EC device. The yearly average solar-to-hydrogen efficiency is significantly lower than the ideal one. Moreover, it is dependent on the tilt angle, whose optimal value for European-like latitude is around 40° . Notably, we also show that the most performing device through the whole year might not necessarily be the one with highest sun-to-hydrogen efficiency for one-sun illumination.

The results presented in this chapter have been reported in: Grimm, A., Sainte-Marie, A., Kramer, G. J., Gazzani, M., Modeling photovoltaic-electrochemical water splitting devices for the production of hydrogen under real working conditions. *International Journal of Hydrogen Energy* 47, 11764 (2022).

5.1 INTRODUCTION

The water splitting reaction is an endothermic reaction at ambient condition with a net free Gibbs energy ΔG^0 of 237.2 kJ/mol, which corresponds to a potential (E°) of 1.23 V. The two redox half-reactions occurring at the electrodes are (i) water oxidation at the anode (Eq. 5.1), or oxygen evolving reaction (OER), and (ii) water reduction at the cathode (Eq. 5.2), or hydrogen evolving reaction (HER):



Solar water splitting, or photolysis of water, is not a new concept; the first experimental demonstration of the splitting of water into hydrogen and oxygen by electrocatalysis was reported by Fujishima and Honda in 1972, who used a rutile titanium dioxide (TiO_2) photoanode and a Pt counter electrode [179]. Since the conduction band of rutile is not negative enough to split H_2O , an applied voltage bias was applied to the TiO_2 working electrode. Although TiO_2 material is stable in aqueous electrolytes, the performance is low due to its large band gap (3.2 eV), which limits the utilization of the solar spectrum to the UV portion.

Since then, an increasing number of experimental concepts has been assembled and tested, improving the technology significantly (e.g. [180–182]). As expected, most studies focused on developing more performant materials for the different components of the device, or on designing optimal reactor configurations to achieve higher solar-to-hydrogen (STH) efficiencies [183]. Notably, solar water splitting systems involve five main ingredients, namely a photoabsorber that converts photons into electron-hole pairs, a catalyst of the oxygen-evolving reaction, a catalyst of the hydrogen-evolving reaction, an electrolyte allowing the protons transportation from one electrode to the other, and, for most reactor designs, a membrane to separate the products.

Depending on the materials used and the design of the system, different types of solar water splitting devices can be identified. In literature, various taxonomies for the different cells can be found, e.g. in [184–186], where detailed reviews of the different solar fuel generators are presented. In Figure 5.1, a simplified overview of the different types and sub-types of solar water splitting devices is given. Three main approaches can be identified: photocatalytic (PC), photoelectrochemical (PEC), and photovoltaic + electrolyzer (PV-E). The presented overview should not be seen as a strict categorization, since there exist also devices that could be attributed to more than one of these categories. Rather, with the presented classification we focus on technological and modeling aspects.

A PC device consists of suspended particles of photocatalyst dispersed in a medium. It is the simplest system, since there is only one light absorber, however,

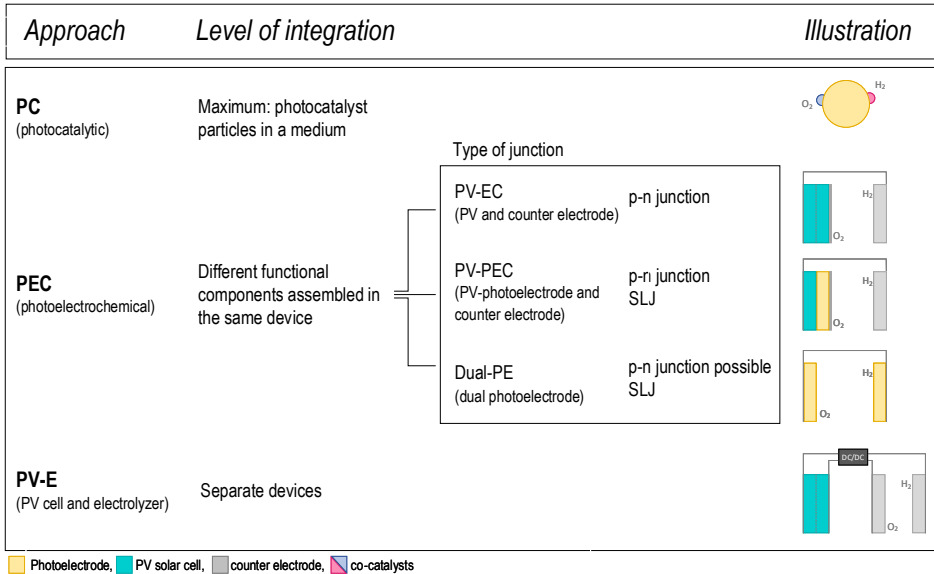


FIGURE 5.1: Different types of solar water splitting devices. PEC cells are divided into photovoltaic-electrochemical (PV-EC) devices, photovoltaic-PEC (PV-PEC) devices and devices with two photoelectrodes (Dual-PE). For each configuration a typical example is illustrated.

the simplicity is paid with low STH efficiencies, which are in the range of 1% [187, 188]. On the other side of the spectrum, combining PV cells with an electrolyzer is a modular approach using two systems: PV panels producing independent power are connected to an electrolyzer (or several electrolyzers). Due to significant advances in solid state photovoltaics, PV-E systems are today the most efficient way to carry out solar water splitting, yielding STH efficiencies as high as 30% [189]. PEC devices lie in the middle, as the integrated version of a PV-E system, where the light absorber is immersed in the electrolyte. Because semiconductors are very sensitive to corrosion, the light absorber has to be protected from the electrolyte, affecting the overall STH efficiency of the system. Typical STH efficiencies of PEC devices range from 1 to 20% [190].

The architecture of a PEC device is mainly based on the type of junction used to separate the electron-hole pair. Band bending, resulting from a local imbalance in charge neutrality, is the phenomenon responsible for the charge separation and transfer in a PEC device. Band bending occurs at a junction between a semiconductor

and another material and depends on the type of junction. Two junctions can be found in a PEC device: a buried PV junction and a solid-liquid junction (SLJ). In a buried PV junction (also called Schottky-junction), the interface between a metal and a semiconductor is responsible for band bending. A buried junction works together with at least one p-n junction, located at the interface between two layers of a semiconductor, one doped positively (p) and the other doped negatively (n). Together, the buried junction and the p-n junction(s) drive efficiently the electrons and holes apart. On the other hand, a solid-liquid junction is located at the interface between a semiconductor and a liquid solution. The effect is the same as in a buried PV junction since it permits the charge separation and transfer between the photoabsorber and the electrolyte. However, a single SLJ is not sufficient to drive the water splitting reaction without any additional bias, thus, a tandem architecture is necessary [191]. PEC devices can be further divided in sub-categories as shown in Figure 5.1: (i) a PEC device with one or more buried PV junctions and two or more p-n junctions (also known as PV-EC device), (ii) a PEC device with one buried PV junction coupled with one solid liquid junction (PV-PEC), and (iii) a dual photoelectrode with two SLJ (Dual-PE).

PV-EC technology benefits from the well-established knowledge of water electrolysis on the one hand, and photovoltaics on the other hand, and can easily achieve STH efficiencies of more than 10% [190]. Several PV-EC devices have been built using various PV technologies such as crystalline silicon [192], thin film (e.g. amorphous silicon (a-Si) [193], copper indium gallium selenide (CIGS) solar cells [194]), and multijunction solar cells [195]. Recently, Cheng and coworkers have demonstrated a record STH efficiency of 19.3% with a monolithic PV-EC device consisting of a GaInP/GaInAs multijunction [89].

On the other hand, PV-PEC devices are hybrid systems combining both a buried PV junction with p-n junction(s) and a SLJ. In this configuration, the PV cell provides the voltage bias necessary for the photoelectrode to drive the water splitting reaction. Such devices are generally built to study and improve the photoelectrode [196].

In a dual-PE device, two different absorbers are in contact with the electrolyte solution, resulting in two SLJs, one at each photoelectrode. This design benefits from cheaper materials but exhibits lower STH efficiencies, around 1% [190]. Multiple studies focus on dual photoelectrodes devices to improve the efficiency of the system. To date, the highest STH efficiency was achieved by using a BiVO₄ photoanode with a CIGS photocathode and reached 3.7% [197].

While dual photoelectrode technology is in its infancy, PV-EC and PV-PEC systems are more mature [191]. This work focuses on PV-EC because of the maturity and relative simplicity of the technology but also due to the better experimental data availability.

While there exist studies providing a detailed overview of the state-of-the-art of solar water splitting devices [198–201], there are no works that focus on modeling and comparing different PV-EC devices under ideal and real light conditions. One reason is that research efforts currently focus mainly on finding innovative materials and architectures to improve the overall performance of the system. As a result, it is difficult to identify the preferred direction of development among the many materials and devices presented in literature. Moreover, the effect of illumination on the hydrogen production efficiency has been largely overlooked in past works, with the exception of Turan et al, who investigated the scale up PV-EC devices [183]. With this work, we aim at contributing to close these gaps by (i) providing a consistent modelling framework of different PV-EC devices using the equivalent electric circuit approach, and by (ii) predicting and comparing the yearly hydrogen production rate under real-world illumination and varying tilt angles. This chapter is organized as follows: Section 5.2 describes the modeling methodology and resulting performance of five different PV-EC devices using the equivalent electric circuit approach, first for ideal conditions, second for varying illumination and tilt angle. This is followed by a yearly comparison of the different devices (Section 5.3). Finally, we discuss the resulting findings.

5.2 MODELING PV-EC SYSTEMS WITH EQUIVALENT ELECTRIC CIRCUIT

In the following, we first present and validate a model for simulating PV-EC using the equivalent electric circuit approach. For the validation we use experimental data from literature. Then, we extend the model to include varying illumination conditions, which allows for computing yearly performance including weather data of different geographical locations. The obtained model is finally used to compare different PV-EC devices at varying (i) location, and (ii) tilt angle.

PV-EC model for ideal sun conditions

Our modeling framework builds upon and extends the work of Winkler et al, who modeled an integrated PV-EC device using steady-state equivalent circuits [202]. The approach of equivalent circuit is relatively simple, yet accurate in describing the behaviour of a PV-EC system. To this end, the device can be divided into two main components: a photoabsorber part, consisting of the different light absorbers and later referred as the ‘solar cell’, and an electrolyzer part, which includes the two electrodes (the catalysts and/or a metal) and the electrolyte solution. A simplified scheme of a PV-EC device is shown in Figure 5.2. We note that the solar cell and the catalysts can be either directly in contact or wired, but since the losses due to

the wires are negligible, we will no further make a differentiation between the two. To model the thermodynamic performance of the system, we need the j - V curves of PV and EC sides as shown in Figure 5.2. The cell operating point is identified by the intersection of the two j - V curves, which depend on the specific materials and architecture.

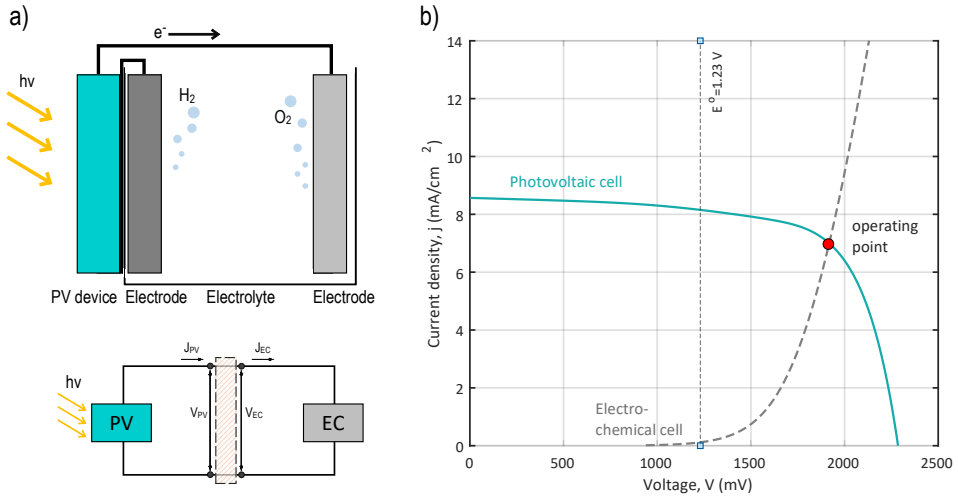


FIGURE 5.2: (a) A simplified setup of an exemplary PV-EC device, and of a PV device which provides power to an electrochemical cell (adapted from [190, 202]). (b) Simplified j - V characteristics of a PV-EC device, the operating point is indicated by a red dot.

The overall electric equivalent circuit of a generic multijunction PV-EC system is shown in Figure 5.3. Each p-n junction in the photoabsorber is represented by a one diode model consisting of a source of current j_L , a diode defined by saturation current density j_0 , a series resistance R_s and a shunt resistance R_{sh} . The source of current j_L represents the photogenerated current, while the diode represents the recombination current induced by the recombination losses of electrons and holes. Both series and shunt resistance are parasitic elements to represent ohmic losses in the PV device. The equivalent steady-state circuit of the electrolyzer part of the system is shown on the right in Figure 5.3. In this model, the thermodynamic potential is depicted by a voltage source, while the resistance R_{sol} represents the voltage drop caused by the electrolyte solution.

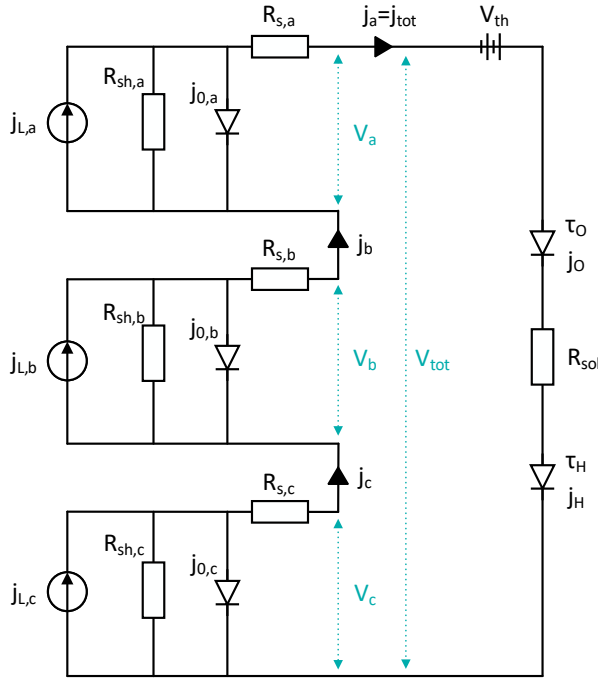


FIGURE 5.3: Equivalent circuit of a multijunction PV-EC device. In this example, the solar system consists of three different p-n junctions which are made of material a, b and c.

The current density of the photoabsorber can be calculated by taking the photo-generated current j_L and subtracting all recombination currents according to the equivalent circuit model [202]. The resulting equation is:

$$j = \frac{1}{n_s} \left[j_L - j_o \exp \left(\frac{V}{n_j V_{th}} + j R_s \right) - \frac{V}{R_{sh}} + j R_s \right] \quad (5.3)$$

where:

- V_{th} is the thermal voltage, i.e. the voltage induced in the p-n junction by the ambient temperature and is calculated based on the Boltzmann constant k_B , the temperature T and the elementary charge q : $V_{th} = \frac{k_B T}{q}$. At room temperature V_{th} is equal to approximately 26 millivolts.

- n_j is the number of junctions (e.g. 3 for a triple junction as shown in Figure 5.3).
- n_s is the number of solar cells connected in series, respectively.

The voltage calculated with Equation 5.3 is the voltage output of one single photoabsorber junction. If a solar cell consists of multiple junctions or if several single junction solar cells are connected in series, the total voltage output is given by the sum of the voltage of each junction [203]:

$$V = \sum_i^{n_j} V_i \quad (5.4)$$

which simplifies to $V = n_j V_i$ if the n_j junctions are identical.

Since the solar cells and the electrolyzer are connected in series, the current is the same in all the components. In case that n_s identical solar cells are connected in series, the photoabsorber area is then multiplied by the number of cells and the current density of the total system is:

$$j_{\text{tot}} = \frac{j}{n_s} \quad (5.5)$$

In order for the electrolyzer to split H_2O , the solar cell(s) must produce a voltage accounting for the thermodynamic potential E° of the water splitting reactions (OER and HER) (1.23 V), and the voltage loss at the cathode and the anode and ohmic losses of the solution. Therefore, the electrolyzer voltage can be written as:

$$V_{\text{electrolyzer}} = E^\circ + V_{\text{cathode}}^{\text{loss}} + V_{\text{anode}}^{\text{loss}} + R_{\text{sol}} j \quad (5.6)$$

The voltage loss at the cathode and anode can be calculated using the Tafel law, which connects the rate of the electrochemical reactions of the electrode to the overpotential:

$$V_{\text{cathode}}^{\text{loss}} + V_{\text{anode}}^{\text{loss}} = \tau_{\text{H}} \log_{10} \frac{j}{j_{\text{H}}^0} + \tau_{\text{O}} \log_{10} \frac{j}{j_{\text{O}}^0} \quad (5.7)$$

where the terms τ_{O} and τ_{H} are the Tafel slopes, j_{O}^0 and j_{H}^0 are the exchange current densities and where the subscripts O and H refer to the OER and HER respectively. The overall equation for the electrolyzer is therefore written as:

$$V_{\text{electrolyzer}} = E^\circ + \tau_{\text{H}} \log_{10} \frac{j}{j_{\text{H}}^0} + \tau_{\text{O}} \log_{10} \frac{j}{j_{\text{O}}^0} + R_{\text{sol}} j \quad (5.8)$$

The system operating point is found evaluating the photoabsorber and electrolyzer voltage (or current) which is obtained in practice by directly coupling or wiring together the two:

$$\sum_i V_{PV,i} = V_{\text{electrolyzer}} \quad (5.9)$$

The resulting equivalent circuit model of the PV-EC system (Equation 5.3-5.9) requires different empirical parameter as input: $j_L, j_0, R_s, R_{sh}, n_i$ for the solar cell and $\tau_H, \tau_O, j_H^0, j_O^0, R_{sol}$ for the electrolyzer part. These can be obtained by fitting the model equations with available experimental points for a specific device, which requires the expression of the equations in the form $V = f(V)$ or $j = f^{-1}(V)$. This can be tackled by using the Lambert function (more details can be found in the Supplemental Information Section D). Once the j-V curve is resolved according to the model equations, it is possible to obtain the operating current j_{op} of the system and the associated STH efficiency. Graphically, that means j_{op} is found at the intersection of the solar cell j-V curve and the electrolyzer j-V curve.

In this work, we calibrate and validate the model using experimental data of five different PV-EC cells which are representative of different possible designs and material combinations. These devices and the sources reporting the results are listed in Table 5.1, together with the light absorber's material, the catalysts used in the cell as well as the reported STH efficiency. Urbain 2015 and Urbain 2016 are both silicon-based devices, the former consists of a solar cell made of a double junction of amorphous silicon (a-Si) while the latter consists of a triple junction made of two layers of amorphous silicon and one layer of micro-crystalline silicon ($\mu\text{c-Si}$) [193] [195]. Jacobsson device includes solar cells connected in series: the photoabsorbers consist of three single-junction copper indium gallium selenide (CIGS) solar cells [194]. Finally, Varadhan and Sun's devices both consist of a double junction solar cell made of an indium gallium phosphide (InGaP) top cell coupled with a gallium arsenide (GaAs) bottom cell [204] [205]. Moreover, Sun is the only device that also includes a bipolar membrane, allowing the separation of the O_2 and H_2 .

Ideally, separate current-voltage data measurements for each component of the device, i.e. the solar cell and the electrolyzer, are used to calibrate and test the model. However, j-V data are often measured and reported for either some of the components, or for a specific group of components. In such case the data must be inferred by subtracting and adding the available j-V data points based on the equations of the equivalent circuits, which was here necessary for the Varadhan device. Details for the available data can be found in the Supporting Information.

TABLE 5.1: List of the 5 PV-EC devices modeled

Device reference	Light absorber	Catalysts OER/HER	STH
Urbain 2015, [193]	a-Si/a-Si	RuO ₂ /Pt	6.8%
Urbain 2016, [195]	a-Si/a-Si/ μ c-Si	RuO ₂ /Ni	8.7%
Jacobsson, [194]	3 CIGS (s)*	Pt/Pt	10.5%
Varadhan, [204]	InGaP/GaAs	NiOx/Ni	12.1%
Sun, [205]	InGaP/GaAs	Ni/Ti-CoP	10.0%

*(s) : solar cells connected in series

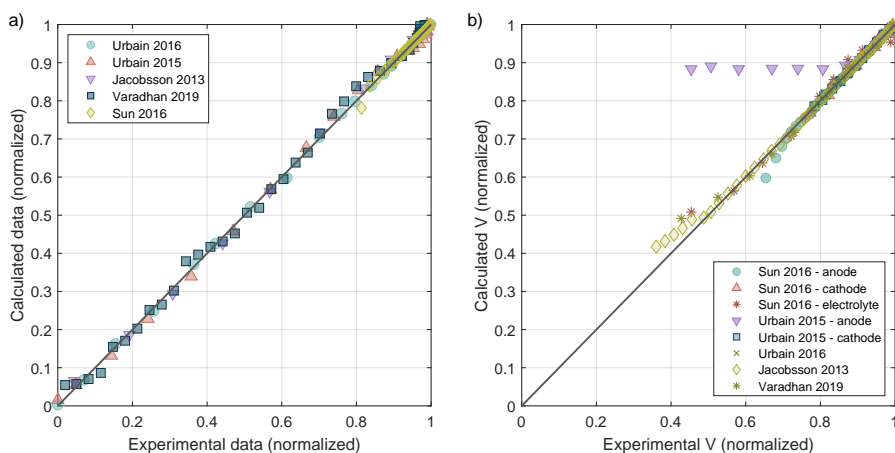


FIGURE 5.4: Normalized parity plots for a) the solar cell and b) the electrolyzer part. On the x-axis, the experimental data points extracted from literature are displayed, while on the y-axis the output of the model is shown. The data is normalized over the experimental data. A separate Figure for each device is shown in the Supplementary Information.

The fitting between model and data is carried out by minimizing the difference between the calculated and measured j-V curve. The objective function $f(y)$ is defined as

$$f(y) = 1 - R^2 = \frac{\sum(y_i - \hat{y}_i)^2}{\sum(y_i - \bar{y})^2} \tag{5.10}$$

where y_i is the experimental data point i obtained from the j-V curve, \hat{y}_i is the predicted value of y_i by the model and \bar{y} is the mean value of y_i . The objective function is minimized with Matlab (R2018b) optimization routine *fmincon* using the *sequential quadratic programming* (SQP) algorithm. Because of the sensitivity of the Lambert function to changes in the boundary conditions, the model can easily become difficult to solve. While this is not the case for the electrolyzer, whose model is fairly simple, the solar cell can easily show convergence problems. This problem can be tackled by following the approach proposed by Bouzidi et al. [206], where Equation 5.3 is divided into two equations, one valid for low voltages and one for higher voltages. Therefore, instead of fitting one complex function, the parameters are found by fitting two simpler equations. The overall model is however not changed. More details can be found in the Supporting Information section D.

In addition to the j-V curve, we compute the solar-to-hydrogen (STH) index, which is a key performance indicator used to compare different solar water splitting devices [207]. It is defined as the ratio between the total chemical energy generated and the total energy input from sunlight illumination:

$$\eta_{\text{STH}} = \frac{|j_{\text{op}}|E^{\circ}\eta_{\text{F}}}{P_{\text{sun}}} \quad (5.11)$$

where j_{op} is the operating current density, E° (V) is the thermodynamic potential needed to split H_2O in H_2 and O_2 and P_{sun} (mW cm^{-2}) is the incident illumination power density: η_{F} is the faradaic efficiency; for water splitting, faradaic efficiencies close to 100 % are commonly reported in the literature [193], meaning that the photocurrent directly corresponds to the molar hydrogen generation rate and assumes selective and stable catalysts for water splitting.

Figure 5.4 reports the parity plots for the solar cells on the left and for the electrolyzer on the right. The parity plots of the solar cells show good agreement with respect to experimental values (R^2 greater than 0.99). For the Sun device, the fitting showed only reliable results for a voltage greater than 1.9 V. This is due to the limited number of experimental data points. Since the j-V curve is nearly horizontal for smaller voltages (see Figure 5.5), the resulting fitting is still accurate. The source of error for Varadhan lies in the uncertainty connected to the type of data reported. However, the root mean square error (RMSE) indicates an error of 40 mV in average, which is not significant.

The parity plots of the electrolyzers show more diverse results. In Varadhan et al. [204], different curves were fitted to obtain the electrolyzer j-V characteristic. The experimental curve of Urbain 2016 electrolyzer was obtained by subtracting the j-V curve of the whole PV-EC device from the solar cell curve. By doing so, some irregularities appeared at high current densities, probably due to the horizontal part of the two curves, which explains the deviation observed in Figure 5.4 b). As for

TABLE 5.2: Solar cell parameters of each junction calculated by fitting the equations of the equivalent circuit to the experimental j-V curves of the 5 PV-EC devices. The light absorber material used in each junction is also being reminded

	Material	j_L mA.cm ⁻²	j_0 mA.cm ⁻²	R_s Ω.cm ²	R_{sh} Ω.cm ²	n_i
Urbain et al. 2015	a-Si	5.2	2×10^{-14}	5.2	1551	1.1
Urbain et al. 2016	a-Si	6.80	9.8×10^{-9}	0.36	3317	1.0
	μ c-Si	6.84	2.25×10^{-8}	1.50	1481	1.6
Jacobsson et al.	CIGS	34.6	3×10^{-10}	1.7	1001	1.0
Varadhan et al.	InGaP	9.7	1×10^{-9}	0.5	2779	1.1
	GaAs	10.0	3×10^{-9}	0.6	2030	1.8
Sun et al.	InGaP	8.1	1×10^{-16}	3.6	8.80×10^5	1.2
	GaAs	9.1	3×10^{-7}	3.6	1.01×10^4	2.7

Jacobsson, the electrolyzer j-V curve is available in [194], but the experimental curve of the electrolyzer is skewed for lower voltages (even below the thermodynamic potential). This anomaly explains the low regression coefficient, which is shown in Figure D.3 b). On the other hand, the parity plot shows good results for voltages higher than 1600 mV corresponding to a current density of around 2 mA.cm⁻², and since the device is mainly operating for current densities around 5 mA.cm⁻² low voltage area should simply be disregarded. The electrolyzer curve of Varadhan depicts the overpotential of the anode combined with the voltage drop due to the solution resistance, and the model describes accurately the system. Urbain 2015 reports a value of R_{sol} which was measured by impedance spectroscopy. The data available for Urbain 2015 is very detailed since the j-V curves of all the components of the electrolyzer are published. Also in this case the model shows good agreement with experimental data (highest RMSE is obtained for the cathod and limited to 6 mV). As for Sun, experimental data for anode, cathode, and electrolyte were available, allowing for a detail tuning of the model.

The values of the fitting parameters of each junction of the solar cells are compiled in Table 5.2. The values of the photogenerated current densities j_L are in line with the experimental short current densities. In the Jacobsson cell, the photogenerated current displayed is approximately three times higher than the rest of the devices due to the fact that the light absorbers consist of three solar cells connected in series.

As for the other devices, the standard construction is a tandem device, where cells are also connected in series, but the whole surface area belongs to the same cell. In the Jacobsson device the cells are connected in series instead of being stacked on top of each other, thus the available light collector area is three times higher. The photogenerated current of the whole device is therefore $j_L/3 \approx 11.5 \text{ mA}\cdot\text{cm}^{-2}$, according to Equation 5.5. CIGS solar cells produce a high current density but suffer from low voltage.

The saturation current densities j_0 range from 10^{-4} to 10^{-16} , showing no clear connection with the respective material. j_0 depends on many factors, among which the type and number of junction [208]. In particular, Urbain 2015 and Sun devices exhibit very low saturation current densities while, on the contrary, the j_0 values of Urbain 2016 device are rather high. The calculated saturation current densities appear to be in range with the values reported in the literature. For example, the modeling results by Winkler et al reveal value of $j_0 = 4 \cdot 10^{-10} \text{ mA cm}^{-2}$ [202].

The calculated series resistance R_s for four out of the five PV-EC devices range from 0.5 to 5 $\Omega\cdot\text{cm}^2$, in line with the few values reported in the literature [202], [206]. Urbain 2016 device shows particularly low values of R_s , which may be explained by a trade-off between j_0 and R_s since both parameters influence the open-circuit voltage, also justifying the high calculated values of j_0 compared to the other devices.

The values obtained for the shunt resistances R_{sh} are satisfactory since the expected range is around 10^3 to 10^6 [209].

Finally, the ideality factor n_i varies typically between 1 and 2 depending on whether the recombination losses occur in the space-charge region ($n_i \approx 1$) or in the depletion region ($n_i \approx 2$) [210], [211]. Yet, ideality factors greater than 2 can sometimes be observed in heterojunction solar cells [212], such as in Urbain 2016 or Sun devices.

The values obtained for the electrolyzer part of the devices are compiled in Table 5.3. The parameters are in line with values provided in literature [202]. Since the experimental data of the cathode of the Varadhan cell was not available (see Supporting Information D), for this device the losses of the cathode were not considered. For all devices, the exchange current density at the anode j_O^0 is lower than the exchange current density at the cathode j_H^0 , which can be explained by the lower kinetics of the OER. The solution resistance varies between 16 to 31 $\Omega\cdot\text{cm}^2$, which is in line with the range provided by Winkler et al (0-60 $\Omega\cdot\text{cm}^2$). The resistance of Sun device is slightly higher, presumably due to the membrane between the electrodes that slows down the circulation of the protons. The solution resistance also depends on the distance between the two electrodes; the distance is usually around 2 cm. But this information is not always provided.

The resulting j-V curves for the solar cell and the electrolyzer are shown in Figure 5.5. When comparing the different devices, we can link the photoabsorber

TABLE 5.3: Electrolyzer parameters found after fitting the experimental j-V curves of the 5 PV-EC devices. τ_O and τ_H are expressed in millivolt per decade. R_{sol} of Sun device was directly provided in the literature.

	τ_O mV/dec	τ_H mV/dec	j_O^0 mA.cm ⁻²	j_H^0 mA.cm ⁻²	R_{sol} Ω .cm ²
Urbain 2015	57	54	1.7×10^{-3}	0.45	21.3
Urbain 2016	154	169	0.11	0.13	16
Jacobsson	177	36	0.04	0.26	22
Varadhan	57	-	2×10^{-4}	-	27
Sun	51	72	1×10^{-9}	0.15	31

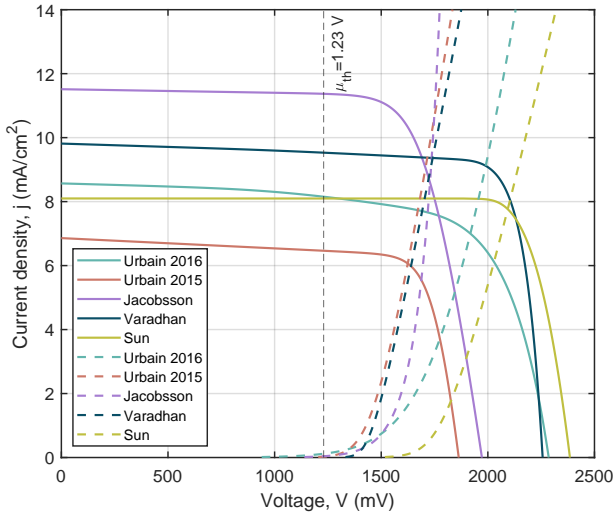


FIGURE 5.5: j-V curves of the solar cells and electrolyzers of the five PV-EC devices modeled. The j-V characteristics of the devices are measured under $P_{sun} = 1$ sun illumination (corresponding to 1000 W.m^{-2} or 100 mW.cm^{-2}).

TABLE 5.4: Calculated STH efficiencies based on the fitted devices.

	Calculated STH	Reported STH
Urbain 2015	7.5%	6.8%
Urbain 2016	8.6%	8.7%
Jacobsson	10.6%	10.5%
Varadhan	11.6%	12.1%
Sun	9.6%	10.0%

and electrolyzer curve to the characteristics of the device in terms of materials and design. For instance, the two devices comprising platinum electrodes, Urbain 2015 and Jacobsson, exhibit very low overpotentials at the electrolyzer even at high current density. Platinum is a very efficient, yet expensive catalyst used to demonstrate proofs of concept [194]. Similarly, the figure shows that CIGS solar cells used in Jacobsson device provide a high current density but suffer from low voltages. Therefore, coupling the CIGS solar cells with the catalysts used in Sun device for example (nickel and cobalt phosphide) would yield a much lower efficiency. Sun device succeeds to exhibit a high efficiency because of the InGaP/GaAs junction that provides a sufficient voltage.

It is worth stressing that PV-EC models based on equivalent electric circuit build upon interpretation of the device physical behaviour but are largely empirical. Therefore the physical interpretation of the model parameters must be taken with caution. Yet, the main scope of such simple model is to reproduce mathematically the j-V characteristics as accurately as possible, which is found to be overall satisfying.

Finally, we can compare the model findings with the experimental value of the sun to hydrogen efficiency. The results are reported in Table 5.4. Overall, we notice that the agreement between experiments and model is good. The largest difference is observed for Urbain 2015 and is mainly due to the error in extracting the experimental data from the graph in the paper. More specifically, while we obtain a R^2 larger than 0.999, we find a $R_{sol}=23.5\Omega.cm^2$ compared to $R_{sol}=21.3\Omega.cm^2$ provided in the paper; this is due to the small discrepancy between the data used to fit the model and those obtained experimentally. For Varadhan and Sun, the difference is probably due to the lack of the component-specific data points. On the other hand, the calculated efficiency of Urbain 2016 and Jacobsson is almost equal to the reported efficiency, while the others are reasonably close for such simple model.

In summary, the model shows good agreement with experimental values, however, data availability and quality are key for tuning the model accurately.

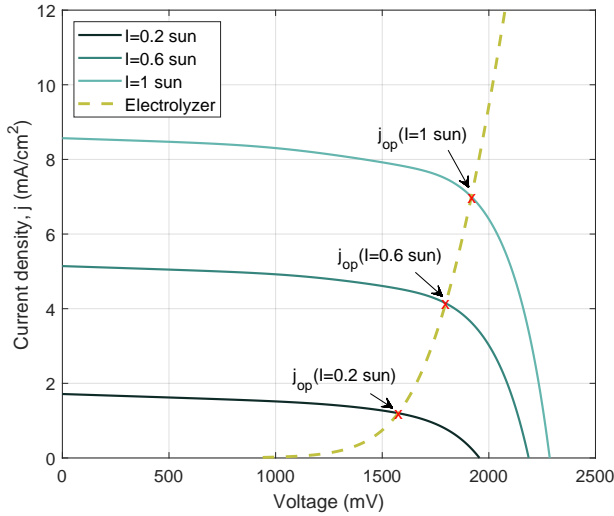


FIGURE 5.6: The effect of different illumination intensities for Urbain 2016 device as an example. The red x shows the operating point j_{op} of the solar cell and the electrolyzer.

PV-EC model for varying illumination and tilt angle

The model presented before was fitted using experimental data measured under artificial sunlight at standard condition, AM 1.5G and an illumination of $100 \text{ mW}\cdot\text{cm}^{-2}$ equal to 1 sun. However, PV-EC devices will hardly work under these conditions, and to reflect more realistic performance and predict the yearly average STH efficiency, we need to include the effect of illumination as well as the influence of different tilt angles.

Solar illumination directly influences the photogenerated current j_L proportionally [213]:

$$j_L = \frac{\hat{j}_L \cdot P_{\text{sun}}}{\hat{P}_{\text{sun}}} \tag{5.12}$$

where \hat{j}_L is the nominal photogenerated current as calculated under $\hat{P}_{\text{sun}}=1$ sun illumination and P_{sun} the real illumination. As shown in Figure 5.6 for Urbain 2016, a new operating point (j_{op}) on the j-V plane is established for every value of j_L . In real application, j_{op} becomes a time-dependent value. As a result, the matching between photoabsorber and electrolyzer needs to be resolved at any time instant

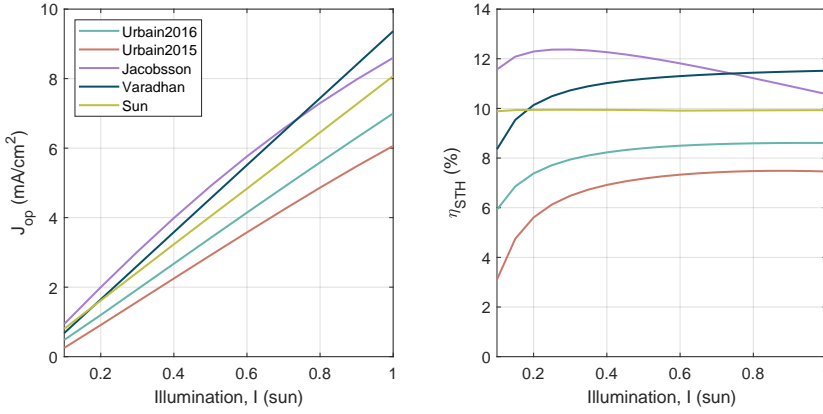


FIGURE 5.7: The effect of different illumination intensities on a) the operating point j_{op} between the PV cell and the electrolyzer, and b) the STH efficiency of the five PV-EC devices.

(i.e. for different irradiation values). When comparing all devices considered in this work for different irradiation values (see Figure 5.7 a) we note that, while Varadhan’s device achieves highest j_{op} and STH efficiency at 1 sun, Jacobsson’s device is the most performing for $P_{sun} < 0.7$ sun. This stems from the current density of the PV cell, which is higher compared to the other devices. On the other hand, Sun’s device shows the most stable performance, since its STH efficiency remains almost constant over the whole illumination range. The high efficiency is due to the InGaP/GaAs tandem-junction, which provides a sufficiently high voltage to drive the watersplitting reaction. The efficiency curves of Urbain 2015 and Urbain 2016 show the same trend as the Varadhan device: the higher the illumination the higher the STH. In order to understand on an yearly base what device is the most performing, a time-discretized analysis is required.

5.3 COMPARISON OF PV-EC CELLS UNDER VARYING WORKING CONDITIONS

In this section, we compare the different devices with regards to their yearly performance under varying time- and space-dependant illumination, and tilt angle. While we do not directly compute H₂ costs, which are highly uncertain and out of the scope here, we compare the devices using the specific area a (in m²/t_{H₂}), i.e. the cell area needed to produce one ton of H₂ per year. This is a proxy for the system cost and it embeds the thermodynamic performance of the device throughout the year. The cell area a can be derived from the amount of energy stored as hydrogen molecules

over the year per square meter of photoabsorber collector area, $e_{\text{H}_2}^{\text{year}}$ (kJ/(m² year)), according to Equation 5.13:

$$a_{\text{H}_2}^{\text{year}} = \frac{\Delta \bar{G}_{\text{H}_2}^0}{e_{\text{H}_2}^{\text{year}}} \quad (5.13)$$

where $\Delta \bar{G}_{\text{H}_2}^0$ the Gibbs free energy of the water splitting reaction ($\Delta \bar{G}_{\text{H}_2}^0 = 118.6$ MJ/kg). Notably, $e_{\text{H}_2}^{\text{year}}$ depends on the solar energy input P_{sun} and on the STH efficiency η_{STH} of the device, where both P_{sun} and η_{STH} are time dependent. We can therefore write:

$$e_{\text{H}_2}^{\text{year}} = \int_{t_0}^{t_{\text{end}}} \eta_{\text{STH}}(t) P_{\text{sun}}(t) dt \quad (5.14)$$

Plugging in η_{STH} from Equation 5.11 in the expression above, and noting that we can include the time dependency via hourly-averaged values of j_{op} in combination with hourly data of solar irradiance (thus substituting the integral with an hourly-resolved sum over the hours of the year), Equation 5.14 can be rewritten as:

$$e_{\text{H}_2}^{\text{year}} = \sum_{i=1}^{i=8760} \bar{j}_{\text{op},i} E^{\circ} \eta_{\text{F}} \quad (5.15)$$

where $e_{\text{H}_2}^{\text{year}}$ is here provided in (kWh). This expression, in combination with irradiance-dependent modelling of the PV-EC cell, allows for calculating the performance of the cell with real-world, space-defined, data and tilt angle. Note that the tilt angle, which for PV applications is typically a design variable that can be freely optimized, it is here bounded by the fluid dynamic within the PV-EC cell: while vertical modules allow for a straightforward gas/liquid dynamic they are penalized from a tilt angle perspective. The contrary holds for horizontal panels. In this work, we consider two different locations as possible PV-EC sites: Sevilla in Spain (with high illumination), and Utrecht in the Netherlands (with lower illumination). The solar irradiance data, more precisely the global horizontal irradiance, in Sevilla and in Utrecht was obtained from Solcast with an hourly resolution for 2019 [214]. Starting from these data, the effect of the tilt angles (in the range of 0 to 90°) was included applying the System Advisor Model (SAM) from the National Renewable Energy Laboratory (NREL) [215]. The azimuth angle was instead kept constant at 180° as well as the temperature of the system. The performance of catalysts and electrolytes were considered independent of the illumination, i.e. no electrodes degradation as function of sunlight were considered [216].

Figure 5.8 shows the daily average η_{STH} for hours with irradiance larger than 0 over the full year. This figure was obtained with Urbain 2016 as exemplary device,

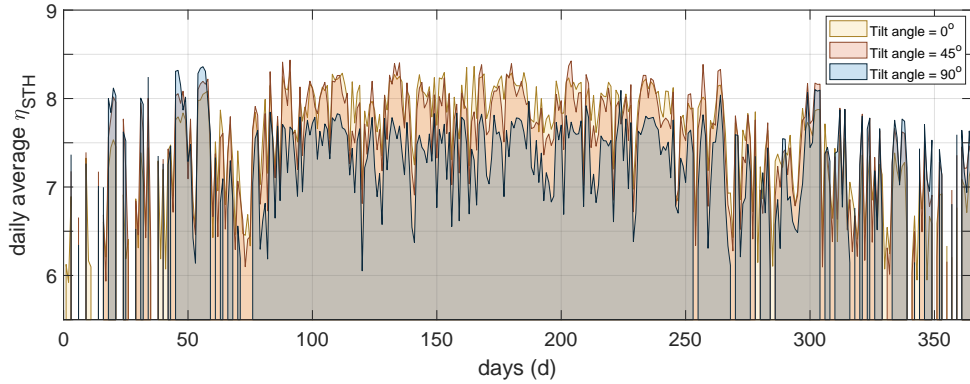


FIGURE 5.8: Average daily STH efficiency over the year for Utrecht using the Urbain 2016 device at different tilt angles (blue for 0° , red for 45° , and yellow for 90°). Change: different order: 90 at the back, 0 in front.

which can reach an efficiency in the range of $\eta_{\text{STH}}=5.9\text{-}8.6\%$ (Figure 5.7). Moreover, three different curves for three different tilt angles are shown (0 , 45 , and 90°). The yearly trend is as expected for any photovoltaic device: the maximum production is reached in summer and the minimum in winter. However, the height of the maximum in summer and the extent of the valley in winter depends on the tilt angle: while low tilt angles favor the maximum STH efficiency in summer, a vertical device has overall a more constant production through the year. Notably, only a minor difference exists between tilt angles in the range $0\text{-}45^\circ$. However, it is worth stressing that tilt angles between $0\text{-}15^\circ$ would be challenging from a practical point of view, as the produced gases would tend to diffuse through the device rather than being collecting because of natural buoyancy. On the other hand, increasing the tilt angle is overall conducive to a lower average STH efficiency throughout the year, although it has a minor impact: for a tilt angle of 60° , the average STH efficiency decreases of about 0.5% compared to a horizontal panel. Finally, it can be noted that the daily STH efficiency is often lower than the STH efficiency measured under one sun constant illumination.

It is important to stress that we do consider the working hours for the calculation of the average η_{STH} . Therefore, effects of shading are not included in our analysis. These effects are dependent on the specific design of the cell, especially on the EC part, and can be an important source of decrease. However, adapting our model to include this effect is out of scope of the present study.

The specific area a for H_2 production brings eventually together all dependencies in one parameter. Figure 5.9 shows a for the different devices considered here, at

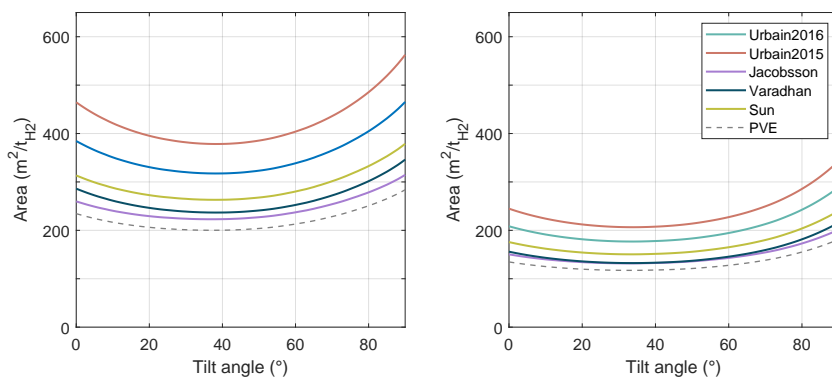


FIGURE 5.9: Specific area a for the 5 PV-EC devices and a PV-E device dependent on the tilt angle (tilt = 0-90°). a) Utrecht. b) Sevilla. The azimuth angle is fixed at 180°.

varying tilt angle and location (Utrecht on the left and Sevilla on the right). Moreover, we benchmark the 5 PV-EC devices with the standalone PV panel + electrolyzer configuration (PV-E), which was calculated using data published by Clarke et al. [217]. The minimum specific area a is found at an angle of around 40°, which can be directly correlated to the profile of the irradiation intensity (maximum at also around 40°). When changing the azimuth angle, the optimum changes slightly. It can be noted that the area requirement for the PV-EC cell is always larger than the PV-E system. However, Jacobsson and Varadhan devices perform close to the reference system; they therefore show rather clearly the preferred direction of PV-EC development (as far as costs are excluded).

When comparing the two locations, and since the total energy input in Utrecht (3.8 GJ/m²) is roughly half of that in Sevilla (6.8 GJ/m²) during the same year, a is in general clearly higher in Utrecht. The associated operating hours amount to 3767 hours in Sevilla and 3034 hours in Utrecht. The distribution of the STH efficiency in Utrecht and Sevilla for the whole year can be found in the Supplemental Information in Figure D.5.

For both locations, the rank order of the PV-EC devices is the same, with Urbain 2015 requiring the largest surface area and Jacobsson the smallest. The ranking is a result of the dependency of the STH efficiency on the illumination intensity shown in Figure 5.7 b. Having the highest efficiency, the PV-E device shows the best performance.

A summary of the effect of location and its comparison with the ideal one-sun conditions is shown in Table 5.5 for a fixed tilt angle of 60°. While the Varadhan device

TABLE 5.5: Specific area a and average STH efficiency based on the solar irradiance data of 2019 in Utrecht, Netherlands, and in Sevilla, Spain with a tilt angle of 60° . The STH efficiency under 1 sun is also reported for comparison purposes. For very low illumination intensities inferior to 0.1 sun, the model assumes no output. The PV-E device was calculated using data from [217].

	Utrecht		Sevilla		η_{STH}
	Area m^2/t_{H_2}	Average η_{STH} %	Area m^2/t_{H_2}	Average η_{STH} %	1 sun %
Urbain 2015	544	5.79	227	7.18	7.5
Urbain 2016	450	7.50	195	8.40	8.6
Jacobsson	309	12.33	143	11.43	10.6
Varadhan	335	10.26	146	11.24	11.6
Sun	367	9.94	165	9.93	9.93
PV-E	213	13.28	135	12.81	12.1

has the highest efficiency under one-sun illumination, the Jacobsson device reaches a higher average efficiency, especially for Utrecht. This is because the Jacobsson cell shows its best performance for an illumination intensity of around 0.2 sun (5.7 b) and the average illumination in Sevilla is 0.50 sun, compared to 0.35 sun in Utrecht (in 2019, but generally valid). Therefore, the Jacobsson system is relatively more efficient in Utrecht than in Sevilla, whereas the Varadhan device performs well under high illumination, and has poor performance in Utrecht. On the other hand, the average STH efficiency of the Jacobsson and Varadhan device are similar in Sevilla, resulting in a similar specific area (Figure 5.9). This analysis shows that different PV-EC devices might be optimal for different locations irrespective of their efficiency under one-sun conditions, and that real operating conditions (time- and space-dependent) are required to fairly compare devices. Overall, PV-EC development should target real world varying conditions: High STH efficiency under ideal illumination does not fully reveal the cell performance.

At the same time, it is worth stressing that the model presented here provides only a first approximation of the behaviour of the system under real-world conditions. In addition to varying irradiation, the ambient temperature should be included as it has a significant impact on the performance of PV-EC devices (it influences both the solar cell, increasing the thermal voltage V_{th}), and the electrolyser, whose potential decreases significantly with the temperature [216]). Moreover, aging and performance decay should also be included for a full evaluation. These effects will

however further exacerbate the dependency of the device on the ambient conditions, making the evaluation under non-ideal conditions even more necessary.

5.4 CONCLUSION

In this chapter, a simple, yet insightful, framework to model photo- electrochemical water splitting devices using an equivalent circuits approach is presented. In the first part, we derived the model equations, described the resolution strategy and validated the model with existing experimental data for ideal one-sun conditions. To this end, current density-voltage data for five different devices were used, where the devices were selected depending on the quality and type of experimental data available. The model showed good agreement with the experimental results. Within the limits of the model, we also tried to provide a physical explanation of the different performance as function of the cell materials and design.

To extend the model to real operating conditions, we presented a simple modification of the model that takes into account real irradiation data. The five devices were therefore compared at varying irradiation: Three of the five devices showed an optimal STH efficiency for ideal illumination, one showed rather constant STH efficiency, while one showed an optimal efficiency for low irradiation, i.e. 0.25 sun. Moreover, the most performing device varies depending on the irradiation.

In the second part of the chapter we used the developed irradiation-dependent model to evaluate the yearly performance of the considered cells at different tilt angles and different locations, i.e. (i) Sevilla in Spain and (ii) Utrecht in the Netherlands. The cells were therefore compared using the specific area needed to produce 1 ton of hydrogen per year. We were able to identify the cell type with lower specific area; moreover we found that irrespective of the cell a tilt angle in the range of $10\text{-}30^\circ$ and $25\text{-}45^\circ$ is optimal for Utrecht and Sevilla, respectively.

Overall, the presented model is a powerful tool for untangling PV-EC performance and comparing different concepts. The availability of high quality experimental data remains however a key requirement for the use of this model.

RENEWABLE HYDROGEN PRODUCTION: A TECHNO-ECONOMIC COMPARISON OF PHOTOELECTROCHEMICAL CELLS AND PHOTOVOLTAIC-ELECTROLYSIS

This chapter reports a techno-economic analysis of two solar-assisted hydrogen production technologies: a photoelectrochemical (PEC) system and its major competitor, a photovoltaic system connected to a conventional water electrolyzer (PV-E system). A comparison between these two types was performed to identify the more promising technology based on the levelized cost of hydrogen (LCOH). The technical evaluation was carried out by considering proven designs and materials for the PV-E system and a conceptual design for the PEC system extrapolated to future, commercial scale.

The LCOH for the off-grid PV-E system was found to be 6.22\$/kg_{H2}, with a solar to hydrogen efficiency of 10.9%. For the PEC system, with a similar efficiency of 10%, the LCOH was calculated to be much higher, namely 8.43\$/kg_{H2}. A sensitivity analysis reveals a great uncertainty in the LCOH of the prospective PEC system. This implies that much effort would be needed for this technology to become competitive on the market.

Therefore we conclude that the potential techno-economic benefits that PEC systems offer over PV-E are uncertain and, even in the best case, limited. While research into photoelectrochemical cells remains of interest, it presents a poor case for dedicated investment in the technology's development and scale-up.

The results presented in this chapter have been reported in: Grimm, A., de Jong, W. A., Kramer, G. J., Renewable hydrogen production: A techno-economic comparison of photoelectrochemical cells and photovoltaic-electrolysis. *International Journal of Hydrogen Energy* 45, 22545 (2020).

6.1 INTRODUCTION

Since the pioneering work of Fujishima and Honda [218] using a TiO_2 photoelectrode coupled with a platinum cathode to describe the photoelectrochemical (PEC) water splitting process nearly five decades ago, extensive efforts have been made to construct efficient photocatalyst systems for solar energy utilization. Most literature focuses on the selection of a suitable material, since it strongly determines the system efficiency; especially the choice for the photoelectrode and for catalysts is of importance [183]. In addition, some laboratory-scale experiments have been carried out to improve the solar-to-hydrogen efficiency [219]. A summary of the latest developments within research on photoelectrochemical cells can be found in [220, 221]. Most literature that focuses on economic evaluation does usually not compare different technologies and therefore concentrates either on solar-driven water electrolysis (PV-E) or PEC systems [222–226]. For example, a detailed techno-economic analysis by the US Department of Energy (DOE), which represents a key reference of the present analysis, gives a detailed overview over four different types of PEC systems [223].

Another key paper is by Shaner et al., who compared two different PEC systems and two types of PV-E systems regarding their technical and economic viability. The results show a lower levelized cost of hydrogen (LCOH) for the PEC system than for the off-grid PV-electrolyzer. However, the cost calculation of some major components of the PEC system were based on commercial PV parts and commercially available electrolyzers, which can be quite different from a real PEC system in which both parts are integrated in one device. In addition, strong cost reduction has occurred since their publication, especially for the PV panels, which makes new research necessary.

Despite intense and promising research during the last years on PEC technology, no system is yet commercially available. In this chapter we will analyze if, and under what conditions, PEC devices can outcompete solar hydrogen production through PV-electrolysis. It builds on the research of [227] and [223], taking into account new developments and details within these technologies.

6.2 METHODOLOGY

The assessment of the hydrogen production technologies includes a technical and an economic evaluation. The latter is based on the results from the technical system analysis, which was carried out by performing a broad review considering relevant literature published from 2014 to the present time. The results are described in detail in section 6.3.

To compare the economic appeal of the two hydrogen production technologies, the levelized cost of hydrogen (LCOH) in \$ per kg was calculated. It reveals the price of hydrogen which the system needs to reach, in order to achieve a desired return on investment. The LCOH includes investment expenses as well as revenues and expenditures during the plant's lifetime, discounted to a reference date. It is calculated by dividing the present value of all expenses by the present value of hydrogen generation, resulting in

$$\text{LCOH} = \frac{I_0 + \sum_{t=0}^n \frac{OM_t + F_t}{(1+r)^t}}{\sum_{t=0}^n \frac{H_t}{(1+r)^t}}, \quad (6.1)$$

where I_0 represents the initial investment in year t , OM_t the annual costs for operation and maintenance, F_t the annual fuel costs, H_t the hydrogen production (kg_{H_2}) and r the real discount rate [228].

The total system costs were calculated using a bottom-up costing method. First, a selection of the relevant components and cost parameters was carried out. Subsequently, the total project costs were calculated. For both technologies, the capital expenditures C_{CAPEX} are comprised of the module itself C_{module} and the balance of system (BoS) costs C_{BoS} in the form of

$$C_{\text{CAPEX}} = C_{\text{module}} + C_{\text{BoS}}. \quad (6.2)$$

BoS costs can then be divided into a hard- and soft-BoS share. The former includes wiring, mounting, the inverter and land acquisition, while the latter is composed of non-material costs such as permits and installation. Due to economies of scale, the BoS costs vary with the size of the plant and are also dependent on the maturity of the observed technology.

Table 6.1 presents a summary of the baseline assumptions for the economic analysis. The production rate of the systems was set to $10 \text{ t}_{\text{H}_2}/\text{day}$, a scale similar to other techno-economic reports discussing photoelectrochemical water splitting [223, 227] and typical of the today's project size, and a scale at which the benefits of scale-up have leveled off, beyond which point cost reductions should come from mass manufacturing of MW-sized units. The scope of the analysis is 20 years, which is a common period for techno-economic analyses [223, 224, 227, 229, 230]. A longer lifetime might be interesting, too, since some elements like PV panels are expected to have a longer lifespan (25 years [231]). However, this will increase uncertainties about costs of other system components. The geographical location has a great impact on the economic viability of the system and is adopted from [223], who assumed the location to be in the USA, in Daggett, California. The site is used for solar measurements and provides an average daily irradiance of $6.19 \text{ kWh}/\text{m}^2/\text{day}$.

TABLE 6.1: Summary of the assumptions required to carry out the economic analysis for the considered PEC and PV-E systems.

Parameter	unit	Value	Source
Hydrogen production rate	t _{H₂} /d	10	[223, 225, 227]
Economic lifetime	years	20	[223, 224, 227, 229, 230]
Construction period	years	1	[223]
Operating capacity factor	%	90	[223]
Inflation rate	%	1.9	[223, 227]
Real discount rate	%	12	[227]
Average labor rate for staff	\$/h	25	[232]
Land cost	\$/m ²	0.15	[223]
Average solar irradiance	kWh/m ² /d	6.19	[223, 226]
Installation	% of hard BoS	20	[223, 225]
Engineering and design	% of hard BoS	5	[223, 225]

The operating capacity factor takes into account planned and unplanned outages and represents the actual work performed in relation to the maximum work which can theoretically be performed. A factor of 90% is chosen, which is similar to the value in [223]. All economic conjectures are drawn upon values from the U.S market and refer to the year 2017, and it is assumed that the investment occurs within a one-year construction time period. The installation costs are assumed to be 20% of the capital costs, which is a value similar to [223, 225]. It is assumed that these costs are the same for both systems. The installation of the PV-E systems requires more cabling and the installation of the electrolyzers. The PEC system on the other hand requires more piping and in addition the installation of the compressors. Again, for engineering and design, the same value is used for both systems, namely 5% of the capital costs which is in the same range as the assumptions made in [223, 225]. In addition, the production of high purity oxygen by-product is vented to the atmosphere and no cost credit is taken into account.

Sensitivity analysis. Since PEC systems are not yet commercialized, the costs estimated in the economic analysis are subject to various assumptions and to a high degree of uncertainty. Therefore, a sensitivity analysis is carried out by including the components and parameters with the greatest influence on the total costs. Generally, it can be assumed that costs for the technologies will decrease over time due to

improvements in technology, new developments and a growing demand on hydrogen. In addition, for the analysis of the PV module, learning curves are used to estimate further potential.

6.3 COMPONENT-LEVEL TECHNICAL ANALYSIS AND COST ASSESSMENT

This section provides the basis for our comparison, starting with an outline over the chosen system designs and the selected components. The second part covers the economic evaluation of the two technologies and this forms the starting point for the calculation of the LCOH.

Technical evaluation

To begin with, a technical analysis was carried out on the basis of a literature study and state of the art technology. For the PV-E system, approved designs and materials were studied. The PEC technology, on the other hand, needs to be examined more closely since a reliable system is not yet available on the market; for example, for some components a better and more stable material needs to be found.

To describe the performance of the technologies, the solar to hydrogen efficiency is used. This parameter is defined as the chemical energy of the produced hydrogen divided by the solar energy input in the form of

$$\eta_{STH} = \frac{m_{H_2} \Delta G}{P_s A_e} \quad (6.3)$$

where m_{H_2} represents the hydrogen production rate (kg/s), ΔG is the change in Gibbs free energy per mol of H_2 (at 25°C $\Delta G=237$ kJ/mol), P_s the solar energy input (kWh/m²) and A_e the illuminated photoelectrode area (cm²) [233].

6.3.0.1 *The PV-E system*

The components of the PV-E system were chosen by considering technical properties and examining current prices for photovoltaic modules and electrolyzers. Since a PV-E system consists of two separate parts, namely the photovoltaic module and the electrolyzer, they are outlined separately. Electrolyzers can produce pressurized H_2 at 30 bar and therefore no compressors need to be added to the overall system [234]. Using these results, an optimization of the PV-E system was performed, which reveals an ideal weighting between the two devices.

Photovoltaic-system. The selection of the photovoltaic system is based on literature analysis and on analyzing the current PV market, which is currently dominated

by crystalline silicon (c-Si) PV cells with commercial efficiencies of up to around 24 % [235]. Silicon is the current standard material used in industry because of its relatively low cost as well as good efficiency, steadiness and durability. Since this type has some drawbacks, such as an energy intensive production and a relatively low theoretical efficiency [236], other types like multi-junction solar cells or CdTe (Cadmium telluride) thin film panels were included in the analysis. However, most technologies are not yet commercially available or need a large scale-up. In addition, an increase in efficiency is often accompanied by higher costs, while cheaper technologies are frequently less efficient and lack durability [236]. Hence, in this research a crystalline silicon single-junction panel was chosen with an efficiency of 18%.

Electrolyzer. Compared to PV panels, the market for electrolyzers is relatively small and is developing more slowly. At present, the alkaline electrolyzer is the current standard technology on the market, and is considered to be technically mature [237]. With a moderate efficiency of 59-70 % [237] and relatively low system costs in the range of 860-1240\$/kW it is favoured in most industrial sectors [238]. Besides alkaline systems, the proton exchange membrane (PEM) electrolyzer represents another emerging technology with efficiencies up to 80-90% [239]. It is also commercially available but more expensive (around 1350-2200\$/kW) and produced in lower quantities [238].

Alkaline electrolyzers have major issues with intermittent and fluctuating power sources, such as cross-diffusion of the product gases under low system loads, a slow start-up as well as a slow loading response [222, 240, 241]. Compared to alkaline systems, PEM water electrolysis is more suitable for the coupling with a PV system. Its flexibility to handle fluctuating input currents and the expectation of large cost reduction in the future will make it a good choice for a combined system [217, 222, 230, 242].

Combined PV-E system. To match the output voltage of the PV system and the voltage of the electrolyzer at its design point, in general a DC-DC converter is needed. However, when using a PEM electrolyzer, a converter is not necessarily required [242], since the loss caused by non-optimal operation is expected to be the same as the loss due to the use of a DC-DC converter [217, 227]. Therefore, a moderate efficiency for the electrolyzer of 61% is chosen, which is lower than the typical efficiencies of PEM electrolyzer in the range of 65-83% [243]. In addition, the electrolyzer does not require a transformer and rectifier, because the PV module delivers direct current.

Scaling the electrolyzer to the maximum power output of the PV plant results in a low capacity factor for the electrolyzer. Since the electrolyzer costs represent a considerable part of the overall costs, an optimization between the scale of the

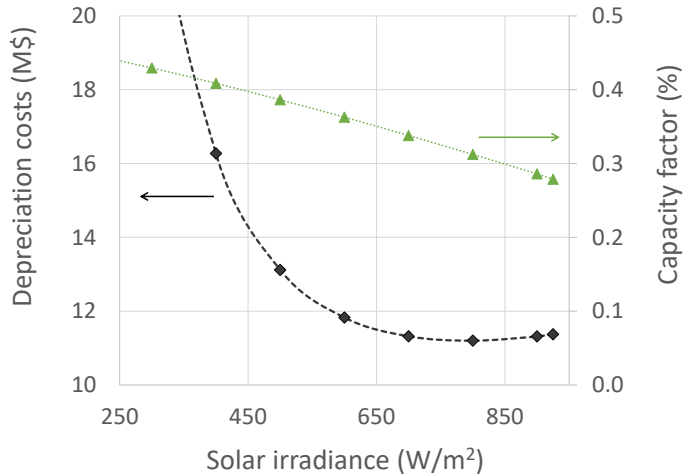


FIGURE 6.1: Resulting curves obtained by optimizing the ratio between the area of the PV panels and the electrolyzer units for the PV-E system. The upper bound of the solar irradiance was given by $P_{S,max} = 925 \text{ W/m}^2$. The black curve shows an optimal design point at around $P_{S,design} = 800 \text{ W/m}^2$, at which the total depreciation costs are lowest. The green curve shows the capacity factor of the electrolyzer.

photovoltaic system and the electrolyzer unit was performed, to find an ideal balance between these two technologies. A detailed description of the optimization can be found in the Supporting Information.

Figure 6.1 presents the resulting curve obtained by the optimization. It reveals an ideal operating point at which the area of the PV panels is designed for a maximal solar irradiance of $P_{S,design} = 800 \text{ W/m}^2$. This leads to an increase of the PV capacity by 4% and a reduction of the electrolyzer size by 11% compared to a design point at $P_{S,max} = 925 \text{ W/m}^2$. As a consequence, the capacity factor of the electrolyzer increases by 3%-points, up to 31%.

6.3.0.2 The PEC system

There exist roughly 30 design alternatives for PEC water-splitting devices [225] with no clear favorite so far. This large amount of design possibilities makes it difficult to strictly separate the PEC system from PV-E systems, as it creates a seamless transition between these two technologies [219]. Therefore, a detailed technical analysis was carried out, starting with a selection of a specific PEC type, followed by a thorough assessment of the main components through analyzing essential properties, i. e. efficiency, lifetime and potential productivity. The selection of the components was

mainly based on a detailed DOE-report by James et al., supplemented and adjusted by updated data amongst others found in [225, 227].

Panel based design. Among the different design possibilities for PEC systems, a non-concentrated panel based layout was selected (similar to type 3 mentioned in the DOE report). A panel design is a more mature design choice compared to solar concentrator systems, which can increase the light intensity. It is similar to a PV panel and absorbs photons to generate electrons for the electrolysis. The electrodes are in direct contact with the electrolyte, generating oxygen gas at the anode and hydrogen at the cathode. The panels are most likely composed of a multi-junction photon absorber to provide sufficient voltage for the reactions. Another design possibility, frequently mentioned in literature, is a PEC system based on nano particles, which tends to be much cheaper [223]. However, an explosive gas mixture is created, which should be avoided due to safety issues and system complexity in terms of additional product separation. In addition, not much research has been done on this type and therefore the existing data is subject to high uncertainties. By comparison, the development in terms of technology readiness level (TRL) and efficiency as well as durability is more advanced for the panel based design [225, 244]. Furthermore, more possible design configurations exist for this type and a broader material portfolio is available.

One liquid-solid-junction. In general, there exist three possible design configurations within the panel based type [183]. First, a zero liquid-solid-junction design, within which the photoactive part is not exposed to the corrosive environment caused by the electrolyte. Since this type of set-up has more similarities with a PV-E system instead of an integrated PEC device, it is not further considered in this analysis. Second, a one liquid-solid-junction design, where one side of the photoelectrode is immersed into the electrolyte. Finally, a system with two-liquid-solid-junctions.

In our work the second alternative was chosen, which is schematically shown in Figure 6.2. One part of the solar panel must withstand electrochemical reactions and corrosion, while the other side is in contact with ambient air. So far, a solar to hydrogen (STH) efficiency of 16.2% has been achieved by using this layout [244].

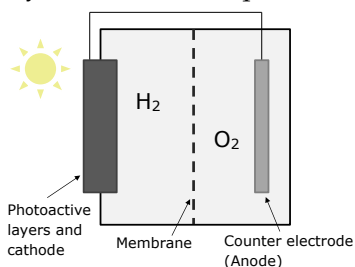


FIGURE 6.2: Schematic illustration of the selected PEC cell.

Compared to the two liquid-solid-junctions, the lifetime can be extended and the

material selection is simplified, which makes it more likely for this configuration to become a stable low-cost system [183, 225].

No external bias. Furthermore it was assumed that the system operates spontaneously and does therefore not require an external electrical bias.

Material selection. The choice of the photoactive material has a significant impact on the efficiency and the lifetime as well as the costs of the PEC system. The photoactive layer consists of a doped semiconductor which absorbs photons and therefore generates a charge separation. Most of the materials in literature are based on thin film technology [183, 223–226, 244]. For the production of hydrogen a voltage of approximately 1.65 V needs to be provided by the cell, to run the HER, OER and make up for additional losses (overpotential) [245]. Since a high output voltage is often accompanied by the ability to use only a small part of the solar spectrum, multi-junction cells are preferred. Triple-junction amorphous Si is one of the promising photoactive materials for PEC cells [183, 224, 226, 246] and was chosen in this work. Other possible materials, e.g. GaAs/GaInP with efficiencies of more than 16,2 % STH [247], were not considered any further since their costs are still too high. The assumed efficiencies for a-Si cell found in literature varied a lot depending on their source, with a resulting range of close to zero to 15 % STH [225, 248, 249]. In this work we chose an efficiency of 10 % which is assumed to represent a realistic value compared to the majority of the considered literature [183, 223, 224, 226]. This is also in line with data found in [226], where the STH efficiency for PEC cells is assumed to be limited to 75-80% of efficiencies for PV cells. For the anode/counter electrode, which promotes the oxygen formation and can be directly attached to the housing of the PEC cell, there are various possible materials like stainless steel, RuO_x with *Pt* gauze or Nickel [225, 226, 244]. Most relevant literature is based on the latter, which is also chosen in this work. For the membrane we chose the same as in [225], which is an anion exchange membrane with the commercial name Nosepta® [225, 250]. The most common material for the membrane is Nafion [227] therefore it is also considered in our analysis. The area of the membrane is assumed to be 10 % of the PV panel area [245].

Economic evaluation

Based on the results of the technical analysis, the following section summarizes the economic evaluation needed to calculate the levelized cost of hydrogen.

PV-E system

In Table 6.3 the specific parameters for the analyzed PV-E system are shown along with its capital expenses. A more detailed distribution of the cost components can

be found in the Supporting Information in Table S1. The costs for the PV module, based on a crystalline silicon panel with an efficiency of 18%, were estimated to be $0.30 \$W^{-1}$ [251]. The solar collection area was calculated by using Equation 6.3 together with the efficiency of the overall PV-E system. The area of the whole PV-E plant is 4.07 times the PV surface area, including e.g. the electrolyzer and the control system. This factor was taken from [223], since we assumed the additional are to increase similar to the total plant area of the PEC system. In this analysis no inverter is included, which is already mentioned earlier while describing the technical analysis. For the PEM electrolyzer no transformer and rectifier is required since the PV panels deliver direct current. The costs for the stack were estimated to be $0.40 \$/W^{-1}$ with an efficiency of 61% [252]. The lifetime of the electrolyzer stack is estimated to be 7 years [227] and the replacement costs for the stack decrease every period, based on learning curves, and were assumed to be 75% of the initial costs after 7 years and 60% after 14 years, respectively. The PV module was assumed to last the whole lifetime of 20 years of the plant. Additional costs e.g. for permit and site preparation, are added with a factor of $5 \$/m^2$ to the calculation which is in line with recent data from [231].

TABLE 6.3: Summary of technical parameters and respective costs for the main components for the considered PV-E system.

	Value	Source
Photovoltaic system		
Efficiency	18 %	[251]
Photovoltaic area	$4.8 * 10^5 \text{ m}^2$	
PV module	0.30 \$/W	[251]
Mounting material	0.08 \$/W	[231]
Wiring	0.09 \$/W	[231]
Electrolysis system		
Efficiency	61 %	[252]
Stack cost	0.40 \$/W	[252]
Hard BoS	0.375 \$/W	[252]
Combined PV-E system		
Efficiency	10.9 %	
Process contingency	20 % of direct costs	[223, 225]
Other soft-BoS	5 \$/m ²	[231]

PEC system

Table 6.5 shows the technical parameters and capital expenses for the main components of a PEC system at commercial scale. In Table S2 a more detailed cost overview can be found. For the costs of the photoactive component 45 \$/m² was estimated. Although some previous reports worked with a more optimistic value of 15 \$/m² [223, 225], a more pessimistic and, in our opinion, more realistic value was used for the calculation. The costs for glass were estimated to be 10 \$/m². We assumed this value to be higher compared to PV systems (5 \$/m² [227]), since the surface is not fully connected to the back side of the housing and therefore needs to be more rigid to give structure to the cell.

The membrane was included with a cost factor of 50 \$/m² [227] which is expected to decrease significantly when produced in large scale [223]. For the housing costs of 20 \$/m² were assumed to be realistic. Compared to PV systems (\approx 5 \$/m²) these costs are higher, since PEC cells set higher demands like a better resistance to the electrolyte as well as a greater stability for the membrane. This value resembles other assumptions in literature [223, 225]. For the whole PEC module the resulting costs are 153.7 \$/m² which corresponds to approximately 1.01 \$/W. In addition to the module costs, a gas processing system comprising two-stage gas compressors [223, 227], piping, condensers and intercooling, as well as water management and system controlling are included by using data published in the DOE analysis [223]. For the contingency a percentage of 30 % of the uninstalled costs was estimated, since PEC systems represent a less mature technology compared to the PV-E system. It should be noted that this study does not take a costs credit for the byproduct O₂ into account, which is generated during the reaction. Finally, the replacement of the PEC cell was expected to be performed every 7 years and the costs for a PEC cell were assumed to decrease alike the electrolyzer by applying learning curve theory.

6.4 RESULTS AND DISCUSSION

PV-E system

The techno-economic analysis of the photovoltaic-electrolysis system results in a LCOH of 6.22 \$/kg_{H₂}. Figure 6.3 shows the breakdown of the overall costs; more details can be found in Table S1. The first three bars reveal the distribution of the costs for the PV-E system in \$ per kg_{H₂}. For the first and second bar, the costs are broken down into the PV and electrolyzer part respectively, to show the ratio between these two parts. The costs for the electrolyzer are higher than the costs for the PV system, namely 3.92 \$/kg_{H₂} compared to 2.30 \$/kg_{H₂}, respectively. This gap is even larger without optimizing the scale of these two plant components. Through

TABLE 6.5: Summary of technical parameters and respective costs for the considered PEC system. More details for the specific costs can be found in the Supporting Information

	Value	Source
Efficiency	10 %	[183, 223, 224, 226]
PEC area	$5.3 * 10^5 \text{ m}^2$	
Module	153.7 \$/m ²	
Hard-BoS	46.0 \$/m ²	
Soft-BoS	115.2 \$/m ²	
Process contingency	30 % of direct costs	

optimization, more PV panels were added to decrease the number of electrolyzer units, which led to an increase in the capacity factor from 28 % to 31 %. Consequently, the area of the photovoltaic panel increased by 4 % while the size of the electrolyzer section was reduced by 11 %. It is likely that the BoS costs of the electrolyzer will experience a significant decline within the next few years since there is room for economies of scale and therefore the production volume can still be increased largely. The third bar reveals the overall system costs, showing that the module costs make up a large part of the costs.

To identify the potential of the PV-E system, a closer look is taken at future costs for the PV module and the electrolyzer unit. A possible decline of the PV module and hard-BoS costs of approximately 50 % in 10 years is assumed by the ITRPV report [231]. For the future costs of the electrolyzer stack a reduction to 148 \$/kW can be expected, adopted from [230]. When including these optimistic assumptions into the cost calculation, a possible LCOH of 3.76 \$/kg_{H₂} can be achieved.

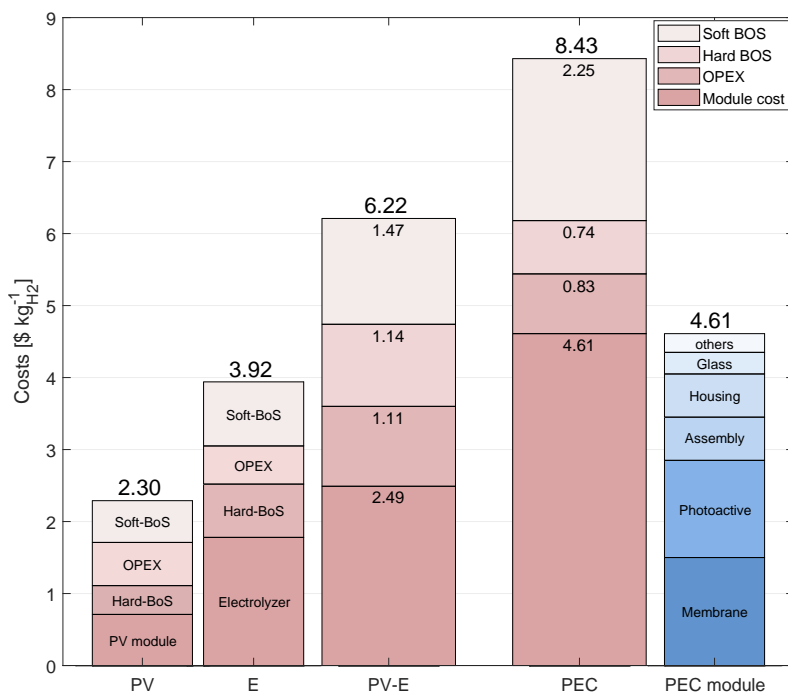


FIGURE 6.3: Breakdown of the costs for the photovoltaic system and the electrolyzer unit as well as the overall costs for the combined PV-E system and the integrated PEC system (brown bars), divided into the module costs, the OPEX as well as the hard- and soft-BoS costs, respectively. In addition, a detailed cost breakdown of the PEC module costs (blue bars).

PEC system

The LCOH for the PEC system is calculated by 8.43 \$/kg_{H2}. The results are summarized in Figure 6.3, in the two bars on the right, and more detailed in Table S2. The first bar reveals the PEC module to be the main cost contributor, accounting for nearly half of the entire costs. This is followed by the soft-BoS costs, where the contingency costs have the biggest influence since the uncertainties are still quite high within this new technology. The bar on the right in Figure 6.3 shows a cost breakdown for the PEC module by oneself. The membrane and the photoactive material have by far the biggest influence on the costs, with 1.50 \$/kg_{H2} and 1.35 \$/kg_{H2} respectively.

Therefore, these two components were included in a sensitivity analysis to show their impact on the overall costs. However, many of the remaining costs are also marked by uncertainty, since PEC cells are not yet commercially build. Therefore, the allocation within this cost block can vary to a certain extend and some module components can even have more impact than expected in this research. The results of the sensitivity analysis are presented in Figure 6.4. For the membrane an optimistic value of $15 \$/m^2$ is estimated which is similar to a value provided by [225, 253]. The pessimistic value is assumed to be $300 \$/m^2$ for a mass-produced membrane. The membrane represents a large factor of uncertainty, even though a strong decrease is possible through mass production [230]. It should be noted that it is still an ongoing challenge to find a suitable and stable membrane. In our PEC design, which is based on the work by [225], a nafion membrane is selected which requires an acidic environment. Some earth-abundant catalysts, like in our case Nickel, are only stable in an neutral or alkaline environment. There are still challenges for the commercial implementation of the presented PEC design and there is a lot of ongoing research focusing on the development of stable membranes. For our techno-economic analysis, the choice of the parameters give a good depiction of the still uncertain profitability of a PEC system.

Starting with an initial value of $45 \$/m^2$ for the photoanode layer a high performance material, namely GaAs/GaInP, was selected for the highest costs. Assuming mass production, the costs were calculated to be $393 \$/m^2$ by using a simplified estimate with data found in [247] and [254]. For the optimistic scenario, $15 \$/m^2$ were chosen, which was found in [225]. From today's view it is a major challenge to find high performance materials which can be competitive on the market.

The preceding analysis of the PEC cell was carried out by using a STH efficiency of 10%. The optimistic case was conducted with an increase of the efficiency to 16.2%, which is to date the highest efficiency reached for a PEC cell and is achieved by [244] on laboratory scale. The pessimistic value was adopted by 5%. The resulting Figure 6.4 shows a strong and non-linear correlation of the efficiency and the LCOH of the system. An increase of the cell efficiency by 6%-points results in a decrease of approximately 25% of the overall costs. This indicates that high efficiencies are crucial for competitive PEC systems.

Another influential parameter is the lifetime of the PEC cell. The initial value is set to 7 years, which is similar to the stack of a PEM electrolyzer. This assumption is quite low compared to other components, since the degradation of the cell is high due to the presence of a corrosive electrolyte, even with the integration of a protective layer on top of the photoactive material. In addition, this value entails great uncertainty as there is no literature found which documents a duration of a PEC cell exceeding a few weeks. Nevertheless, other literature even suggest higher values for the lifetime [223, 225, 226]. The optimistic value was therefore chosen to be

12 years whereas for the pessimistic case 3 years was selected. Lifetime is important in order to achieve commercial success, but has a relatively small effect on the overall system costs, since it concerns mainly the cell component.

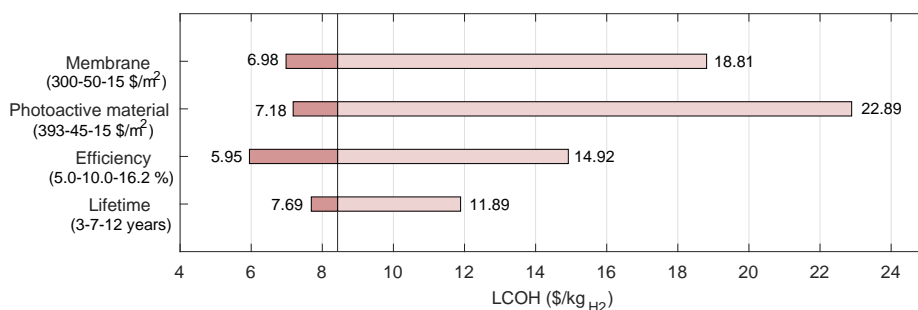


FIGURE 6.4: Sensitivity analysis for the PEC system on the basis of the costs for the membrane and the photoactive material as well as the efficiency and the lifetime of the whole plant. Each analysis represents the variation of a single parameter from the initial LCOH of 8.43 \$/kg_{H2} to a higher and lower value.

Comparison between PV-E and PEC

As shown in Figure 6.3, the estimated LCOH is significantly higher for the PEC system compared to the PV-E system with 8.43 \$/kg_{H2} and 6.22 \$/kg_{H2} respectively. The PV-E module costs account only for 40 % of the overall system costs compared to the PEC module which constitutes more than half of the overall costs. This can be explained mainly by additional components in the PEC device and more stringent requirements for the photoactive material. Another reason for the large influence of the PEC module on the overall costs is the relatively short lifetime of 7 years and complementarily the replacement costs, which applies also to the electrolyzer. The difference between the soft-BoS costs for both systems are, among others, the higher costs for contingency for the PEC system, which is due to greater uncertainties within this technology. The difference of the hard-BoS costs for the PEC and PV-E plant is because the PV-E system comprises two hard-BoS blocks, for the photovoltaic part and the electrolyzer. In addition, representing an integrated unit, less wiring material is needed for the PEC system.

In the present study we considered an off-grid PV-E system for the production of solar hydrogen. An advantage of this system is, that it has the possibility of connecting to the grid, resulting in a significant increase in the capacity factor of the electrolyzer. An approximate calculation by using data provided in [227] reveals a

LCOH of $4.17\$/\text{kg}_{\text{H}_2}$ for the grid connected device. It is important to stress that the produced hydrogen is then no more a solar hydrogen and not comparable to the PEC device, but shows the flexibility of the PV-E system.

The graph in Figure 6.5 shows the resulting LCOH and its uncertainty for the PEC system. The latter was calculated by combining the results of the sensitivity analysis outlined in the previous sections. Since the different parameters influences each other, the resulting range for the hydrogen costs takes on a huge value. The figure elucidates the high uncertainty of the considered parameters and highlights the great range of the LCOH for the overall PEC system. For an optimistic case the LCOH of the PEC-system can go down to $2.51\$/\text{kg}_{\text{H}_2}$. A PV-E system, on the other hand, can reach a hydrogen cost of $3.76\$/\text{kg}_{\text{H}_2}$. However, for a pessimistic view the costs of the PEC system can be more than ten times higher than the considered LCOH of $8.43\$/\text{kg}_{\text{H}_2}$. The probability that such high costs will incur is, as shown by the graph, almost zero. Still, the results reveal a huge range for the LCOH and since the PEC system is not yet mass produced, many assumptions are afflicted with high uncertainty.

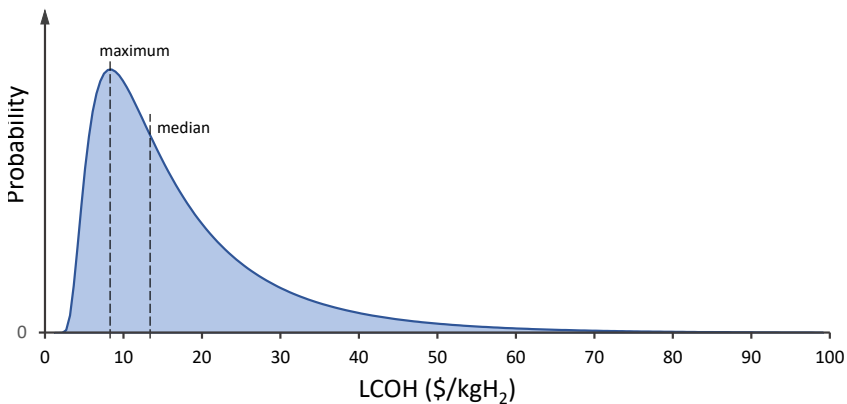


FIGURE 6.5: Schematic diagram illustrating the probability distribution of the LCOH for a PEC system using the results of the sensitivity analysis.

For the calculation of the land cost we included the same proportional increase of the solar collection area to get the overall plant area. For simplicity reasons, this proportional factor was assumed to be the same for both technologies. The land costs are a minor contributor to the overall costs, to be more accurate, a detailed analysis of the auxiliary devices needs to be carried out.

Since there is not much data available on long term degradation of especially the PEC module, we assumed that both systems run with maximal efficiency over the

whole lifetime. Therefore we assumed that the cell performance does not degrade over time and also for the other components no degradation occurs over the lifetime.

It should be noted that the precise location of the plants has a significant influence on the LCOH when looking at the solar energy input. For our analysis we chosen a location with an average daily irradiation of $6.19 \text{ kWh/m}^2\text{day}$. When carrying out this analysis for e.g. northern Europe with a much lower sun irradiation ($\approx 3.0 \text{ kWh/m}^2\text{day}$) the LCOH would increase by more than 70%.

Comparison with previous literature

The results found during this techno-economic analysis were compared with previous studies. In [227] a similar comparison between two different PEC and two PV-E systems was performed. However, the resulting LCOH were higher, especially for the PV-E system (base-case $12.1 \text{ \$/kg}_{\text{H}_2}$). The difference between the values stems from the fact that our analysis includes updated prices for the PV panels and a higher efficiency, since a significant development occurred within this technology in the last few years. Another factor is that we include an optimization between the PV system and the electrolyzer, which lead to an increase in the capacity factor of the electrolyzer. The normalized costs for the PEC module published in [227] are in a similar range with a value of $11.4 \text{ \$/kg}_{\text{H}_2}$ for the base-case. The main difference is that we are considering a different PEC design and we consider a different panel area, similar to [223, 225]. In addition, our estimated hard-BoS costs are lower since we considered lower costs for the mounting material. On the other hand, our calculation is based on higher soft-BoS share, as we expect higher values for the installation and contingency costs.

In the DOE report a LCOH of $10.36 \text{ \$/kg}_{\text{H}_2}$ was calculated, which is slightly higher compared to our value. The main difference lies in the different material costs for the PEC module and slightly lower soft-BoS costs, since we expect the installation costs to be lower which is mainly due to a higher production rate of our considered systems.

In [255] and [229] a similar range for the LCOH of PEC systems was published, showing a value of approximately $8 \text{ \$/kg}_{\text{H}_2}$ and $10.40 \text{ \$/kg}_{\text{H}_2}$, respectively. However, their sensitivity analysis reveals a much lower error bar for the cost of hydrogen compared to our results. This is mainly due to the higher material costs for the membrane and photoactive layer which were assumed in this analysis. Both studies do not show a detailed cost breakdown for the different material components.

6.5 CONCLUSION

This chapter concerns a comparative techno-economic analysis between a photoelectrochemical system (PEC) and an already commercially available system comprising a photovoltaic device connected to an electrolyzer (PV-E). The evaluated conceptual PEC system was based on a non-concentrated panel design with an efficiency of 10 %.

For a benchmark system, a crystalline silicon PV cell combined with an off-grid PEM electrolyzer with an overall efficiency of 10.9% was chosen. The calculated levelized production cost of hydrogen (LCOH) resulted in 6.22 \$/kg_{H₂} for the PV-E system and 8.43 \$/kg_{H₂} for the PEC system, respectively. The sensitivity analysis for the PEC device revealed a significant level of uncertainty with regard to the LCOH. It was carried out by varying the costs for the membrane as well as the semiconductor material and by changing the efficiency and lifetime of the overall system. The best-case scenario shows that there is a possibility to quarter the LCOH, resulting in 2.51 \$/kg_{H₂}. However, according to our findings, this cost is more likely to be higher than the initial LCOH; for the median scenario, it is expected to nearly double.

This work demonstrates that it is unlikely for the PEC system to achieve lower hydrogen production costs compared to photovoltaic-electrolysis systems. Even under generous assumptions, PEC devices are costlier and less flexible in their application. As to the cost, we have shown that at present, the main obstacles are the stability of catalysts and an unfavorable trade-off between cost and lifetime of the semiconductor materials. Concerning the flexibility of utilization, a PV-E system can be more efficiently embedded into the future energy system than a PEC device because “PV” and “E” can be separately size-optimized to fit the needs of the future energy system and the electricity grid. This leads us to conclude that while PEC, as a research field, remains of interest for science, the prospects for successful commercialization are effectively absent. Therefore, a dedicated technology development effort is unwarranted.

SUMMARY AND CONCLUSION

The transition toward a carbon-neutral society requires reshaping the world's energy system. But even a world with net-zero emissions will depend on hydrocarbon fuels (but not necessarily of fossil origin), e.g., in the chemical industry or within the transport sector. While this requires sequestration of CO₂ from large point sources combined with storage and the application of negative emission technologies, the transition can be accelerated by the implementation of power-to-X (PtX) technologies, especially for the harder-to-abate sectors like aviation, maritime shipping, and the chemical industry. These products can also be called solar fuels when using solar energy as the electricity source. The concept of solar fuels builds on combining renewable energy with two abundant reactants, i.e., H₂O and CO₂, to produce carbon neutral fuels. While technological pathways already exist to supply the two initial components, i.e., capturing CO₂ from fossil power plants or the ambient air and water splitting to produce H₂, the uncertainties are high in terms of technical performance and economic feasibility. Therefore, the research reported in this thesis addresses the capturing and sourcing of these two key components for the production of hydrocarbon solar fuels: i) carbon dioxide obtained from the air and ii) renewable hydrogen produced from water using solar energy. The aim is to assess different routes for the supply of CO₂ and H₂ in terms of technological and economic performance and to identify the key challenges for bringing down the costs.

The following central research questions were raised within this work, and the answers are summarized in the following paragraphs.

1. Which are the main technological pathways to capture CO₂ from the air and how do they compare in terms of performance and economics?

This research question is addressed in Chapter 2, where the main processes for direct air capture (DAC) have been analyzed: two liquid scrubbing processes and one solid sorbent vacuum temperature swing adsorption (VTSA) process. These processes have been optimized with the aim of maximizing productivity and minimizing energy demand. The results have shown that all processes were able to capture high purity CO₂ from the air, with the solid sorbent process performing best. The productivity of the adsorbent process was in the range of 3.8 to 10.6 kg_{CO₂}/m³/h and the specific exergy demand 1.4 to 3.7 MJ/kg_{CO₂}. However, the uncertainty with regard to the mass transfer was high and, depending on the driving force coefficient, broadens the productivity range to 0.13 to 10.6 kg_{CO₂}/m³/h. When comparing the three processes

from an economic point of view, the solid sorbent VTSA process again showed the most promising performance. While the solid sorbent process came out to be the most attractive option, the uncertainties are also highest for this process. Therefore, in the second part of Chapter 2 the effect of climatic conditions (i.e. geographic locations) on the optimal design of a solid sorbent process is investigated. It is shown that the annual average ambient temperature is the main climatic driver for both capturing costs and energy requirements, while humidity plays a subordinate role. In cold (and humid) climates, the capturing costs and energy requirements can be significantly lower than in warmer locations: we found that the cost and the energy consumption of DAC deployed in The Netherlands are about 16% and 33% lower compared to Spain or California, respectively.

2. *Are there already existing adsorbents in databases that show promising performance for DAC applications, and how can we find them across several thousands of possible structures?* In Chapter 3, several thousand adsorbent materials were screened to identify suitable candidates for capturing CO₂ from dilute streams. For this purpose, an equilibrium model of vacuum temperature swing adsorption cycles was designed, with which it is possible to rapidly screen a huge amount of materials. The accuracy and prediction capabilities of the equilibrium model are improved by incorporating feed-forward neural networks, which are trained with data from rate-based models. This allows, for example, to include process productivity, a key performance indicator typically obtained in 1D models. The equilibrium model was first validated against a rate-based model, showing a good prediction of the different performance indicators, i.e., productivity and thermal energy consumption. The screening of a large number of materials revealed a ranking of the best performing adsorbents for different CO₂ concentrations in the feed stream. For the DAC case, 12 promising materials were identified, but no new materials for DAC were found. This naturally leads to the next research question:

3. *What are the performance and cost limits for DAC using an ideal adsorbent with VTSA?* This question is addressed in Chapter 4, where, through an approach called *process inversion*, the limits of solid sorbents for VTSA processes for DAC application were explored. The aim was to identify ideal sorbents showing optimal process performance by both including the adsorbent properties and process performance parameters as decision variables. To keep this assessment broad, a variety of CO₂ isotherm models was included in the analysis, i.e., the Langmuir-Freundlich, the Toth, the extended Toth (Toth-cp), the Dual-site-Langmuir (DSL) and an S-shape model. The water isotherm was kept the same. When comparing with materials from several databases, the results show that with the optimized isotherm models, it was possible to outperform the existing adsorbents. The best performing isotherm models for the ultra-dilute feed concentration were the extended Toth equation showing the highest productivity with up to 17 kg/m³/h and the S-shaped model showing the lowest thermal energy consumption of 0.5 MJ/kg_{CO₂}. Using the optimal hypothetical isotherms from the Toth-cp model, an economic analysis was carried out. Depending on the mass transfer coefficient, the levelized cost of CO₂ was found to be in the range of 450 to 2500 \$/t_{CO₂}. A cost breakdown revealed that the economic performance of a DAC process centers around the adsorbent material, with the working capacity and the kinetics determining the productivity, but also the sorbent price and the lifetime having the greatest impact. With moderate assumptions for these factors, it was not possible to reach the targeted DAC costs of 100 \$/t_{CO₂} using one of the optimized adsorbents. Only with optimistic assumptions similar to a commercialized adsorbent like Zeolite 13X could costs be brought down to reach this value.

The following two questions address the production of renewable H₂ using solar energy.

4. *What technologies are available for electrochemical production of hydrogen from solar energy and water, and how do they operate under real working conditions?*

In the first part of Chapter 5, different types of solar water splitting devices were presented, and the most promising one, a photoelectrochemical (PEC) cell, was chosen for further investigation. An equivalent circuit model was developed, with which the steady state performance of PEC devices can be computed. The model allows for a computationally efficient yet precise prediction of the system performance and a comparison of different devices. Furthermore, the model was extended to include the effect of illumination and tilt angle on hydrogen production efficiency. The yearly performance of five PEC devices was evaluated at different tilt angles and different locations. The results show that including real illumination data has a considerable impact on the efficiency of the PEC device. The yearly average solar-to-hydrogen efficiency is significantly lower than the ideal one. Moreover, it is dependent on the

tilt angle, whose optimal value for European-like latitude is around 40° .

5. What is the techno-economic performance of PEC and PV-E systems, and how do they compare?

Photoelectrochemical water splitting is potentially a sustainable and affordable solution to produce hydrogen from sunlight. Given the infancy stage of technology development, it is important to compare not only different integrated devices with each other but also include other possible pathways. In Chapter 6 a techno-economic analysis of two solar-assisted hydrogen production technologies: a photoelectrochemical (PEC) system and its major competitor, a photovoltaic system connected to a conventional water electrolyzer (PV-E system) was carried out. The technical evaluation was performed by considering proven designs and materials for the PV-E system and a conceptual design for the PEC system extrapolated to future scale. The levelized cost of hydrogen (LCOH) for the off-grid PV-E system was found to be $6.22 \text{ \$/kg}_{\text{H}_2}$, with a solar to hydrogen efficiency of 10.9%. For the PEC system, with a similar efficiency of 10%, the LCOH was calculated to be higher, namely $8.43 \text{ \$/kg}_{\text{H}_2}$. The results show that the potential techno-economic benefits PEC systems offer over PV-E are uncertain and, even in the best case, limited. The main obstacles are the stability of catalysts and an unfavorable trade-off between the cost and lifetime of the semiconductor materials. Concerning the flexibility of utilization, a PV-E system can be more efficiently embedded into the future energy system than a PEC device because "PV" and "E" can be separately size-optimized to fit the needs of the future energy system and the electricity grid.

7.1 RECOMMENDATIONS

In Chapter 2, it was shown that water could have a strong effect on the CO_2 working capacity, which can significantly affect the performance and the capital cost of a DAC plant. While water adsorption was included throughout the whole research in this thesis, the data is based only on a few experimental analyses presented in the literature. In addition, the effect of water on the CO_2 capacity was only included within Chapter 2 by considering an enhancement factor for CO_2 adsorption dependent on the humidity and temperature. With the few experimental data of H_2O adsorption on materials like amine-functionalized adsorbents or MOFs, it was not possible to make more general assumptions, and therefore, in Chapter 3-4, the enhancement factor was not included. The same limit holds true for the second part of Chapter 2, where the effect of temperature and humidity on the technical and economic performance of DAC processes was investigated. This analysis was again carried out by using the limited set of experimental data on water adsorption.

Another major factor determining the performance of the adsorbents is the mass transfer coefficient. Here again, the uncertainty is high since experimental data for low CO₂ concentration, combined with water adsorption, is still rare. In Chapter 2 and 4 an optimistic value of $k_{LDF} = 0.1 \text{ s}^{-1}$ was chosen, which was complemented by a sensitivity analysis. In addition, while using the approach of the linear driving force is a common approach for modeling adsorption processes, there might be more suitable methods for modeling DAC processes.

In Chapter 5, several isotherm models were optimized to find the limits for capturing CO₂ from dilute feed streams. The oD model was used for this analysis, complemented by the rate-based model. Since the simplified model, as the name indicates, has its limitations e.g., by considering an isothermal adsorption step or not including kinetics, the results do give a possible design spectrum for promising hypothetical adsorbents, but carrying out the same analysis using a rate-based model will show different results. Still, the computational time would then increase strongly.

7.2 OUTLOOK

For solar fuels to become competitive, the cost must be drastically reduced. Kraan et al. [256] analyzed the production costs of solar fuels from CO₂ captured from the air, and H₂ produced via electrolysis. Their results show, that the main cost contributors for solar fuels are the capturing of CO₂ from air, followed by the H₂ production, as shown by the *current* and *target* case in Figure 7.1. The target costs can be reached when the overall production costs reach the 200 \$/barrel mark. Taking their simplified approach, the results gathered within this thesis are shown by the third bar (*present study*). For this simple comparison, only the costs for the CO₂ capture and H₂ production are changed, by including DAC costs obtained from optimizing a hypothetical sorbent ($c_s = 30 \text{ \$/kg}$ and $l_s = 2 \text{ years}$) and optimistic H₂ production costs from the PEC analysis. It can be clearly seen that the total costs are still far from reaching the target. While the technology for capturing CO₂ from the air has experienced remarkable progress within the past decade, there is still a lot of potential to bring down the costs, mainly by improving the solid sorbent materials with a focus on lower costs and longer lifetime. For the production of renewable H₂ from water splitting, on the other hand, there exist already commercially available technologies, i.e., photovoltaic devices connected to an electrolyzer. The *present study* case in Figure 7.1 shows H₂ production costs using PEC devices with already highly optimistic assumptions for mass-produced cells. This reveals that with current materials and existing PEC technologies, the target costs of 200 \$/barrel cannot be reached.

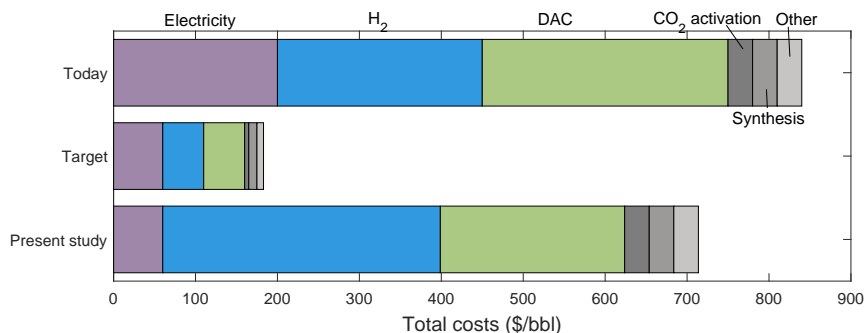


FIGURE 7.1: Estimated costs for the production of a solar fuel from CO₂ and water, adapted from Kraan et al. [256].

A number of recent studies [257, 258], like the latest report of the Internal Panel on Climate Change [257], have collectively stressed the need for negative emissions technology to limit the average global temperature increase to 1.5 °C by 2100. While there are several scenarios to meet the short-term goals, capturing CO₂ from the air is one of the technologies which is required to meet the longer-term goals in a large-scale format [258]. DAC is currently being commercialized, and although it is not economically feasible at present, it shows a promising means of mitigating the effects of climate change.

APPENDIX FOR CHAPTER 2

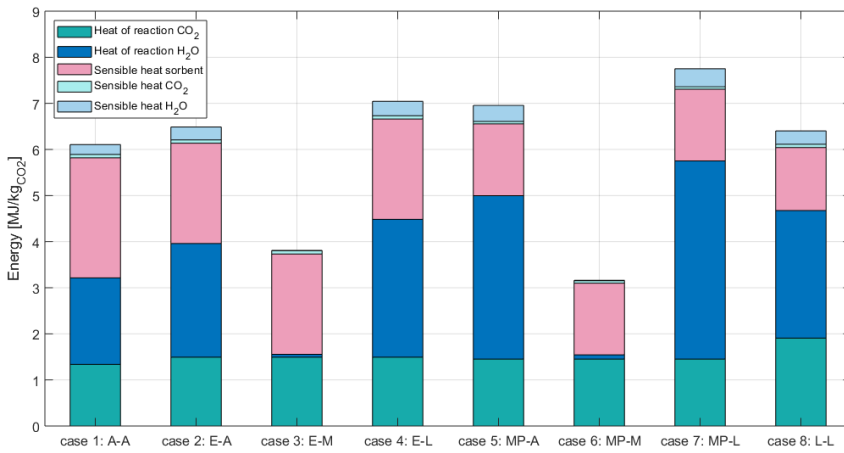


FIGURE A.1: Breakdown of the equilibrium energy requirement for regeneration of the different sorbent cases using a simplified calculation ($T = 373K$, $p = 0.1bar$).

TABLE A.1: Main specification adopted in the Aspen flowsheets for the alkali scrubbing process [25] and the amine scrubbing process.

Alkali Scrubbing		Amine Scrubbing	
<i>Air contactor</i>		<i>Air contactor</i>	
Number of blocks	6	Number of blocks	3
Number of stages per block	20	Number of stages per block	20
Diameter	5.64 m	Diameter	5.64 m
Height	1.16 m	Height	2.32 m
Packing	Sulzer 250Y	Packing	Sulzer 250Y
		w_{MEA}	30 wt. %
<i>Pellet reactor</i>		<i>Washing section</i>	
Temperature	25°C	Diameter	5.64 m
$X_{\text{Ca(OH)}_2}$	1	Height	1 m
<i>Calcliner</i>		Packing	Sulzer 250Y
Temperature	900°C	L/G ratio	0.05
X_{CaCO_3}	0.98	<i>Heat exchanger</i>	
<i>Slaker</i>		Minimum ΔT^*	10°C
Temperature	300 °C	<i>Stripper</i>	
X_{CaO}	0.85	Number of stages	10
ASU		Pressure	2 bar
W_{ASU}	1000 kJ/kgO ₂	$T_{\text{CONDENSER}}$	35°C
		T_{REBOILER}	124°C

*Enforced by a design specification.

TABLE A.3: Fitted Parameters for single CO₂ isotherms of the different solid sorbents and the exemplary isotherm using the Toth or the Toth-cp model.

Parameter	APDES- NFC	Tri-PE- MCM-41	MIL- 101(Cr)- PEI-800	Lewatit VP OC 106	Exemplary isotherm
T_0 (K)	296	298	270	278	298
Chemisorption					
b_0 (1/MPa)	0.560×10^6	3.135×10^6	9.96×10^6	2.54×10^6	0.426×10^6
ΔH (kJ/mol)	50.0	117.8	68.3	91.2	64.19
t_0 (-)	0.368	0.236	0.243	0.442	0.282
α (-)	0.368	0.482	1.802	0.520	0.886
n_{so} (mol/kg)	2.310	2.897	3.450	2.211	3.296
χ (-)	2.501	0.207	4.504	0	3.850
Physisorption					
b_0 (1/MPa)	-	0.636	93.2	1.51×10^2	15.91
ΔH (kJ/mol)	-	2.64	40.1	5.19	3.44
t_0 (-)	-	0.872	0.163	0.636	0.150
α (-)	-	0.003	2.287	2.407	6.814
n_{so} (mol/kg)	-	8.208	6.205	1.840	1.243
χ (-)	-	4.539	0.579	7.186	2.873
R ₂ (-)	0.99	0.996	0.997	0.99	

TABLE A.5: Fitted Parameters for the single water isotherms of the different solid sorbents using the GAB model.

Parameter	MCF-APS-hi	Lewatit	APDES-NFC ¹	APDES-NFC ²
C_0 (-)	21.375	1.715	6.86	6.86
ΔH_C (kJ/mol)	-1.957	-24.636	-4.120	-5.088
K_0 (-)	0.013	0.008	2.27	2.27
ΔH_K (kJ/mol)	-1.0002	9.4384	-2.530	-3.443
$C_{m,0}$ (mol/kg)	0.051	4.697	0.0208	0.0208
β (K)	995.3	3083.0	1540	1797
R_2 (-)	0.98	0.87	-	0.99

¹ fitting by [41]; ² own fitting

TABLE A.7: Design variables for the three different processes, including lower and upper bound.

Variable	Range				
KOH process					
ζ (kmol _{KOH} /kmol _{CO2})	1-35				
u_{air} (m/s)	0.4-2.4				
w_{H2O} (-)	0.11-0.26				
MEA process					
ζ (kmol _{MEA} /kmol _{CO2})	1-25				
u_{air} (m/s)	1.0-3.0				
d (MJ/kg _{lean})	0.28-0.8				
f_{Split} (-)	0.02-0.2				
Solid sorbent process					
	APDES-NFC	MIL-101(Cr)- PEI-800	Lewatit OC 106	VP	Exemplary
t_{ads} (s)	100-10000				
t_{prod} (s)	50-2200				
t_{purge} (s)	1-400				
p_{vac} (bar)	0.01-0.9				
T_{prod} (K)	363-393				
ΔT_{purge} (K)	1-60				
\dot{V}_{air}^* (m ³ /s)	0.28 – 16.50	0.28 – 12.24	0.28 – 5.09	0.28 – 12.24	

* values refer to one full module

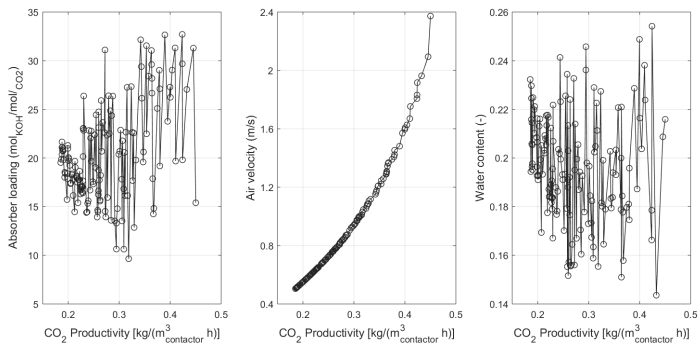


FIGURE A.2: Resulting design variables for the different points on the Pareto line: a) absorber loading; b) air velocity; c) water content in the CaCO₃ slurry.

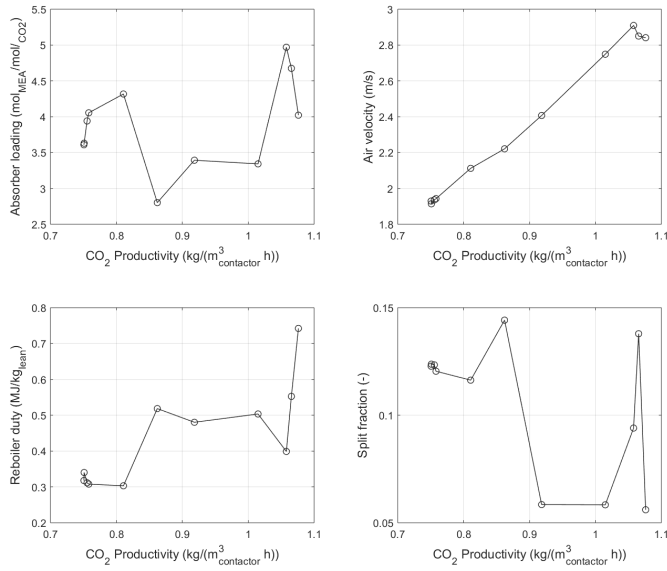


FIGURE A.3: Resulting design variables for the different points on the Pareto line: a) absorber loading; b) air velocity; c) specific reboiler duty; d) split fraction.

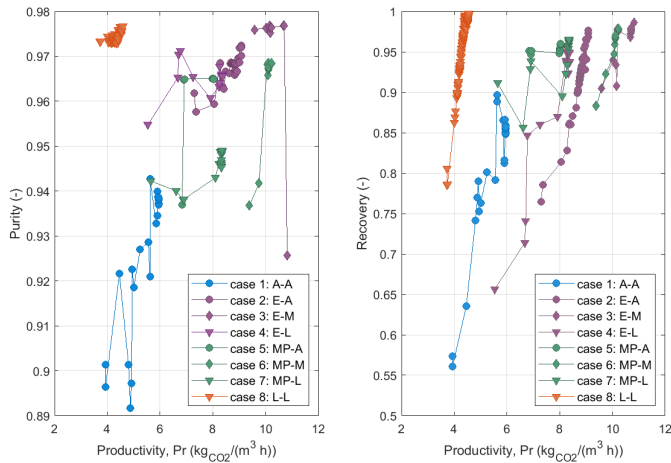


FIGURE A.4: CO₂ purity and recovery over the productivity for the different points on the resulting Pareto line.

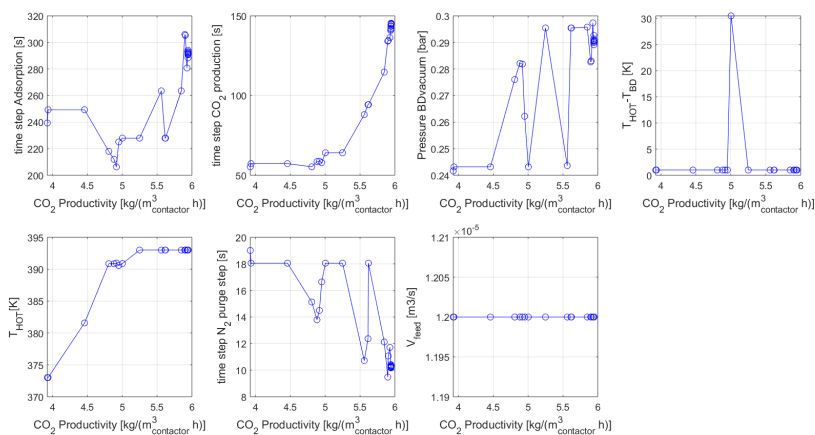


FIGURE A.5: Resulting design variables for the different points on the Pareto line for the APDES-NFC sorbent (case A-A). The design variables are the adsorption time, the CO₂ production time, the vacuum pressure, the temperature difference between the production and purge step, the temperature during the production step, the purge time and the volume stream of the air.

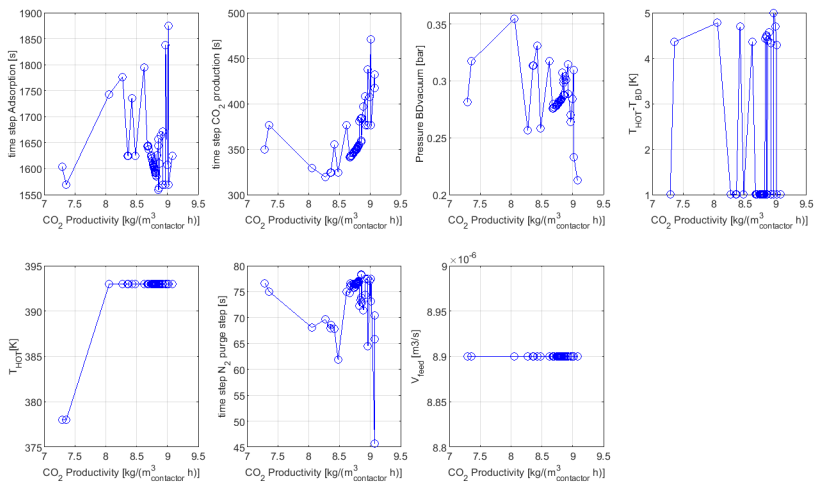


FIGURE A.6: Resulting design variables for the different points on the Pareto line for the exemplary isotherm for CO₂ with the water isotherm of the APDES-NFC sorbent (case E-A). The design variables are the adsorption time, the CO₂ production time, the vacuum pressure, the temperature difference between the production and purge step, the temperature during the production step, the purge time and the volume stream of the air.

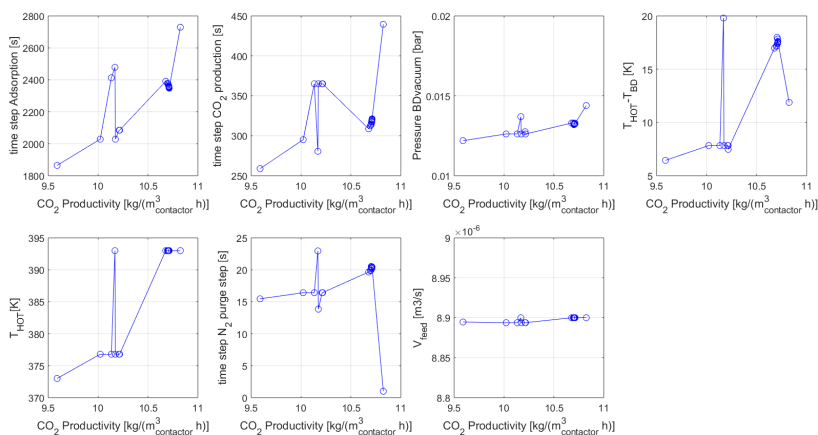


FIGURE A.7: Resulting design variables for the different points on the Pareto line for the exemplary isotherm for CO₂ with the water isotherm of the MCF-APS-hi sorbent (case E-M). The design variables are the adsorption time, the CO₂ production time, the vacuum pressure, the temperature difference between the production and purge step, the temperature during the production step, the purge time and the volume stream of the air.

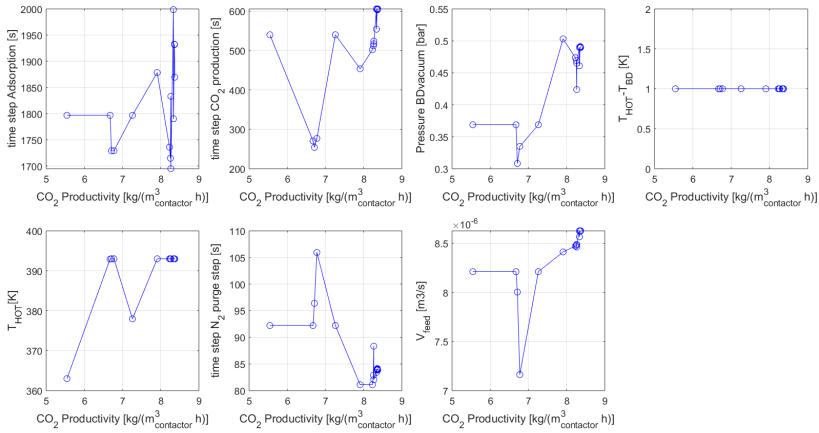


FIGURE A.8: Resulting design variables for the different points on the Pareto line for the exemplary isotherm for CO₂ with the water isotherm of the Lewatit sorbent (case E-L). The design variables are the adsorption time, the CO₂ production time, the vacuum pressure, the temperature difference between the production and purge step, the temperature during the production step, the purge time and the volume stream of the air.

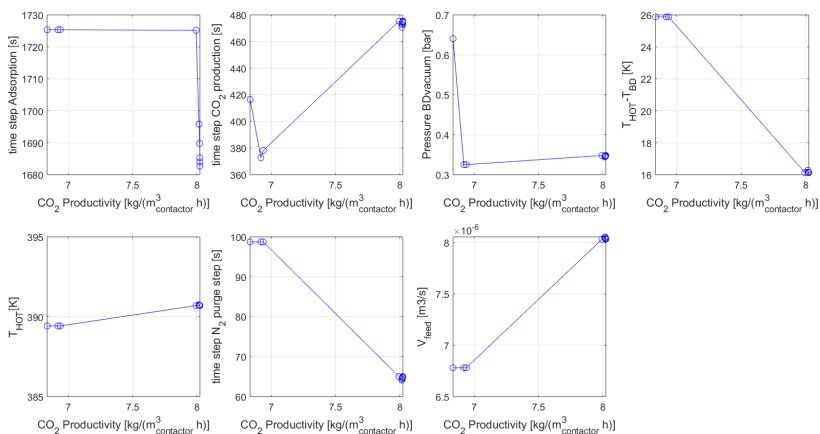


FIGURE A.9: Resulting design variables for the different points on the Pareto line for the MIL-101(Cr)-PEI-800 isotherm for CO₂ with the water isotherm of the APDES-NFC sorbent (case MP-A). The design variables are the adsorption time, the CO₂ production time, the vacuum pressure, the temperature difference between the production and purge step, the temperature during the production step, the purge time and the volume stream of the air.

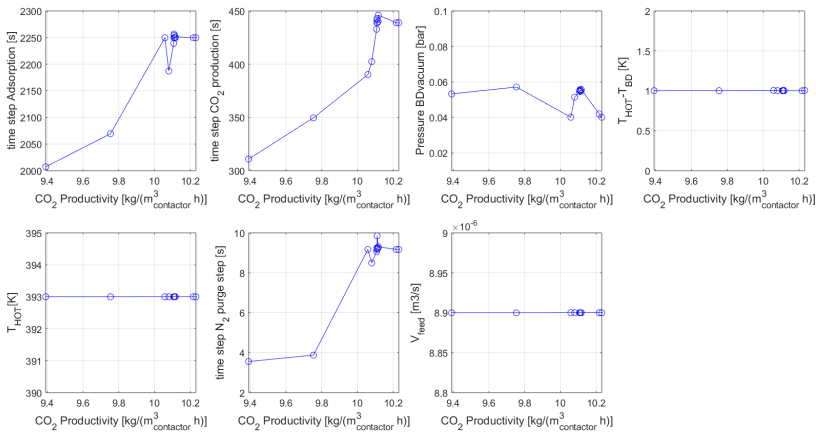


FIGURE A.10: Resulting design variables for the different points on the Pareto line for the MIL-101(Cr)-PEI-800 isotherm for CO₂ with the water isotherm of the MCF-APS-hi sorbent (case MP-M). The design variables are the adsorption time, the CO₂ production time, the vacuum pressure, the temperature difference between the production and purge step, the temperature during the production step, the purge time and the volume stream of the air.

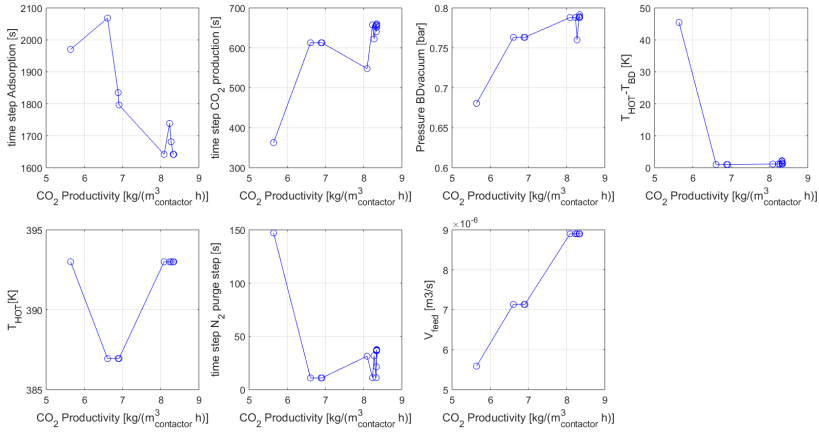


FIGURE A.11: Resulting design variables for the different points on the Pareto line for the MIL-101(Cr)-PEI-800 isotherm for CO₂ with the water isotherm of the Lewatit sorbent (case MP-L). The design variables are the adsorption time, the CO₂ production time, the vacuum pressure, the temperature difference between the production and purge step, the temperature during the production step, the purge time and the volume stream of the air.

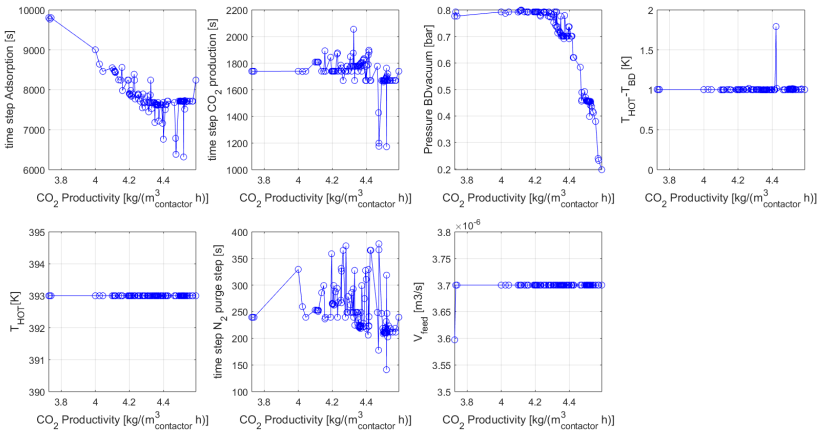


FIGURE A.12: Resulting design variables for the different points on the Pareto line for the sorbent Lewatit VP OC 106 (case L-L). The design variables are the adsorption time, the CO₂ production time, the vacuum pressure, the temperature difference between the production and purge step, the temperature during the production step, the purge time and the volume stream of the air.

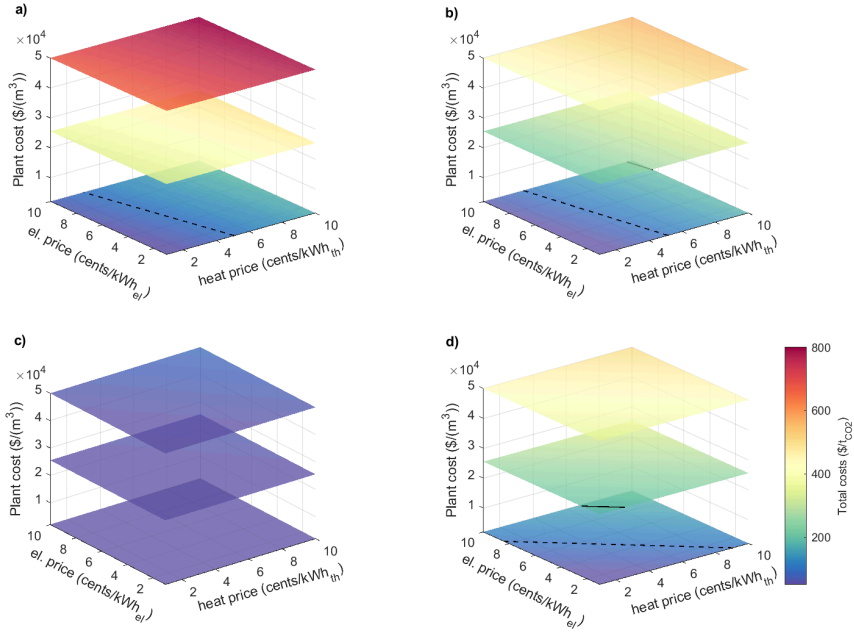


FIGURE A.13: Maps of total system cost using the exergy consumption, as a function of electricity price, heat price and plant cost, referring to the m^3 of air contactor, for the three different processes: KOH using point B on the Pareto chart (highest productivity) (a), MEA using point A on Pareto chart (lowest exergy consumption) (b) and solid sorbent case E-A (c: high kinetics $k = 0.1 \text{ s}^{-1}$ using point B on Pareto chart and d: low kinetics $k = 0.0001 \text{ s}^{-1}$ using a middle point on the Pareto chart with an exergy consumption similar to the KOH process). We have assumed full-load operation plant, a 20 year project life and an 10% discount rate. The dashed lines show total costs with a value of $100 \text{ \$/tCO}_2$ and the continuous lines a value of $200 \text{ \$/tCO}_2$. As an example: when assuming heat costs of $c_{\text{th}}=5 \text{ \$/cents/kWh}_{\text{th}}$, electricity costs of $c_{\text{el}}=10 \text{ \$/cents/kWh}_{\text{el}}$ and contactor costs of $\gamma = 25000 \text{ \$/m}^3$, this would result in total costs of $419 \text{ \$/tCO}_2$, $300 \text{ \$/tCO}_2$, $58 \text{ \$/tCO}_2$ and $301 \text{ \$/tCO}_2$ for the KOH, MEA and the two solid sorbent processes, respectively.

*Supplemental Experimental Procedure***Supplementary information for the liquid scrubbing processes****Alkali Scrubbing**

The key parameters used for modeling the alkali scrubbing and the amine scrubbing processes are listed in Table A.1.

KOH units details

In Carbon Engineering's design, an open, cross-flow configuration is used, meaning that the KOH solution trickles from top to bottom while air flows horizontally. This design, which has been proven at pilot-scale [24], supposedly provides a fourfold reduction in capture costs over conventional absorption towers. In order to reproduce this cross-flow configuration, the air contactor was simulated using six rate-based RadFrac blocks arranged in parallel, as represented in the following Figure.

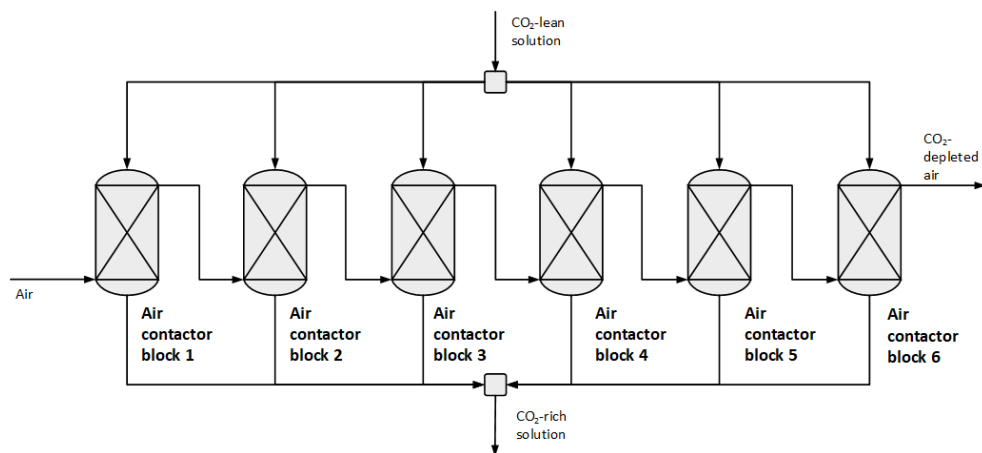


FIGURE A.14: Representation of the approach adopted to model the air contactor.

The diameter and height of the blocks have been fixed to reproduce the inlet area and packing depth of Carbon Engineering's air contactor.

The kinetic model used in the alkali scrubbing flowsheet has been validated under DAC conditions using experimental data reported by Mahmoudkhani et al. [57] and Keith et al. [25].

The results are shown in the following Figure, while the key parameters adopted in the two validation cases are reported in the Table below.

TABLE A.9: Key operating parameters adopted in the validation cases.

	Mahmoud- khani et al.	Keith et al.
Air velocity (m/s)	0.7	1.4
Lean flowrate (L/s)	4.2	21
KOH concentration in the lean (mol/L)	3	1.1
K ₂ CO ₃ concentration in the lean (mol/L)	0	0.5
Packing depth (m)	1.5	7
Packing diameter (m)	1.22	5.64
Packing type	Sulzer 250X	Sulzer 250Y
Number of air contactor blocks	1	6

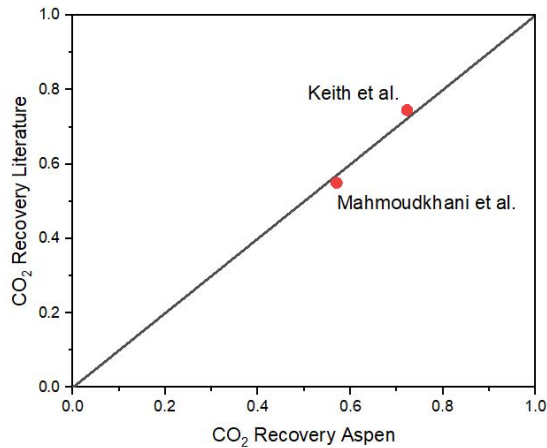


FIGURE A.15: Validation of the KOH kinetic model based on experimental data reported by Mahmoudkhani et al. [57] and Keith et al. [25].

It can be observed that the model is able to adequately predict the CO_2 recovery in different operating conditions.

Slaker

The slaker is operated with steam at a temperature of 300°C . The heat released by CaO dissolution in water is used to dry and preheat the CaCO_3 particles, yielding enough steam to self-sustain the reaction itself. The advantage of steam slaking over the conventional water slaking carried out in the Kraft process is that the heat of the slaking reaction is released at a higher temperature, thus making it more valuable.

Pellet reactor

The pellet reactor designed by Carbon Engineering provides a conversion of the fed $\text{Ca}(\text{OH})_2$ of roughly 90% [25].

Calciner and Air Separation Unit

The calciner is operated at 900°C , a temperature that is reached through oxy-fuel combustion of methane. An air separation unit (ASU) provides the required oxygen. The gas stream coming out of the calciner, which contains exclusively CO_2 , steam, unreacted O_2 and inerts from the ASU oxygen supply, is used to preheat the CaCO_3 particles in two counter-current cyclones and it is eventually cooled down, dried and compressed. The specific energy demand of the calciner is calculated from the methane feed required to reach the target CaCO_3 conversion, while the energy consumption of the ASU is according to the state of the art. The energy demand for the CO_2 compression, and this holds true for all the processes, is calculated in Aspen Plus according to Manzoloni et al. [259].

The pellet reactor, the calciner and the slaker are simulated using equilibrium (RGIBBS in Aspen Plus) or constrained equilibrium (RSTOIC in Aspen Plus) units.

Amine Scrubbing

The approach used to model the alkali scrubbing process was also adopted for the amine technology. The most important parameters are reported in Table A.1.

Supplementary information for the solid sorbent process

Pure component isotherms CO₂

Working capacity. One criteria for choosing the representative sorbents was a working capacity greater than zero, Δq_{CO_2} in molCO₂/kg_{sorbent}. It was calculated in the form of

$$\Delta q_{\text{CO}_2} = q_{\text{ads}} - q_{\text{des}} \quad (\text{A.1})$$

with q_{ads} being the capacity of the sorbent at $y_{\text{CO}_2} = 400$ ppm and ambient temperature and q_{des} the capacity at desorption conditions with varying vacuum pressure and desorption temperature. The resulting graph is shown in the following Figure. For our study we chose a maximum desorption temperature of 120°C.

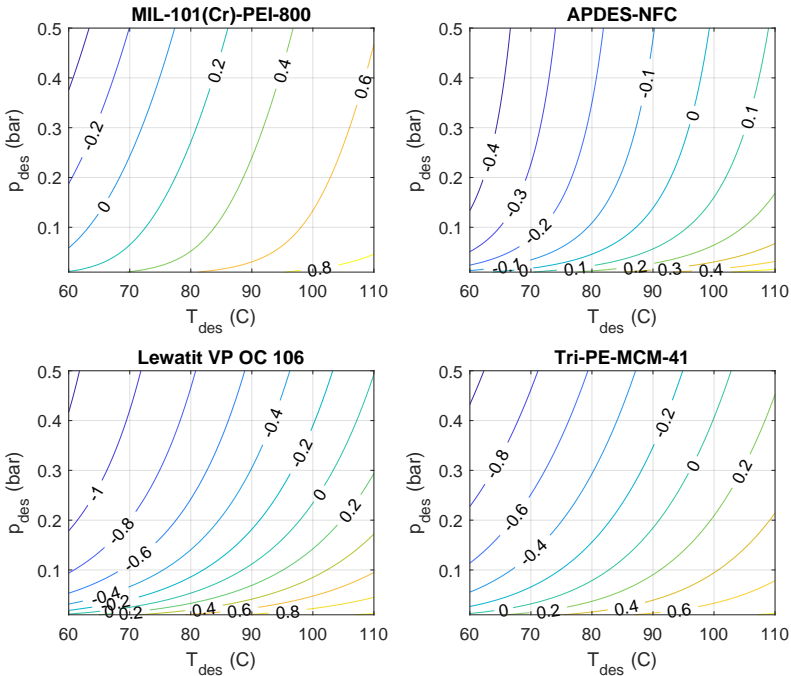


FIGURE A.16: Working capacity for the different sorbents dependent on the vacuum pressure P_{des} and the desorption temperature T_{des} .

Fitting equilibrium data. The parameters for the Toth and Toth-cp isotherms were estimated by fitting the experimental data for the single component adsorption

isotherm provided by different authors, namely APDES-NFC [41], Tri-PE-MCM-41 [68], MIL-101(Cr)-PEI-800 [45] and Lewatit VP OC 106 [48, 69, 70]. For the adsorption of water we took the data provided in [41] for APDES-NFC and in addition fitted the experimental points for MCF-APS-hi [71] and Lewatit VP OC 106 [76]. For the latter the Guggenheim-Anderson-de Boer (GAB) model is used [41, 75]. The experimental data points were extracted by making use of a Web Plot Digitizer tool [260].

For the objective function the normalized standard deviation was applied, which is commonly used to fit isotherm models to experimental data [41, 87, 261, 262]. It includes the adsorbed amount determined experimentally q_{exp} , the amount adsorbed as predicted by the model q_{fit} and the total number of experimental points N , and is calculated in the form of

$$err = \sqrt{\frac{\sum \left[\frac{(q_{\text{exp}} - q_{\text{fit}})}{q_{\text{exp}}} \right]^2}{N - 1}} \cdot 100 \quad (\text{A.2})$$

which is minimized using the inbuilt Matlab optimization routine *fmincon* together with the *sequential quadratic programming* (SQP) algorithm.

The error is expressed by

$$R2 = \frac{\sum (q_{\text{exp}} - q_{\text{fit}})^2}{\sum (q_{\text{exp}} - \overline{q_{\text{exp}}})^2} \quad (\text{A.3})$$

with $\overline{q_{\text{exp}}}$ being the mean of the experimental data.

The fitted data is plotted in the Figure below for the CO₂ isotherms. The parameters for each sorbent are listed in Table A.3 for CO₂. For the APDES-NFC and the MIL-101(Cr)-PEI-800 sorbent, the middle temperature was left out from the fitting, since like this we were able to get a better fitting for the operating temperatures, i.e. the adsorption and desorption temperature.

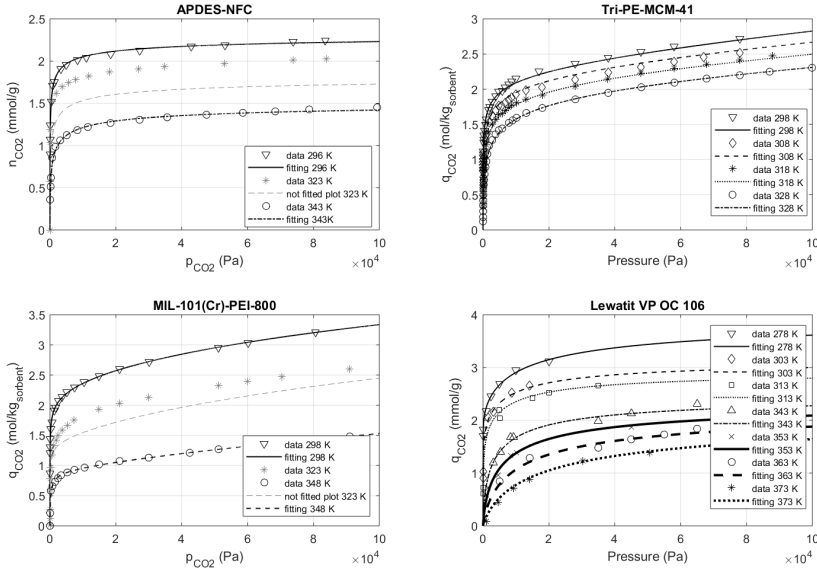


FIGURE A.17: Experimental data points and fitted profile of the CO₂ isotherms for different materials (the experimental points in grey were not included in the fitting). The experimental data was found in [41] for APDES-NFC, [68] for Tri-PE-MCM-41, [45] for MIL-101(Cr)-PEI-800 and [48, 69, 70] for Lewatit VP OC 106.

The exemplary isotherm is representing a mean isotherm of the four materials shown above. It was determined by first calculating a mean isotherm for three different temperatures (298K, 340K, 373K) in the form of

$$q_{CO_2,exempl}(T, p_{CO_2}) = \frac{1}{n} \sum_{i=1}^n q_{CO_2,i}(T, p_{CO_2}) \tag{A.4}$$

with i representing the different sorbent and n the amount of the input sorbents. In a second step the resulting isotherm for the different temperatures was fitted. In the Figure below, the resulting exemplary isotherm is shown.

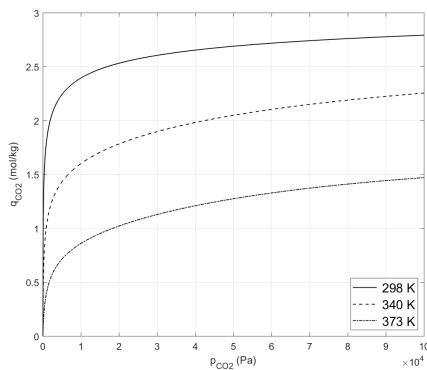


FIGURE A.18: Resulting experimental isotherm plotted for three temperatures.

Pure component isotherms H₂O

Fitting equilibrium data. For the adsorption of water we took the data provided in [41] for APDES-NFC and in addition fitted the experimental points for MCF-APS-hi [71] and Lewatit VP OC 106 [76] using the the Guggenheim-Anderson-de Boer (GAB) model [41, 75]. The fitting is carried out using the same approach as for the CO₂ isotherm. The fitted data is plotted in the following Figure and the parameters for each sorbent are listed in Table A.5 for H₂O.

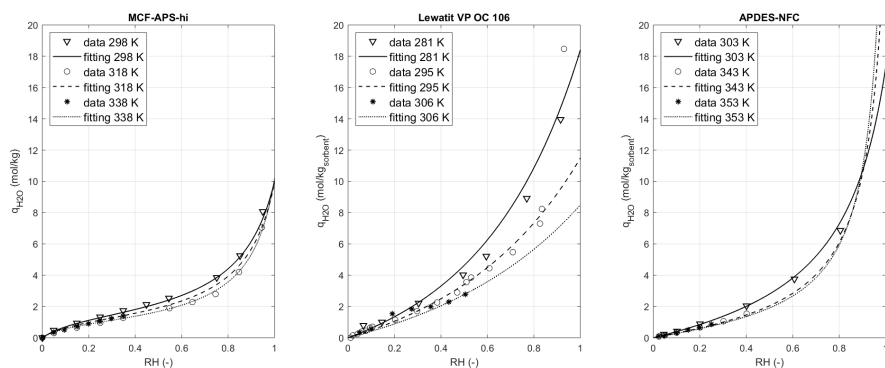


FIGURE A.19: Experimental data points and fitted profiles of the H₂O isotherms for MCF-APS-hi [71] and Lewatit VP-OC [76]. The fitting of APDES-NFC was taken from [41].

In our analysis we used the fitting by Wurzbacher et al [75] for the water isotherm of the APDES-NFC sorbent. For a humidity $< 70\%$ this fitting seems reliable. However, for a higher humidity there are no experimental points, and the fitting of the experimental points seems not accurate anymore, since the isotherm of higher temperatures overlap the isotherm of the ambient temperature which is shown in the following Figure a). Therefore, an own fitting using the GAB model was carried out to check the influence of a change in the isotherm shape. The fitted parameters are listed in Table A.5. In the following Figure b), the resulting Pareto curves for the APDES-NFC sorbent (A-A case) as well as the exemplary isotherm (E-A case) is shown, using the fitting by Wurzbacher et al and our own fitting. A difference in the Pareto curves can be seen, but the effect is not significant, and compared to other uncertainty parameters like the kinetics, this influence is minor. Therefore, and because of the lack of experimental points, the fitting by Wurzbacher et al is used for our analysis.

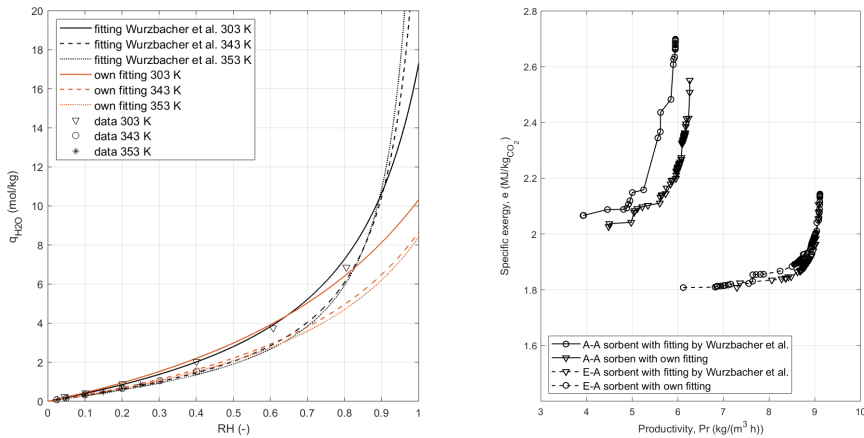


FIGURE A.20: Analysis of different fittings for of the APDES-NFC water isotherm. a) Comparison of different fittings of the water isotherm for the APDES-NFC sorbent with experimental points from [41]. The black lines show the fitting by [75] and the grey lines show our own fitting. b) The resulting Pareto curves for the APDES-NFC sorbent and the exemplary sorbent using the two different water isotherm fittings.

Isosteric Heat of Adsorption

The isosteric heat of adsorption (Δh_{iso}) is defined as the difference between the activation energy for adsorption and desorption. It represents the strength of the adsorbate-adsorbent interaction and can be calculated from the Clausius-Clapeyron [263] equation as

$$\left(\frac{\partial(\ln p_{\text{CO}_2})}{\partial T} \right)_{q_{\text{equ}}} = \frac{-\Delta h_{\text{iso}}}{RT^2} \quad (\text{A.5})$$

where p_{CO_2} is the partial pressure of CO_2 (Pa), T is the absolute temperature (K) and R is the universal gas constant. The isosteres were calculated at various capacities from the experimental data points of the different materials. The average heat of adsorption calculated from the slopes of the isosteres is shown in the Table below.

TABLE A.11: Resulting average isosteric heat for the different solid sorbents calculated by fitting experimental data.

Material	Δh_{iso} (kJ/mol)	Source data
CO ₂		
APDES-NFC	58.8	[41]
Tri-PE-MCM-41	96.7	[68]
MIL-101(Cr)-PEI-800	83.9	[45]
Lewatit VP OC 106	58.2	[70]
Exemplary isotherm	71.7	
H ₂ O		
APDES-NFC	49.0	[41]
MCF-APS-hi	58.0	[71]
Lewatit VP OC 106	53.2	[76]

Modelling H₂O-CO₂ cooperative adsorption

The equivalent temperature was calculated by fitting data provided in [48] for Lewatit. Veneman et al reported experimental data showing the capacity of the sorbent for different humidity and temperature at a partial pressure of CO₂ of 400 ppm. Through interpolation we calculated q_{CO_2} for 6 different humidity's, from 0-50%, for three temperatures, 288 K, 298 K and 308 K. The effect of humidity is decreasing with increasing temperature, meaning that the gain in CO₂ adsorption is higher at lower temperature and lower at higher temperature [261], we added a fourth temperature at 373 K where we assumed that there is no increase in the capacity for an increasing humidity. The fitted data is shown in the Figure below and the parameters can be found in the following Table.

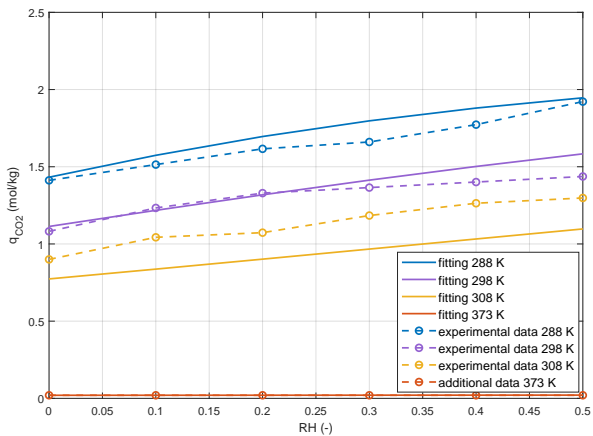


FIGURE A.21: Equivalent temperature fit to experimental data provided in [48].

TABLE A.12: Fitted parameters for the equivalent temperature included in the Toth-cp model for the chemisorption part.

a	b	R_2
116.87	15.00	92.12%

When comparing our fitting of the equivalent temperature with the experimental data by [41] for the APDES-NFC sorbent, the CO_2 uptake for the ambient condition can be represented as well.

The following Figure shows the experimental points for the APDES-NFC sorbent for humid conditions provided by [41] for two temperatures. In addition we show our fitted equilibrium data of CO_2 for the same sorbent in dry and humid conditions, by including the equivalent temperature to the isotherm model. For the lower temperature and low partial pressure, which represents ambient condition, the equivalent temperature gives a good representation of the experimental data. For higher partial pressure the error increases, since our fitting was carried out for a pressure of 0.04 Pa and the factor is independent of pressure. Contrary to the findings in [261], the experimental data points of [41] show an increase in the enhancing effect of humidity with increasing temperature. Therefore, the data points for 323 K can not be represented by the equivalent temperature.

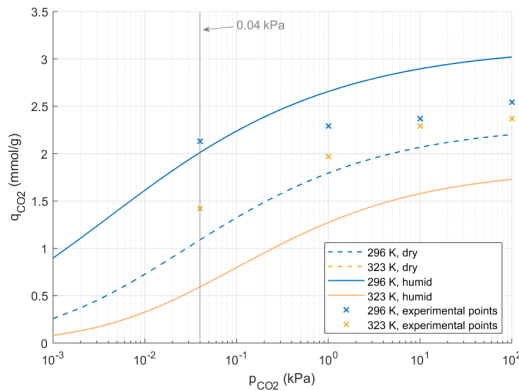


FIGURE A.22: Fitted equilibrium data of CO_2 for the APDES-NFC sorbent in dry (solid line) and humid (dashed line, $p_{\text{H}_2\text{O}} = 2.55 \text{ kPa}$) conditions. The x-markers represent the experimental data by [41]. Note that the lines of the dry and humid isotherm for 323K are almost identical.

Physical properties and model assumptions

The material specific parameters which were used for the modeling are listed in the following Table. For the exemplary isotherm a mean value was calculated using the data of the other sorbents. The bulk density ρ_b was determined by using a bulk factor f_b which is the bed density divided by the particle density ρ_p .

TABLE A.13: Specific properties for the different sorbents used for the simulations.

Parameter	APDES- NFC	Tri-PE- MCM-41	MIL- 101(Cr)-PEI- 800	Lewatit VP OC 106	Exemplary isotherm
d_p (mm)	1.3 [75]	1.0 [77]*	0.996*	0.688 [264]	0.996*
ρ_s (kg/m ³)	1589.9 [265]	2120 [266]	1590*	1070 [267]	1590*
ρ_p (kg/m ³)	61 [268]	550	500 [53]	880 [264]	497.8*
f_b (-)	0.908*	0.582*	-	0.773*	0.754*
ρ_b (kg/m ³)	55.4 [75]	320.0 [266]	377.1*	680.0 [269]	375.4*
$c_{p,s}$ (J/kg/K)	2070 [75]	1000 [73]	892.5 [53]	1580 [270]	1514.2*

*calculated values

Details regarding the modeling of the solid sorbent process are listed in the table below.

TABLE A.15: Parameters for modeling the adsorption unit

Parameter	Value	Source
Plate containing sorbent		
Length	0.05 m	
Internal radius	0.005 m	
External radius	0.005001 m	
Heat capacity wall	2.457×10^6 J/(K m ³)	
Heat transfer fluid/wall/bed	6.7 W/(m ² K)	Modeled using [41]
Contactor geometry		
LxWxH	1.5x1.5x1.5m	[41]
Void fraction, $\epsilon = 1 - V_{\text{sorbent}}/V_{\text{aircontactor}}$	0.6	[41]

Heat transfer

The heat transfer coefficient was calculated by using experimental data provided in [41], where two temperature curves over the desorption time t_{des} are shown. Temperature T_1 was measured at the heating pipe, the second T_2 in the middle between two heating pipes in a frame filled with the sorbent. First, the experimental data was extracted by using a Web Plot Digitizer tool [260]. The two curves were fitted using lsqcurvefit in Matlab, as shown in the following Figure.

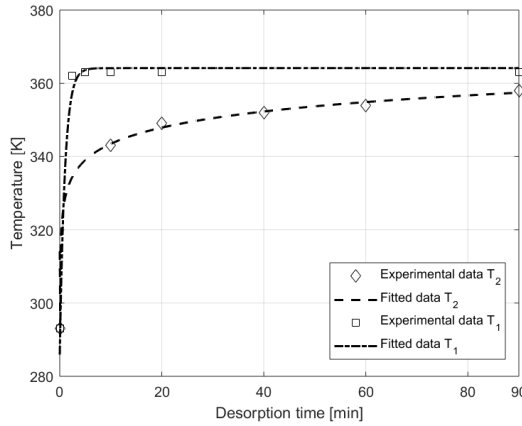


FIGURE A.23: Extracted points from experimental data by [41] and fitted curves for two different temperature curves measured at two locations in the frame.

Each temperature is calculated by using one of the following equations

$$T_1 = a + b \left(1 - \exp \left(-\frac{1}{t_{des}} \right) \right) \quad (\text{A.6})$$

$$T_2 = c + d \log(t_{des} + e) \quad (\text{A.7})$$

with t_{des} being the desorption time and parameter $a - e$ empirical constants. The fitted parameters are listed in the following Table.

TABLE A.17: Fitted Parameters for the two temperatures at different locations in the frame.

Parameter	T ₁	T ₂
a	12.94	
b	78.21	
c		55.97
d		6.33
e		-0.097
R ₂	0.999	0.995

The heat transfer was then calculated resolving a simple heat transfer equation over the length l , including the sorbent density $\rho_s = 500 \text{ kg/m}^3$ and the specific heat capacity $c_{p,s} = 1.4 \text{ kJ/kg/K}$ as well as the volume of the considered element by Gebald et al $V_s = A \cdot l = 460 \text{ cm}^3$ [41].

$$h = \frac{\alpha \frac{dT_2}{dt}}{A(T_1 - T_2) \cdot 2} \quad (\text{A.8})$$

with

$$\alpha = \rho_s V_s c_{p,s} \quad (\text{A.9})$$

Finally the resulting heat transfer coefficient is determined by calculating the mean of Equation A.8, revealing a value of $6.7 \text{ W/m}^2/\text{K}$.

Mass transfer

To account for the effect of adsorption kinetics, different values for the kinetic parameter of the linear driving force model were considered. The adopted range can be justified through mass transfer considerations.

For spherical pellets, the kinetic parameter for the linear driving force model in the case of limiting pore diffusion can be calculated with Equation A.10 [271, 272]:

$$k_p = \frac{15D_e}{R^2} \quad (\text{A.10})$$

with

$$D_e = D \frac{\epsilon}{\tau} \quad (\text{A.11})$$

Where τ is the pore tortuosity and ϵ the porosity of the sorbent particles, which in this analysis are assumed to be equal to, respectively, 3 and 0.33 [272]. D is the

diffusivity of CO₂ in air, equal to 1.6×10^{-5} m²/s. The results are reported in the following Figure.

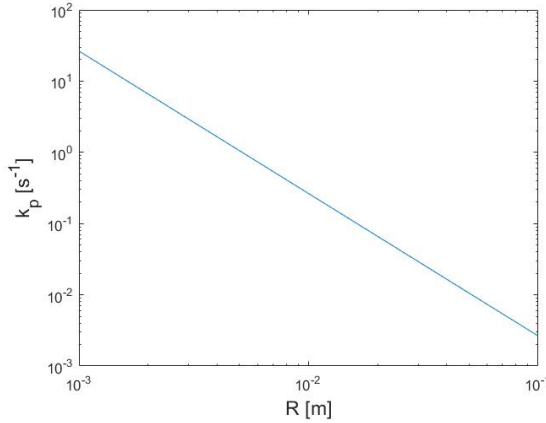


FIGURE A.24: Kinetic parameter for the linear driving force model in the case of controlling pore diffusion as a function of particle radius.

Electric energy requirement

In addition to the thermal energy requirement calculated with our model, which includes the sensible heat duty of the system as well as the isosteric heat of adsorption [77, 78], we considered the electrical energy consumption of the air blowers, the vacuum pumps and the compressors. The first two were calculated as

$$W_{\text{AirBlower}} = \frac{1}{\eta_{\text{AB}}} \Delta p \dot{V}_{\text{air}} \quad (\text{A.12})$$

$$W_{\text{pump}} = \frac{1}{\eta_{\text{VP}}} \dot{m} c_p T \left(\frac{p_{\text{out}}^{(\frac{\gamma-1}{\gamma})}}{p_{\text{in}}} - 1 \right) \quad (\text{A.13})$$

with

$$\gamma = \frac{c_p}{c_p - R} \quad (\text{A.14})$$

For the air blower the pressure drop is modeled during our simulation, with an efficiency of 60%. The efficiency of the vacuum pump depends on the vacuum pressure and decreases linearly in the range 0.7-0.6 for high to medium pressure and 0.6-0.3 for medium to low pressure.

The energy consumption for the compression of CO₂ was calculated for all three DAC technologies in the same way using a model in Aspen Plus.

Simple model for heat requirement

The heat requirement for this chapter is calculated using a 1-D rate-based model as explained in the main text. However, a simple method can be used to estimate reasonably well the heat requirement for solid sorbent. The equilibrium thermal energy $Q_{\text{equ,th}}$ for regeneration of the sorbents are given by the sum of the heat of reactions and the sensible heats

$$Q_{\text{equ,th}} = \sum Q_{\text{reaction}} + \sum Q_{\text{sens}} \quad (\text{A.15})$$

The specific heat of reaction $Q_{\text{reaction},i}$ of CO_2 and H_2O is calculated using equation A.16 and A.17 with the heat of reaction ΔH_i from Table A.11, the molar mass MW_i and the working capacity of the two components Δq_i calculated using the isotherm models.

$$Q_{\text{reaction,CO}_2} = \frac{\Delta H_{\text{CO}_2}}{MW_{\text{CO}_2}} \quad (\text{A.16})$$

$$Q_{\text{reaction,H}_2\text{O}} = \Delta H_{\text{H}_2\text{O}} \frac{\Delta q_{\text{H}_2\text{O}}}{\Delta q_{\text{CO}_2} MW_{\text{CO}_2}} \quad (\text{A.17})$$

The calculation of the sensible heat of the sorbent $Q_{\text{sens,sorbent}}$ is carried out using equation A.18, with the ambient temperature $T_{\text{ads}} = 298 \text{ K}$, the desorption temperature $T_{\text{des}} = 373 \text{ K}$ the heat capacity of the sorbent $c_{p,\text{sorbent}}$ from Table A.14 and the working capacity of CO_2 .

$$Q_{\text{sens,sorbent}} = c_{p,\text{sorbent}}(T_{\text{des}} - T_{\text{ads}}) \frac{1}{\Delta q_{\text{CO}_2} MW_{\text{CO}_2}} \quad (\text{A.18})$$

For the sensible heat of CO_2 and H_2O the two following equations were used, with $T_{\text{sat}} = 373 \text{ K}$ being the saturation temperature and the heat capacity $c_{p,i}$.

$$Q_{\text{sens,CO}_2} = c_{p,\text{CO}_2}(T_{\text{des}} - T_{\text{ads}}) \quad (\text{A.19})$$

$$Q_{\text{sens,H}_2\text{O}} = (c_{p,\text{H}_2\text{O}}(T_{\text{sat}} - T_{\text{ads}}) + c_{p,\text{vap}}(T_{\text{ads}} - T_{\text{sat}})) \frac{\Delta q_{\text{H}_2\text{O}} MW_{\text{H}_2\text{O}}}{\Delta q_{\text{CO}_2} MW_{\text{CO}_2}} \quad (\text{A.20})$$

Supplementary information for optimization

Methodology and ranges

For the optimization of both liquid solvent processes, a direct connection between Matlab R2018b and Aspen Plus V11 was set up. This was done by creating a Microsoft Component Object Model (COM) through an actxserver, with which an external

program like Aspen Plus can be controlled. Using this interface, Matlab can call Aspen Plus, write data into the program, run it and then read and close it again. The alkali scrubbing process has been simulated in Aspen Plus using two separate flowsheets: one devoted to modelling the capture of CO_2 and a second for the solvent regeneration cycle. A direct connection between the two flowsheets has been established again via Matlab. For the multi-objective optimization in Matlab, a non dominated sorting genetic algorithm version II (NSGA-II) was applied [273]. For the algorithm the size of the population is set to 100 and the number of generations, i.e. iterations, is set to 20.

The decision variables for the three processes are listed in Table A.7.

Maximum air velocity for the solid sorbent process

Identifying the upper velocity limits of the presented air contactor design would require experimental pressure drops-velocity insights, therefore, as proxy for this, we use the minimum fluidization velocity u_{mf} as the upper bound for the velocity of the feed stream. The velocity is calculated in the form of [274]

$$\frac{d_p u_{mf} \rho_a}{\mu} = \left[(28.7)^2 + 0.0494 \left(\frac{d_p^3 \rho_a (\rho_s - \rho_a) g}{\mu^2} \right) \right]^{1/2} - 28.7 \quad (\text{A.21})$$

with the particle diameter d_p , the sorbent ρ_s and air $\rho_a=1.1839 \text{ kg m}^{-3}$ density, the viscosity of the air stream $\mu=0.02 \text{ g m}^{-1} \text{ s}^{-1}$ and the gravity constant $g=9.81 \text{ m s}^{-2}$. The resulting velocity is shown in the Table below.

TABLE A.18: Maximal velocity for the considered materials.

Material	u_{air} (m/s)
APDES-NFC	0.619
Tri-PE-MCM-41	0.453
Lewatit VP OC 106	0.187
Exemplary isotherm	0.453

Supplementary information: results

Alkali Scrubbing

The effect of the design variables is shown in Figure A.2. The absorber loading tends to increase, albeit in a scattered fashion, when moving on the Pareto towards higher productivity; this is because higher loading allows for more CO_2 capture when keeping the contactor volume fixed. In addition, the effect of the moisture

content on the performance seems to be negligible. The air velocity, on the other hand, has a great influence on the energy demand and productivity. We examined this behaviour in more detail, by carrying out a second optimization where we only varied the air velocity within a range in line with absorption, $u_{\text{air}} = 0.5 - 2.5$ m/s, while keeping the absorber loading and the water content constant at $\zeta = 20$ kmol_{KOH}/kmol_{CO₂} and $w_{\text{H}_2\text{O}} = 0.18$ respectively. The comparison of the resulting Pareto front is can be found in following Figure a), showing a similar performance for both curves. In addition, in the following Figure b) the breakdown of the energy consumption for two extreme Pareto points and both optimization runs is plotted. The main difference between the Pareto points A and B is due to an increase in the energy consumption of the air blower for a higher productivity, while the resulting breakdown of both optimization runs is similar. For a higher air velocity, the increase in the energy consumption of the air blower is proportionally higher than the increase in the captured amount of CO₂, which results in a higher specific energy consumption of the air blower.

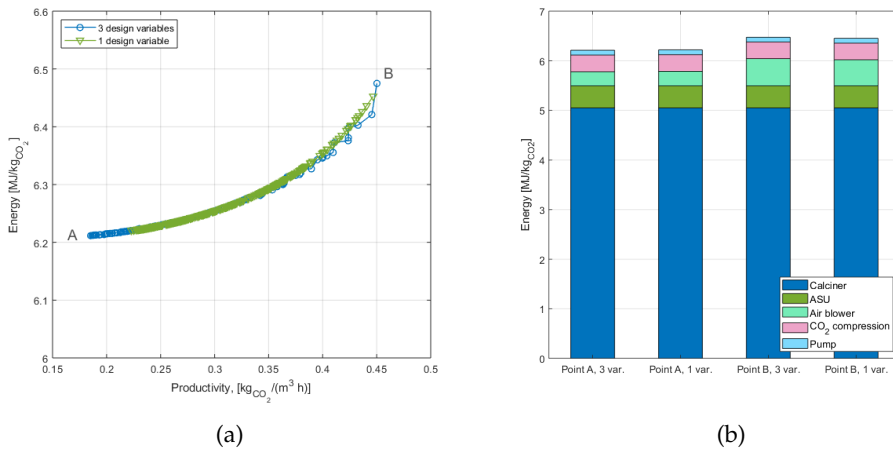


FIGURE A.25: Comparison of different design variables for the KOH process. a) Pareto front for optimizing three design variables, i.e. absorber loading, air velocity and water content, in blue and one design variable, i.e. air velocity, in green. b) Breakdown of the energy consumption for the two extreme Pareto points and both optimization runs using 3 design variables (3 var.) and one design variable (1 var.).

In addition, the capture rate decreases for higher air velocity, see the Figure below.

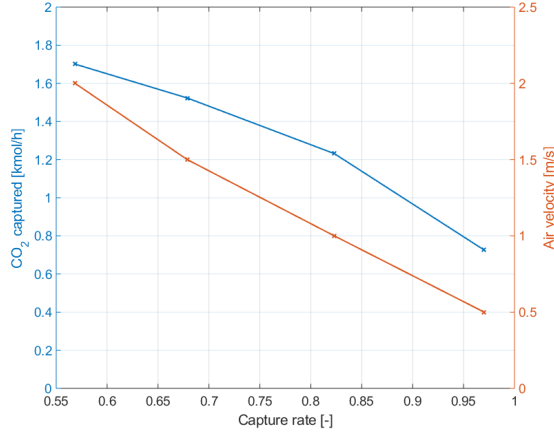


FIGURE A.26: Relation of the captured CO₂ in kmol/h, simulated with 6 air contactor blocks, and the air velocity with the capture rate.

Supplemental Material for Analysis with varying ambient conditions

Thermodynamic Model

The model equations are given below. For a further explanation, we refer to literature. [50, 120, 275]. Component mass balance:

$$\varepsilon_t \frac{\partial c_i}{\partial t} + \frac{\partial(uc_i)}{\partial z} + \rho_b \frac{\partial q_i}{\partial t} = 0 \quad i = 1, \dots, N \quad (\text{A.22})$$

Total mass balance:

$$\varepsilon_t \frac{\partial c}{\partial t} + \frac{\partial(uc)}{\partial z} + \rho_b \sum_{j=1}^N \frac{\partial q_j}{\partial t} = 0 \quad (\text{A.23})$$

Mass transfer: linear driving force model:

$$\frac{\partial q_i}{\partial t} = k_i(q_i^* - q_i) \quad i = 1, \dots, N \quad (\text{A.24})$$

Energy balance fluid and solid phase:

$$(\varepsilon_t C_g + \rho_b C_s + \rho_b C_{\text{ads}}) \frac{\partial T}{\partial t} - \varepsilon_t \frac{\partial P}{\partial t} + u C_g \frac{\partial T}{\partial z} - \rho_b \sum_{j=1}^N (-\Delta H_j) \frac{\partial q_j}{\partial t} + \frac{2h_L}{R_i} (T - T_{\text{amb}}) = 0 \quad (\text{A.25})$$

Momentum balance: Ergun equation:

$$\frac{\partial P}{\partial z} = - \frac{150\mu(1 - \varepsilon_b)^2 \rho}{\varepsilon_b^3 d_P^2} u - \frac{1.75(1 - \varepsilon_b) \rho}{\varepsilon_b^3 d_P} |u|u \quad (\text{A.26})$$

Equation of state: ideal gas law:

$$c_i = \frac{y_i P}{RT} \quad (\text{A.27})$$

The optimization problem is defined as:

$$Pr = \frac{\dot{m}_{\text{CO}_2}}{V_{\text{aircontactor}}} \quad (\text{A.28})$$

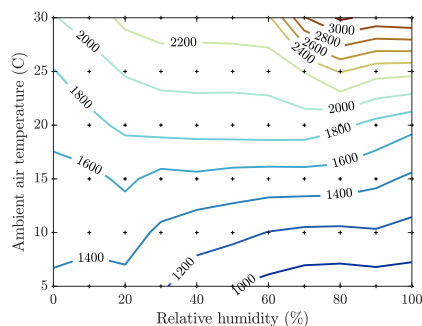
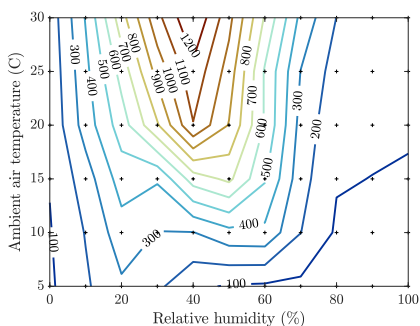
where \dot{m}_{CO_2} is the mass rate of CO₂ captured from the air and $V_{\text{aircontactor}}$ the volume of the air contactor. Total energy consumption reads as:

$$e = \frac{1}{\dot{m}_{\text{CO}_2}} \left[\dot{Q}_{\text{purge}} \left(1 - \frac{T_0}{T_{\text{purge}}} \right) + \dot{Q}_{\text{reg}} \left(1 - \frac{T_0}{T_{\text{reg}}} \right) + \dot{W}_{\text{vac,purge}} + \dot{W}_{\text{vac,prod}} + \dot{W}_{\text{blower}} + \dot{W}_{\text{comp}} \right] \quad (\text{A.29})$$

where \dot{Q}_{purge} and \dot{Q}_{reg} represent the heat required for the purge and regeneration step, $\dot{W}_{\text{vac,purge}}$ as well as $\dot{W}_{\text{vac,prod}}$ the required electrical energy of the vacuum pump, \dot{W}_{blower} the energy for the air blower and \dot{W}_{comp} the energy for CO₂ compression. All input variables are calculated in our optimization framework.

TABLE A.19: Fitted Parameters for single CO₂ and H₂O isotherms using the Toth-cp as well as the GAB model, respectively. The fitted data of the exemplary isotherm for CO₂ was taken from [120] and for the H₂O isotherm from APDES-NFC sorbent fitted by Gebald et al. [41].

Toth-cp ($T_0 = 298K$)					
Chemisorption					
b_0 (1/MPa)	ΔH (kJ/mol)	t_0 (-)	α (-)	n_{so} (mol/kg)	χ (-)
426000	64.19	0.282	0.886	3.296	3.850
Physisorption					
b_0 (1/MPa)	ΔH (kJ/mol)	t_0 (-)	α (-)	n_{so} (mol/kg)	χ (-)
15.91	3.44	0.150	6.814	1.243	2.873
GAB					
C_0 (-)	ΔH_C (kJ/mol)	K_0 (-)	ΔH_K (kJ/mol)	$C_{m,o}$ (mol/kg)	β (K)
6.86	-5.088	2.27	-3.443	0.0208	1797



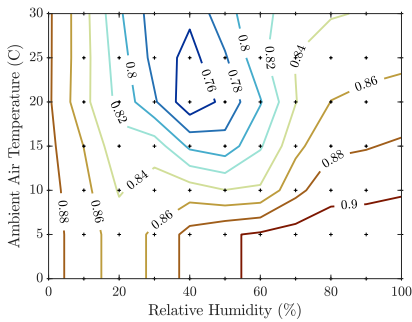
(a) Electric energy demand in kWh per t CO₂ captured (b) Thermal energy demand in kWh per t CO₂ captured

FIGURE A.27: Thermal and electric energy requirements of a DAC unit with different temperature-humidity combinations

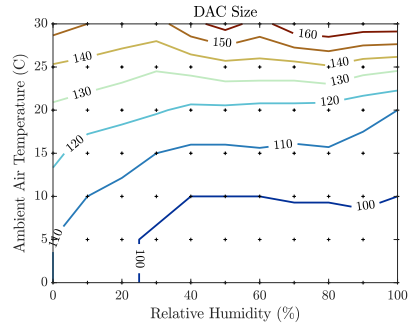
TABLE A.20: Parameters for modeling the adsorption unit

Parameter	Value	Source
Plate containing sorbent		
Length	0.05 m	
Internal radius	0.005 m	
External radius	0.005001 m	
Heat capacity wall	$2.457 \times 10^6 \text{ J/(K m}^3\text{)}$	
Heat transfer fluid/wall/bed	$6.7 \text{ W/(m}^2\text{K)}$	Modeled using data from Gebald et al. (2012) [276]
Contactor geometry		
LxWxH	$1.5 \times 1.5 \times 1.5 \text{ m}$	[276]
Void fraction*	0.6	[276]

* $\epsilon = 1 - V_{\text{sorbent}}/V_{\text{aircontactor}}$



(a) Investment Cost Share



(b) Size of the DAC unit

FIGURE A.28: Investment Cost Share and Size of the DAC unit

TABLE A.22: Input Data to the standalone DAC model

	Netherlands	Spain	California
Average Relative Humidity (%)	80.2	62.6	41.1
SD Relative Humidity	13.3	14.4	23.1
Average Temperature (°C)	11.1	18.2	17.7
SD Temperature (°C)	6.4	6.1	10.3
Average Irradiance (W/m ²)	120.2	191.4	239.3
SD Irradiance (W/m ²)	194.6	274.9	320.5
Average Wind Speed (m/s)	4.8	1.4	2.2
SD Wind Speed (m/s)	2.7	0.8	1.4
Price (el, EUR ct/kWh)		3.20	
Price (th, EUR ct/kWh)		0.50	
Module Investment Cost (EUR)		200000	
Lifetime (years)		25	
Interest rate		0.1	
Annual Maintenance Cost per Module (% of annualized investment costs)		4%	
Efficiency of ohmic heating		0.97	

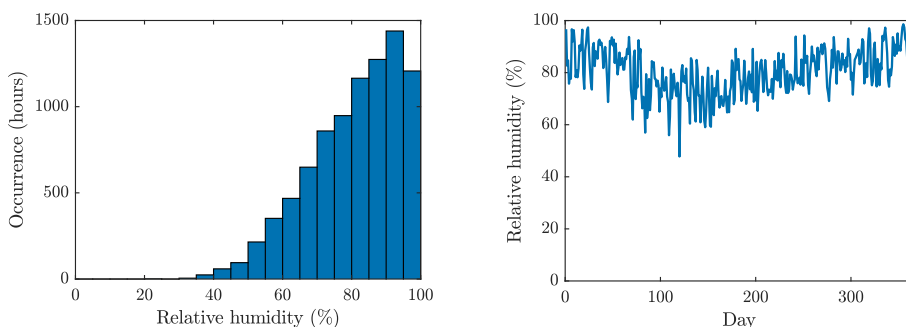


FIGURE A.29: Humidity, Schiphol (NL), 2017.

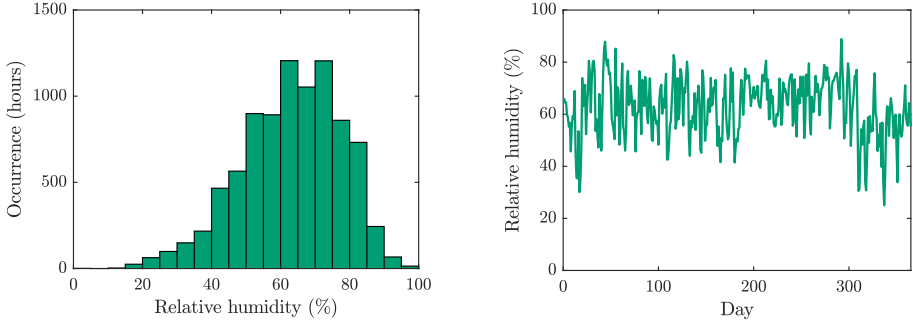


FIGURE A.30: Humidity, Barcelona (ES), 2017.

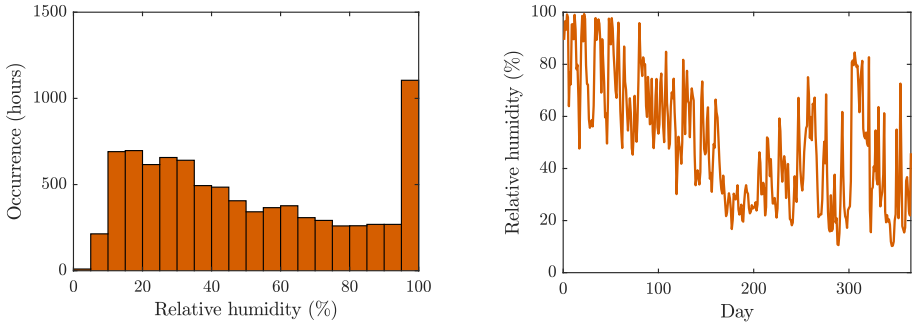


FIGURE A.31: Humidity, Lancaster (US), 2017.

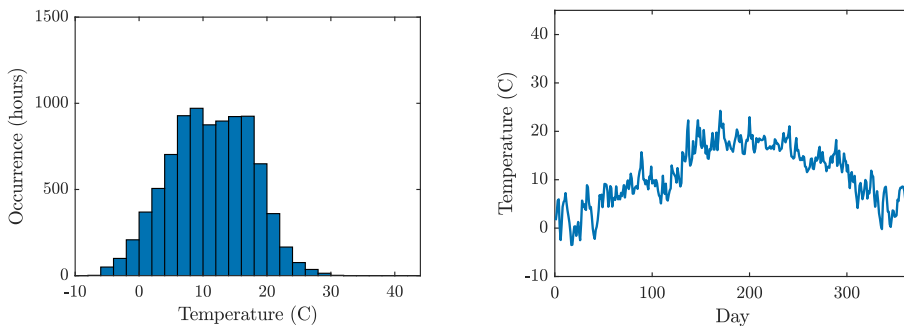


FIGURE A.32: Ambient Temperature, Schiphol (NL), 2017.

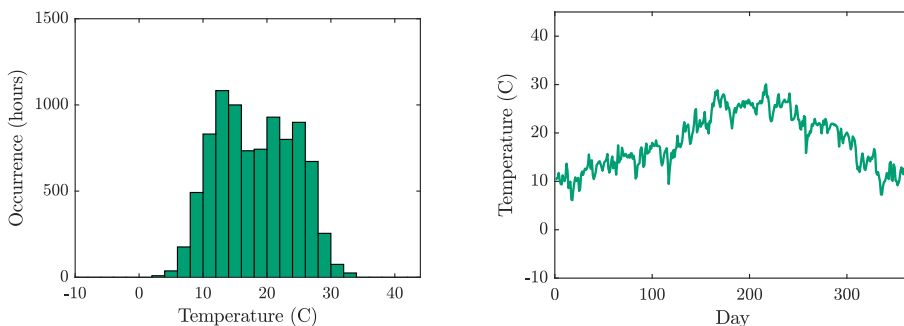


FIGURE A.33: Ambient Temperature, Barcelona (ES), 2017.

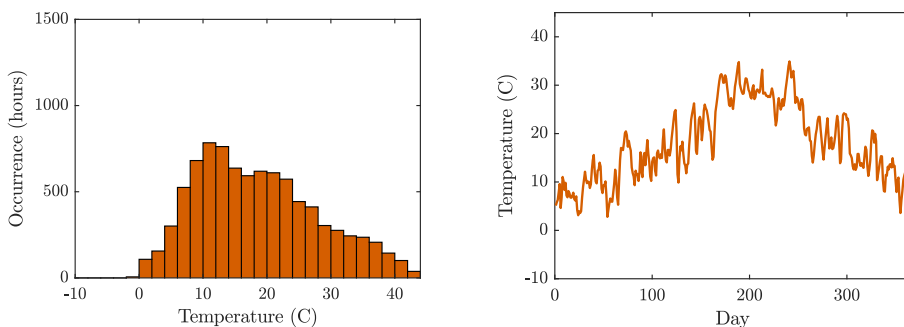


FIGURE A.34: Ambient Temperature, Lancaster (US), 2017.

Testing different sorbent behaviors Different sorbents are expected to behave similarly from ambient temperature increases, however, they might have a different

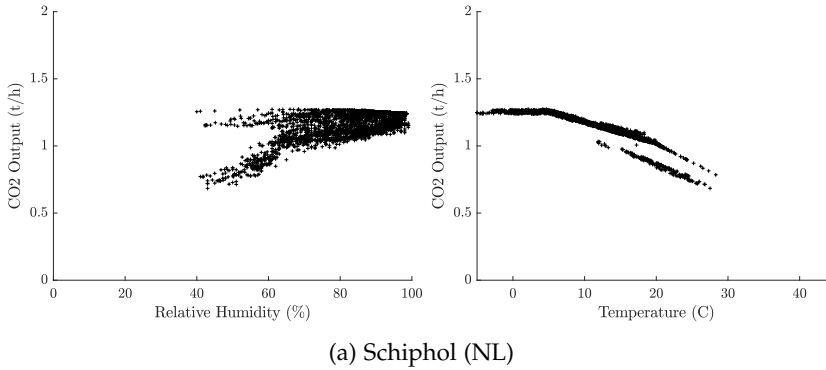


FIGURE A.35: Productivity of the DAC unit for flexible demand and flexible operation

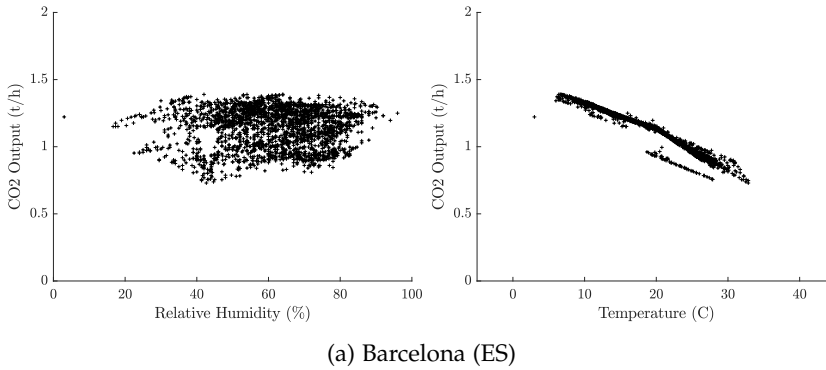


FIGURE A.36: Productivity of the DAC unit for flexible demand and flexible operation

performance dependency with humidity. We thus used the available performance data from the thermodynamic model and (i) removed the humidity dependency by taking performance data for a relative humidity of 0% for all temperatures and (ii) inverted the humidity dependency. Figure A.41 and A.43 show the original performance data and the performance data with the two modifications. The respective capture costs and energy requirements are depicted in Figure A.38.

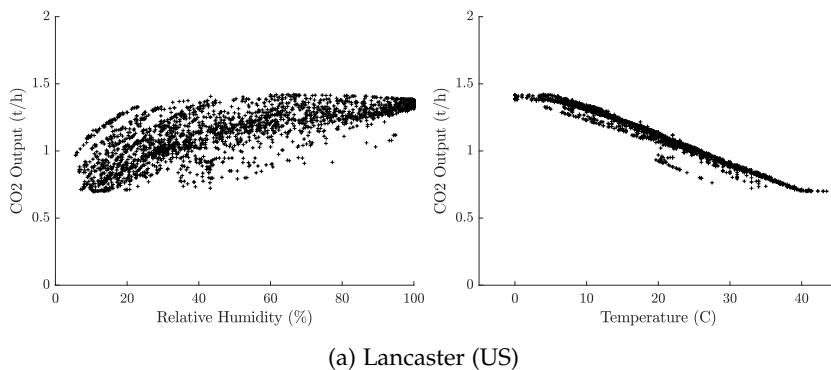


FIGURE A.37: Productivity of the DAC unit for flexible demand and flexible operation

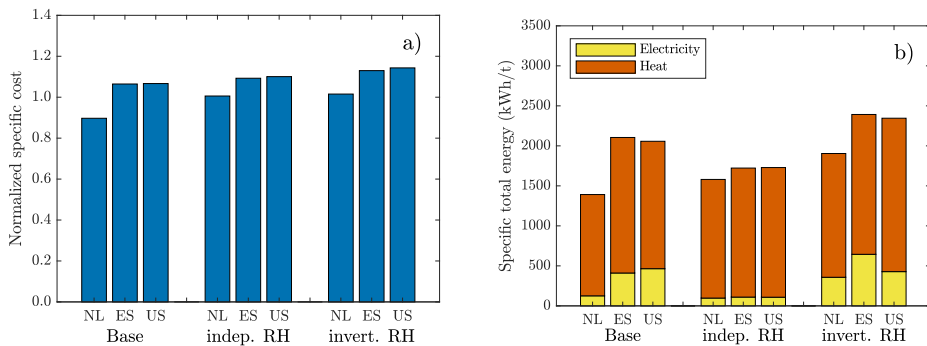


FIGURE A.38: Cost and energy results for the stand-alone model for different sorbent behaviors. a) Specific CO₂ capturing cost (Normalized to 300Dollar/t). b) Specific energy requirements.

FIGURE A.39: Original Performance Data

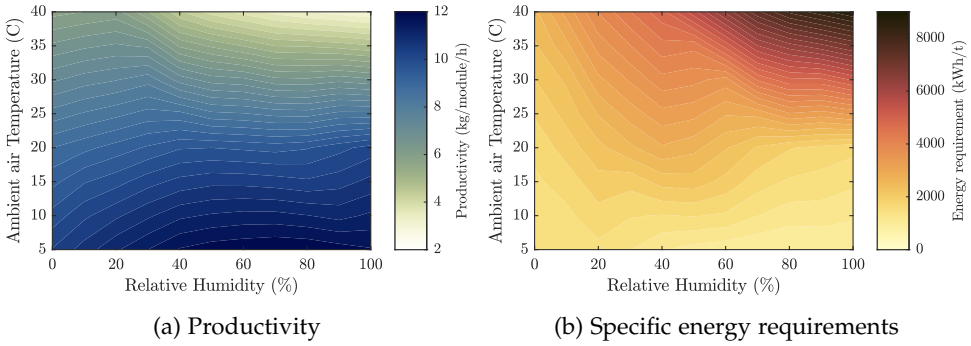


FIGURE A.40: Performance Data for independent humidity dependency

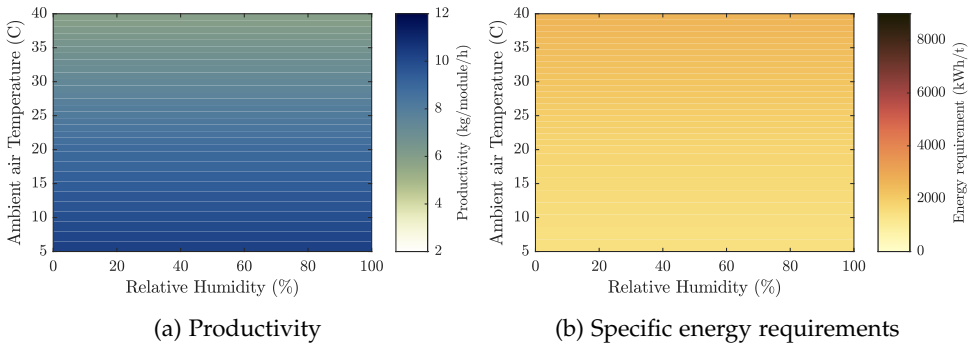


FIGURE A.41: Productivity and specific energy requirements for maximal productivity optimization for different sorbent behaviors

FIGURE A.42: Performance Data for inverted humidity dependency

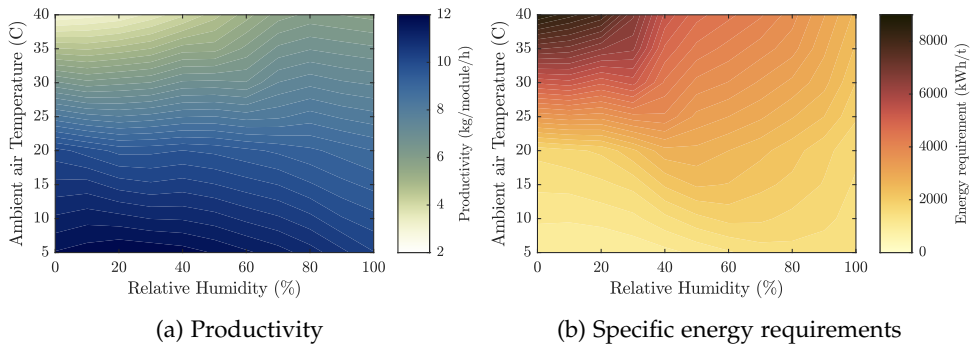


FIGURE A.43: Productivity and specific energy requirements for maximal productivity optimization for different sorbent behaviors

B

APPENDIX FOR CHAPTER 3

Modelling details

Blow-down step: pressure profile and time

The time for the blow-down step is mainly dependent on the vacuum pressure. By fitting simulation data from the 1D model, the following equation was received

$$t_{\text{BD}} = \frac{-10p_{\text{vac}} + a}{b} \quad (\text{B.1})$$

with the parameters listed in Table B.1. Since the profile mainly varies with pressure and does not show a notable dependence on the density or temperature of the material, the fitting was carried out for a small dataset for one material (case s2 E-A) and different vacuum pressures over time.

TABLE B.1: Fitting parameters for the time of the blow-down step.

a	b
20.70	20 000

The pressure at each sub-step p_{vac}^k is calculated using the following equation

$$p_{\text{vac}}^k = \frac{1}{10} \left(\frac{a}{p_{\text{vac}}^b} \exp\left(c t_{\text{BD}}^k\right) + p_{\text{vac}} \exp\left(\frac{d}{p_{\text{vac}}^b} t_{\text{BD}}^k\right) \right) \quad (\text{B.2})$$

The fitted parameters are listed in Table B.2

TABLE B.2: Fitting parameters for the pressure profile of the blow-down step.

a	b	c	d
0.18627	0.85	-0.1238	-7.138 10^{-05}

Heating step: temperature profile and time

The training data of the neural network for determining the heating time can be found in Figure B.1.

The temperature profile was received by fitting several profiles retrieved from simulations using the 1D model. The profile is dependent on the desorption temperature and the heating time

$$T_{\text{heat}}^k = (a + T_{\text{des}} + b \cdot T_{\text{des}}^c) * \text{atan} \left(\frac{t_{\text{heat}}^k - d \cdot 10^9 \cdot T_{\text{des}}^e}{f} \right) + (T_{\text{des}} - g) \cdot h \quad (\text{B.3})$$

The fitted parameters are listed in Table B.4.

TABLE B.4: Fitting parameters for the temperature profile of the heating step.

a	b	c	d	e	f	g	h
-687.31	2791.97	0.346	-661.53	-4.296	42.005	-34162.55	0.00867

Cooling step: profile

The time of the cooling step is fixed to 350 seconds, similar to the 1D model simulations. The temperature profile is calculated similar to the heating step, by fitting data from the 1D model. The fitting equation is

$$T_{\text{cooling}}^k = 293 + a \cdot T_{\text{des}} \cdot \exp\left(b \cdot t_{\text{cool}}^k\right) \quad (\text{B.4})$$

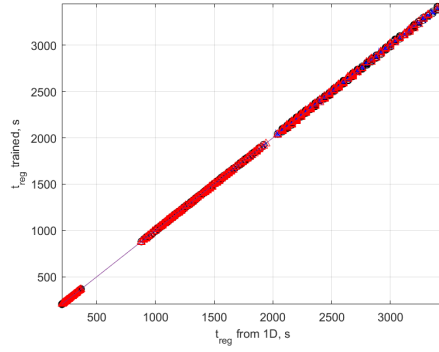


FIGURE B.1: Resulting training data (blue symbols) from the neural network together with the validation data (red) and the testing data (black).

with the parameters listed in Table B.5.

TABLE B.5: Fitting parameters for the temperature profile of the cooling step.

a	b
0.17485	-0.02629

Adsorption step

The total time of the adsorption step can be determined by including the air velocity u_{air} and the geometry of the considered sorbent

$$t_{\text{ads}} = \frac{N_{\text{ads}}^{\text{feed}} M_{\text{air}}}{u_{\text{air}} A \rho_{\text{air}}} \quad (\text{B.5})$$

with M_{air} being the molar mass of the air, A the column cross section and ρ_{air} the density of the air.

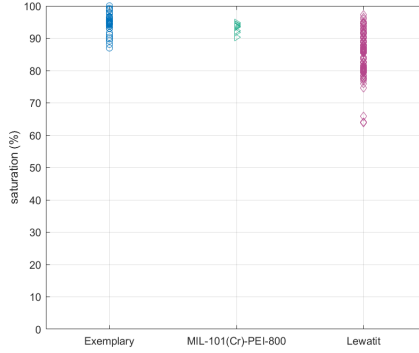


FIGURE B.2: Saturation level from simulations using the 1D model.

Saturation level

Since we are considering an equilibrium model, the saturation at the end of the adsorption step or rather at the begin of the blow-down step is generally 100%. A more realistic picture of the saturation level gives the simulation with the detailed model, which shows a lower saturation level. Figure B.2 shows the saturation level calculated for the Pareto points from the optimization of three different materials (the same optimization as used for the validation). The saturation level α was calculated for each grid point of the bed by calculating the actual loading referred to the full saturation at ambient conditions

$$\alpha = \sum_{n=1}^{N_{\text{grid}}} \frac{q_{\text{CO}_2}^* ((T_{\text{amb}}, p_{\text{amb}}, y_{\text{CO}_2, \text{feed}}) - q_{\text{CO}_2}^n ((T, p, y_{\text{CO}_2}))}{q_{\text{CO}_2}^* ((T_{\text{amb}}, p_{\text{amb}}, y_{\text{CO}_2, \text{feed}})} \quad (\text{B.6})$$

with $q_{\text{CO}_2}^n$ being the actual loading at the respective grid point and $q_{\text{CO}_2}^*$ the loading at equilibrium.

Using this data, a neural network was trained to determine the saturation level dependent on the particle density ρ_p , the desorption temperature T_{des} , the vacuum pressure p_{vac} as well as the air volume flow \dot{V}_{feed}

$$\alpha = \text{NN}(\rho_{\text{particle}}, T_{\text{des}}, p_{\text{vac}}, \dot{V}_{\text{feed}}) \quad (\text{B.7})$$

The training, testing and validation results can be found in Figure B.3.

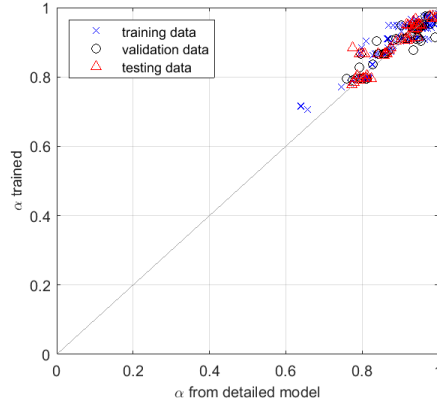


FIGURE B.3: Training, testing and validation results.

Isosteric heat of adsorption

The isosteric heat of adsorption (ΔH_{ads}) represents the strength of the adsorbate-adsorbent interaction and is defined as the difference between the activation energy for adsorption and desorption. It can be calculated from the Clausius-Clapeyron [263] equation

$$\left(\frac{\partial(\ln p_{\text{CO}_2})}{\partial T} \right)_{q_{\text{equ}}} = \frac{-\Delta H_{\text{ads}}}{RT^2} \quad (\text{B.8})$$

where p_{CO_2} is the partial pressure of CO_2 (Pa), T is the absolute temperature (K) and R is the universal gas constant.

Equations of model

TABLE B.6: Equations of D model (first part).

<p>Blow-down step</p> <p>Known: $q_{\text{CO}_2}^0, q_{\text{H}_2\text{O}}^0, y_{\text{CO}_2}^0, y_{\text{H}_2\text{O}}^0, y_{\text{N}_2}^0, p$</p> <p>Calculated: $N_{\text{out}}, y_{\text{CO}_2}^k, y_{\text{H}_2\text{O}}^k, y_{\text{N}_2}^k, T^k$</p> $\left(m_{s,q_{\text{CO}_2}}^{k-1} + \frac{y_{\text{CO}_2}^{k-1} p^{k-1} V \epsilon}{RT^{k-1}} \right) - y_{\text{CO}_2}^k N_{\text{out}}^k - \left(m_{s,q_{\text{CO}_2}}^k + \frac{y_{\text{CO}_2}^k p^k V \epsilon}{RT^k} \right) = 0$ $\left(m_{s,q_{\text{H}_2\text{O}}}^{k-1} + \frac{y_{\text{H}_2\text{O}}^{k-1} p^{k-1} V \epsilon}{RT^{k-1}} \right) - y_{\text{H}_2\text{O}}^k N_{\text{out}}^k - \left(m_{s,q_{\text{H}_2\text{O}}}^k + \frac{y_{\text{H}_2\text{O}}^k p^k V \epsilon}{RT^k} \right) = 0$ $\left[\left(m_{s,q_{\text{CO}_2}}^{k-1} + \frac{y_{\text{CO}_2}^{k-1} p^{k-1} V \epsilon}{RT^{k-1}} \right) + \left(m_{s,q_{\text{H}_2\text{O}}}^{k-1} + \frac{y_{\text{H}_2\text{O}}^{k-1} p^{k-1} V \epsilon}{RT^{k-1}} \right) + \left(\frac{y_{\text{N}_2}^{k-1} p^{k-1} V \epsilon}{RT^{k-1}} \right) \right] - N_{\text{out}}^k - \left[\left(m_{s,q_{\text{CO}_2}}^k + \frac{y_{\text{CO}_2}^k p^k V \epsilon}{RT^k} \right) + \left(m_{s,q_{\text{H}_2\text{O}}}^k + \frac{y_{\text{H}_2\text{O}}^k p^k V \epsilon}{RT^k} \right) + \left(\frac{y_{\text{N}_2}^k p^k V \epsilon}{RT^k} \right) \right] = 0$ $m_{s,c_p} (T^k - T^{k-1}) - \Delta H_{i,s,\text{CO}_2}^{k-1} (m_{s,q_{\text{CO}_2}}^{k-1} - m_{s,q_{\text{CO}_2}}^k) - \Delta H_{i,s,\text{H}_2\text{O}}^{k-1} (m_{s,q_{\text{H}_2\text{O}}}^{k-1} - m_{s,q_{\text{H}_2\text{O}}}^k) = 0$ $1 - y_{\text{CO}_2}^k - y_{\text{H}_2\text{O}}^k - y_{\text{N}_2}^k = 0$
<p>Heating step</p> <p>Known: $q_{\text{CO}_2}^0, q_{\text{H}_2\text{O}}^0, y_{\text{CO}_2}^0, y_{\text{H}_2\text{O}}^0, y_{\text{N}_2}^0, p, T$</p> <p>Calculated: $N_{\text{out}}, y_{\text{CO}_2}^k, y_{\text{H}_2\text{O}}^k, y_{\text{N}_2}^k, Q_{\text{ex}}$</p> $\left(m_{s,q_{\text{CO}_2}}^{k-1} + \frac{y_{\text{CO}_2}^{k-1} p^{k-1} V \epsilon}{RT^{k-1}} \right) - y_{\text{CO}_2}^k N_{\text{out}}^k - \left(m_{s,q_{\text{CO}_2}}^k + \frac{y_{\text{CO}_2}^k p^k V \epsilon}{RT^k} \right) = 0$ $\left(m_{s,q_{\text{H}_2\text{O}}}^{k-1} + \frac{y_{\text{H}_2\text{O}}^{k-1} p^{k-1} V \epsilon}{RT^{k-1}} \right) - y_{\text{H}_2\text{O}}^k N_{\text{out}}^k - \left(m_{s,q_{\text{H}_2\text{O}}}^k + \frac{y_{\text{H}_2\text{O}}^k p^k V \epsilon}{RT^k} \right) = 0$ $\left[\left(m_{s,q_{\text{CO}_2}}^{k-1} + \frac{y_{\text{CO}_2}^{k-1} p^{k-1} V \epsilon}{RT^{k-1}} \right) + \left(m_{s,q_{\text{H}_2\text{O}}}^{k-1} + \frac{y_{\text{H}_2\text{O}}^{k-1} p^{k-1} V \epsilon}{RT^{k-1}} \right) + \left(\frac{y_{\text{N}_2}^{k-1} p^{k-1} V \epsilon}{RT^{k-1}} \right) \right] - N_{\text{out}}^k - \left[\left(m_{s,q_{\text{CO}_2}}^k + \frac{y_{\text{CO}_2}^k p^k V \epsilon}{RT^k} \right) + \left(m_{s,q_{\text{H}_2\text{O}}}^k + \frac{y_{\text{H}_2\text{O}}^k p^k V \epsilon}{RT^k} \right) + \left(\frac{y_{\text{N}_2}^k p^k V \epsilon}{RT^k} \right) \right] = 0$ $1 - y_{\text{CO}_2}^k - y_{\text{H}_2\text{O}}^k - y_{\text{N}_2}^k = 0$ $Q_{\text{ex}}^k - m_{s,c_p} (T^k - T^{k-1}) + \Delta H_{i,s,\text{CO}_2}^{k-1} (m_{s,q_{\text{CO}_2}}^{k-1} - m_{s,q_{\text{CO}_2}}^k) + \Delta H_{i,s,\text{H}_2\text{O}}^{k-1} (m_{s,q_{\text{H}_2\text{O}}}^{k-1} - m_{s,q_{\text{H}_2\text{O}}}^k) = 0$

TABLE B.7: Equations oD model (second part).

Cooling step

Known: $q_{\text{CO}_2}^0, q_{\text{H}_2\text{O}}^0, y_{\text{CO}_2}^0, y_{\text{H}_2\text{O}}^0, y_{\text{N}_2}^0, p, T$

Calculated: $N_{\text{in}}, y_{\text{CO}_2}^k, y_{\text{H}_2\text{O}}^k, y_{\text{N}_2}^k, Q_{\text{cool}}$

$$\left(m_s q_{\text{CO}_2}^{k-1} + \frac{y_{\text{CO}_2}^{k-1} p^{k-1} V \epsilon}{RT^{k-1}} \right) + y_{\text{CO}_2}^k N_{\text{in}}^k - \left(m_s q_{\text{CO}_2}^k + \frac{y_{\text{CO}_2}^k p^k V \epsilon}{RT^k} \right) = 0$$

$$\left(m_s q_{\text{H}_2\text{O}}^{k-1} + \frac{y_{\text{H}_2\text{O}}^{k-1} p^{k-1} V \epsilon}{RT^{k-1}} \right) + y_{\text{H}_2\text{O}}^k N_{\text{in}}^k - \left(m_s q_{\text{H}_2\text{O}}^k + \frac{y_{\text{H}_2\text{O}}^k p^k V \epsilon}{RT^k} \right) = 0$$

$$\left[\left(m_s q_{\text{CO}_2}^{k-1} + \frac{y_{\text{CO}_2}^{k-1} p^{k-1} V \epsilon}{RT^{k-1}} \right) + \left(m_s q_{\text{H}_2\text{O}}^{k-1} + \frac{y_{\text{H}_2\text{O}}^{k-1} p^{k-1} V \epsilon}{RT^{k-1}} \right) + \left(\frac{y_{\text{N}_2}^{k-1} p^{k-1} V \epsilon}{RT^{k-1}} \right) \right] + N_{\text{in}}^k - \left[\left(m_s q_{\text{CO}_2}^k + \frac{y_{\text{CO}_2}^k p^k V \epsilon}{RT^k} \right) + \left(m_s q_{\text{H}_2\text{O}}^k + \frac{y_{\text{H}_2\text{O}}^k p^k V \epsilon}{RT^k} \right) + \left(\frac{y_{\text{N}_2}^k p^k V \epsilon}{RT^k} \right) \right] = 0$$

$$1 - y_{\text{CO}_2}^k - y_{\text{H}_2\text{O}}^k - y_{\text{N}_2}^k = 0$$

$$Q_{\text{cool}}^k - m_s c_p (T^k - T^{k-1}) + \Delta H_{f,s,\text{CO}_2}^{k-1} (m_s q_{\text{CO}_2}^k - m_s q_{\text{CO}_2}^{k-1}) + \Delta H_{f,s,\text{H}_2\text{O}}^{k-1} (m_s q_{\text{H}_2\text{O}}^k - m_s q_{\text{H}_2\text{O}}^{k-1}) = 0$$

Adsorption step

Sub-step 1

Known: $q_{\text{CO}_2}^{\text{cool}}, q_{\text{H}_2\text{O}}^{\text{cool}}, y_{\text{CO}_2}^{\text{cool}}, y_{\text{CO}_2}^{\text{sat}}, p, T$

Calculated: $N_{\text{waste}}, N_{\text{feed}}, y_{\text{H}_2\text{O}}, y_{\text{N}_2}$

$$\left(m_s q_{\text{CO}_2}^{\text{cool}} + \frac{y_{\text{CO}_2}^{\text{cool}} p_{\text{amb}} V \epsilon}{RT_{\text{amb}}} \right) + y_{\text{CO}_2}^{\text{feed}} N_{\text{feed}} - \left(m_s q_{\text{CO}_2}^{\text{sat}} + \frac{y_{\text{CO}_2}^{\text{sat}} p_{\text{amb}} V \epsilon}{RT_{\text{amb}}} \right) - y_{\text{CO}_2}^{\text{cool}} N_{\text{waste}} = 0$$

$$\left(m_s q_{\text{H}_2\text{O}}^{\text{cool}} + \frac{y_{\text{H}_2\text{O}}^{\text{cool}} p_{\text{amb}} V \epsilon}{RT_{\text{amb}}} \right) + y_{\text{H}_2\text{O}}^{\text{feed}} N_{\text{feed}} - \left(m_s q_{\text{H}_2\text{O}} + \frac{y_{\text{H}_2\text{O}} p_{\text{amb}} V \epsilon}{RT_{\text{amb}}} \right) - y_{\text{H}_2\text{O}}^{\text{cool}} N_{\text{waste}} = 0$$

$$\frac{y_{\text{N}_2}^{\text{cool}} p_{\text{amb}} V \epsilon}{RT_{\text{amb}}} + y_{\text{N}_2}^{\text{feed}} N_{\text{feed}} - \frac{y_{\text{N}_2} p_{\text{amb}} V \epsilon}{RT_{\text{amb}}} - y_{\text{N}_2}^{\text{cool}} N_{\text{waste}} = 0$$

$$1 - y_{\text{CO}_2}^{\text{sat}} - y_{\text{H}_2\text{O}} - y_{\text{N}_2} = 0$$

TABLE B.8: Equations oD model (third part).

Sub-step 2

Known: $q_{\text{CO}_2}^1, y_{\text{CO}_2}^{\text{sat}}, y_{\text{H}_2\text{O}}^{\text{sat}}, y_{\text{N}_2}^1, p, T$ Calculated: $N_{\text{waste}}, N_{\text{feed}}, y_{\text{N}_2}^2$

$$\left(m_s q_{\text{CO}_2}^1 + \frac{y_{\text{CO}_2}^1 p_{\text{amb}} V \epsilon}{R T_{\text{amb}}} \right) + y_{\text{CO}_2}^{\text{feed}} N_{\text{feed}} - \left(m_s q_{\text{CO}_2}^{\text{sat}} + \frac{y_{\text{CO}_2}^{\text{sat}} p_{\text{amb}} V \epsilon}{R T_{\text{amb}}} \right) - y_{\text{CO}_2}^1 N_{\text{waste}} = 0$$

$$\frac{y_{\text{N}_2}^1 p_{\text{amb}} V \epsilon}{R T_{\text{amb}}} + y_{\text{N}_2}^{\text{feed}} N_{\text{feed}} - \frac{y_{\text{N}_2}^2 p_{\text{amb}} V \epsilon}{R T_{\text{amb}}} - y_{\text{N}_2}^1 N_{\text{waste}} = 0$$

$$1 - y_{\text{CO}_2}^{\text{sat}} - y_{\text{H}_2\text{O}}^{\text{sat}} - y_{\text{N}_2}^1 = 0$$

Details 1D model

TABLE B.9: Equations for 1D adsorption model [84]

Total mass balance
$\epsilon_t \frac{\partial(\frac{p}{T})}{\partial t} + \frac{\partial(\frac{up}{T})}{\partial x} + \rho_b R \sum_{j=1}^N \frac{\partial n_j}{\partial t} = 0$
Component mass balance
$\epsilon \frac{\partial(\frac{y_i p}{T})}{\partial t} + \frac{\partial(\frac{u y_i p}{T})}{\partial x} + \rho_b R \frac{\partial n_i}{\partial t} = 0 \quad i = 1, \dots, N$
Mass transfer (Linear driving force model)
$\frac{\partial n_i}{\partial t} = k_i (n_i^{eq} - n_i) \quad i = 1, \dots, N$
Energy balance for the fixed bed
$\begin{aligned} & (\epsilon_t C_g + \rho_b C_s + \rho_b C_{ads}) \frac{\partial p}{\partial t} - \epsilon \frac{\partial p}{\partial t} + u C_g \frac{\partial T}{\partial x} - \rho_b \sum_{j=1}^N (-\Delta H_j) \frac{\partial n_j}{\partial t} \\ & + \frac{4h_{\text{wall-bed}}}{d_i} (T - T_W) = 0 \end{aligned}$
Energy balance for the bed wall
$\frac{\partial T_W}{\partial t} = \frac{4}{C_{p,W}(d_0^2 - d_i^2)} (d_i h_{\text{wall-bed}} (T - T_W) + d_0 h_{\text{fluid-wall}} (T_{\text{fluid}} - T_w))$
Momentum balance (Ergun equation)
$\frac{\partial p}{\partial x} = - \frac{150\mu(1-\epsilon_b)^2}{\epsilon_b^3 d_p^2} u - \frac{1.75(1-\epsilon_b)\rho}{\epsilon_b^3 d_p} u u$

The decision variables for the detailed process simulation are listed in Table B.11.

TABLE B.11: Design variables for optimizing the process, including lower and upper bound. The upper bound for the air volume stream is calculated using the minimum fluidization velocity [120]. For the oD model only T_{des} , p_{vac} and \dot{V}_{air} are considered as decision variables.

Variable	Range			
	APDES-NFC	MIL-101(Cr)- PEI-800	Lewatit VP OC 106	Exemplary
t_{ads} (s)			100-10000	
t_{des} (s)			50-2200	
t_{purge} (s)			1-400	
p_{vac} (bar)			0.1-0.9	
T_{des} (K)			363-373	
ΔT_{purge} (K)			1-60	
\dot{V}_{air} (m^3/s)	2.0×10^{-7} -1.2×10^{-5}	2.0×10^{-7} -8.9×10^{-6}	2.0×10^{-7} -3.7×10^{-6}	2.0×10^{-7} -8.9×10^{-6}

Details regarding the modeling of the solid sorbent process are shown in Table B.12.

TABLE B.12: Parameters for modeling the adsorption unit using the 1D model.

Parameter	Value	Source
Plate containing sorbent		
Length	0.05 m	
Internal radius	0.005 m	
External radius	0.005001 m	
Heat capacity wall	$2.457 \times 10^6 \text{ J}/(\text{K m}^3)$	
Heat transfer fluid/wall/bed	$6.7 \text{ W}/(\text{m}^2\text{K})$	Modeled using [41]
Contactor geometry		
LxWxH	1.5x1.5x1.5m	[41]
Void fraction, $\epsilon = 1 - \frac{V_{\text{sorbent}}}{V_{\text{aircontactor}}}$	0.6	[41]

Validation

TABLE B.14: Different combinations for CO₂ and H₂O isotherms.

CO ₂ isotherm	H ₂ O isotherm		
	APDES-NFC	MCF-APS-hi	Lewatit VP OC 106
APDES-NFC	s1: A-A	-	-
Exemplary	s2: E-A	s3: E-M	s4: E-L
MIL-101(Cr)-PEI-800	s5: MP-A	s6: MP-M	s7: MP-L
Lewatit VP OC 106	-	-	s8: L-L

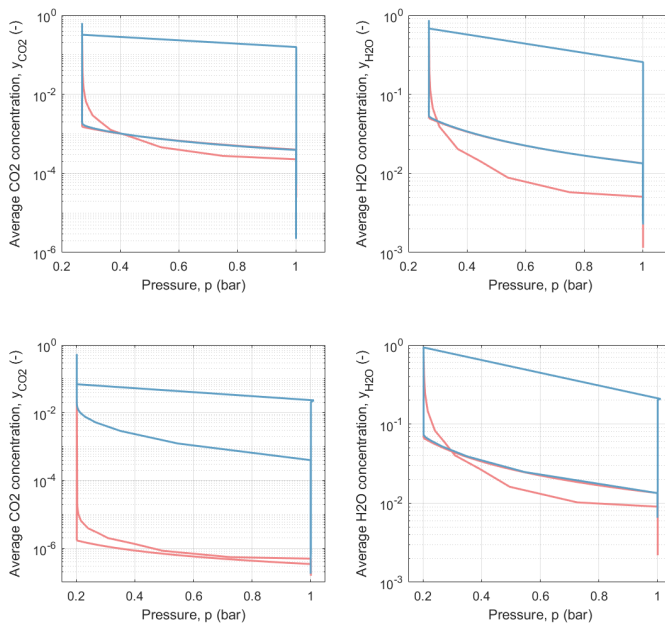


FIGURE B.4: Composition of CO₂ and H₂O over the pressure for the whole cycle for case s2/E-A (a) and b)), and Cr-MIL(101) (c) and d)).

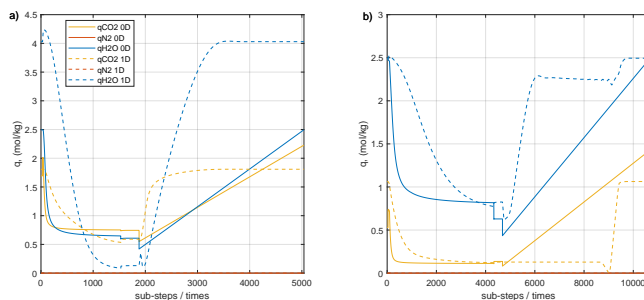


FIGURE B.5: Profiles of the adsorbed amount during one cycle, corresponding to Figure 4 in the main text. a) shows case s2/E-A and b) Cr-MIL(101).

Parity plots varying CO₂ concentration

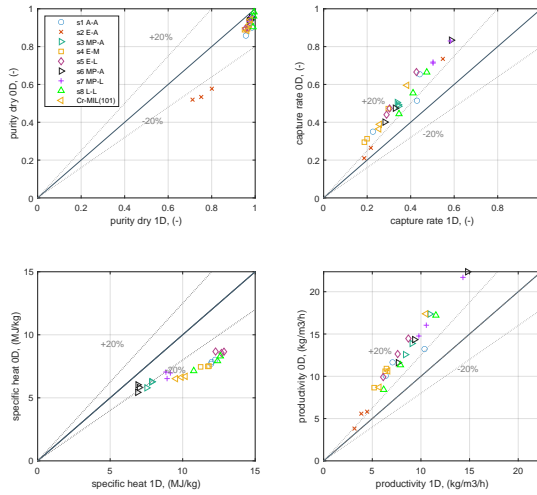


FIGURE B.6: Parity plot for $y_{CO_2} = 0.1\%$.

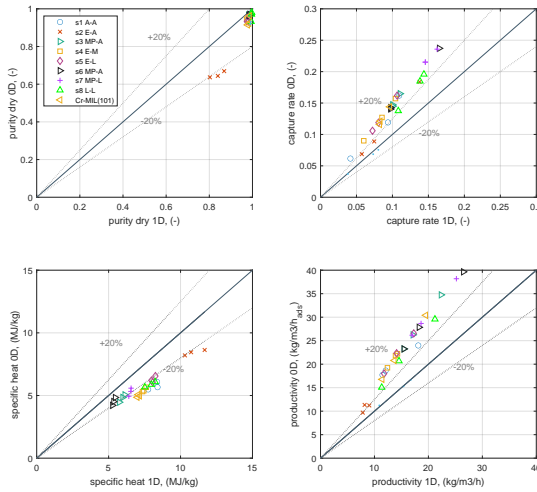


FIGURE B.7: Parity plot for $y_{CO_2} = 1.0\%$.

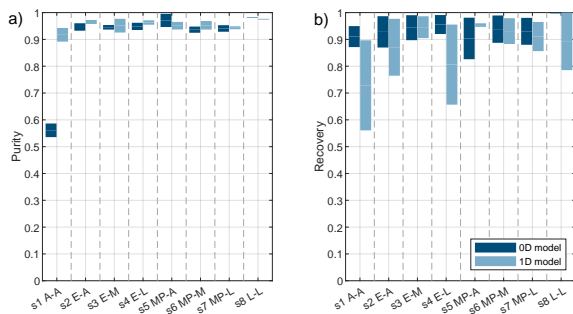


FIGURE B.8: a) Purity and b) capture rate from optimizing the materials during the validation for the oD and 1D model.

The range of the resulting purity and recovery for both the oD and the 1D model are shown in Figure B.8.

Screening

The NIST/ARPA-E database, the database of novel and emerging adsorbents by the National Institute of Standards and Technology (NIST) includes data from published studies, both real and hypothetical. Since the database includes thousands of isotherm data files, not only for CO₂ adsorption, but also many other gases, it is important to first filter the materials. We use a script written in MATLAB to run through the materials filter the suitable adsorbents. The approach is graphically shown in Figure B.9. During the filtering process, we are also excluding all data sets for which only one temperature is available. This is necessary for the following step, where the remaining isotherms are fitted by temperature dependent isotherm models. The fitting process itself includes several steps, which are shown in the flowchart in Figure B.10. For the objective function during the fitting, the normalized standard deviation was applied, which is commonly used to fit isotherm models to experimental data [41, 87, 261, 262]. It includes the adsorbed amount determined experimentally q_{exp} , the amount adsorbed as predicted by the model q_{fit} and the total number of experimental points N , and is calculated in the form of

$$err = \sqrt{\frac{\sum \left[\frac{(q_{exp} - q_{fit})}{q_{exp}} \right]^2}{N - 1}} \cdot 100 \quad (\text{B.9})$$

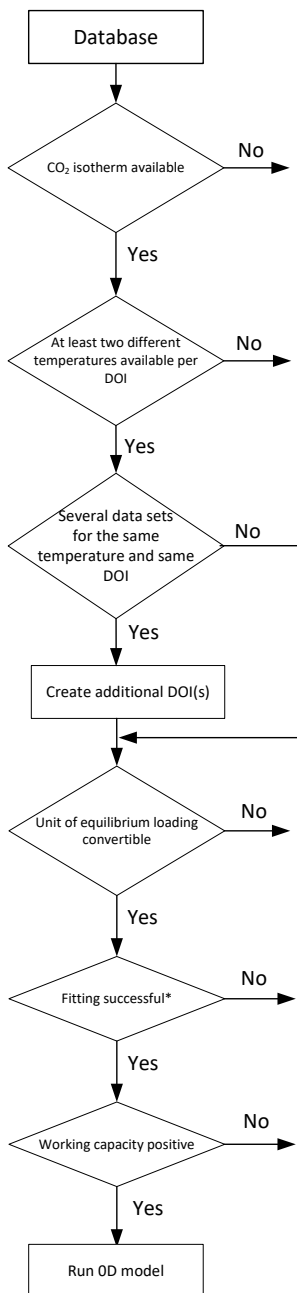


FIGURE B.9: Flowchart describing the filtering process of the adsorbents from the NIST/ARPA-E database.

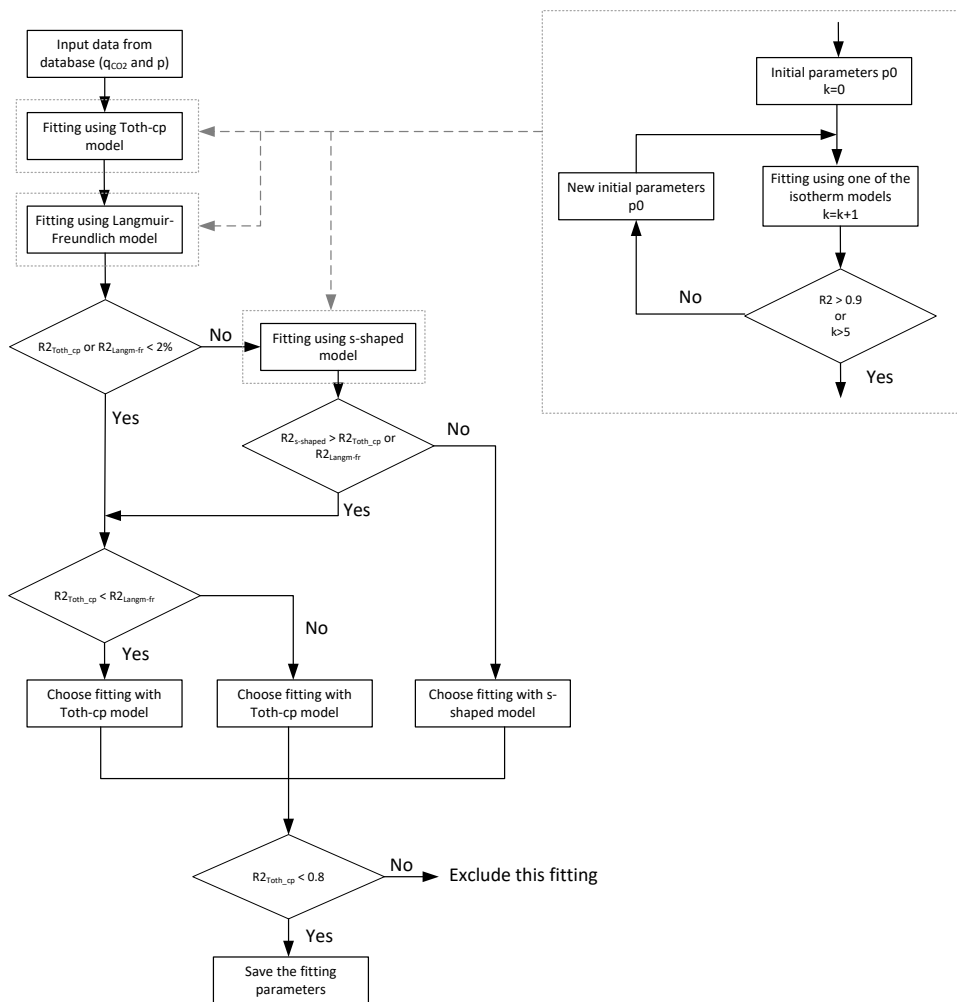


FIGURE B.10: Flowchart fitting.

which is minimized using the inbuilt Matlab optimization routine *fmincon* together with the *sequential quadratic programming (SQP)* algorithm.

The error is expressed by

$$R2 = \frac{\sum (q_{\text{exp}} - q_{\text{fit}})^2}{\sum (q_{\text{exp}} - \overline{q_{\text{exp}}})^2} \quad (\text{B.10})$$

with $\overline{q_{\text{exp}}}$ being the mean of the experimental data.

TABLE B.15: Equations of the different isotherm models.

Model	Equation
Toth-cp	equ. 1 $q_{\text{CO}_2} = n_{s,c} \frac{b_c p y_{\text{CO}_2}}{(1+(b_c p y_{\text{CO}_2})^{t_c})^{1/t_c}} + n_{s,p} \frac{b_p p y_{\text{CO}_2}}{(1+(b_p p y_{\text{CO}_2})^{t_p})^{1/t_p}}$ $n_{s,c/p} = n_{s0,c/p} \exp\left(Xi_{c/p} \left(1 - \frac{T}{T_0}\right)\right)$ $b_{c/p} = b_{0,c/p} \exp\left(\frac{\Delta H_{c/p}}{RT_0} \left(\frac{T_0}{T} - 1\right)\right),$ $t_{c/p} = t_{0,c/p} + \alpha_{c/p} \left(1 - \frac{T_0}{T}\right)$
DSL	equ. 2 $q_{\text{CO}_2} = n_1 \frac{b(y_{\text{CO}_2} p)}{1+b(y_{\text{CO}_2} p)} + n_2 \frac{d(y_{\text{CO}_2} p)}{(1+d(y_{\text{CO}_2} p))}$ $b = b_0 \exp\left(\frac{H_b}{RT}\right), d = d_0 \exp\left(\frac{H_d}{RT}\right)$
Toth	equ. 3 $q_{\text{CO}_2} = n_s \frac{b p y_{\text{CO}_2}}{(1+(b p y_{\text{CO}_2})^t)^{1/t}}$ $n_s = n_{s0} \exp\left(Xi \left(1 - \frac{T}{T_0}\right)\right)$ $b = b_0 \exp\left(\frac{\Delta H}{RT_0} \left(\frac{T_0}{T} - 1\right)\right), t = t_0 + \alpha \left(1 - \frac{T_0}{T}\right)$
Langmuir-Freundlich	equ. 4 $q_{\text{CO}_2} = n_s \frac{(b p y_{\text{CO}_2})^{1/t}}{(1+(b p y_{\text{CO}_2})^{1/t})}$ $n_s = n_{s0} \exp\left(Xi \left(1 - \frac{T}{T_0}\right)\right)$ $b = b_0 * \exp\left(\frac{\Delta H}{(RT_0)} \left(\frac{T_0}{T} - 1\right)\right)$ $t = t_0 + \alpha \left(1 - \frac{T_0}{T}\right)$
S-shaped	equ. 5 $q_{\text{CO}_2} = q_L (1 - w) + q_U w$ $q_L = \frac{q_{L,0} b_L (y_{\text{CO}_2} p)}{(1+b_L (y_{\text{CO}_2} p))}$ $b_{L/U/H} = b_{L/U/H,0} \exp\left(\frac{\Delta U_{L/U/H}}{RT}\right)$ $w = \left(\exp\left(\frac{(\log(y_{\text{CO}_2} p) - \log(p_{\text{step}}))}{\sigma}\right) \right)$ $/ \left(1 + \exp\left(\frac{(\log(y_{\text{CO}_2} p) - \log(p_{\text{step}}))}{\sigma}\right) \right) \right)^\gamma$ $p_{\text{step}} = p_{\text{step},0} \exp\left(\frac{-\Delta H_{\text{step}}}{R} \left(\frac{1}{T_0} - \frac{1}{T}\right)\right)$ $\sigma = Xi_1 * \exp\left(Xi_2 \left(\frac{1}{T_0} - \frac{1}{T}\right)\right),$ $q_U = \frac{q_{U,0} * b_U (y_{\text{CO}_2} p)}{1+b_U (y_{\text{CO}_2} p)} + b_H (y_{\text{CO}_2} p)$

TABLE B.16: Resulting ranking showing the 10 best performing materials for $y_{\text{CO}_2} = 0.4\%$. The values of the maximum productivity and the corresponding thermal energy consumption are given for the best performing adsorbent. For the remaining materials, the deviation to the best performing one is given in percentage.

	Adsorbent	Pr	Q_{th}
1	Cr-MIL(101)	20.6 kg/m ³ /h	14.4 MJ/kg
2	MIL-101	-5%	-4%
3	CuBTC	-24%	+9%
4	MIL-53(Al)	-10%	+42%
5	Zn-DABCO	-24%	+49%
6	MIL-101(Cr)-PEI-800	-66%	-11%
7	Lewatit	-74%	+9%
8	Exemplary	-77%	+18%
9	Zeolite Na-LSX	-21%	+61%
10	Ca-X	-27%	+52%

TABLE B.18: Resulting ranking showing the 10 best performing materials for $y_{\text{CO}_2} = 0.1\%$. The values of the maximum productivity and the corresponding thermal energy consumption are given for the best performing adsorbent. For the remaining materials, the deviation to the best performing one is given in percentage.

	Adsorbent	Pr	Q_{th}
1	PCN-11	43.8 kg/m ³ /h	14.9 MJ/kg
2	MIL-101	-8%	-2%
3	Cr-MIL(101)	0%	+33%
4	Ca-X	-25%	+12%
5	Zeolite Na-LSX	-32%	+32%
6	Cu-BTC powder	-31%	+52%
7	CuBTC	-29%	+54%
8	MIL-53(Al)	-15%	+96%
9	Zn-DABCO	-26%	+53%
10	MIL-101(Cr)-PEI-800	-71%	-30%

TABLE B.20: Resulting ranking showing the 10 best performing materials for $y_{\text{CO}_2} = 1.0\%$. The values of the maximum productivity and the corresponding thermal energy consumption are given for the best performing adsorbent. For the remaining materials, the deviation to the best performing one is given in percentage.

	Adsorbent	Pr	Q_{th}
1	Mg-MOF-74	207.7 kg/m ³ /h	4.72 MJ/kg
2	Ca-X	-32%	+68%
3	MIL-101(Cr)-250nm-PEI-300	-36%	+88%
4	Zeolite Na-LSX	-47%	+118%
5	Zeolite 13X	-49%	+106%
6	PCN-11	-41%	+205%
7	MIL-101	-52%	+206%
8	Carbon	-54%	+139%
9	Cr-MIL(101)	-43%	+318%
10	Mg-X	-60%	+164%

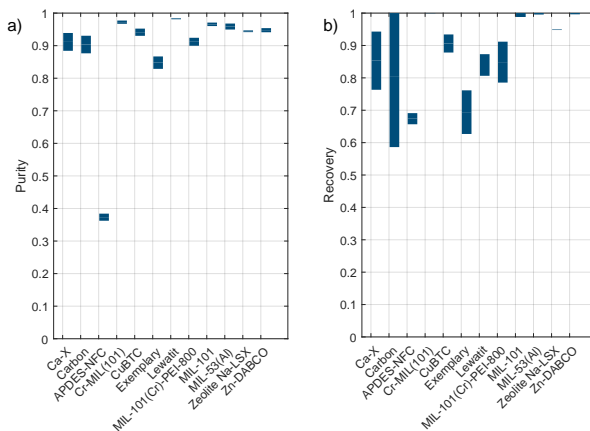


FIGURE B.11: a) Purity and b) recovery for resulting materials from screening with 0.04% CO₂ in the feed.

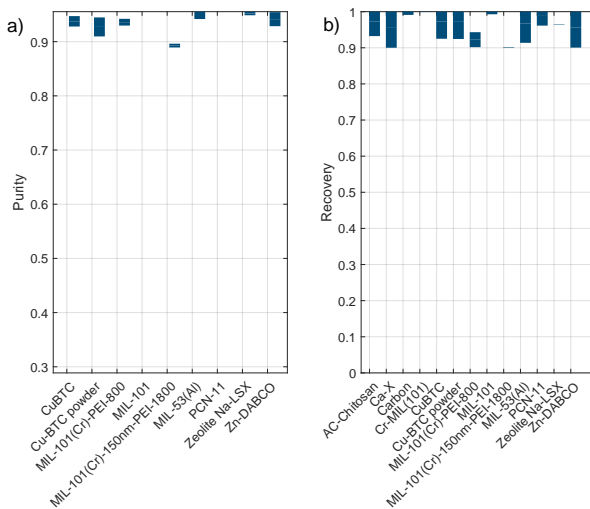


FIGURE B.12: a) Purity and b) recovery for resulting materials from screening with 0.1% CO₂ in the feed.

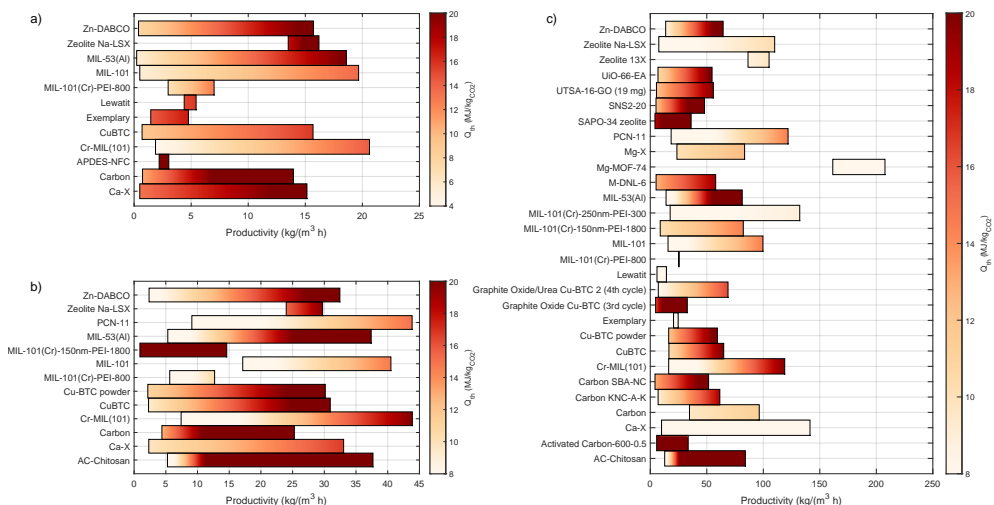


FIGURE B.14: Resulting objectives humid using Lewatit H₂O isotherm for a) 0.04%, b) 0.1% and c) 1.0% CO₂ in the feed.

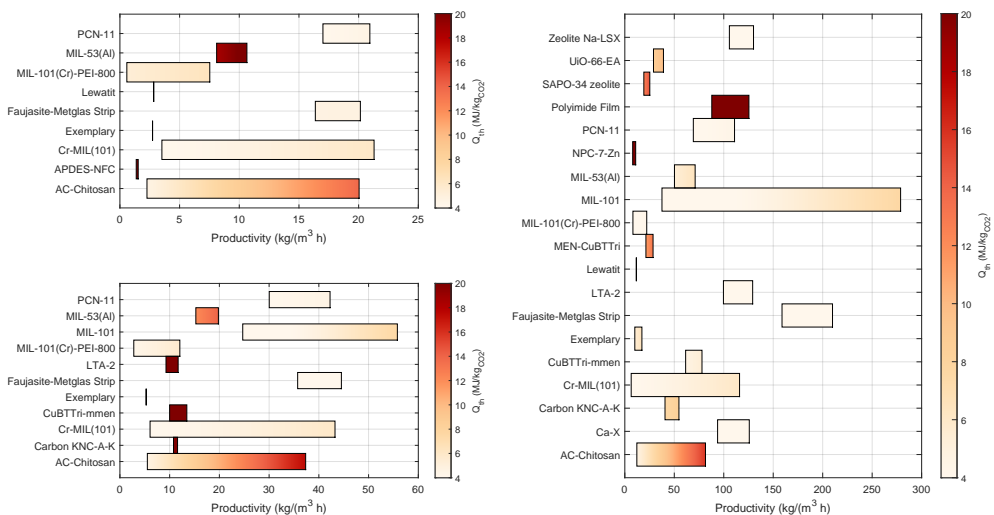


FIGURE B.15: Resulting objectives with dry feed for a) 0.04%, b) 0.1% and c) 1.0% CO₂ in the feed.

The following three Tables B.22, B.24, and B.27 list the resulting materials from the screening with different CO_2 concentrations for the case with the APDES-NFC isotherm for water.

TABLE B.22: Resulting materials with their DOI from screening with $y_{\text{CO}_2} = 40Pa$ and the APDES-NFC isotherm for the water.

Material	DOI
Ca-X	10.1039/c2ee23337a
Carbon	10.1021/la4004998
APDES-NFC	10.1021/es404430g
Cr-MIL(101)	10.1039/C2ra20641b
CuBTC	10.1016/j.cej.2015.07.020
Exemplary	10.1016/j.joule.2021.05.023
Lewatit	10.1016/j.ijggc.2015.07.014
MIL-101(Cr)-PEI-800	10.1021/acssuschemeng.6b01692
MIL-101	10.1021/Jp811418r
MIL-53(Al)	10.1021/Ie5006146
Zeolite Na-LSX	10.1016/S0167-2991(02)80202-6
Zn-DABCO	10.1016/j.seppur.2011.09.041

TABLE B.24: Resulting materials with their DOI from screening with $y_{\text{CO}_2} = 100Pa$ and the APDES-NFC isotherm for the water.

Material	DOI
AC-Chitosan	10.1016/j.physe.2013.10.024
Ca-X	10.1039/c2ee23337a
Carbon	10.1021/la4004998
Cr-MIL(101)	10.1039/C2ra20641b
CuBTC	10.1016/j.cej.2015.07.020
Exemplary	10.1016/j.joule.2021.05.023
Lewatit	10.1016/j.ijggc.2015.07.014
MIL-101(Cr)-PEI-800	10.1021/acssuschemeng.6b01692
MIL-101	10.1021/Jp811418r
MIL-101(Cr)-150nm-PEI-1800	10.1039/C4ta01174k
MIL-53(Al)	10.1021/Ie5006146
PCN-11	10.1039/Coe00700e
Zeolite Na-LSX	10.1016/S0167-2991(02)80202-6
Zn-DABCO	10.1016/j.seppur.2011.09.041

TABLE B.27: Resulting materials with their DOI from screening with $y_{\text{CO}_2} = 1000\text{Pa}$ and the APDES-NFC isotherm for the water.

Material	DOI
AC-Chitosan	10.1016/j.physe.2013.10.024
Activated Carbon-600-0.5	10.1039/C2cp44436d
Ca-X	10.1039/c2ee23337a
Carbon	10.1021/1a4004998
Carbon KNC-A-K	10.1021/Cm303072n
Carbon SBA-NC	10.1021/Cm303072n
Cr-MIL(101)	10.1039/C2ra20641b
CuBTC	10.1016/j.cej.2015.07.020
Exemplary	10.1016/j.joule.2021.05.023
Graphite Oxide Cu-BTC (3rd cycle)	10.1021/am404952z
Graphite Oxide/Urea Cu-BTC 2 (4th cycle)	10.1021/am404952z
Lewatit	10.1016/j.ijggc.2015.07.014
MIL-101(Cr)-PEI-800	10.1021/acssuschemeng.6b01692
MIL-101	10.1021/Jp811418r
MIL-101(Cr)-150nm-PEI-1800	10.1039/C4ta01174k
MIL-101(Cr)-250nm-PEI-300	10.1039/C4ta01174k
MIL-53(Al)	10.1021/1e5006146
M-DNL-6	10.1002/cssc.201200907
Mg-MOF-74	10.1016/j.ijggc.2013.01.009
Mg-X	10.1039/c2ee23337a
PCN-11	10.1039/Coee00700e
SAPO-34 zeolite	10.1080/01496395.2013.812118
SNS2-20	10.1039/c5ta01776a
UTSA-16-GO (19 mg)	10.1039/c4ta04770b
UiO-66-EA	10.1039/c5ta05997f
Zeolite 13X	10.1021/Je800900a
Zeolite Na-LSX	10.1016/S0167-2991(02)80202-6
Zn-DABCO	10.1016/j.seppur.2011.09.041

APPENDIX FOR CHAPTER 4

Summary databases

A list of the databases included in the analysis:

- NIST database (3000) [142]
- Leperi et al. (280) [155]
- Sholl et al. (300) [277]
- Core database [278] with cleaned data by Arvind et al. (1200) [157]

Isotherm metrics

To describe and compare the shape of different isotherm models, characteristic parameters can be used. There are several ways to define these metrics. Table C.1 and Figure C.1 give an overview of the properties used here.

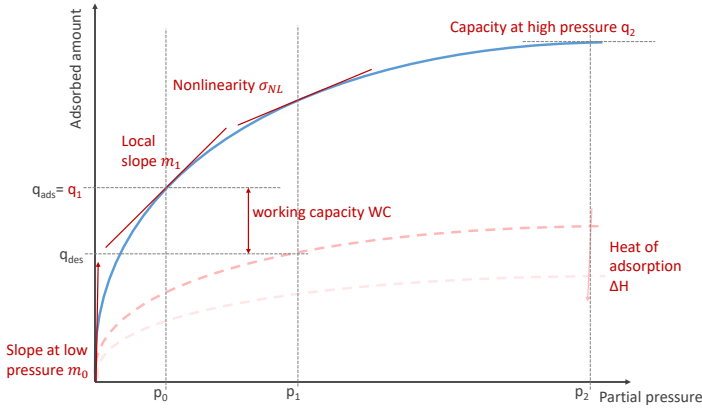


FIGURE C.1: Overview characteristics as an example on a Type I isotherm.

TABLE C.1: Performance evaluation metrics.

Metric	Definition
Enthalpy of adsorption	$\Delta H = \sum_{i=1}^n \Delta H^i$
Initial slope m_0	$m_0 = \lim_{p \rightarrow 0} \frac{q}{p} = \lim_{p \rightarrow 0} \frac{dq}{dp}$
Capacity at high pressure	q_s
Local loading	$q_1 = q(T_{amb}, p_{amb}, y_{CO_2}^{feed})$
Local slope	$m_1 = \frac{dq(T_{amb}, p_{amb}, y_{CO_2}^{feed})}{dp_{CO_2}^{feed}}$
Nonlinearity	$\sigma_{NL} = \sqrt{\frac{\sum_{p_{CO_2}=0}^{p_{CO_2}=p_{CO_2}^{feed}} \left(\frac{dq(T_{amb}, p_{CO_2})}{dp_{CO_2}} - \frac{dq}{dp} \right)^2}{n}}$
Working capacity	$WC = q_{ads} - q_{des}$
Selectivity	$S = \frac{q_{CO_2,ads}}{q_{H_2O,ads}} \frac{p_{CO_2,ads}}{p_{H_2O,ads}}$
Selectivity initial slope	$S_m = \frac{m_{CO_2,0}}{m_{H_2O,0}}$

A short description of the different metrics:

Slope at low pressure m_0 . When using specific metrics to describe the shape of the isotherm, most studies use the Henry constant K_H as an important characteristic. The Henry constant represents the initial slope of an isotherm, but cannot be calculated from every isotherm. E.g. for the Langmuir-Freundlich [279] as well as the s-shaped isotherm models [280] the Henry condition is not fulfilled. Instead, we calculate a slope at low pressure, i.e. assuming a linear slope between $p_0 = 0Pa$ and $p_1 = 1Pa$ and calculate the steepness between these points.

Capacity at high pressure q_2 . By measuring the CO₂ adsorption capacity at high pressure, we can evaluate the potential of the material to adsorb CO₂. A similar metric which is often used is the saturation capacity q_s^{equ} . Since we include different isotherm shapes of which not all reach a plateau at high pressure, we use the loading at a specific pressure.

Loading at feed concentration q_1 . Similar to the capacity at high pressure, but describes the number of moles of CO₂ that a kg of adsorbent can adsorb at feed concentration.

Local slope m_1 . This metric describes the slope of the isotherm at feed condition, i.e. at a specific temperature T and partial pressure p_{CO_2} .

Nonlinearity σ_{NL} . The nonlinearity is a measure for the shape of the isotherm at low pressure, i.e. from zero pressure to the feed concentration. It represents the change in the curvature between this pressure range.

Working capacity WC . The working capacity is the difference between the equilibrium capacity at adsorption and desorption conditions.

Enthalpy of adsorption ΔH . This is a metric of the strength of the adsorbent to bind CO₂. A high value enables a high adsorption capacity at low CO₂ partial pressures. Typical DAC adsorbents like amine-based adsorbents, e.g., have high isosteric heats of adsorption [41, 48, 87].

Selectivity S . The mixture selectivity of CO₂ over H₂O at adsorption conditions and feed concentration.

Selectivity initial slope S_m . Comparing the slope of the CO₂ and H₂O isotherm at ambient condition and feed concentration.

In Figures C.2-C.4 the distribution of the isotherm metrics is shown for the isotherm of the databases. The red 'x' shows the position of the resulting isotherms when screening the databases using $y_{\text{CO}_2} = 0.04\%$. In Fig. C.2 a) and b) the slope at very low pressure and at feed concentration is plotted, respectively. The majority of the screened isotherms show low values for both metrics, but most of the selected isotherms for DAC application can be found in the upper region. Therefore, also the loading at feed concentration is higher for these isotherms, which can be seen by Fig. C.2 c). A clear trend can be found between the loading and the slope at feed conditions and the selectivity.

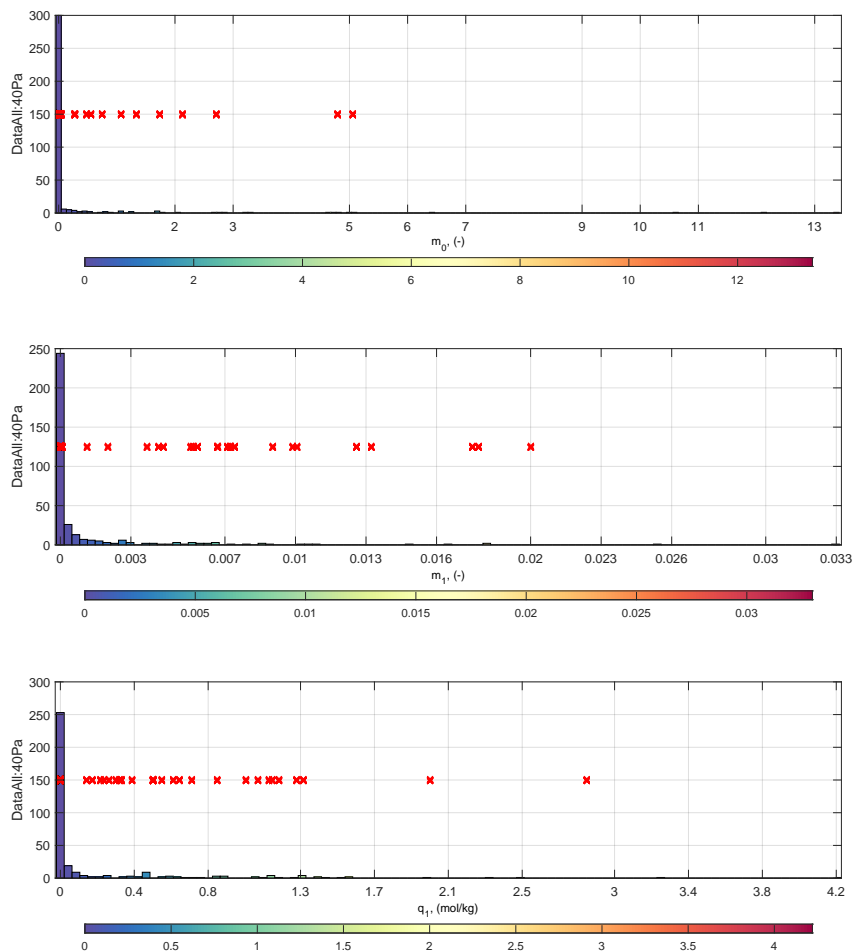


FIGURE C.2: Distribution of the isotherm metrics for the materials of the databases, part I : a) slope at low pressure, b) slope at feed conditions ($T = T_{\text{amb}}, y_{\text{CO}_2} = 0.04\%, p = p_{\text{amb}}$), and c) loading at feed conditions in mol/kg . The red crosses show the materials left after the screening (case $y_{\text{CO}_2} = 0.04\%$).

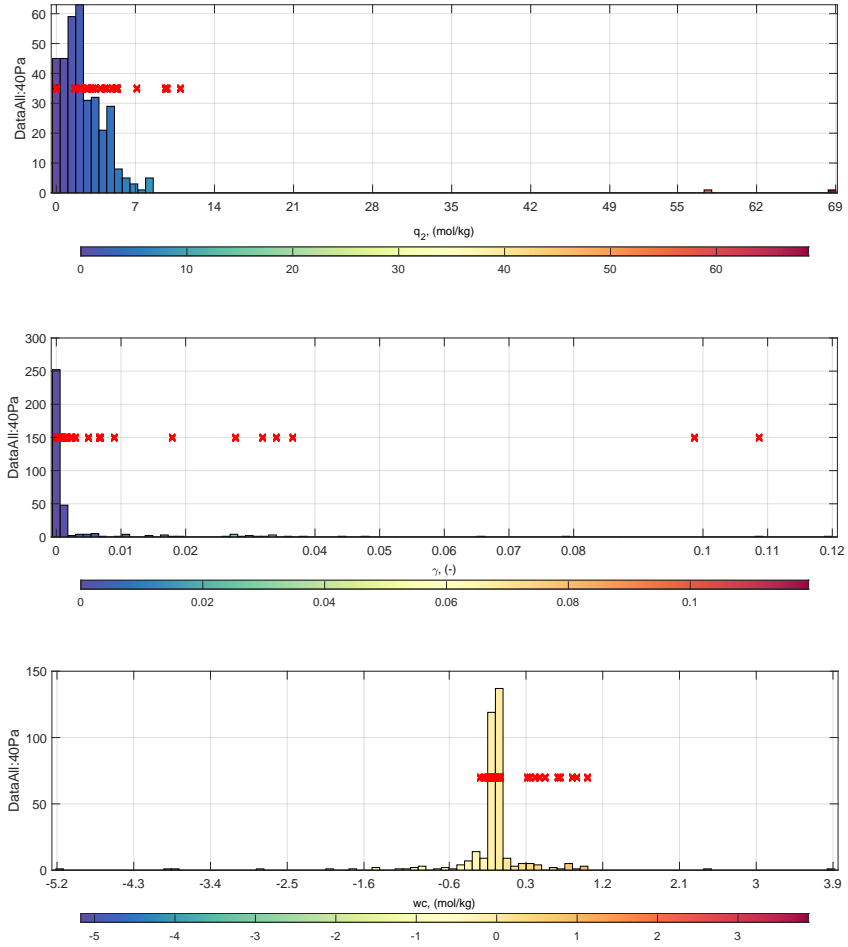


FIGURE C.3: Distribution of the isotherm metrics for the materials of the databases, part II : a) loading at high pressure (mol/kg), b) nonlinearity, and c) working capacity. The red crosses show the materials left after the screening (case $y_{CO_2} = 0.04\%$).

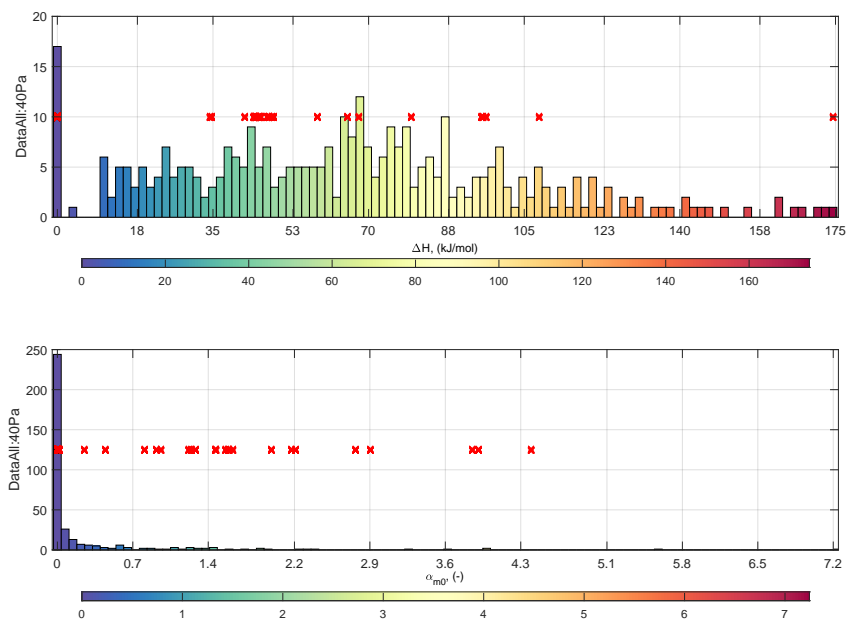


FIGURE C.4: Distribution of the isotherm metrics for the materials of the databases, part III : a) Heat of adsorption and b) selectivity. The red crosses show the materials left after the screening (case $y_{CO_2} = 0.04\%$).

Isotherm optimization

Since it can happen, that the resulting isotherm shapes are not physically meaningful; for example, a decreasing CO₂ loading with increasing partial pressure or with decreasing temperature, a penalty function is included within the optimization of the isotherm parameters.

The criteria for which the hypothetical isotherm is checked are:

- $q_{\text{CO}_2}(p_{\text{CO}_2} = 1\text{bar}, T = T_{\text{ads}}) > q_{\text{CO}_2}^{\text{max}}$
- $q_{\text{CO}_2}(p_{\text{CO}_2} = p_{\text{CO}_2}^{\text{feed}}, T = T_{\text{ads}}) - q_{\text{CO}_2}(p_{\text{CO}_2} = p_{\text{CO}_2}^{\text{des}}, T = T_{\text{des}}) > 0$

The verification of the hypothetical isotherm takes place at the beginning of the optimization. If at least one of the points mentioned above is not fulfilled, the optimization stops, the objectives are set to $-Pr = 1e10$ and $Q_{\text{th}} = 1e10$, and new isotherm parameters are chosen.

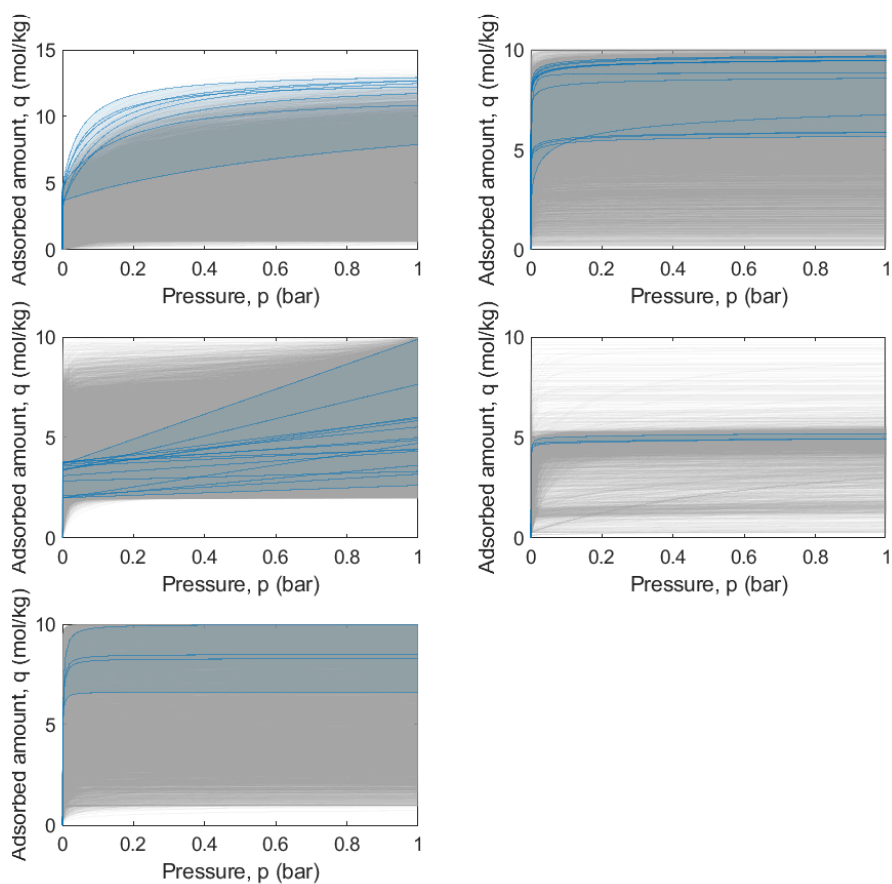


FIGURE C.5: Optimized isotherms: a) Langmuir-Freundlich, b) Toth, c) Toth-cp, d) DSL, and e) s-shaped. All hypothetical isotherms which were simulated during the optimization are presented in grey, while the optimal isotherms are shown in blue.

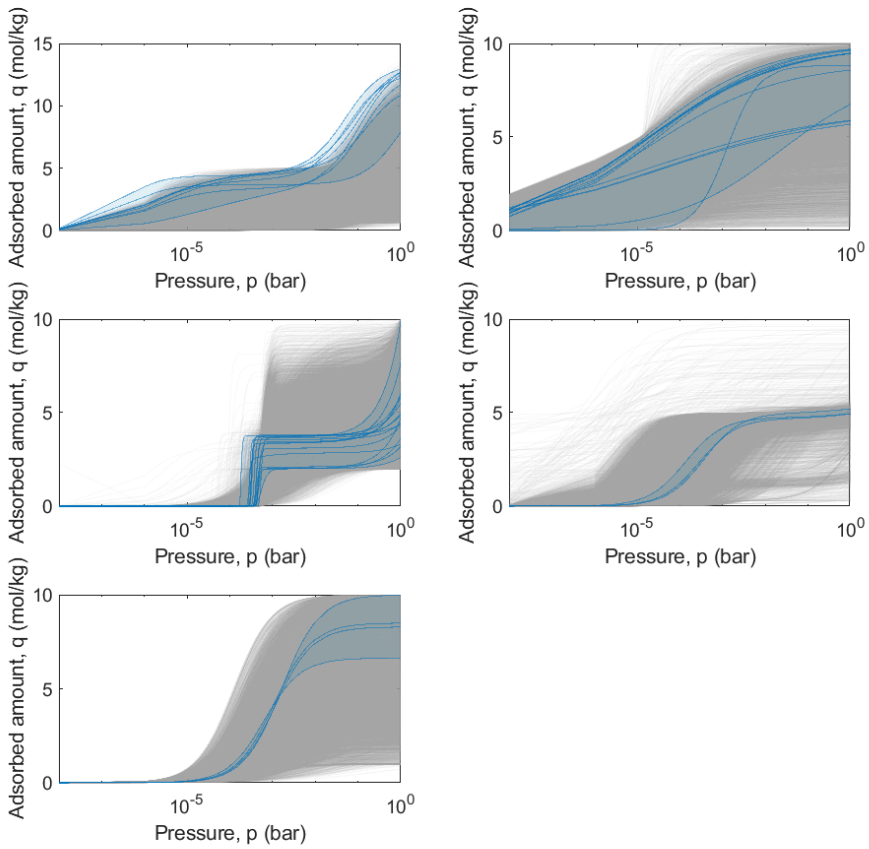


FIGURE C.6: Optimized isotherms: a) Langmuir-Freundlich, b) Toth, c) Toth-cp, d) DSL, and e) s-shaped. All hypothetical isotherms which were simulated during the optimization are presented in grey, while the optimal isotherms are shown in blue.

Details oD and 1D modelling and optimization

Details regarding the modeling of the solid sorbent process are listed in Table C.3.

The optimization of the oD model is carried out using a particle swarm algorithm adapted for multi-objectives (MOPSO), as implemented in Matlab R2021 [147]. The settings for the algorithm like size of the particle and repository were set to 250, which is higher compared to the optimization in our previous research [149], since the optimization is more complex.

TABLE C.3: Properties for modeling the adsorption unit for both the oD and 1D model.

Parameter	Value	Source
Plate containing sorbent		
Length	0.05 m	
Internal radius	0.005 m	
External radius	0.005001 m	
Heat capacity wall	2.457×10^6 J/(K m ³)	
Heat transfer fluid/wall/bed	6.7 W/(m ² K)	Modeled using [41]
Contactor geometry		
LxWxH	1.5x1.5x1.5m	[41]
Void fraction, $\epsilon = 1 - V_{\text{sorbent}}/V_{\text{aircontactor}}$	0.6	[41]

TABLE C.5: Material properties and geometry of the plate containing the sorbent for both the oD and 1D model used for the simulations.

Parameter	Value
Material density	1590 kg/m ³
Particle voidage	0.35
Column void fraction	0.6
Particle radius	0.001 m

TABLE C.6: Design variables for optimizing the process, including lower and upper bound. The upper bound for the air volume stream is calculated using the minimum fluidization velocity [120]. For the oD model only T_{des} , p_{vac} and \dot{V}_{air} are considered as decision variables.

Variable	Range
t_{ads} (s)	100-10000
t_{des} (s)	50-2200
t_{purge} (s)	1-400
p_{vac} (bar)	0.1-0.9
T_{des} (K)	363-373
ΔT_{purge} (K)	1-60
\dot{V}_{air} (m^3/s)	$2.0 \times 10^{-7} - 8.9 \times 10^{-6}$

Additional information on optimized isotherms

TABLE C.7: Boundaries decision variables process.

Process parameters	
T_{des} (K)	363-373
p_{vac} (bar)	0.1-0.9 bar
V_{feed} (m ³ /s)	$7.0e^{-08}$ - $8.9e^{-06}$
Isotherm parameters	
Langmuir Freundlich	
$n_{\text{s,o}}$ (mol/kg)	0.1-160
X_i (-)	0-15
t_0 (-)	0-5
α (-)	0-10
b_0 (1/Pa)	0-1
dH (kJ/mol)	0-100
Toth-cp	
$X_{i,c}$ (-)	0-5
dH_c (kJ/mol)	40-110
α_c (-)	0-2.5
$X_{i,p}$ (-)	$1e^{-3}$ - 12
dH_p	2-60
α_p (-)	0-13
$n_{\text{s,o,c}}$ (mol/kg)	1-5
$b_{0,c}$ (1/Pa)	$1e^{-2}$ - 10
$t_{0,c}$ (-)	0-1
$n_{\text{s,o,p}}$ (mol/kg)	1-160
$b_{0,p}$ (1/Pa)	$5e^{-5}$ - $2e^{-4}$
$t_{0,p}$ (-)	$1e^{-3}$ - 1

TABLE C.8: Boundaries decision variables materials II.

Toth		
X_i (-)		0.01-5
dH (kJ/mol)		40-130
α (-)		0.001-3.0
$n_{s,o}$ (mol/kg)		1-160
b_0 (1/Pa)		$1e^{-2}$ - 0.1
t_0 (-)		0.001-1
S-shaped		
q_{L_o} (mol/kg)		0.1-10
b_{L_o} (1/Pa)		$1e^{-14}$ - $1e^{-6}$
dU_L (kJ/mol)		10-60
q_{U_o} (mol/kg)		2-80
b_{U_o} (1/Pa)		$1e^{-15}$ - $1e^{-9}$
dU_U (kJ/mol)		25-75
b_{H_o} (mol/kg/Pa)		$1e^{-11}$ - $1e^{-6}$
dU_H (kJ/mol)		5-45
X_{i_1} (-)		$5e^{-3}$ -0.2
X_{i_2} (-)		$0-1e^4$
$p_{step,o}$ (Pa)		$1e^{-1}$ - $1e^5$
dH_{step} (kJ/mol)		-80- -40
γ (-)		4
DSL		
n_1 (mol/kg)		0.15-80
b_0 (m ³ /mol)		$1e^{-13}$ - $1e^{-4}$
H_b (kJ/mol)		5-65
n_2 (mol/kg)		0.3-80
d_0 (m ³ /mol)		$1e^{-11}$ - $1e^{-2}$
H_d (kJ/mol)		1-60

TABLE C.9: Isotherm parameters for the optimized isotherm models and the process condition using the oD model. The parameters correspond to point A in the Pareto charts (see Figure 4.8). Part I.

S-shaped isotherm					
Parameter	Value	Parameter	Value	Parameter	Value
T_0 (K)	313.5	$b_{H,o}$ (mol/kg/MPa)	3.78e-02	T_{des} (K)	363.89
$q_{L,o}$ (mol/kg)	10.0	ΔU_H (J/mol)	5000.0	p_{vac} (MPa)	0.010
$b_{L,o}$ (1/MPa)	9.00e-08	Xi_1 (-)	5.92e-02	\dot{V}_{feed} (m ³ /s)	8.86e-06
ΔU_L (J/mol)	3.12e+04	Xi_2 (1/K)	1.031e+03	ΔH_{ads} (J/mol)	-6.849e+04
$q_{U,o}$ (mol/kg)	9.765	$p_{step,o}$ (MPa)	1.32e-04		
$b_{U,o}$ (1/MPa)	1.124e+15	ΔH_{step} (J/mol)	-7.250e+04		
ΔU_U (J/mol)	4.181e+04	γ (-)	4		
Toth-cp isotherm					
Parameter	Value	Parameter	Value	Parameter	Value
T_0 (K)	293	α_p (-)	13.0	$t_{o,p}$ (-)	1.0
Xi_c (-)	4.69	$n_{s,o,c}$ (mol/kg)	5.0	T_{des} (K)	363.66
ΔH_c (J/mol)	9.240e+04	$b_{o,c}$ (1/MPa)	1.653e+07	p_{vac} (MPa)	0.078
α_c (-)	1.68	$t_{o,c}$ (-)	9.56e-01	\dot{V}_{feed} (m ³ /s)	2.63e-06
Xi_p (-)	3.09e-02	$n_{s,o,p}$ (mol/kg)	2.74	ΔH_{ads} (J/mol)	-1.072e+05
ΔH_p (J/mol)	2.865e+04	$b_{o,p}$ (1/MPa)	1.30e+02		
Toth isotherm					
Parameter	Value	Parameter	Value	Parameter	Value
T_0 (K)	293	$n_{s,o}$ (mol/kg)	7.77	p_{vac} (MPa)	0.080
Xi (-)	6.51e-01	b_0 (1/MPa)	3.611e+04	\dot{V}_{feed} (m ³ /s)	6.93e-06
ΔH (J/mol)	9.773e+04	t_0 (-)	6.79e-01	ΔH_{ads} (J/mol)	-9.793e+04
α (-)	1.89	T_{des} (K)	369.22		

TABLE C.11: Isotherm parameters for the optimized isotherm models and the process condition using the oD model. The parameters correspond to point A in the Pareto charts (see Figure 4.8). Part II.

Langmuir-Freundlich isotherm					
Parameter	Value	Parameter	Value	Parameter	Value
T_0 (K)	293	b_0 (1/MPa)	5.168e+02	T_{des} (K)	371.62
Xi (-)	8.23	ΔH (J/mol)	3.876e+04	p_{vac} (MPa)	0.038
$1/t_0$ (-)	2.79e-01	$n_{s,o}$ (mol/kg)	9.31	\dot{V}_{feed} (m ³ /s)	6.69e-06
α (-)	6.8	ΔH_{ads} (J/mol)	-1.091e+05		
DSL isotherm					
Parameter	Value	Parameter	Value	Parameter	Value
n_1 (mol/kg)	4.69	d_0 (m ³ /mol)	1.00e-02	T_{des} (K)	402.76
b_0 (m ³ /mol)	9.09e-10	ΔH_d (J/mol)	2.325e+03	p_{vac} (MPa)	0.010
ΔH_b (J/mol)	6.223e+04	ΔH_{ads} (J/mol)	-6.217e+04	\dot{V}_{feed} (m ³ /s)	7.15e-06
n_2 (mol/kg)	4.73e-01				

TABLE C.13: Isotherm parameters for the optimized Toth-cp isotherm model, showing Pareto points B and C. Point A can be found in Table C.9.

Toth-cp point B					
Parameter	Value	Parameter	Value	Parameter	Value
T_0 (K)	293	α_p (-)	1.27e+01	$t_{o,p}$ (-)	3.63e-01
Xi_c (-)	4.98	$n_{s,o,c}$ (mol/kg)	4.92	T_{des} (K)	363.62
ΔH_c (J/mol)	11.00e+04	$b_{o,c}$ (1/MPa)	3.879e+07	p_{vac} (MPa)	0.080
α_c (-)	1.35	$t_{o,c}$ (-)	1.00	\dot{V}_{feed} (m ³ /s)	8.90e-06
Xi_p (-)	1.00e-03	$n_{s,o,p}$ (mol/kg)	1.63	ΔH_{ads} (J/mol)	-1.22e+05
ΔH_p (J/mol)	2.748e+04	$b_{o,p}$ (1/MPa)	1.09e+02		
Toth-cp point C					
Parameter	Value	Parameter	Value	Parameter	Value
T_0 (K)	293	α_p (-)	13.0	$t_{o,p}$ (-)	1.00e-03
Xi_c (-)	5.00	$n_{s,o,c}$ (mol/kg)	5.0	T_{des} (K)	363.00
ΔH_c (J/mol)	1.001e+05	$b_{o,c}$ (1/MPa)	5.000e+07	p_{vac} (MPa)	0.080
α_c (-)	2.50	$t_{o,c}$ (-)	1.00	\dot{V}_{feed} (m ³ /s)	8.90e-06
Xi_p (-)	1.00e-03	$n_{s,o,p}$ (mol/kg)	6.51	ΔH_{ads} (J/mol)	-1.160e+05
ΔH_p (J/mol)	5.416e+04	$b_{o,p}$ (1/MPa)	200		

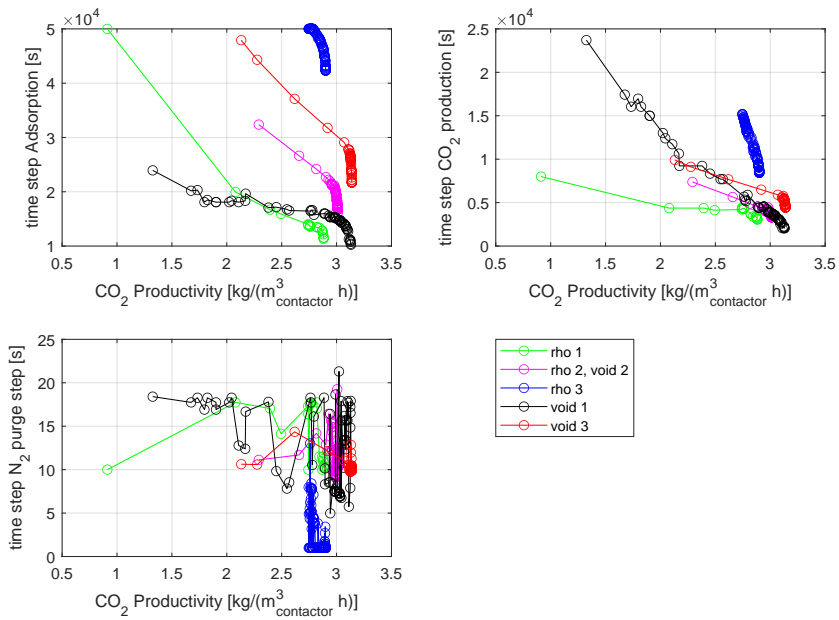


FIGURE C.7: Decision variables for optimizing the optimal Toth-cp isotherm using the 1D model (point A, $k_{\text{LDF}} = 0.11/\text{s}$) and including the density and void fraction as decision variables.

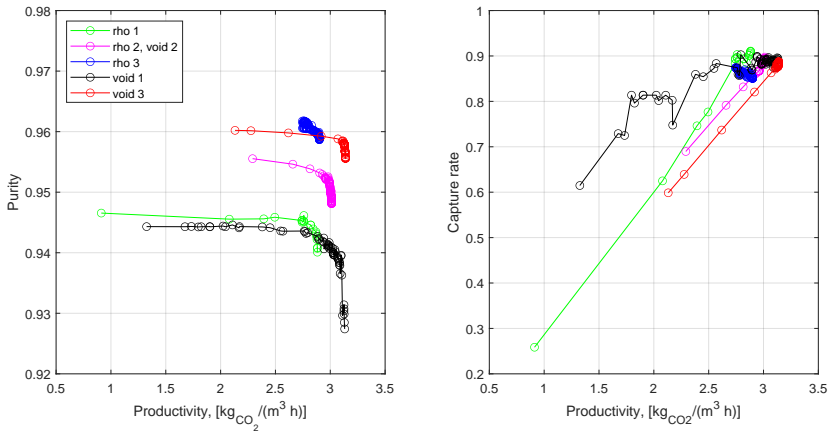


FIGURE C.8: Purity and recovery for optimizing the optimal Toth-cp isotherm using the 1D model (point A, $k_{\text{LDF}} = 0.11/\text{s}$) and including the density and void fraction as decision variables.

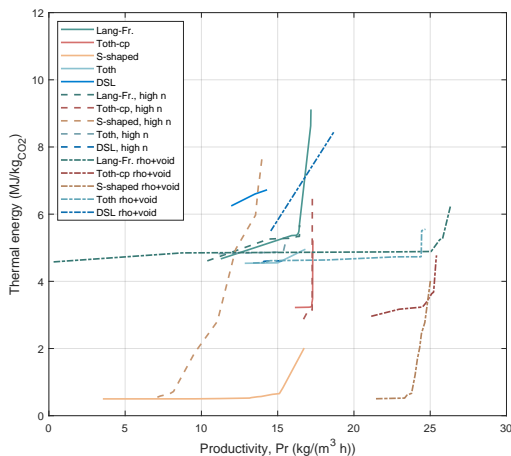


FIGURE C.9: Pareto charts showing different cases for all five isotherm models and a feed concentration of $y_{CO_2} = 0.04\%$: standard case, increased physisorption value ($n=160$ mol/kg), and including the sorbent density and the void fraction as decision variables.

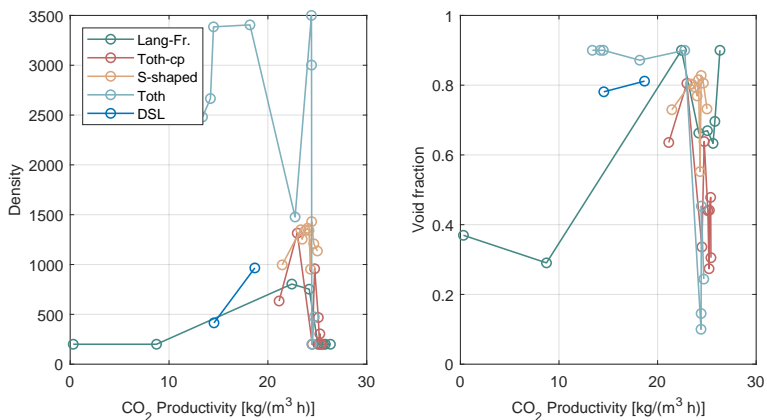


FIGURE C.10: Density and void fraction for the Pareto points in graph C.9.

Economic Analysis

The cost model is written in Excel and called by a Matlab code, which also includes the simulation and optimization of the process. For the optimization, we are using a particle swarm algorithm adapted for multi-objectives (MOPSO) for the first optimization [147, 149]. For the second part of the cost analysis, where the optimization is run having the total cost as a single objective, a particle swarm algorithm (PSO) was used [281–283]. While details for the former can be found in chapter 3, for the PSO, the maximum number of iterations and the swarm size were set to 3000 and 100, respectively.

Operating costs

The thermal and electrical energy demand for the operating costs is calculated within the 1D or oD model. The thermal energy demand includes the regeneration of the adsorbent. The electrical energy demand includes the air blower and the vacuum pump. More details can be found in Sabatino et al. [26] for the 1D model and in [149] for the oD model.

Contactor module capital cost

The capital cost of one air contactor is calculated. Because of the modular construction of these modules, they are duplicated depending on the size of the capture plant. The module consists of the following components:

Air blower capital cost

The air blower is of the type vane-axial fan [172].

$$C_{P-AB} = \exp \left(9.6487 - 0.97566 \ln(Q_{AB}) + 0.08532 (\ln(Q_{AB}))^2 \right) \quad (C.1)$$

where Q_{AB} is the flow rate of the air feed stream in ft^3/min .

Vacuum pump capital cost

The cost is calculated by using the following equation [159]

$$C_{P-VP} = \exp(11.23543)VF^{0.750473} \quad (C.2)$$

where VF is the vacuum factor, which is defined as the equivalent air mass flow, depending on the vacuum pressure, in pounds per hour.

Air contactor

The design of the air contactor frame is similar to the type published in patents by Climeworks [41, 66]. We consider two separate parts: the vacuum chamber and inside the frames containing the sorbent. The chamber was considered a pressure

vessel, while for the frames the costs were included by considering the material cost. The dimension of the air contactor was assumed to be 1.5m×1.5m×1.5m [41] and the costs are calculated using [172]

$$C_{p\text{-chamber}} = \exp \left(5.6334 + 0.4599 \ln (W_{\text{chamber}}) + 0.00582 \ln (W_{\text{chamber}})^2 \right) \quad (C.3)$$

with W_{chamber} being the mass of the material needed (in *lb*). We assumed the chamber to be made of stainless steel with a price of 4\$/kg [284] and a density of 8 t/m³. The data is presented in Table C.15.

TABLE C.15: Specification of the vacuum chamber.

Components	amount	mass (kg)
lids	2	100.53
walls (axial)	4	288.00
walls (vertical)	2	93.73
W_{chamber}		482.27

The area of the frames is 1.5m×1m and is assumed to be made of Aluminum and Ultramid PA with prices of $c_{Al} = 2.37$ \$/kg [285] and $c_{PA} = 1.8$ \$/kg [286], respectively. The data for one frame is presented in Table C.16. We assume that one air contactor includes $N_{\text{frames}} = 48$ frames and the overall costs are calculated with

$$C_{p\text{-frames}} = N_{\text{frames}} \sum_{i=1}^n (m_i * c_i) \quad (C.4)$$

with n being the amount of components in one frame, m_i the mass of the material, and c_i the price of the material. The overall costs per air contactor $C_{p\text{-AC}}$ is the sum of the chamber $C_{p\text{-chamber}}$ and the frames $C_{p\text{-frames}}$.

Storage tank

The capital cost of the storage tank can be calculated with Equation C.3 with the mass of the tank [172]

$$W_{\text{tank}} = \pi (D_i + t_s) (L + 0.8D_i) t_s \rho \quad (C.5)$$

with the thickness

$$t_s = \frac{P_d D_i}{2SE - 1.2P_d} \quad (C.6)$$

TABLE C.16: Specification of the frames in the air contactor module.

Components for 1 frame	amount	material	mass (kg)
support structures (profiles)	4	Aluminum	0.74
wedge spacers and sealing strips	-	Ultramide (PA)	0.158
primary HEX (pipes)	10	Aluminum	1.070
secondary HEX (fins)	100	Aluminum	2.025

and the internal gauge design pressure (in psi)

$$P_d = \exp \left(0.60608 + 0.91615 \ln (P_0) + 0.0015655 \ln (P_0)^2 \right) \quad (\text{C.7})$$

Here D_i is the internal diameter, L the tangent-tangent length, S the maximum allowable stress of the shell material (13570 psi for stainless steel [172]), E the fractional weld efficiency (assuming 0.85 [172]), and P_0 the operation pressure (assumed to be ambient pressure).

The overall capital cost of the tank are [172]

$$C_{p\text{-tank}} = C_{p\text{-vessel}} + C_{p\text{-PL}} = C_{p\text{-vessel}} + 2275D_i^{0.2094} \quad (\text{C.8})$$

The size of the tank is dependent on the size of the air capture plant and for the type a carbon steel-horizontal tank with two ellipsoidal heads is chosen. We assume that the volume of CO_2 produced, V_{CO_2} during two cycles needs to be stored as a buffer. In addition, we assume that the capacity of the tank has to be 20% larger than V_{CO_2} and the ratio between the internal diameter D_i and tangent-to-tangent length L is 1:5, i.e.

$$L = 5D_i \quad (\text{C.9})$$

With Equation C.9 and the following equation for calculating the tank volume V_{tan} of a tank with two ellipsoidal heads

$$V_{\text{tan}} = \frac{D_i^2 \pi}{4} L + \frac{D_i^3 \pi}{24} 2 \quad (\text{C.10})$$

the dimension of the tank can be specified.

Condenser

To extract the water in the product stream, a condenser is included. The capital cost is calculated by [159]

$$C_{p\text{-cond}} = \exp(7.169723) A_{\text{cond}}^{0.726108} \quad (\text{C.11})$$

with A_{cond} being the area required to condense the water. The thermal coefficient is assumed to be $200 \text{ Wm}^2/\text{K}$. The temperature of the product steam is assumed to be at desorption temperature and the water content in the stream is given by the model.

Energy requirement

While the thermal energy demand is dependent on the regeneration of the sorbent and is calculated within the model, we include the electrical energy consumption of the air blowers W_{AB} and the vacuum pump W_{pump} :

$$W_{\text{AB}} = \frac{1}{\eta_{\text{AB}}} \Delta p \dot{V}_{\text{air}} \quad (\text{C.12})$$

$$W_{\text{pump}} = \frac{1}{\eta_{\text{VP}}} \dot{m} c_p T \left(\frac{p_{\text{out}}^{(\frac{\gamma-1}{\gamma})}}{p_{\text{in}}} - 1 \right) \quad (\text{C.13})$$

with

$$\gamma = \frac{c_p}{c_p - R} \quad (\text{C.14})$$

For the air blower the pressure drop is modeled during our simulation, with an efficiency of 60%. The efficiency of the vacuum pump depends on the vacuum pressure and decreases linearly in the range 0.7-0.6 for high to medium pressure and 0.6-0.3 for medium to low pressure.

Scaling

The Chemical Engineering Plant Cost Index (CEPCI) of the year 2020 was applied to convert the purchase cost using a value of 596

$$C_{2020} = C_{\text{ref}} \left(\frac{I_{2020}}{I_{\text{ref}}} \right) \quad (\text{C.15})$$

For the storage tank and the condenser, the economy of scale approach is applied

$$C_i^{\text{new}} = C_i^{\text{base}} \cdot \left(\frac{\text{capi}^{\text{new}}}{\text{capi}^{\text{base}}} \right)^m \quad (\text{C.16})$$

with C being the cost of equipment i with the capacity cap , new corresponds to the targeted case and $base$ to the known cost with the related capacity, and m the scaling factor as shown in Table C.18.

The second approach is the concept of learning-by-doing which is applied to the air contactor module including the air blower, the housing of the air contactor, and the vacuum pump:

$$C_{\text{module}}^{\text{new}} = C_{\text{module}}^{\text{base}} \left(\frac{P^{\text{new}}}{P^{\text{base}}} \right)^b \quad (\text{C.17})$$

with

$$C_{\text{module}}^{\text{base}} = \sum_{i=1}^n C_i \quad (\text{C.18})$$

and

$$LR = 1 - 2^b \quad (\text{C.19})$$

where P^{new} refers to the cumulative production, i.e. the assumed targeting production of this study, P^{base} the production of the base-case, LR the learning rage, and b the experience index related to the rate of cost reduction.

TABLE C.18: Summary of economic parameters used in this study.

Lang Factor	4.67
Delivery cost factor	1.05
annual capacity factor	90%
scaling factor storage tank	0.3 [287]
scaling factor condenser	0.59 [287]
learning rate	0.101
discount rate	7.0%
electricity price	0.108 USD/kg
heat price	0.026 UDS/kg
sorbent price	30 USD/kg
sorbent lifetime	2 years
economic life plant	10 years

Additional results economic analysis

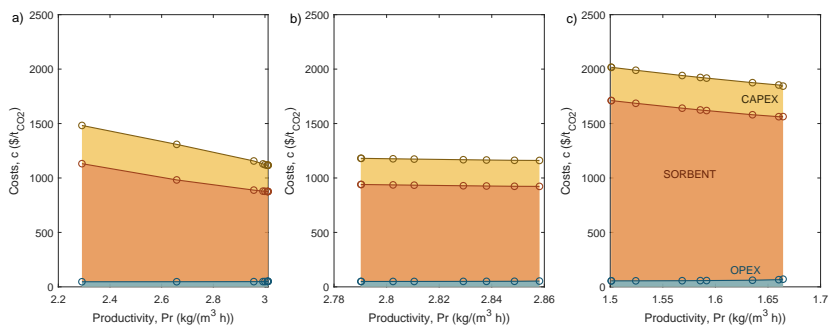


FIGURE C.11: Cost calculation for different LDF coefficients: a) 0.1 1/s, b) 0.001 1/s, and c) 0.0001 1/s. Using results from point A.

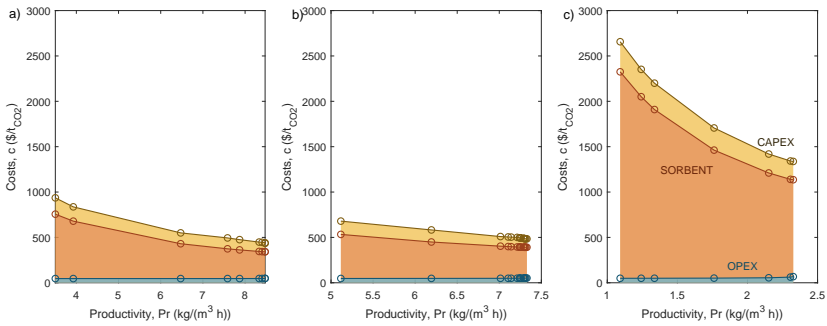


FIGURE C.12: Cost calculation for different LDF coefficients: a) 0.1 1/s, b) 0.001 1/s, and c) 0.0001 1/s. Using results from point B.

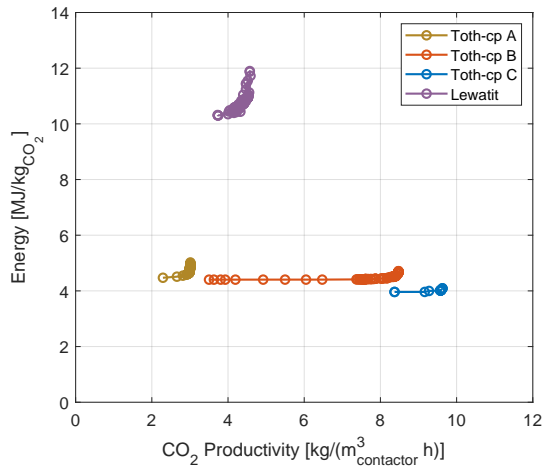


FIGURE C.13: Pareto chart Toth-cp all points and Lewatit.

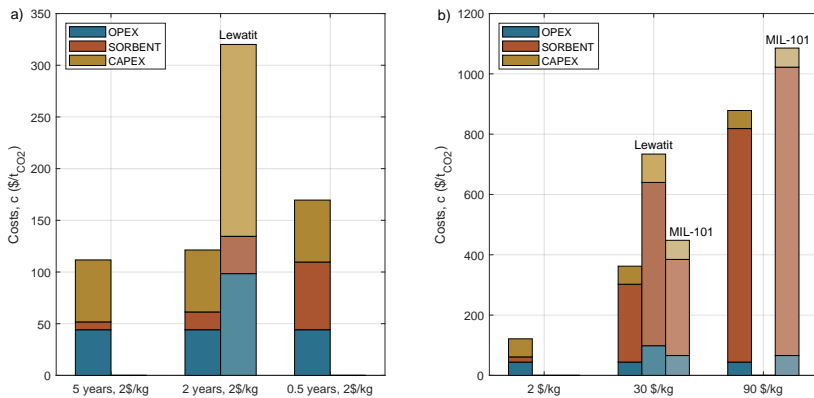


FIGURE C.14: Overview cost breakdown: a) Comparing optimized isotherm case C using one point at 1D Pareto front (point A), costs 2 $\$/kg$ and varying lifetime. b) including MOF MIL-101, lifetime 2 years, varying sorbent costs.

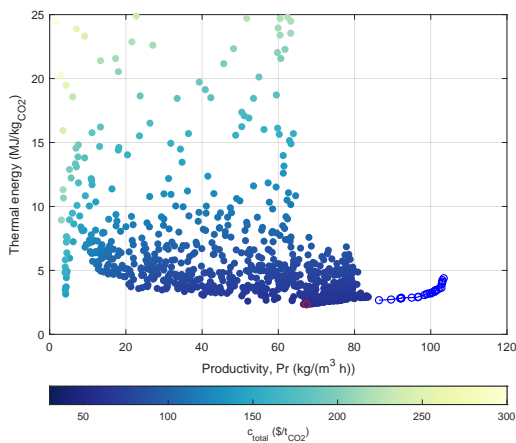


FIGURE C.15: Cost optimization using the oD model for $y_{CO_2} = 1.0\%$ using the Toth-cp isotherm model, a sorbent price of $c_s = 30\$/kg$ and a sorbent lifetime of 2 years.

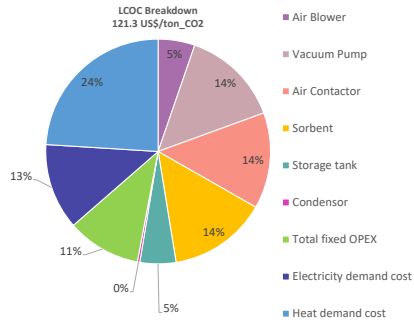


FIGURE C.16: Cost chart $c_s = 2 \text{ \$}/\text{kg}$.

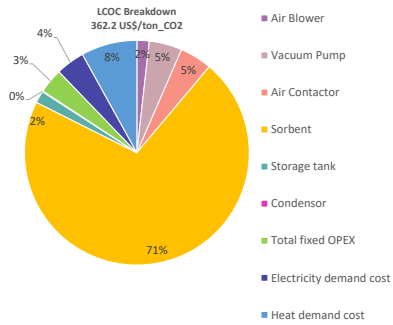


FIGURE C.17: Cost chart $c_s = 30 \text{ \$}/\text{kg}$.

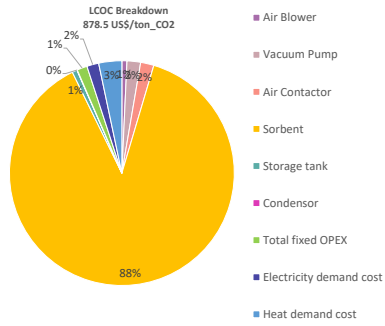


FIGURE C.18: Cost chart $c_s = 90 \text{ \$/kg}$.

D

APPENDIX FOR CHAPTER 5

Lambert function

The equation derived from the equivalent circuit of the PV part, Equation 3 from the main text, is implicit and not solvable analytically. The equation must be expressed as a function of J in the form $V = f(J)$ or as a function of V as $J = f^{-1}(V)$ in order to be solvable. To that end, the Lambert W function can be used [203]:

$$W(x)e^{W(x)} = x \quad (\text{D.1})$$

The Lambert function is especially useful when trying to solve an equation in which the unknown variable appears both inside and outside of an exponential function, i.e. like in Equation 3 from the main text. Using the Lambert function W within Matlab, Equation 3 can be rewritten in two ways; with J as the dependent variable and V_{PV} as the independent variable:

$$J = \frac{J_L - \frac{V}{n_i R_{sh}}}{n_s \left(1 + \frac{R_s}{R_{sh}}\right)} - \frac{n_i V_{th}}{n_s R_s} W \left[\frac{R_s J_0}{n_i V_{th} \left(1 + \frac{R_s}{R_{sh}}\right)} \exp \left(\frac{V}{n_j n_i V_{th}} + \frac{R_s (J_L - \frac{V}{n_i R_{sh}})}{n_i V_{th} \left(1 + \frac{R_s}{R_{sh}}\right)} \right) \right] \quad (\text{D.2})$$

or in the form $V = f(J)$:

$$V = -J R_s - (J - J_L) R_{sh} - n_i V_{th} W \left[\frac{J_0 R_{sh}}{n_i V_{th}} \exp \left(\frac{(J_L - J) R_{sh}}{n_i V_{th}} \right) \right] \quad (\text{D.3})$$

where J_L , J_0 , R_s , R_{sh} , n_j are the parameters defined previously. n_i is the ideality factor, a fitting parameter that describes how closely the experimental behaviour of the solar cell matches the theory. In an ideal solar cell, the p-n junction behaves as an infinite plane, there is no recombination losses in the space-charge region and n_i is equal to 1.

One disadvantage of Equation D.3 is the presence of the shunt resistance R_{sh} - often in the range of 10^3 - in the exponential which can cause some calculation problems when using Matlab. In brief, Equation D.2 is preferred and is used when

possible, but Equation D.3 is necessary when dealing with solar cells made of different materials.

RESOLUTION ACCORDING TO BOUZIDI

Because of the sensitivity of the Lambert function to changes in the boundary conditions, the model can easily become difficult to solve and therefore another approach is applied to fit the j-V curves for the solar cell. Using the method proposed by Bouzidi et al., Equation 3 from the main text is divided into two equations, one valid for low voltages and one for higher voltages. The method is presented hereinafter for a solar cell consisting of one single junction; for a heterojunction solar cell, Equation 4 from the main text needs to be considered as well.

To fit all the parameters with two separate equations, Equation 3 first needs to be rewritten in the form of [206]

$$J = J_{Pa} - J_s \left[\exp \left(\frac{1}{n_i V_{th}} \left(\frac{V}{n_j} + J R_s \right) \right) \right] - G_a \frac{V}{n_j} \tag{D.4}$$

with the photocurrent J_{Pa} , the diode saturation current J_s as well as the shunt and series conductance G_a defined as

$$\begin{cases} J_{Pa} = \frac{J_L}{1 + \frac{R_s}{R_{sh}}} \\ J_s = \frac{J_0}{1 + \frac{R_s}{R_{sh}}} \\ G_a = \frac{1}{R_s + R_{sh}} \end{cases} \tag{D.5}$$

For low voltages, the linear part of Equation D.4 dominates and a simple linear fit is sufficient:

$$J = J_{Pa} - G_a \frac{V}{n_j} \tag{D.6}$$

Using this equation in the form $J=f(V)$, both parameters J_{Pa} and G_a are fitted against the experimental data.

In a second step, for higher voltages with $\frac{V}{n_j} + J R_s \gg n_i V_{th}$, the j-V curve is fitted using the previously calculated parameters, i.e. J_{Pa} and G_a . As proposed by [206], first, a corrected current density J_c across the solar cell is calculated

$$J_c = J + G_a \frac{V}{n_j} \tag{D.7}$$

Here, G_a is the series conductance calculated by the linear fitting, and J and V are given by the experimental data points.

Using the corrected current density, Equation D.4 can be rewritten for high voltages as

$$J_c = J_{Pa} - J_s \left[\exp \left(\frac{1}{n_i V_{th}} \left(\frac{V}{n_j} + J R_s \right) \right) \right] \tag{D.8}$$

For the fitting, Equation D.8 needs to be rearranged in the form of $V = f(J, J_c)$

$$\frac{V}{n_j} = f(J, J_c) = C_0 + C_1 J + C_2 \ln \left(1 - \frac{J_c}{J_{Pa}} \right) \tag{D.9}$$

where

$$\begin{cases} C_0 = -n_i V_{th} \ln \frac{J_s}{J_{Pa}} \\ C_1 = -R_s \\ C_2 = n_i V_{th} \end{cases} \tag{D.10}$$

Using Equation D.9 the coefficients C_0 , C_1 , and C_2 can be fitted using the experimental data points as well as the previously calculated J_{Pa} and J_c . Finally, with the results of both fittings, the parameters R_s , J_L , J_0 and R_{sh} can be deduced using Equations D.10.

DATA AVAILABILITY

The components or group of components for which the j-V curve was available are shown in Table D.1.

TABLE D.1: List of the data availability of the J-V curves of the five PV-EC devices modeled.

Urbain 2015	Urbain 2016	Jacobsson	Varadhan	Sun
- Solar cell	- Solar cell	- Solar cell	- Solar cell	- Solar cell
			+ anode	+ anode
			+ electrolyte	+ electrolyte
- Anode	- Whole device	- Electrolyser	- Anode	- Anode
- Cathode				- Cathode
- Electrolyte				- Electrolyte

As a matter of fact, the j-V characteristics of the whole Varadhan device together with the j-V curve of the electrolyzer were available, but the data was not consistent

and therefore these curves could not be used. Indeed, the data extracted from the published j - V measurements of the electrolyzer are implying that the overpotential caused by the electrolyzer is smaller than the overpotential of the anode alone, which is not possible since the electrolyzer includes both the anode and the cathode. Since no additional information could be found, it was decided to neglect the overpotential of the cathode. Neglecting the losses at the cathode has a minimal impact on the overall output of the model, since the losses of the electrolyzer in its entirety are mainly due to the slow kinetics of the OER and its resulting high overpotential [288].

In Figure D.1 the j - V curves of the different components of the Urbain 2016 device are plotted. The curve of the whole PV-EC device and the curve of the solar cell were extracted from literature [195]. The electrolyser curve in yellow was deduced from the two previous curves and the purple curve, showing the electrolyzer, is obtained from the model.

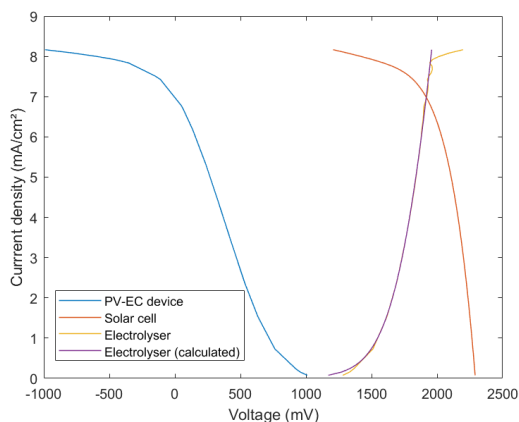


FIGURE D.1: j - V curve of the different components of the Urbain 2016 device.

PARITY PLOTS

Figure D.2 shows the parity plots for the solar cell part, comparing the experimental data points from literature with the calculated data using the model. In Figure D.3 the parity plots of the electrolyzer part are plotted.

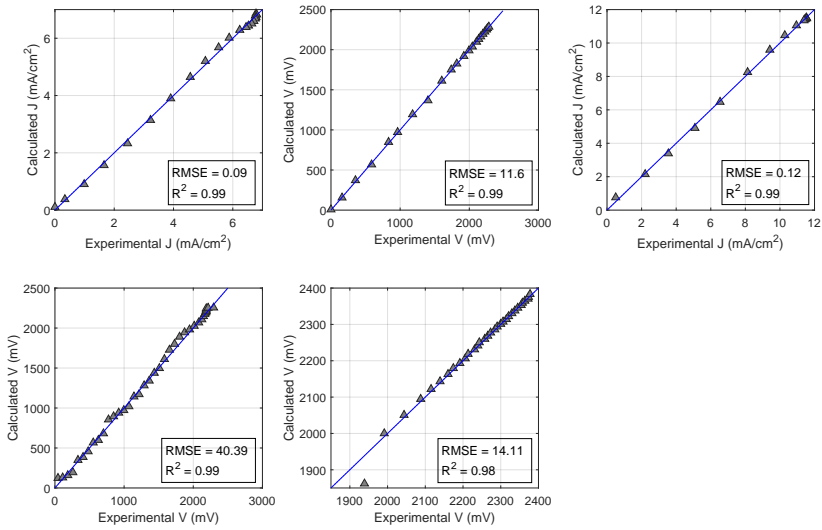


FIGURE D.2: a) Urbain 2015, b) Urbain 2016 c) Jacobsson d) Varadhan e) Sun. Parity plots of the model for the solar cell part of the devices. On the x-axis, the experimental data points extracted from the literature are displayed while on the y-axis, the output of the model is shown. The regression coefficient R^2 indicates the relative accuracy while the root mean square error RMSE shows the absolute accuracy.

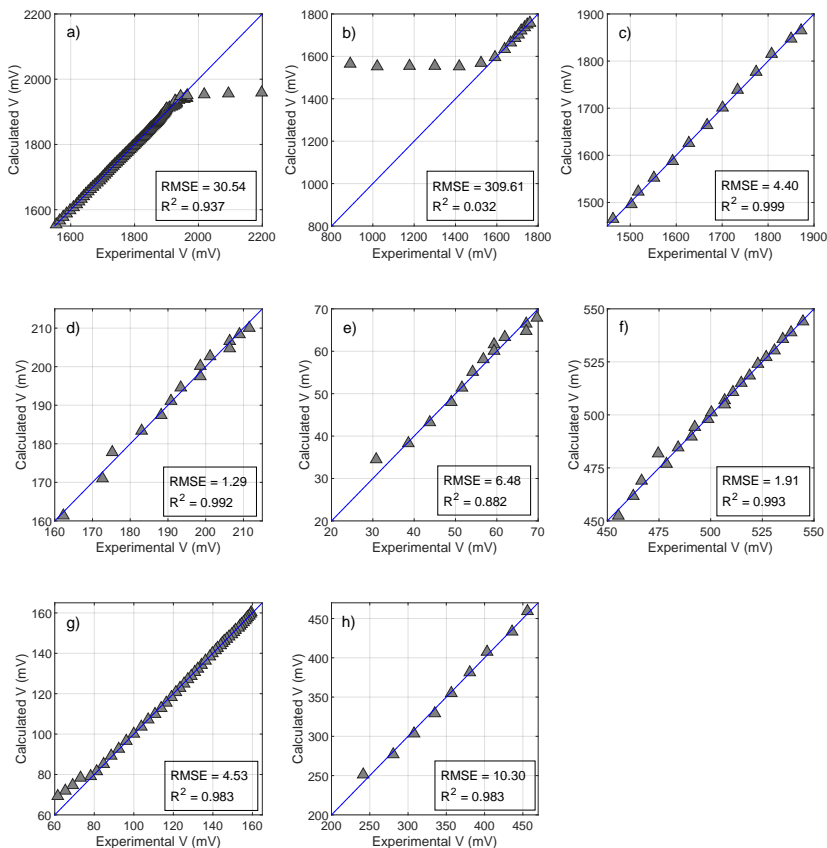


FIGURE D.3: a) Urbain 2016 - electrolyser, b) Jacobsson - electrolyser, c) Varadhan - electrolyser, d) Urbain 2015 - Anode, e) Urbain 2015 - Cathode, f) Sun - Anode, g) Sun - Cathode, h) Sun - Electrolyte. Parity plots of the model for the different components of the electrolyser part of the devices. On the x-axis, the experimental data points extracted from the literature are displayed while on the y-axis, the output of the model is shown. The R^2 and the RMSE of each fitting is also displayed.

Illumination for Utrecht and Sevilla

Figure D.4 shows the distribution of the illumination for Utrecht and Sevilla over the year 2019.

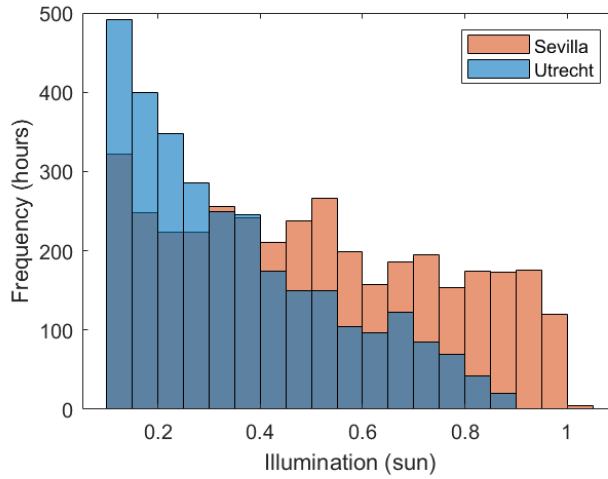


FIGURE D.4: Illumination distribution in 2019 in Sevilla and in Utrecht.

DETAILED STH DISTRIBUTION

In Figure D.5 the distribution of the STH efficiency over one year for all five devices is shown. For the calculation the illumination data from Figure D.4 was used.

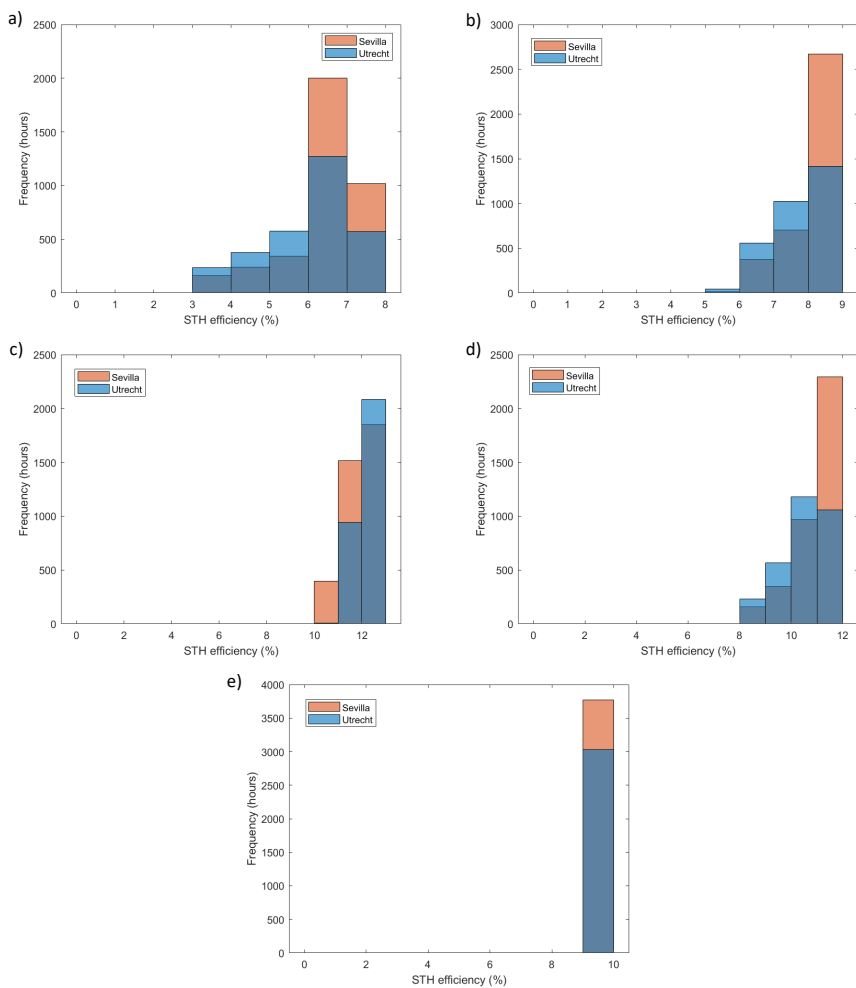


FIGURE D.5: STH efficiency distribution over the year 2019 in Sevilla and in Utrecht for the 5 PV-EC devices: a) Urbain 2015, b) Urbain 2016, c) Jacobsson, d) Varadhan and e) Sun.

BIBLIOGRAPHY

1. NASA Global Climate Change Center: *Vital Signs of the Planet*
2. Arias, P., Bellouin, N., Coppola, E., Jones, R., Krinner, G., Marotzke, J., Naik, V., Palmer, M., Plattner, G.-K., Rogelj, J., *et al.* Climate Change 2021: The Physical Science Basis. Contribution of Working Group 14 I to the Sixth Assessment Report of the Intergovernmental Panel on Climate Change; Technical Summary (2021).
3. Metz, B., Davidson, O., Coninck, H. d., Loos, M. & Meyer, L. IPCC special report on carbon dioxide capture and storage (2005).
4. IEA. *World Energy Outlook 2021, Paris*
5. Rogelj, J., Popp, A., Calvin, K. V., Luderer, G., Emmerling, J., Gernaat, D., Fujimori, S., Strefler, J., Hasegawa, T., Marangoni, G., Krey, V., Kriegler, E., Riahi, K., Van Vuuren, D. P., Doelman, J., Drouet, L., Edmonds, J., Fricko, O., Harmsen, M., Havlík, P., Humpenöder, F., Stehfest, E. & Tavoni, M. Scenarios towards limiting global mean temperature increase below 1.5 °C. *Nat. Clim. Chang.* **8**, 325 (2018).
6. Schaller, R., Markus, T., Korte, K. & Gawel, E. Atmospheric CO₂ as a resource for renewable energy production: A European energy law appraisal of direct air capture fuels. *Review of European, Comparative and International Environmental Law* (2022).
7. Olah, G. A., Prakash, G. K. & Goepfert, A. Anthropogenic chemical carbon cycle for a sustainable future. *Journal of the American Chemical Society* **133**, 12881 (2011).
8. Gasser, T., Guivarch, C., Tachiiri, K., Jones, C. D. & Ciais, P. Negative emissions physically needed to keep global warming below 2 °C. *Nature Communications* **2015 6:1** **6**, 1 (2015).
9. Beuttler, C., Charles, L. & Wurzbacher, J. The Role of Direct Air Capture in Mitigation of Anthropogenic Greenhouse Gas Emissions. *Frontiers in Climate* **1**, 10 (2019).
10. Dogutan, D. K. & Nocera, D. G. Artificial Photosynthesis at Efficiencies Greatly Exceeding That of Natural Photosynthesis. *Accounts of Chemical Research*, 3143 (2019).
11. Zhang, B. & Sun, L. Artificial photosynthesis: opportunities and challenges of molecular catalysts. *Chemical Society Reviews* **48**, 2216 (2019).

12. Royal Society, T. Sustainable synthetic carbon based fuels for transport POLICY BRIEFING Sustainable synthetic carbon based fuels for transport: Policy briefing. *The Royal society* (2019).
13. Herron, J. A., Kim, J., Upadhye, A. A., Huber, G. W. & Maravelias, C. T. A general framework for the assessment of solar fuel technologies. *Energy & Environmental Science* **8**, 126 (2015).
14. IEA (2019), *The Future of Hydrogen*, IEA, Paris 2019.
15. De Conick, H., Loos, M., Metz, B. & Meyer, L. *IPCC Special Report on Carbon Dioxide Capture and Storage* (2005).
16. Fernández, J. R., Abanades, J. C., Murillo, R. & Grasa, G. Conceptual design of a hydrogen production process from natural gas with CO₂ capture using a Ca-Cu chemical loop. *Int. J. Greenh. Gas Control* **6**, 126 (2012).
17. Voldsund, M., Jordal, K. & Anantharaman, R. Hydrogen production with CO₂ capture. *International Journal of Hydrogen Energy* **41**, 4969 (2016).
18. IEA. *Technology Roadmap Hydrogen and Fuel Cells* tech. rep. (2015).
19. Van Der Spek, M., Banet, C., Bauer, C., Gabrielli, P., Goldthorpe, W., Mazzotti, M., Munkejord, S. T., Røkke, N. A., Shah, N., Sunny, N., Sutter, D., Trusler, J. M. & Gazzani, M. Perspective on the hydrogen economy as a pathway to reach net-zero CO₂ emissions in Europe †. *This journal is Cite this: Energy Environ. Sci* **15**, 1034 (2022).
20. Zeman, F. S. & Lackner, K. S. Capturing carbon dioxide directly from the atmosphere. *World Resour. Rev.* **16**, 157 (2004).
21. Baciocchi, R., Storti, G. & Mazzotti, M. Process design and energy requirements for the capture of carbon dioxide from air. *Chemical Engineering and Processing: Process Intensification* **45**, 1047 (2006).
22. Socolow, R., Desmond, M., Aines, R., Blackstock, J., Bolland, O., Kaarsberg, T., Lewis, N., Mazzotti, M., Pfeffer, A., Sawyer, K., Sirola, J., Smit, B. & Wilcox, J. *Direct Air Capture of CO₂ with Chemicals: A Technology Assessment for the APS Panel on Public Affairs* 100 (American Physical Society, 2011).
23. Holmes, G. & Keith, D. W. An air-liquid contactor for large-scale capture of CO₂ from air. *Philosophical Transactions of the Royal Society A: Mathematical, Physical and Engineering Sciences* **370**, 4380 (2012).
24. Holmes, G., Nold, K., Walsh, T., Heidel, K., Henderson, M. A., Ritchie, J., Klavins, P., Singh, A. & Keith, D. W. Outdoor prototype results for direct atmospheric capture of carbon dioxide. *Energy Procedia* **37**, 6079 (2013).
25. Keith, D. W., Holmes, G., St. Angelo, D. & Heidel, K. A Process for Capturing CO₂ from the Atmosphere. *Joule* **2**, 1573 (2018).

26. Sabatino, F., Mehta, M., Grimm, A., Gazzani, M., Gallucci, F., Kramer, G. J. & van Sint Annaland, M. Evaluation of a Direct Air Capture Process Combining Wet Scrubbing and Bipolar Membrane Electrodialysis. *Ind. Eng. Chem. Res.* **59**, 7007 (2020).
27. Brethomé, F. M., Williams, N. J., Seipp, C. A., Kidder, M. K. & Custelcean, R. Direct air capture of CO₂ via aqueous-phase absorption and crystalline-phase release using concentrated solar power. *Nat. Energy* **3**, 553 (2018).
28. Custelcean, R., Williams, N. J., Garrabrant, K. A., Agullo, P., Brethomé, F. M., Martin, H. J. & Kidder, M. K. Direct Air Capture of CO₂ with Aqueous Amino Acids and Solid Bis-iminoguanidines (BIGs). *Ind. Eng. Chem. Res.* **58**, 23338 (2019).
29. Rochelle, G. T. Amine Scrubbing for CO₂ Capture. *Science (80-.)*. **325**, 1652 (2009).
30. Lackner, K. S. Capture of carbon dioxide from ambient air. *Eur. Phys. J. Spec. Top.* **176**, 93 (2009).
31. Barzagli, F., Giorgi, C., Mani, F. & Peruzzini, M. Screening Study of Different Amine-Based Solutions as Sorbents for Direct CO₂ Capture from Air. *ACS Sustain. Chem. Eng.* **8**, 14013 (2020).
32. Kiani, A., Jiang, K. & Feron, P. Techno-Economic Assessment for CO₂ Capture From Air Using a Conventional Liquid-Based Absorption Process. *Front. Energy Res.* **8**, 1 (2020).
33. Goepfert, A., Czaun, M., Surya Prakash, G. K. & Olah, G. A. Air as the renewable carbon source of the future: an overview of CO₂ capture from the atmosphere. *Energy Environ. Sci.* **5**, 7833 (2012).
34. Eisenberger, P. M., Cohen, R. W., Chichilnisky, G., Eisenberger, N. M., Chance, R. R. & Jones, C. W. Global warming and carbon-negative technology: Prospects for a lower-cost route to a lower-risk atmosphere. *Energy Environ.* **20**, 973 (2009).
35. Choi, S., Drese, J. H. & Jones, C. W. Adsorbent Materials for Carbon Dioxide Capture from Large Anthropogenic Point Sources. *ChemSusChem* **2**, 796 (2009).
36. Sanz-Pérez, E. S., Murdock, C. R., Didas, S. A. & Jones, C. W. Direct Capture of CO₂ from Ambient Air. *Chem. Rev.* **116**, 11840 (2016).
37. Didas, S. A., Choi, S., Chaikittisilp, W. & Jones, C. W. Amine-Oxide Hybrid Materials for CO₂ Capture from Ambient Air. *Acc. Chem. Res.* **48**, 2680 (2015).
38. Gebald, C., Repond, N. & Wurzbacher, J. A. *Steam assisted vacuum desorption process for carbon dioxide capture 2017*.

39. Gebald, C., Wurzbacher, J. A., Tingaut, P. & Steinfeld, A. Stability of Amine-Functionalized Cellulose during Temperature-Vacuum-Swing Cycling for CO₂ Capture from Air. *Environmental Science & Technology* **47**, 10063 (2013).
40. Fasihi, M., Efimova, O. & Breyer, C. Techno-economic assessment of CO₂ direct air capture plants. *Journal of Cleaner Production* **224**, 957 (2019).
41. Gebald, C., Platkowskl, N., Rüesch, T. & Wurzbacher, J. A. *Low-pressure drop structure of particle adsorbent bed for gas adsorption separation process* 2014.
42. Ping, E., Sakwa-novak, M. & Eisenberger, P. *Global Thermostat Low Cost Direct Air Capture Technology* in *Int. Conf. Negat. CO₂ Emiss.* (Goteborg, 2018), 1.
43. Bhatt, P. M., Belmabkhout, Y., Cadiau, A., Adil, K., Shekhah, O., Shkurenko, A., Barbour, L. J. & Eddaoudi, M. A Fine-Tuned Fluorinated MOF Addresses the Needs for Trace CO₂ Removal and Air Capture Using Physisorption. *J. Am. Chem. Soc.* **138**, 9301 (2016).
44. Shekhah, O., Belmabkhout, Y., Chen, Z., Guillerm, V., Cairns, A., Adil, K. & Eddaoudi, M. Made-to-order metal-organic frameworks for trace carbon dioxide removal and air capture. *Nat. Commun.* **5**, 1 (2014).
45. Darunte, L. A., Oetomo, A. D., Walton, K. S., Sholl, D. S. & Jones, C. W. Direct Air Capture of CO₂ Using Amine Functionalized MIL-101(Cr). *ACS Sustainable Chemistry and Engineering* **4**, 5761 (2016).
46. McDonald, T. M., Lee, W. R., Mason, J. A., Wiers, B. M., Hong, C. S. & Long, J. R. Capture of carbon dioxide from air and flue gas in the alkylamine-appended metal-organic framework mmen-Mg₂(dobpdc). *J. Am. Chem. Soc.* **134**, 7056 (2012).
47. Belmabkhout, Y., Guillerm, V. & Eddaoudi, M. Low concentration CO₂ capture using physical adsorbents: Are metal-organic frameworks becoming the new benchmark materials? *Chem. Eng. J.* **296**, 386 (2016).
48. Veneman, R., Frigka, N., Zhao, W., Li, Z., Kersten, S. & Brilman, W. Adsorption of H₂O and CO₂ on supported amine sorbents. *International Journal of Greenhouse Gas Control* **41**, 268 (2015).
49. Wurzbacher, J. A., Gebald, C., Piatkowski, N. & Steinfeld, A. Concurrent Separation of CO₂ and H₂O from Air by a Temperature-Vacuum Swing Adsorption/Desorption Cycle. *Environ. Sci. Technol.* **46**, 9191 (2012).
50. Casas, N., Schell, J., Pini, R. & Mazzotti, M. Fixed bed adsorption of CO₂/H₂ mixtures on activated carbon: experiments and modeling. *Adsorption* **18**, 143 (2012).
51. Azarabadi, H. & Lackner, K. S. A sorbent-focused techno-economic analysis of direct air capture. *Appl. Energy* **250**, 959 (2019).

52. Deutz, S. & Bardow, A. Life-cycle assessment of an industrial direct air capture process based on temperature–vacuum swing adsorption. *Nat. Energy* **1**, 235 (2021).
53. Sinha, A., Darunte, L. A., Jones, C. W., Realff, M. J. & Kawajiri, Y. Systems Design and Economic Analysis of Direct Air Capture of CO₂ through Temperature Vacuum Swing Adsorption Using MIL-101(Cr)-PEI-800 and mmen-Mg₂(dobpdc) MOF Adsorbents. *Industrial and Engineering Chemistry Research* **56**, 750 (2017).
54. Sinha, A. & Realff, M. J. A parametric study of the techno-economics of direct CO₂ air capture systems using solid adsorbents. *AIChE Journal* **65**, e16607 (2019).
55. Stampi-Bombelli, V., van der Spek, M. & Mazzotti, M. Analysis of direct capture of CO₂ from ambient air via steam-assisted temperature–vacuum swing adsorption. *Adsorption* **26**, 1183 (2020).
56. Astarita, G. Absorption of carbon dioxide into alkaline solutions in packed towers. *Ind. Eng. Chem. Fundam.* **2**, 294 (1963).
57. Mahmoudkhani, M., Heidel, K. R., Ferreira, J. C., Keith, D. W. & Cherry, R. S. Low energy packed tower and caustic recovery for direct capture of CO₂ from air. *Energy Procedia* **1**, 1535 (2009).
58. Pinsent, B. R. & Roughton, F. J. The kinetics of combination of carbon dioxide with water and hydroxide ions. *Trans. Faraday Soc.* **47**, 263 (1956).
59. Keith, D. W., Heidel, K. & Cherry, R. in *Geo-Engineering Clim. Chang. Environ. necessity or Pandora's box?* 107 (2010).
60. Heidel, K. R., Ritchie, J. A., Kainth, A. P. S. & Keith, D. W. *Recovering a Caustic Solution via Calcium Carbonate Crystal Aggregates* 2014.
61. Danckwerts, P. V. The reaction of CO₂ with ethanalamines. *Chem. Eng. Sci.* **34**, 443 (1979).
62. Veltman, K., Singh, B. & Hertwich, E. G. Human and environmental impact assessment of postcombustion CO₂ capture focusing on emissions from amine-based scrubbing solvents to air. *Environ. Sci. Technol.* **44**, 1496 (2010).
63. Le Moulec, Y., Neveux, T., Al Azki, A., Chikukwa, A. & Hoff, K. A. Process modifications for solvent-based post-combustion CO₂ capture. *Int. J. Greenh. Gas Control* **31**, 96 (2014).
64. Austgen, D. M., Rochelle, G. T., Peng, X. & Chen, C. C. Model of vapor-liquid equilibria for aqueous acid gas-alkanolamine systems using the electrolyte-NRTL equation. *Ind. Eng. Chem. Res.* **28**, 1060 (1989).

65. Amirkhosrow, M., Pérez-Calvo, J.-F., Gazzani, M., Mazzotti, M. & Nematı Lay, E. Rigorous rate-based model for CO₂ capture via monoethanolamine-based solutions: effect of kinetic models, mass transfer, and holdup correlations on prediction accuracy. *Sep. Sci. Technol.* **00**, 1 (2020).
66. Gebald, C., Meier, W., Repond, N., Rüesch, T. & Wurzbacher, J. A. *Direct air capture device* 2015.
67. Wurzbacher, J. A., Repond, N., Rüesch, T., Sauerbeck, S. & Gebald, C. *Low-pressure drop structure of particle adsorbent bed for improved adsorption gas separation process* 2018.
68. Belmabkhout, Y., Serna-Guerrero, R. & Sayari, A. Adsorption of CO₂-containing gas mixtures over amine-bearing pore-expanded MCM-41 silica: Application for gas purification. *Industrial and Engineering Chemistry Research* **49**, 359 (2010).
69. Sutanto, S., Dijkstra, J. W., Pieterse, J. A., Boon, J., Hauwert, P. & Brilman, D. W. CO₂ removal from biogas with supported amine sorbents: First technical evaluation based on experimental data. *Separation and Purification Technology* **184**, 12 (2017).
70. Bos, M. J., Kreuger, T., Kersten, S. R. & Brilman, D. W. Study on transport phenomena and intrinsic kinetics for CO₂ adsorption in solid amine sorbent. *Chemical Engineering Journal* **377** (2019).
71. Didas, S. A., Kulkarni, A. R., Sholl, D. S. & Jones, C. W. Role of amine structure on carbon dioxide adsorption from ultradilute gas streams such as ambient air. *ChemSusChem* **5**, 2058 (2012).
72. Elfving, J., Bajamundi, C., Kauppinen, J. & Sainio, T. Modelling of equilibrium working capacity of PSA, TSA and TVSA processes for CO₂ adsorption under direct air capture conditions. *J. CO₂ Util.* **22**, 270 (2017).
73. Kulkarni, A. R. & Sholl, D. S. Analysis of Equilibrium-Based TSA Processes for Direct Capture of CO₂ from Air. *Industrial & Engineering Chemistry Research* **51**, 8631 (2012).
74. Do, D. D. *Adsorption Analysis: Equilibria and Kinetics* (Imperial College Press, 1998).
75. Wurzbacher, J. A., Gebald, C., Brunner, S. & Steinfeld, A. Heat and mass transfer of temperature–vacuum swing desorption for CO₂ capture from air. *Chemical Engineering Journal* **283**, 1329 (2016).
76. García Martínez, J. Study of water adsorption on an amine adsorbent for Direct Air Capture of CO₂ (2020).

77. Casas, N., Schell, J., Blom, R. & Mazzotti, M. MOF and UiO-67/MCM-41 adsorbents for pre-combustion CO₂ capture by PSA: Breakthrough experiments and process design (2013).
78. Joss, L., Gazzani, M., Hefti, M., Marx, D. & Mazzotti, M. Temperature Swing Adsorption for the Recovery of the Heavy Component: An Equilibrium-Based Shortcut Model. *Industrial & Engineering Chemistry Research* **54**, 3027 (2015).
79. Haghpanah, R., Majumder, A., Nilam, R., Rajendran, A., Farooq, S., Karimi, I. A. & Amanullah, M. Multiobjective optimization of a four-step adsorption process for postcombustion CO₂ capture via finite volume simulation. *Ind. Eng. Chem. Res.* **52**, 4249 (2013).
80. Dantas, T. L., Luna, F. M. T., Silva, I. J., de Azevedo, D. C., Grande, C. A., Rodrigues, A. E. & Moreira, R. F. Carbon dioxide-nitrogen separation through adsorption on activated carbon in a fixed bed. *Chem. Eng. J.* **169**, 11 (2011).
81. Streb, A. & Mazzotti, M. Adsorption for efficient low carbon hydrogen production: part 2—Cyclic experiments and model predictions. *Adsorption* (2021).
82. Marx, D., Joss, L., Hefti, M. & Mazzotti, M. Temperature Swing Adsorption for Postcombustion CO₂ Capture: Single- and Multicolumn Experiments and Simulations. *Industrial and Engineering Chemistry Research* **55**, 1401 (2016).
83. Marx, D., Joss, L., Hefti, M., Gazzani, M. & Mazzotti, M. CO₂ Capture from a Binary CO₂/N₂ and a Ternary CO₂/N₂/H₂ Mixture by PSA: Experiments and Predictions. *Industrial and Engineering Chemistry Research* **54**, 6035 (2015).
84. Joss, L., Gazzani, M. & Mazzotti, M. Rational design of temperature swing adsorption cycles for post-combustion CO₂ capture. *Chemical Engineering Science* **158**, 381 (2017).
85. Streb, A., Hefti, M., Gazzani, M. & Mazzotti, M. Novel Adsorption Process for Co-Production of Hydrogen and CO₂ from a Multicomponent Stream. *Industrial and Engineering Chemistry Research* **58**, 17489 (2019).
86. Belmabkhout, Y. & Sayari, A. Effect of pore expansion and amine functionalization of mesoporous silica on CO₂ adsorption over a wide range of conditions. *Adsorption* **15**, 318 (2009).
87. Serna-Guerrero, R., Belmabkhout, Y. & Sayari, A. Modeling CO₂ adsorption on amine-functionalized mesoporous silica: 1. A semi-empirical equilibrium model. *Chemical Engineering Journal* **161**, 173 (2010).
88. Wurzbacher, J. A., Gebald, C., Piatkowski, N. & Steinfeld, A. Concurrent Separation of CO₂ and H₂O from Air by a Temperature-Vacuum Swing Adsorption/Desorption Cycle (2012).

89. Ng, Y. C., Yang, L. & Jovanovic, Z. R. The Development and Validation of a Closed-Loop Experimental Setup for Investigating CO₂ and H₂O Coadsorption Kinetics under Conditions Relevant to Direct Air Capture (2018).
90. Rajagopalan, A. K. & Rajendran, A. The effect of nitrogen adsorption on vacuum swing adsorption based post-combustion CO₂ capture. *International Journal of Greenhouse Gas Control* **78**, 437 (2018).
91. Joss, L., Capra, F., Gazzani, M., Mazzotti, M. & Martelli, E. MO-MCS: An Efficient Multi-objective Optimization Algorithm for the Optimization of Temperature/Pressure Swing Adsorption Cycles. *Comput. Aided Chem. Eng.* **38**, 1467 (2016).
92. Deutz, S. & Bardow, A. Life-cycle assessment of an industrial direct air capture process based on temperature–vacuum swing adsorption. *Nature Energy* **6**, 203 (2021).
93. Bajamundi, C. J. E., Koponen, J., Ruuskanen, V., Elfving, J., Kosonen, A., Kauppinen, J. & Ahola, J. Capturing CO₂ from air: Technical performance and process control improvement. *Journal of CO₂ Utilization* **30**, 232 (2019).
94. Yu, Q. & Brillman, D. W. *Design Strategy for CO₂ Adsorption from Ambient Air Using a Supported Amine Based Sorbent in a Fixed Bed Reactor* in *Energy Procedia* **114** (Elsevier Ltd, 2017), 6102.
95. Deeg, K. S., Damasceno Borges, D., Ongari, D., Rampal, N., Talirz, L., Yakutovich, A. V., Huck, J. M. & Smit, B. In Silico Discovery of Covalent Organic Frameworks for Carbon Capture. *ACS Applied Materials and Interfaces* **12**, 21559 (2020).
96. Beuttler, C., Charles, L. & Wurzbacher, J. The Role of Direct Air Capture in Mitigation of Anthropogenic Greenhouse Gas Emissions. *Frontiers in Climate* **1**, 3 (2019).
97. Chen, C. & Tavoni, M. Direct air capture of CO₂ and climate stabilization: A model based assessment. *Climatic Change* **118**, 59 (2013).
98. Hanna, R., Abdulla, A., Xu, Y. & Victor, D. G. Emergency deployment of direct air capture as a response to the climate crisis. *Nat. Commun.* **12**, 1 (2021).
99. Marcucci, A., Kypreos, S. & Panos, E. The road to achieving the long-term Paris targets: energy transition and the role of direct air capture. *Climatic Change* **144**, 181 (2017).
100. Meckling, J. & Biber, E. A policy roadmap for negative emissions using direct air capture. *Nature Communications* **12**, 1 (2021).

101. Realmonte, G., Drouet, L., Gambhir, A., Glynn, J., Hawkes, A., Köberle, A. C. & Tavoni, M. An inter-model assessment of the role of direct air capture in deep mitigation pathways. *Nature Communications* **10**, 1 (2019).
102. Choi, S., Gray, M. L. & Jones, C. W. Amine-tethered solid adsorbents coupling high adsorption capacity and regenerability for CO₂ capture from ambient air. *ChemSusChem* **4**, 628 (2011).
103. Elfving, J., Bajamundi, C. & Kauppinen, J. *Characterization and Performance of Direct Air Capture Sorbent in Energy Procedia* **114** (Elsevier Ltd, 2017), 6087.
104. Goepfert, A., Czaun, M., May, R. B., Prakash, G. K. S., Olah, G. A. & Narayanan, S. R. Carbon dioxide capture from the air using a polyamine based regenerable solid adsorbent. *Journal of the American Chemical Society* **133**, 20164 (2011).
105. Hou, C., Wu, Y., Wang, T., Wang, X. & Gao, X. Preparation of Quaternized Bamboo Cellulose and Its Implication in Direct Air Capture of CO₂. *Energy & Fuels* **33**, 1745 (2019).
106. Kwon, H. T., Sakwa-Novak, M. A., Pang, S. H., Sujan, A. R., Ping, E. W. & Jones, C. W. Aminopolymer-Impregnated Hierarchical Silica Structures: Unexpected Equivalent CO₂ Uptake under Simulated Air Capture and Flue Gas Capture Conditions. *Chemistry of Materials* **31**, 5229 (2019).
107. Sanz-Pérez, E. S., Murdock, C. R., Didas, S. A. & Jones, C. W. Direct Capture of CO₂ from Ambient Air. *Chemical Reviews* **116**, 11840 (2016).
108. Sehaqui, H., Gálvez, M. E., Becatinni, V., Cheng Ng, Y., Steinfeld, A., Zimmermann, T. & Tingaut, P. Fast and reversible direct CO₂ capture from air onto all-polymer nanofibrillated cellulose-polyethylenimine foams. *Environmental Science and Technology* **49**, 3167 (2015).
109. Sujan, A. R., Kumar, D. R., Sakwa-Novak, M., Ping, E. W., Hu, B., Park, S. J. & Jones, C. W. Poly(glycidyl amine)-Loaded SBA-15 Sorbents for CO₂ Capture from Dilute and Ultradilute Gas Mixtures. *ACS Appl. Polym. Mater.* **1**, 3137 (2019).
110. Rim, G., Kong, F., Song, M., Rosu, C., Priyadarshini, P., Lively, R. P. & Jones, C. W. Sub-Ambient Temperature Direct Air Capture of CO₂ using Amine-Impregnated MIL-101(Cr) Enables Ambient Temperature CO₂ Recovery. *JACS Au* **2**, 380 (2022).
111. Deutz, S. & Bardow, A. Life-cycle assessment of an industrial direct air capture process based on temperature-vacuum swing adsorption. *Nature Energy* **6**, 203 (2021).

112. Terlouw, T., Treyer, K., Bauer, C. & Mazzotti, M. Life Cycle Assessment of Direct Air Carbon Capture and Storage with Low-Carbon Energy Sources. *Environmental Science and Technology* **55**, 11397 (2021).
113. Breyer, C., Fasihi, M. & Aghahosseini, A. Carbon dioxide direct air capture for effective climate change mitigation based on renewable electricity: a new type of energy system sector coupling. *Mitigation and Adaptation Strategies for Global Change* **25**, 43 (2020).
114. Fasihi, M., Efimova, O. & Breyer, C. Techno-economic assessment of CO₂ direct air capture plants. *Journal of Cleaner Production* **224**, 957 (2019).
115. House, K. Z., Baclig, A. C., Ranjan, M., Van Nierop, E. A., Wilcox, J. & Herzog, H. J. Economic and energetic analysis of capturing CO₂ from ambient air. *Proceedings of the National Academy of Sciences of the United States of America* **108**, 20428 (2011).
116. Erans, M., Sanz-Pérez, E. S., Hanak, D. P., Clulow, Z., Reiner, D. M. & Mutch, G. A. Direct air capture: process technology, techno-economic and socio-political challenges. *Energy Environ. Sci.* **15**, 1360 (4 2022).
117. Shi, X., Xiao, H., Azarabadi, H., Song, J., Wu, X., Chen, X. & Lackner, K. S. Sorbents for Direct Capture of CO₂ from Ambient Air. *Angewandte Chemie International Edition* (2019).
118. Kong, F., Rim, G., Song, M. G., Rosu, C., Priyadarshini, P., Lively, R. P., Realf, M. J. & Jones, C. W. Research needs targeting direct air capture of carbon dioxide: Material & process performance characteristics under realistic environmental conditions. *Korean Journal of Chemical Engineering* **39**, 1 (2022).
119. Gebald, C., Zimmermann, T. & Tingaut, P. *Porous adsorbent structure for adsorption of CO₂ from a gas mixture* 2014.
120. Sabatino, F., Grimm, A., Gallucci, F., van Sint Annaland, M., Kramer, G. J. & Gazzani, M. A comparative energy and costs assessment and optimization for direct air capture technologies. *Joule* **5**, 2047 (2021).
121. Joss, L., Gazzani, M., Hefti, M., Marx, D. & Mazzotti, M. Temperature swing adsorption for the recovery of the heavy component: An equilibrium-based shortcut model. *Ind. Eng. Chem. Res.* **54**, 3027 (2015).
122. Wiegner, J., Grimm, A., Weimann, L. & Gazzani, M. On the optimal design and operation of solid sorbent direct air capture processes at varying ambient conditions. *Industrial & Engineering Chemistry Research* **61**, 12649 (2022).
123. *Climeworks direct air capture plant Capricorn*
124. *Orca is Climeworks' new large-scale carbon dioxide removal plant*

125. Sanz-Pérez, E. S., Murdock, C. R., Didas, S. A. & Jones, C. W. Direct Capture of CO₂ from Ambient Air. *Chemical Reviews* **116**, 11840 (2016).
126. Jansen, D., Gazzani, M., Manzolini, G., Dijk, E. V. & Carbo, M. Pre-combustion CO₂ capture. *International Journal of Greenhouse Gas Control* **40**, 167 (2015).
127. Samanta, A., Zhao, A., Shimizu, G. K., Sarkar, P. & Gupta, R. Post-Combustion CO₂ Capture Using Solid Sorbents: A Review. *Industrial and Engineering Chemistry Research* **51**, 1438 (2011).
128. Colón, Y. J., Gómez-Gualdrón, D. A. & Snurr, R. Q. Topologically Guided, Automated Construction of Metal-Organic Frameworks and Their Evaluation for Energy-Related Applications. *Crystal Growth and Design* **17**, 5801 (2017).
129. Henle, E. A., Gantzler, N., Thallapally, P. K., Fern, X. Z. & Simon, C. M. PoreMatMod.jl: Julia Package for in Silico Postsynthetic Modification of Crystal Structure Models. *Journal of Chemical Information and Modeling* **62**, 423 (2022).
130. Harlick, P. J. & Tezel, F. H. An experimental adsorbent screening study for CO₂ removal from N₂. *Microporous and Mesoporous Materials* **76**, 71 (2004).
131. Lin, L. C., Berger, A. H., Martin, R. L., Kim, J., Swisher, J. A., Jariwala, K., Rycroft, C. H., Bhowan, A. S., Deem, M. W., Haranczyk, M. & Smit, B. In silico screening of carbon-capture materials. *Nature Materials* **2012** *11*:7 **11**, 633 (2012).
132. Bae, Y. S. & Snurr, R. Q. Development and Evaluation of Porous Materials for Carbon Dioxide Separation and Capture. *Angewandte Chemie International Edition* **50**, 11586 (2011).
133. Khurana, M. & Farooq, S. Adsorbent Screening for Postcombustion CO₂ Capture: A Method Relating Equilibrium Isotherm Characteristics to an Optimum Vacuum Swing Adsorption Process Performance. *Industrial and Engineering Chemistry Research* **55**, 2447 (2016).
134. Farmahini, A. H., Krishnamurthy, S., Friedrich, D., Brandani, S. & Sarkisov, L. From Crystal to Adsorption Column: Challenges in Multiscale Computational Screening of Materials for Adsorption Separation Processes (2018).
135. Leperi, K. T., Snurr, R. Q. & You, F. Optimization of Two-Stage Pressure/Vacuum Swing Adsorption with Variable Dehydration Level for Post-combustion Carbon Capture. *Industrial and Engineering Chemistry Research* **55**, 3338 (2016).
136. Park, J., Rubiera Landa, H. O., Kawajiri, Y., Realff, M. J., Lively, R. P. & Sholl, D. S. How Well Do Approximate Models of Adsorption-Based CO₂ Capture Processes Predict Results of Detailed Process Models? *Industrial and Engineering Chemistry Research* **59**, 7097 (2020).

137. Khurana, M. & Farooq, S. Integrated adsorbent-process optimization for carbon capture and concentration using vacuum swing adsorption cycles. *AIChE Journal* **63**, 2987 (2017).
138. Pai, K. N., Prasad, V. & Rajendran, A. Experimentally validated machine learning frameworks for accelerated prediction of cyclic steady state and optimization of pressure swing adsorption processes. *Separation and Purification Technology* **241**, 116651 (2020).
139. Maring, B. J. & Webley, P. A. A new simplified pressure/vacuum swing adsorption model for rapid adsorbent screening for CO₂ capture applications. *International Journal of Greenhouse Gas Control* **15**, 16 (2013).
140. Balashankar, V. S., Rajagopalan, A. K., de Pauw, R., Avila, A. M. & Rajendran, A. Analysis of a Batch Adsorber Analogue for Rapid Screening of Adsorbents for Postcombustion CO₂ Capture. *Industrial & Engineering Chemistry Research* **58**, 3314 (2019).
141. Ajenifuja, A., Joss, L. & Jobson, M. A New Equilibrium Shortcut Temperature Swing Adsorption Model for Fast Adsorbent Screening. *Industrial & Engineering Chemistry Research* **59**, 3485 (2020).
142. Linstrom, P., Mallard, W. & Eds. *NIST Chemistry WebBook, NIST Standard Reference Database Number 69* Gaithersburg MD, 20899.
143. Park, J., Howe, J. D. & Sholl, D. S. How Reproducible Are Isotherm Measurements in Metal-Organic Frameworks? *Chemistry of Materials* **29**, 10487 (2017).
144. Iacomi, P. & Llewellyn, P. L. Data Mining for Binary Separation Materials in Published Adsorption Isotherms. *Chemistry of Materials* **32**, 982 (2020).
145. Elfving, J. Direct capture of CO₂ from air using amine-functionalized resin - Effect of humidity in modelling and evaluation of process concepts (2021).
146. Coleman, T. F. & Li, Y. An Interior Trust Region Approach for Nonlinear Minimization Subject to Bounds. <http://dx.doi.org/10.1137/0806023> **6**, 418 (2006).
147. *Multi-Objective Particle Swarm Optimization (MOPSO) - File Exchange - MATLAB Central*
148. Coello, C. A. C., Pulido, G. T. & Lechuga, M. S. Handling Multiple Objectives With Particle Swarm Optimization Evolutionary multi-objective optimization View project Nature-Inspired Constrained Optimization View project Handling Multiple Objectives With Particle Swarm Optimization. *IEEE TRANSACTIONS ON EVOLUTIONARY COMPUTATION* **8** (2004).

149. Grimm, A. & Gazzani, M. A machine learning-aided equilibrium model of VTSA processes for sorbents screening applied to CO₂ capture from diluted sources. *Industrial & Engineering Chemistry Research* **61**, 14004 (2022).
150. Wilmer, C. E., Leaf, M., Lee, C. Y., Farha, O. K., Hauser, B. G., Hupp, J. T. & Snurr, R. Q. Large-scale screening of hypothetical metal–organic frameworks. *Nature Chemistry* **2011** 4:2 **4**, 83 (2011).
151. Yazaydin, A. Ö., Snurr, R. Q., Park, T. H., Koh, K., Liu, J., LeVan, M. D., Benin, A. I., Jakubczak, P., Lanuza, M., Galloway, D. B., Low, J. J. & Willis, R. R. Screening of metal-organic frameworks for carbon dioxide capture from flue gas using a combined experimental and modeling approach. *Journal of the American Chemical Society* **131**, 18198 (2009).
152. Colón, Y. J. & Snurr, R. Q. High-throughput computational screening of metal–organic frameworks. *Chemical Society Reviews* **43**, 5735 (2014).
153. Huck, J. M., Lin, L. C., Berger, A. H., Shahrak, M. N., Martin, R. L., Bhowm, A. S., Haranczyk, M., Reuter, K. & Smit, B. Evaluating different classes of porous materials for carbon capture. *Energy Environ. Sci.* **7**, 4132 (2014).
154. Rajagopalan, A. K., Avila, A. M. & Rajendran, A. Do adsorbent screening metrics predict process performance? A process optimisation based study for post-combustion capture of CO₂. *Int. J. Greenh. Gas Control* **46**, 76 (2016).
155. Leperi, K. T., Chung, Y. G., You, F. & Snurr, R. Q. Development of a General Evaluation Metric for Rapid Screening of Adsorbent Materials for Postcombustion CO₂ Capture. *ACS Sustainable Chemistry and Engineering* **7**, 11529 (2019).
156. Farmahini, A. H., Friedrich, D., Brandani, S. & Sarkisov, L. Exploring new sources of efficiency in process-driven materials screening for post-combustion carbon capture †. *Energy Environ. Sci.* **13**, 1018 (2020).
157. Burns, T. D., Pai, K. N., Subraveti, S. G., Collins, S. P., Krykunov, M., Rajendran, A. & Woo, T. K. Prediction of MOF Performance in Vacuum Swing Adsorption Systems for Postcombustion CO₂ Capture Based on Integrated Molecular Simulations, Process Optimizations, and Machine Learning Models. *Environmental Science and Technology* **54**, 4536 (2020).
158. Khurana, M. & Farooq, S. Integrated Adsorbent Process Optimization for Minimum Cost of Electricity Including Carbon Capture by a VSA Process. *AIChE Journal* **65**, 184 (2019).
159. Danaci, D., Bui, M., Mac Dowell, N. & Petit, C. Exploring the limits of adsorption-based CO₂ capture using MOFs with PVSA – from molecular design to process economics. *Molecular Systems Design & Engineering* **5**, 212 (2020).

160. Subraveti, S. G., Roussanaly, S., Anantharaman, R., Riboldi, L. & Rajendran, A. Techno-economic assessment of optimised vacuum swing adsorption for post-combustion CO₂ capture from steam-methane reformer flue gas. *Separation and Purification Technology* **256**, 117832 (2021).
161. Ayawei, N., Ebelegi, N. & Wankasi, D. Modelling and Interpretation of Adsorption Isotherms (2017).
162. Al-Ghouti, M. A. & Da'ana, D. A. Guidelines for the use and interpretation of adsorption isotherm models: A review. *Journal of Hazardous Materials* **393** (2020).
163. Giles, C. H., Smith, D. & Huitson, A. A general treatment and classification of the solute adsorption isotherm. I. Theoretical. *Journal of Colloid And Interface Science* **47**, 755 (1974).
164. Limousin, G., Gaudet, J. P., Charlet, L., Szenknect, S., Barthès, V. & Krimissa, M. Sorption isotherms: A review on physical bases, modeling and measurement. *Applied Geochemistry* **22**, 249 (2007).
165. Keller, J. U. & Staudt, R. Gas adsorption equilibria : experimental methods and adsorptive isotherms, 422 (2005).
166. Hefti, M. & Mazzotti, M. Postcombustion CO₂ Capture from Wet Flue Gas by Temperature Swing Adsorption. *Ind. Eng. Chem. Res.* **57**, 15542 (2018).
167. Pai, K. N., Baboolal, J. D., Sharp, D. A. & Rajendran, A. Evaluation of diamine-appended metal-organic frameworks for post-combustion CO₂ capture by vacuum swing adsorption. *Separation and Purification Technology* **211**, 540 (2019).
168. Hughes, R., Kotamreddy, G., Ostace, A., Bhattacharyya, D., Siegelman, R. L., Parker, S. T., Didas, S. A., Long, J. R., Omell, B. & Matuszewski, M. Isotherm, Kinetic, Process Modeling, and Techno-Economic Analysis of a Diamine-Appended Metal-Organic Framework for CO₂ Capture Using Fixed Bed Contactors (2021).
169. Danaci, D., Bui, M., Mac Dowell, N. & Petit, C. Exploring the limits of adsorption-based CO₂ capture using MOFs with PVSA-from molecular design to process economics. *Mol. Syst. Des. Eng.* **5**, 212 (2020).
170. David J. Brennan. *Process Industry Economics: An International Perspective* 1998.
171. Danaci, D., Webley, P. A. & Petit, C. Guidelines for Techno-Economic Analysis of Adsorption Processes. *Frontiers in Chemical Engineering* **0**, 30 (2021).
172. Seider, W. D., Lewin, D. R., Seader, J. D., engineer) Widagdo, S. (, Gani, R. (& Ng, K. M. Product and process design principles : synthesis, analysis, and evaluation, 738 (2016).

173. Lackner, K. S. & Azarabadi, H. Buying down the Cost of Direct Air Capture (2021).
174. Ranjan, M. & Herzog, H. J. Feasibility of air capture. *Energy Procedia* **4**, 2869 (2011).
175. Broehm, M., Strefler, J. & Bauer, N. Techno-Economic Review of Direct Air Capture Systems for Large Scale Mitigation of Atmospheric CO₂. *SSRN Electronic Journal* (2015).
176. Board, O. S., National Academies of Sciences, E., Medicine, *et al.* Negative emissions technologies and reliable sequestration: A research agenda (2019).
177. Tollefson, J. Sucking carbon dioxide from air is cheaper than scientists thought news. *Nature* **558**, 173 (2018).
178. Zanco, S. E., Pérez-Calvo, J.-F., Gasós, A., Cordiano, B., Becattini, V. & Mazzotti, M. Postcombustion CO₂ Capture: A Comparative Techno-Economic Assessment of Three Technologies Using a Solvent, an Adsorbent, and a Membrane. **1**, 50 (2021).
179. Fujishima, A. & Honda, K. Electrochemical photolysis of water at a semiconductor electrode. *Nature* (1972).
180. Rabell, G. O., Alfaro Cruz, M. & Juárez-Ramírez, I. Photoelectrochemical (PEC) analysis of ZnO/Al photoelectrodes and its photocatalytic activity for hydrogen production. *International Journal of Hydrogen Energy* (2022).
181. Braiek, Z., Ben Naceur, J., Jrad, F., Ben Assaker, I. & Chtourou, R. Novel synthesis of graphene oxide/In₂S₃/TiO₂ NRs heterojunction photoanode for enhanced photoelectrochemical (PEC) performance. *International Journal of Hydrogen Energy* **47**, 3655 (2022).
182. Bai, S., Han, J., Zhang, K., Zhao, Y., Luo, R., Li, D. & Chen, A. rGO decorated semiconductor heterojunction of BiVO₄/NiO to enhance PEC water splitting efficiency. *International Journal of Hydrogen Energy* **47**, 4375 (2022).
183. Turan, B., Becker, J. P., Urbain, F., Finger, F., Rau, U. & Haas, S. Upscaling of integrated photoelectrochemical water-splitting devices to large areas. *Nature Communications* **7**, 1 (2016).
184. Nielander, A. C., Shaner, M. R., Papadantonakis, K. M., Francis, S. A. & Lewis, N. S. A taxonomy for solar fuels generators. *Energy and Environmental Science* **8**, 16 (2015).
185. Jacobsson, T. J., Fjällström, V., Edoff, M. & Edvinsson, T. Sustainable solar hydrogen production: From photoelectrochemical cells to PV-electrolyzers and back again. *Energy and Environmental Science* **7**, 2056 (2014).

186. Hamdani, I. R. & Bhaskarwar, A. N. Recent progress in material selection and device designs for photoelectrochemical water-splitting. *Renewable and Sustainable Energy Reviews* **138**, 110503 (2021).
187. Wang, Q., Hisatomi, T., Jia, Q., Tokudome, H., Zhong, M., Wang, C., Pan, Z., Takata, T., Nakabayashi, M., Shibata, N., Li, Y., Sharp, I. D., Kudo, A., Yamada, T. & Domen, K. Scalable water splitting on particulate photocatalyst sheets with a solar-to-hydrogen energy conversion efficiency exceeding 1% (2016).
188. Maeda, K., Takata, T., Hara, M., Saito, N., Inoue, Y., Kobayashi, H. & Domen, K. GaN:ZnO Solid Solution as a Photocatalyst for Visible-Light-Driven Overall Water Splitting (2005).
189. Jia, J., Seitz, L. C., Benck, J. D., Huo, Y., Chen, Y., Ng, J. W. D., Bilir, T., Harris, J. S. & Jaramillo, T. F. Solar water splitting by photovoltaic-electrolysis with a solar-to-hydrogen efficiency over 30%. *Nat. Commun.* **7**, 13237 (2016).
190. Kim, J. H., Hansora, D., Sharma, P., Jang, J. W. & Lee, J. S. Toward practical solar hydrogen production-an artificial photosynthetic leaf-to-farm challenge. *Chemical Society Reviews* **48**, 1908 (2019).
191. Rongé, J., Bosserez, T., Martel, D., Nervi, C., Boarino, L., Taulelle, F., Decher, G., Bordiga, S. & Martens, J. A. *Monolithic cells for solar fuels* 2014.
192. Reece, S. Y., Hamel, J. A., Sung, K., Jarvi, T. D., Esswein, A. J., Pijpers, J. J. & Nocera, D. G. *Wireless solar water splitting using silicon-based semiconductors and earth-abundant catalysts* tech. rep. 6056 (2011), 645.
193. Urbain, F., Smirnov, V., Becker, J. P., Rau, U., Ziegler, J., Kaiser, B., Jaegermann, W. & Finger, F. Application and modeling of an integrated amorphous silicon tandem based device for solar water splitting. *Solar Energy Materials and Solar Cells* **140**, 275 (2015).
194. Jacobsson, T. J., Fjällström, V., Sahlberg, M., Edoff, M. & Edvinsson, T. A monolithic device for solar water splitting based on series interconnected thin film absorbers reaching over 10% solar-to-hydrogen efficiency. *Energy & Environmental Science* **6**, 3676 (2013).
195. Urbain, F., Smirnov, V., Becker, J. P., Lambert, A., Yang, F., Ziegler, J., Kaiser, B., Jaegermann, W., Rau, U. & Finger, F. Multijunction Si photocathodes with tunable photovoltages from 2.0 v to 2.8 v for light induced water splitting. *Energy and Environmental Science* **9**, 145 (2016).
196. Han, L., Abdi, F. F., Van De Krol, R., Liu, R., Huang, Z., Lewerenz, H. J., Dam, B., Zeman, M. & Smets, A. H. Efficient Water-Splitting Device Based on a Bismuth Vanadate Photoanode and Thin-Film Silicon Solar Cells. *ChemSusChem* **7**, 2832 (2014).

197. Kobayashi, H., Sato, N., Orita, M., Kuang, Y., Kaneko, H., Minegishi, T., Yamada, T. & Domen, K. Development of highly efficient CuIn_{0.5}Ga_{0.5}Se₂-based photocathode and application to overall solar driven water splitting. *Energy and Environmental Science* **11**, 3003 (2018).
198. Sharifi, T., Larsen, C., Wang, J., Kwong, W. L., Gracia-Espino, E., Mercier, G., Messinger, J., Wågberg, T. & Edman, L. Toward a Low-Cost Artificial Leaf: Driving Carbon-Based and Bifunctional Catalyst Electrodes with Solution-Processed Perovskite Photovoltaics. *Advanced Energy Materials* **6**, 1 (2016).
199. Nguyen, P. D., Duong, T. M. & Tran, P. D. Current progress and challenges in engineering viable artificial leaf for solar water splitting. *Journal of Science: Advanced Materials and Devices* **2**, 399 (2017).
200. Ager, J. W., Shaner, M. R., Walczak, K. A., Sharp, I. D. & Ardo, S. Experimental demonstrations of spontaneous, solar-driven photoelectrochemical water splitting. *Energy and Environmental Science* **8**, 2811 (2015).
201. Alfaifi, B. Y., Ullah, H., Alfaifi, S., Tahir, A. A. & Mallick, T. K. Photoelectrochemical solar water splitting: From basic principles to advanced devices. *Veruscript Functional Nanomaterials* **2**, BDJOC₃ (2018).
202. Winkler, M. T., Cox, C. R., Nocera, D. G. & Buonassisi, T. Modeling integrated photovoltaic-electrochemical devices using steady-state equivalent circuits. *Proceedings of the National Academy of Sciences of the United States of America* **110**, E1076 (2013).
203. Fathabadi, H. Lambert W function-based technique for tracking the maximum power point of PV modules connected in various configurations. *Renewable Energy* **74**, 214 (2015).
204. Varadhan, P., Fu, H. C., Kao, Y. C., Horng, R. H. & He, J. H. An efficient and stable photoelectrochemical system with 9% solar-to-hydrogen conversion efficiency via InGaP/GaAs double junction. *Nature Communications* **10**, 1 (2019).
205. Sun, K., Liu, R., Chen, Y., Verlage, E., Lewis, N. S. & Xiang, C. A Stabilized, Intrinsically Safe, 10% Efficient, Solar-Driven Water-Splitting Cell Incorporating Earth-Abundant Electrocatalysts with Steady-State pH Gradients and Product Separation Enabled by a Bipolar Membrane. *Advanced Energy Materials* **6**, 1600379 (2016).
206. Bouzidi, K., Chegaar, M. & Bouhemadou, A. Solar cells parameters evaluation considering the series and shunt resistance. *Solar Energy Materials and Solar Cells* **91**, 1647 (2007).
207. Döscher, H., Geisz, J. F., Deutsch, T. G. & Turner, J. A. Sunlight absorption in water-efficiency and design implications for photoelectrochemical devices. *Energy Environ. Sci* (2014).

208. Neville, R. C. in *Solar Energy Conversion: The Solar Cell (Second Edition)* 197 (Elsevier B.V., 1995).
209. Somasundaran, P. & Gupta, R. Evaluation of Shunt Losses in Industrial Silicon Solar Cells. *International Journal of Photoenergy* (2016).
210. Usami, A. in *Nanostructured Materials for Solar Energy Conversion* (2006).
211. Honsberg, C. & Bowden, S. *PVEducation* 2019.
212. Chavali, R. V. K., Wilcox, J. R., Ray, B., Gray, J. L. & Alam, M. A. Correlated Non-ideal Effects of Dark and Light I–V Characteristics in a-Si/c-Si Heterojunction Solar Cells. *IEEE Journal of Photovoltaics* **4**, 763 (2014).
213. Sayedin, F., Maroufmashat, A., Sattari, S., Elkamel, A. & Fowler, M. Optimization of Photovoltaic Electrolyzer Hybrid systems; Taking into account the effect of climate conditions. *Energy Conversion and Management* (2016).
214. Solcast. *Solar Forecasting & Solar Irradiance Data* <https://solcast.com/>. 2020.
215. National Renewable Energy Laboratory. *System Advisor Model (SAM) Version 2020.2.29 (SAM 2020.2.29)* (Golden, CO (United States), 2020).
216. Dias, P., Lopes, T., Andrade, L. & Mendes, A. Temperature effect on water splitting using a Si-doped hematite photoanode. *Journal of Power Sources* **272**, 567 (2014).
217. Clarke, R., Giddey, S., Ciacchi, F. T., Badwal, S. P., Paul, B. & Andrews, J. Direct coupling of an electrolyser to a solar PV system for generating hydrogen. *International Journal of Hydrogen Energy* **34**, 2531 (2009).
218. Fujishima, A. & Honda, K. Electrochemical Photolysis of Water at a Semiconductor Electrode. *Nature* **238**, 37 (1972).
219. Jacobsson, T. J., Fjällström, V., Edoff, M. & Edvinsson, T. CIGS based devices for solar hydrogen production spanning from PEC-cells to PV-electrolyzers: A comparison of efficiency, stability and device topology. *Solar Energy Materials and Solar Cells* **134**, 185 (2015).
220. Li, R. *Latest progress in hydrogen production from solar water splitting via photocatalysis, photoelectrochemical, and photovoltaic-photoelectrochemical solutions* 2017.
221. Iqbal, M. Z. & Siddique, S. *Recent progress in efficiency of hydrogen evolution process based photoelectrochemical cell* 2018.
222. Hinkley, J., Hayward, J., Mcnaughton, R., Gillespie, R., Watt, M. & Lovegrove, K. *Cost assessment of hydrogen production from PV and electrolysis Ayako Matsumoto (Mitsui Global Strategic Studies Institute)* tech. rep. (Csiro Energy, 2016).

223. James, B. D., Baum, G. N., Perez, J. & Baum, K. N. *Technoeconomic Analysis of Photoelectrochemical (PEC) Hydrogen Production* tech. rep. December (DOE report, 2009).
224. Rodriguez, C. A., Modestino, M. A., Psaltis, D. & Moser, C. Design and cost considerations for practical solar-hydrogen generators. *Energy Environ. Sci.* **7**, 3828 (2014).
225. Victoria, M. *Conceptual design of an industrial-scale artificial leaf device* tech. rep. (Delft, 2015).
226. Xu, L., Deng, X., Abken, A., Cao, X., Du, W., Vijn, A., Ingler, W., Chen, C., Fan, Q., Collins, R., Compaan, A., Yan, Y., Giolando, D. & Turner, J. *Critical Research for Cost-Effective Photoelectrochemical Production of Hydrogen* tech. rep. (Golden Field Office, Golden, CO (United States), 2014).
227. Shaner, M. R., Atwater, H. A., Lewis, N. S. & McFarland, E. W. A comparative technoeconomic analysis of renewable hydrogen production using solar energy. *Energy Environ. Sci.* **9**, 2354 (2016).
228. Blok, K. & Nieuwlaar, E. *Introduction to Energy Analysis*. 337 (Taylor and Francis, 2016).
229. Pinaud, B. A., Benck, J. D., Seitz, L. C., Forman, A. J., Chen, Z., Deutsch, T. G., James, B. D., Baum, K. N., Baum, G. N., Ardo, S., Wang, H., Miller, E. & Jaramillo, T. F. Technical and economic feasibility of centralized facilities for solar hydrogen production via photocatalysis and photoelectrochemistry. *Cite this: Energy Environ. Sci* (2013).
230. James, B. D., Colella, W. G. & Moton, J. M. Techno-Economic Analysis of Hydrogen Production Pathways. *Strategic Analysis* (2013).
231. *International Technology Roadmap for Photovoltaic - ITRPV 2017*.
232. U.S. Department of Labor. *May 2017 National Occupational Employment and Wage Estimates 2017*.
233. Chen, Z., Jaramillo, T. F., Deutsch, T. G., Kleiman-Shwarsstein, A., Forman, A. J., Gaillard, N., Garland, R., Takanabe, K., Heske, C., Sunkara, M., McFarland, E. W., Domen, K., Milled, E. L. & Dinh, H. N. *Accelerating materials development for photoelectrochemical hydrogen production: Standards for methods, definitions, and reporting protocols* 2010.
234. Kalinci, Y., Hepbasli, A. & Dincer, I. Techno-economic analysis of a stand-alone hybrid renewable energy system with hydrogen production and storage options. *International Journal of Hydrogen Energy* **40**, 7652 (2015).
235. Masson, G. & Kaizuka, I. *Trends 2017 in photovoltaic applications* tech. rep. (IEA International Energy Agency, 2017).

236. Jacoby, M. The future of low-cost solar cells. *c&en* **94**, 30 (2016).
237. Sapountzi, F. M., Gracia, J. M., Weststrate, C. (-J., Fredriksson, H. O. & Niemantsverdriet, J. (Electrochemicals for the generation of hydrogen, oxygen and synthesis gas. *Progress in Energy and Combustion Science* **58**, 1 (2017).
238. Bertuccioli, L., Chan, A., Hart, D., Lehner, F., Madden, B. & Standen, E. *Development of Water Electrolysis in the European Union Final Report Fuel cells and hydrogen tech. rep.* (Fuel Cells and Hydrogen Joint Undertaking, 2014).
239. Falcão, D. S. & Pinto, A. M. A review on PEM electrolyzer modelling: Guidelines for beginners. *J. Clean. Prod.* **261** (2020).
240. Carmo, M., Fritz, D. L., Mergel, J. & Stolten, D. *A comprehensive review on PEM water electrolysis* 2013.
241. Chi, J. & Yu, H. *Water electrolysis based on renewable energy for hydrogen production* 2018.
242. Rau, S., Vierrath, S., Ohlmann, J., Fallisch, A., Lackner, D., Dimroth, F. & Smolinka, T. Highly Efficient Solar Hydrogen Generation-An Integrated Concept Joining III-V Solar Cells with PEM Electrolysis Cells. *Energy Technology* **2**, 43 (2014).
243. Holladay, J. D., Hu, J., King, D. L. & Wang, Y. *An overview of hydrogen production technologies* 2009.
244. Young, J. L., Steiner, M. A., Döscher, H., France, R. M., Turner, J. A. & Deutsch, T. G. Direct solar-to-hydrogen conversion via inverted metamorphic multi-junction semiconductor architectures. *Nature Energy* **2**, 17028 (2017).
245. Haussener, S., Xiang, C., Spurgeon, J. M., Ardo, S., Lewis, N. S. & Weber, A. Z. Modeling, simulation, and design criteria for photoelectrochemical water-splitting systems. *Energy & Environmental Science* **5**, 9922 (2012).
246. Colville, F. *Thin-film solar production to collapse to seven-year low in 2017* 2017.
247. Hicks, W. NREL, *Swiss Scientists Power Past Solar Efficiency Records* 2017.
248. Lee, T. D. & Ebong, A. U. A review of thin film solar cell technologies and challenges. *Renewable and Sustainable Energy Reviews* **70**, 1286 (2017).
249. Green, M. A., Hishikawa, Y., Warta, W., Dunlop, E. D., Levi, D. H., Hohl-Ebinger, J. & Ho-Baillie, A. W. Solar cell efficiency tables (version 50). *Progress in Photovoltaics: Research and Applications* **25**, 668 (2017).
250. Godula-Jopek, A. Hydrogen production: by electrolysis (2015).
251. *EnergyTrend PV Spot Price* 2018.

252. Sathre, R., Scown, C. D., Morrow, W. R., Stevens, J. C., Sharp, I. D., Ager, J. W., Walczak, K., Houle, F. A. & Greenblatt, J. B. Life-cycle net energy assessment of large-scale hydrogen production via photoelectrochemical water splitting. *Energy Environ. Sci.* **7**, 3264 (2014).
253. James, B. D. & Spisak, A. B. *Mass Production Cost Estimation of Direct Hydrogen PEM Fuel Cell Systems for Transportation Applications: 2012 Update* tech. rep. (2012).
254. Chueh, A. *Price Quotes EnergyTrend PV* 2017.
255. Rongé, J., Bosserez, T., Huguenin, L., Dumortier, M., Haussener, S. & Martens, J. A. Solar Hydrogen Reaching Maturity. *Oil & Gas Science and Technology – Revue d'IFP Energies nouvelles* **70**, 863 (2015).
256. Kraan, O., Kramer, G. J., Haigh, M. & Laurens, C. An Energy Transition That Relies Only on Technology Leads to a Bet on Solar Fuels. *Joule* **3**, 2286 (2019).
257. IPCC, I. *Summary for Policymakers" in Global warming of 1.5° C. An IPCC Special Report on the impacts of global warming of 1.5° C above pre-industrial levels and related global greenhouse gas emission pathways, in the context of strengthening the global response to the threat of climate change, sustainable development, and efforts to eradicate poverty.* 2018.
258. National Academies of Sciences, Engineering & Medicine. Negative Emissions Technologies and Reliable Sequestration: A Research Agenda. *Negative Emissions Technologies and Reliable Sequestration* (2018).
259. Manzolini, G., Macchi, E., Binotti, M. & Gazzani, M. Integration of SEWGS for carbon capture in Natural Gas Combined Cycle. Part B: Reference case comparison. *Int. J. Greenh. Gas Control* **5**, 214 (2011).
260. Rohatgi, A. *WebPlotDigitizer*
261. Elfving, J., Bajamundi, C., Kauppinen, J. & Sainio, T. Modelling of equilibrium working capacity of PSA, TSA and TVSA processes for CO₂ adsorption under direct air capture conditions. *Journal of CO₂ Utilization* **22**, 270 (2017).
262. Lin, Y., Yan, Q., Kong, C. & Chen, L. Polyethyleneimine incorporated metal-organic frameworks adsorbent for highly selective CO₂ capture. *Scientific Reports* **3** (2013).
263. Douglas M., R. *Principles of Adsorption and Adsorption Processes* (John Wiley & Sons, New York, 1984).
264. Veneman, R., Hilbers, T., Brilman, D. W. & Kersten, S. R. CO₂ capture in a continuous gas-solid trickle flow reactor. *Chemical Engineering Journal* **289**, 191 (2016).

265. Sehaqui, H., Salajková, M., Zhou, Q. & Berglund, L. A. Mechanical performance tailoring of tough ultra-high porosity foams prepared from cellulose i nanofiber suspensions. *Soft Matter* **6**, 1824 (2010).
266. Schell, J., Casas, N., Blom, R., Spjelkavik, A. I., Andersen, A., Cavka, J. H. & Mazzotti, M. MCM-41, MOF and UiO-67/MCM-41 adsorbents for pre-combustion CO₂ capture by PSA: Adsorption equilibria. *Adsorption* **18**, 213 (2012).
267. LEWATIT® VP OC 1600 - *Liquid Purification Technologies*
268. Gebald, C., Wurzbacher, J. A., Tingaut, P., Zimmermann, T. & Steinfeld, A. Amine-Based Nanofibrillated Cellulose As Adsorbent for CO₂ Capture from Air. *Environmental Science & Technology* **45**, 9101 (2011).
269. LEWATIT® VP OC 1065 - *Liquid Purification Technologies*
270. Sonnleitner, E., Schöny, G. & Hofbauer, H. Assessment of zeolite 13X and Lewatit® VP OC 1065 for application in a continuous temperature swing adsorption process for biogas upgrading. *Biomass Conversion and Biorefinery* **8**, 379 (2018).
271. Yang, R. T. *Gas Separation by Adsorption Processes* (Elsevier, 1987).
272. Goyal, P., Purdue, M. J. & Farooq, S. Adsorption and Diffusion of N₂ and CO₂ and Their Mixture on Silica Gel. *Ind. Eng. Chem. Res.* **58**, 19611 (2019).
273. Deb, K., Pratap, A., Agarwal, S. & Meyarivan, T. A fast and elitist multiobjective genetic algorithm: NSGA-II. *IEEE Transactions on Evolutionary Computation* **6**, 182 (2002).
274. Daizo, K. & Levenspiel, O. *Fluidization engineering, 2nd edition* 1991.
275. Casas, N., Schell, J., Joss, L. & Mazzotti, M. A parametric study of a PSA process for pre-combustion CO₂ capture. *Separation and Purification Technology* **104**, 183 (2013).
276. Gebald, C., Tanja, Z. & Tingaut, P. WO2012168346A1 (2012).
277. Thyagarajan, R. & Sholl, D. S. A Database of Porous Rigid Amorphous Materials. *Chemistry of Materials* **32**, 8020 (2020).
278. Chung, Y. G., Haldoupis, E., Bucior, B. J., Haranczyk, M., Lee, S., Vogiatzis, K. D., Ling, S., Milisavljevic, M., Zhang, H., Camp, J. S., Slater, B., Siepmann, J. I., Sholl, D. S. & Snurr, R. Q. Computation-Ready Experimental Metal-Organic Framework (CoRE MOF) 2019 Dataset. *Chemistry of Materials* (2019).
279. Do, D. D. *Adsorption Analysis: Equilibria and Kinetics* (PUBLISHED BY IMPERIAL COLLEGE PRESS and DISTRIBUTED BY WORLD SCIENTIFIC PUBLISHING CO., 1998).

280. Buttersack, C. Modeling of type IV and V sigmoidal adsorption isotherms †. *Phys. Chem. Chem. Phys* **5614**, 5614 (2019).
281. Pedersen, M. E. H. Good parameters for particle swarm optimization. *Hvass Lab., Copenhagen, Denmark, Tech. Rep. HL1001*, 1551 (2010).
282. Kennedy, J. & Eberhart, R. Particle swarm optimization. *Proceedings of ICNN'95 - International Conference on Neural Networks* **4**, 1942 (1995).
283. Mezura-Montes, E. & Coello Coello, C. A. Constraint-handling in nature-inspired numerical optimization: Past, present and future. *Swarm and Evolutionary Computation* **1**, 173 (2011).
284. *Europe Stainless Steel Prices | 3 Year's Historical Data | MEPS*
285. *Aluminum - 2022 Data - 1989-2021 Historical - 2023 Forecast - Price - Quote - Chart*
286. *Polymer BASF price from \$1444 / MT [05.07.2022]*
287. Turton, R., Bailie, R. C., Whiting, W. B. & Shaeiwitz, J. A. *Analysis, synthesis and design of chemical processes* (Pearson Education, 2008).
288. Narayanan, H., Viswanathan, B., Krishnamurthy, K. R. & Nair, H. in *Solar Hydrogen Production: Processes, Systems and Technologies* (2019).

NOMENCLATURE

Acronyms

\hat{j}_L	nominal photogenerated current density, mA/cm ²
\hat{P}_{sun}	ideal illumination, sun
α	Isotherm exponent
α	saturation level
β	parameter of the GAB model
χ	Isotherm isotherm parameter
$\Delta\overline{G^0}_{H_2}$	Gibbs free energy, kJ/g
$\Delta H_C, \Delta H_K$	GAB isotherm parameters, kJ/mol
ΔH	heat of adsorption, kJ/mol
$\Delta q, wc$	working capacity, mol/kg
\dot{m}	mass flow, kg/s
\dot{Q}	heat requirement, kJ
\dot{V}	volume flow, m ³ /s
\dot{V}_{feed}	feed volume stream, m ³ /s
\dot{W}	specific work, kJ
ϵ	Void fraction
η	efficiency
η_F	Faradaic efficiency
η_{2nd}	second law efficiency
η_{STH}	solar to hydrogen efficiency
γ	contactor/module cost, \$m ³

- γ parameter for vacuum pump
- μ viscosity, g/m/s
- Φ purity
- ρ density, kg/m³
- σ S-shaped parameter
- τ pore tortuosity
- τ_H Tafel slope of HER, mV/dec
- τ_O Tafel slope of HER, mV/dec
- c_{el} electrical energy cost, \$cents/kWh
- c_{th} thermal energy cost, \$cents/kWh
- ζ absorber loading, kmol/kmol
- A area, m²
- a Fitting parameter equivalent temperature
- a specific area, m²/t_{H₂}
- a, b, c, d, e empirical constants
- b Fitting parameter equivalent temperature
- b Isotherm affinity coefficient, 1/kPa
- b_0 Isotherm affinity coefficient at reference temperature, 1/kPa
- $C_{G/G,0/m/m,0}$ GAB isotherm parameter
- $C_{G/G,0/m/m,0}$ GAB isotherm parameter
- D mass diffusivity, m²/s
- d diameter, mm
- d specific reboiler duty, MJ/kg_{lean}
- e, E specific exergy/energy, MJ/kg_{CO₂}
- E° thermodynamic potential

$e_{\text{H}_2}^{\text{year}}$	energy stored in hydrogen molecules in a square meter of PV-EC over the year, kJ/m^2
f_{split}	split fraction
f_b	bulk factor
g	gravity constant, m/s^2
H	height, m
h	heat transfer coefficient, $\text{W}/\text{m}^2/\text{K}$
j	current density, mA/cm^2
j_0	saturation (dark) current density, mA/cm^2
j_H^0	exchange current density at HER, mA/cm^2
j_L	photogenerated current density, mA/cm^2
j_O^0	exchange current density at OER, mA/cm^2
k	mass transfer coefficient, $1/\text{s}$
$K_{\text{ads/o}}$	GAB isotherm parameter
k_B	Boltzmann constant, J/K
L	length, m
m	mass, kg
$m_{\text{H}_2}^{\text{year}}$	hydrogen produced over the year per square meter, $\text{t}_{\text{H}_2}/\text{m}^2$
MW	molar mass, mol
N	amount of moles, mol
n_{so}	Isotherm maximum capacity at reference temperature, mol/kg
n_s	Isotherm maximum capacity, mol/kg
n_i	ideality factor
n_j	number of junctions
n_s	number of solar cells connected in series

p	pressure, Pa
p_0	saturation pressure of water vapor, kPa
p_{step}	step partial pressure, MPa
P_{sun}	real illumination, mW/cm
Pr	productivity, kg/m ³ /h
q	adsorbed phase concentration, mol/kg
q	elementary charge, C
q	solid phase concentration, mol/kg
R	ideal gas constant, J/mol/K
R	universal gas constant, J/mol/K
R^2	error
R_s	series resistance, Ω/cm^2
R_{sh}	shunt resistance, Ω/cm^2
R_{sol}	electrolyte solution resistance, $\Omega.cm^2$
T	temperature, K
t	Isotherm exponent
t	time, s
T_0	reference temperature, K
t_0	Isotherm exponent at reference temperature
u	velocity, m/s
u_{mf}	minimum fluidizing velocity, m/s
V	voltage, mV
V	volume, m ³
V_c	column volume, m ³
V_{th}	thermal voltage (25.9 mV at T = 300K)

W	width, m
W	work, MJ
w	mass fraction
w	weighting function
X	conversion factor
y	concentration, ppm
y	molar fraction
ΔH_{ads}	isosteric heat of adsorption, J/mol
Δg^{min}	specific minimum Gibbs free energy, kJ/mol
\dot{Q}	specific heat, kJ/kg
Φ	purity
c_p	specific heat capacity at constant pressure, kJ/kg/K
e^{th}	Specific thermal energy, kJ/kg _{CO₂}
r	capture rate

Abbreviations, Subscripts and Superscripts

AB	air blower
ads	adsorption
ASU	air separation unit
b	bulk
BD	blow-down
CAPEX	capital expenditures
CCS	Carbon Capture and Storage
chem	chemisorption
comp	compression
cp	chemisorption-physisorption

CSS	cyclic steady state
DAC	direct air capture
des	desorption
DSL	dual-site Langmuir
EC	electrochemical
el	electrical
eq	equivalent
equ	equilibrium
err	error
exempl	exemplary
exp	experimental
f	fluid,final
fit	fitted
GAB	Guggenheim, Anderson, and de Boer
GCMC	Grand Canonical Monte Carlo
HER	hydrogen-evolving reaction
i	component
KOH	Potassium hydroxide
LHV	lower heating value, MJ/kg
max	referring to maximum
MEA	Monoethanolamine
mf	minimum fluidization
min	referring to minimum
MOF	metal-organic framework
N	number of experimental points

n	amount of sorbents
NET	Negative Emissions Technology
NRTL	Non-Random-Two-Liquid-Modell
OER	oxygen-evolving reaction
OPEX	operational expenditures
p	particle
PC	photocatalytic
PE	photoelectrodes
PEC	photoelectrochemical
phys	physisorption
prod	production
PSA	pressure swing adsorption
PV	photovoltaic
PV-E	photovoltaic + electrolyzer
PVSA	pressure-vacuum swing adsorption
refr	refrigeration
reg	regeneration
RH	relative humidity
RK	Redlich-Kwong
s	solid, sorbent
sat	saturation
sens	sensible
SLJ	solid-liquid junction
spec	specified
SRK	Soave-Redlich-Kwong

STH solar-to-hydrogen

th thermal

vac vacuum

vap vapor

VP vacuum pump

VPTSA vacuum-pressure temperature swing adsorption

ACKNOWLEDGEMENTS

This dissertation is the result of nearly five years of inspiring discussions and dedicated research, and I am so grateful to the people who made this possible. Apart from the subject of my Ph.D., all the people I have met and worked with made me enjoy my time at Utrecht university. Therefore, I would like to express my gratitude for the practical, intellectual, and emotional support I received from these people in the years leading up to this work.

First and foremost, I would like to thank Matteo for sharing his many insights and deep knowledge with me over the past five years. You are an outstanding supervisor and a great researcher, and I have been fortunate to do my Ph.D. under your supervision. I value your practical suggestions, moral support, and encouragement, which led me to believe in myself. Your detailed, hand-written feedback always pushed my articles in the right direction. It is a time I will never forget, and I will always think about it with joy.

I am also indebted to Gert Jan for his invaluable supervision during the course of my Ph.D. degree. I am thankful for your support and trust. Your calm and thorough advice elevated the quality of my work and gave me confidence at every stage of the process, even in very stressful times. I very much liked the scientific and less-scientific discussions we had.

It has been a true privilege to work with a number of wonderful collaborators for this Ph.D. project. From TU Eindhoven, I would like to thank Francesco, my collaborator during this project. I really enjoyed working with you and the meetings we had together. I also would like to thank Martin, during our meetings, you always had a challenging question, which made me think deeper about my work. Fausto, thank you for your support; it has been a pleasure working with you. I would also like to acknowledge Shell for making this research possible and organizing team meetings that provided precious feedback. I especially want to thank Alexander, your comments and insights during the many project meetings we had over the years were very valuable; thank you for sharing them. I am also very grateful to Mark and Sayee for their support of the project. The discussions with you were always something I was looking forward to; thank you all for the wonderful collaboration. I am also grateful to my local collaborators Jan and Lukas. In addition, I would like to thank Arvind for the detailed discussions on the draft version of Chapter 3.

Furthermore, I appreciate very much that Prof. dr. M. van Sint Annaland, Prof. dr. C.A. Ramirez Ramirez, Prof. dr. C. Petit, Prof. dr. A. Rajendran, and Dr. A. van

der Made accepted the task of being the co-examiners of this thesis. Thank you very much for taking the time to read and evaluate my dissertation.

I am very grateful to all the students I worked with during this thesis. Wouter de J., Leonie, Wouter K., Janet, Alix, and Xiao, thanks a lot for your great work.

I also owe a big thank you to all of my Copernicus colleagues. Thank you for the welcoming working environment and the interesting, amusing lunches and coffee breaks: Lennard, Nico, Anand, Anna, Jing, Wouter, Vincent, Gijs, Christian, Paul, and all the others. I was also lucky enough to share my office with amazing office mates during my time at the university. Vincent, Gijs, Swarnendu, and Swantje, you made the office work much more enjoyable. A special thanks also to the colleagues of my group Jan, Lukas, Julia, Shiyu, and Zhi. Thank you for the friendly working climate; it was great working with you and enjoying our secret coffee breaks. Jan, to you, in particular, I am very grateful. Thank you for all the nice moments and great talks, both on academia and on life.

Last but most certainly not least, I would like to thank my family. My parents, who supported me throughout my studies and my Ph.D. I could always recharge my batteries and clear my head when I was at your home. Laura, you always had time to talk, which helped me a lot, especially during frustrating times. Arno, thank you for your support and the great cover for my thesis. Adrian and Simon, you are my inspiration to achieve great things. You have made me stronger, better, and more fulfilled than I could have ever imagined. And to Thomas for your constant support, love, and motivation that got me through the last years and helped me complete my research.

CURRICULUM VITAE

Alexa Grimm was born in Malsch, Germany, on October 11th 1988. She studied mechanical engineering at Technical University Hamburg-Harburg (TUHH). After completing her bachelor's degree in 2011, she began a master's program at the Technical University Munich (TUM) with a specialization in Energy and Process Engineering. In 2014, her Master's thesis was completed on the Design of Microgasturbines in collaboration with Robert Bosch GmbH. After graduating, she joined a start-up company in Munich (Elcore GmbH) that develops fuel cell systems. Here she began working in the Engineering and Research Department and became a team leader in the engineering department. In 2017, she started as a guest researcher at TU Delft in the group of prof. dr. A. P. Vellayani, working on the production of hydrogen using non-thermal plasma.



Begin of 2018, Alexa started her Ph.D. project at the Copernicus Institute of Sustainable Development, Utrecht University, under the supervision of prof. dr. Gert Jan Kramer and dr. Matteo Gazzani. In collaboration with Eindhoven University of Technology and with the support of Shell Global Solutions, her research mainly focuses on capturing carbon dioxide from the air and the production of hydrogen using solar energy.

As of November 2022, Alexa works as Process Engineer and R&D Engineer at Nordsol in Bunnik, Netherlands.